An Ultra-High Vacuum Scanning Tunneling Microscope with Pulse Tube and Joule-Thomson cooling operating with sub-pm z-noise

Von der Fakultät für Mathematik und Naturwissenschaften der

RWTH Aachen University

zur Erlangung des akademischen Grades eines Doktors der Naturwissenschaften genehmigte Dissertation

vorgelegt von

Marcus Pascal Eßer, Master of Science RWTH Aachen University

aus Viersen

Berichter: Univ.-Prof. Dr. rer. nat. Markus Morgenstern
Univ.-Prof. Dr. ès Sciences Markus Ternes

Tag der mündlichen Prüfung: 15.12.2025

Diese Dissertation ist auf den Internetseiten der Universitätsbibliothek online verfügbar.

Abstract

Vibrations pose a significant challenge for scanning tunneling microscopy (STM) and spectroscopy (STS). STS is a key technique for investigating electronic and magnetic properties on the atomic scale. Due to the energy resolution limited by temperature, STS is often performed at cryogenic temperatures. Primary cooling is typically achieved using cryogenic liquids such as LN_2 or L^4He. To counteract the rising helium costs, a transition to alternative cooling concepts is necessary. However, inherently introduced vibrations of novel helium-loss-free cooling methods, such as pulse tube cryocoolers (PTC), make their implementation in STM systems particularly challenging.

This work presents the development of a compact ultra-high vacuum (UHV) STM system primarily cooled by a TransMIT PTC (PTD 411 DN160CF Option). The PTC is bakeable up to 150 °C, operates at an adjustable frequency (1.1 – 1.6 Hz), and is controlled via a rotary valve connected only by a flexible hose to the PTC. A subsequent Joule-Thomson (JT) cooling stage from CryoVac enables further cooling of the STM to below 1.5 K. The achieved tip-sample distance stability is below $1\,pm_{RMS}$ at 5 kHz bandwidth, making it as good as conventional STM systems cooled with L^4He. This high level of stability is attained through a soft mechanical coupling of the PTC to the STM system ($\leq$1 Hz), while simultaneously ensuring sufficient thermal coupling. These two requirements are inherently conflicting, but solved through an optimized design. The mechanical isolation between the PTC, which is rigidly mounted to the floor, and the UHV chamber, which is supported by isolators, is realized using highly flexible stainless steel membrane bellows, while the remaining stiffness is compensated using an opposing force spring mechanism. As a result, the UHV chamber oscillates freely in all directions with a resonance frequency below the PTC's operating frequency. The thermal coupling to the PTC is achieved via flexible stranded copper wire (diameter: 50 µm) connections, linking the PTC to a two-stage, coaxial arrangement of cooling plates with radiation shields. These plates are rigidly mounted to the chamber using stiff, yet thermally low-conductive hexagonal grid structures. The subsequent JT cooling stage is thus also rigidly connected to the chamber. The STM itself is suspended from the JT stage using three soft spiral springs (4 Hz resonance frequency). The final isolation stage is the STM itself. It is mechanically optimized and constructed from ceramic, featuring resonance frequencies, all exceeding 4 kHz and a measured transmission of vibrational amplitudes to the tunneling junction of

10^{-5} at 10 Hz. The performance of the system was tested using various sample systems. Atomic resolution and standing electron waves were demonstrated on Au(111) surfaces. Key system parameters include an electronic temperature of 1.7 K, determined from the shape of the superconducting energy gap of lead (Pb), a low voltage noise, determined by the investigation of Cooper-pair tunneling at a Pb-vacuum-Pb junction, which is reflected by a FWHM of the Josephson peak of 120 µV, as well as a minimal lateral drift of 18 pm/h. Furthermore, an integrated antenna within the STM allows the coupling of radio-frequency electric fields with frequencies up to 40 GHz and amplitudes exceeding 10 mV into the tunneling junction. This allowed a successful demonstration of microwave-assisted Cooper-pair tunneling.

Importantly, this design permits the integration of a superconducting magnet and can be extended to lower temperatures through the use of ^{3}He in the JT stage or additional subsequent cooling stages such as dilution refrigerators. Consequently, STM operation across the full relevant temperature range can be maintained in the future using helium-loss-free cryostats.

Parts of the thesis have been published in [1] promoting the main achievement of the working 1 K STM using a PTC.

Kurzfassung

Vibrationen stellen eine erhebliche Herausforderung für die Rastertunnelmikroskopie (STM) und Spektroskopie (STS) dar. STS ist eine Schlüsselmethode zur Untersuchung elektronischer und magnetischer Eigenschaften auf atomarer Längenskala. Aufgrund der durch die Temperatur limitierten Energieauflösung wird STS häufig bei tiefen Temperaturen durchgeführt. Die primäre Kühlung erfolgt in der Regel durch Kryoflüssigkeiten wie flüssigem N_2 oder ^{4}He. Ein Entgegenwirken der aktuell steigenden Heliumpreise erfordert den Übergang zu alternativen Kühlkonzepten. Neuartige, heliumverlustfreie Kühlmethoden, wie beispielsweise Pulsröhrenkühler (PTC), weisen jedoch inhärente Vibrationen auf, wodurch deren Einsatz in STM-Anlagen anspruchsvoll ist.
In dieser Arbeit wird die Entwicklung einer kompakten Ultrahochvakuum (UHV) STM-Anlage beschrieben, deren primäre Kühlung durch einen PTC der Firma TransMIT (PTD 411 DN160CF Option) erfolgt. Der PTC ist bis zu einer Temperatur von 150 °C ausheizbar, arbeitet mit einer regelbaren Betriebsfrequenz (1.1 – 1.6 Hz) und einem Drehventil, welches lediglich durch einen flexiblen Schlauch mit dem PTC Kühler verbunden ist. Eine nachgeschaltete Joule-Thomson (JT) Kühleinheit der Firma CryoVac ermöglicht eine weitere Abkühlung des STM's auf eine Temperatur von unter 1.5 K. Die erreichte Stabilität des Spitzen-Proben Abstands beträgt dabei weniger als 1 $\mathrm{pm_{RMS}}$ bei einer Bandbreite von 5 kHz und ist somit genau so gut wie konventionelle, mit flüssigem Helium gekühlte STM-Anlagen. Diese hohe Stabilität wurde durch eine möglichst weiche mechanische Ankopplung des PTC zum STM System erzielt ($\leq$1 Hz), die zugleich eine ausreichende thermische Ankopplung gewährleisten muss. Dies sind zwei sich widersprechende Anforderungen, die in einem optimierten Design vereint wurden. Die mechanische Entkopplung zwischen dem fest mit dem Boden verbundenem PTC und der durch Isolatoren getragenen UHV Kammer, basiert auf einer Kombination aus möglichst flexiblen Membranbälgen aus Edelstahl in Kombination mit einem Konzept der Kompensation der verbleibenden Steifigkeit durch entgegenwirkende Federkräfte. Als Resultat ergibt sich eine in alle Richtungen schwingende UHV Kammer mit einer Eigenresonanzfrequenz unterhalb der Betriebsfrequenz des PTC. Die thermische Ankopplung an den PTC erfolgt über flexible Verbindungen aus feinadrigen Kupferlitzen (Durchmesser: 50 µm) zwischen PTC und einer zweistufigen, koaxialen Anordnung aus Kühlplatten mit Strahlungsschildern. Diese sind mittels steifer, aber niedriger wärmeleitfähiger Strukturen aus einer hexagonalen

Gitterstruktur mit der Kammer fest verschraubt. Die nachfolgende JT Kühleinheit ist somit fest an der Kammer verschraubt. Das STM ist an drei weichen Spiralfedern (4 Hz Resonanzfrequenz) an der JT-Stufe hängend befestigt. Als letzte Isolationsstufe dient das mechanisch optimierte STM aus Keramik selbst. Es weist Resonanzfrequenzen oberhalb von 4 kHz auf und zeigt eine gemessene Dämpfung mechanischer Schwingungsamplituden zum Tunnelkontakt von 10^{-5} bei 10 Hz. Die Leistungsfähigkeit des Systems wurde anhand verschiedener Probensysteme getestet. Atomare Auflösung und stehende Elektronenwellen konnten an Au(111)-Oberflächen demonstriert werden. Die ermittelten Eckdaten des Systems sind unter anderem eine elektronische Temperatur von 1.7 K, ermittelt an der supraleitenden Bandlücke von Blei (Pb), sowie ein geringes Spannungsrauschen, ermittelt durch die Untersuchung von Cooper-Paar Tunneln an einem Pb-Vakuum-Pb Übergang, wiedergespiegelt durch eine Breite (FWHM) des Josephson Peaks von 120 µV, als auch eine geringe laterale Drift von 18 pm/h. Des Weiteren ermöglicht eine im STM verbaute Antenne das Einkoppeln von hochfrequenten elektrischen Wechselfeldern mit Frequenzen von bis zu 40 GHz und Amplituden größer als 10 mV im Tunnelkontakt. Mikrowellen unterstütztes Cooper-Paar Tunneln konnte hierdurch demonstriert werden.
Darüber hinaus eröffnet das Konzept die Möglichkeit für den Einbau eines supraleitenden Magneten sowie eine Erweiterung hin zu tieferen Temperaturen durch den Einsatz von ^{3}He in der JT stage oder weiterer nachgeschalteten Kühleinheiten wie Entmischungskryostaten. Somit ist ein weiterer Betrieb von STM Systemen über den gesamten interessanten Temperaturbereich hinweg durch Helium verlustfreie Kryostaten in der Zukunft weiterhin sichergestellt.
Teile der Arbeit wurden in [1] veröffentlicht und heben die Errungenschaft des funktionsfähigen 1 K STM mit einem PTC hervor.

Contents

1. Introduction **11**

2. Background **17**

2.1. Fundamentals of Scanning Tunneling Microscopy 17

2.1.1. Scanning tunneling microscopy (STM) 17

2.1.2. Technical aspects of STM 20

2.1.3. Scanning tunneling spectroscopy (STS) 22

2.1.4. Limits of the energy resolution of STS 23

2.2. Closed-cycle cryocooler 24

2.2.1. Pulse tube cryocooler 24

2.2.2. Joule-Thomson cryocooler 38

2.3. STM vibration isolation in particular the concept of minimal stiffness . . 44

3. Design and Development of the STM System **49**

3.1. Room concept and integration into UHV 49

3.2. Selection of pulse tube cryocoolers 53

3.3. Vibration isolation concept, implementation into the overall concept . . . 63

3.3.1. Complemented vibration isolation 64

3.3.2. Linear minimal stiffness setup realization 65

3.3.3. Stiff support structure 69

3.3.4. STM spring suspension 73

3.4. Cryostat design 75

3.4.1. Supply lines for the JT stage 75

3.4.2. Radiation shields 76

3.4.3. Joule-Thomson stage 78

3.4.4. Precooling of the STM 79

3.4.5. Cryostat: thermal consideration . . . 79
3.5. STM . . . 84
3.5.1. STM design . . . 84
3.5.2. Optical access . . . 94
3.5.3. Radio frequency antenna . . . 95
3.6. Wiring concept . . . 97

4. Performance **109**
4.1. Vibration isolation performance . . . 109
4.1.1. STM . . . 109
4.1.2. Minimal stiffness . . . 113
4.1.3. Movement of decoupled STM chamber and z-noise in the tunneling junction . . . 116
4.2. Cryostat performance . . . 121
4.2.1. Temperature drop at the Cu stranded links . . . 121
4.2.2. Cooldown of the finalized system . . . 122
4.2.3. Temperature during a sample exchange . . . 123
4.2.4. Temperature stability . . . 123
4.2.5. Lowest temperatures . . . 125
4.3. STM and STS performance . . . 125
4.3.1. Sample and tip preparation . . . 126
4.3.2. Sample positioning . . . 126
4.3.3. Atomic resolution and standing electron waves . . . 128
4.3.4. Lateral drift . . . 131
4.3.5. Electronic temperature . . . 132
4.3.6. Voltage noise . . . 133
4.3.7. Subgap features in tip-sample Josephson junction . . . 137
4.3.8. Radio frequency in the tunneling junction . . . 140

5. Summary and outlook **153**

Bibliography **155**

A. Appendix **177**

B. Acknowledgments **183**

List of Acronyms

Al	aluminium
AR	atomic resolution
Au	gold
CAD	computer aided design
Ce	cerium
CF	conflat
CFD	computational fluid dynamics
Cu	copper
DC	direct current
DN	diameter nominal
DOS	density of states
ESR	electron spin resonance
EXG	exchange gas
fcc	face centered cubic
Fe	iron
FEM	finite elements method
FFT	fast Fourier transform
FM	ferromagnetic
FWHM	full width at half maximum
GM	Gifford-McMahon
GMC	Gifford-McMahon cryocooler
hcp	hexagonal close packed
HE	heat exchanger
HOPG	highly oriented pyrolytic graphite
Ir	iridium
JT	Joule-Thomson
LDOS	local density of states
L^{4}He	liquid helium 4
L^{3}He	liquid helium 3
^{4}He	helium 4
^{3}He	helium 3
LN_2	liquid nitrogen
LP	low-pass
MARs	multiple Andreev reflections
Mg	magnesium
Mn	manganese
Mo	molybdenum
mod	modulation
MS	minimal stiffness
N_2	nitrogen
p	peak
Pb	lead
pp	peak to peak
Pt	platinum
PT	pulse tube
PTC	pulse tube cryocooler
PTFE	polytetrafluoroethylene
RF	radio frequency
RL	remote liquefaction
RMS	root mean square
RT	room temperature
SS	stainless steal
STM	scanning tunneling microscope (microscopy)
STS	scanning tunneling spectroscopy
TDR	time-domain reflectometer
TP	twisted pair
TS	temperature sensor
UHV	ultra high vacuum
US	United States
VNA	vector network analyzer
W	tungsten

1. Introduction

Scanning Tunneling Microscopy (STM), invented by Binnig and Rohrer [2], stands as an indispensable tool across a spectrum of scientific disciplines, including condensed matter physics, nanotechnology, surface science, material science, chemistry [3–5], and biology [6]. Its versatility lies in its ability to aid the understanding and manipulation of matter at the molecular or even atomic scale [7] facilitating access to their electronic and magnetic fundamental properties. However, the energy resolution of scanning tunneling spectroscopy (STS) is limited upon thermal broadening of states in the tip and/or sample, potentially obscuring features such as inhibited topological backscattering [8], standing electron waves [9], superconducting gap structures [10–12], electron spin precession [13], Landau level quantization [14–16], magnetic excitations [17, 18], the Kondo effect [19–21], phonon excitations [22, 23], plasmon excitations [24], electron induced light emission [25], Majorana modes [26], Luttinger liquid properties [27–29], and the dynamics between a spin of a nucleus and an orbiting electron [30]. Cooling down a STM within a cryostat [31, 32] is required, leading to an energy resolution of better than 1 meV below 4 K [33, 34] which also minimizes thermal drift (<1 pm/min) [35]), thus ensuring precise tip location relative to the sample with low noise.

The cooling of STMs with L^{4}He by bath or flux cryostats suffers from ^{4}He losses that get increasingly expensive. Closed-cycle cryostats are being used more frequently to avoid such losses. In this thesis, a pulse tube cryocooler (PTC) in combination with a Joule-Thomson (JT) stage is used to reach temperatures of ∼1 K. With conventional cooling by a bath or flux cryostat in combination with an ^{4}He recovery and liquefaction system, losses of about 10 % are usual. This is, e.g. due to a combination of leakages, technical faults, and handling of the LHe during transport of the dewars or during purging of a transfer line. Assuming a cryostat that requires 100 L of L^{4}He in a week, the resulting loss is about 7000 L ^{4}He gas per week (20 °C, 1.013 bar) amounting to costs of 200 € to 500 € depending on the actual contract. On the other hand, reports of ^{4}He

shortage appear more and more often [36–40]. This is also reflected in the price trend. The price development without surcharges for ^{4}He Grade A (99.9 % purity) increased from the year 2000 to 2022 by more than 600 % [41, 42]. The worldwide ^{4}He demand continuously increases, predicting an overall demand growth by up to 4 % until 2028 [43] and an increase in global helium consumption until 2040 of ∼50 % [44]. There are several reasons for the ^{4}He shortage. In 1996, a law was passed to sell the US reserve of ^{4}He [45]. The US ^{4}He reserve, which started selling in 2005, flooded the market with below-market prices of ^{4}He. It changed with a reformed pricing starting in 2014. The Mineral Commodity in the US gives a list of unplanned shutdowns or problems in other parts of the world, often in correlation with political trends [41, 42]. Despite this intimidating trend, our developed closed-cycle STM system should continue to enable research in all SPM fields in the future.

This thesis focuses on the cooling using a closed-cycle cryostat and its challenges. One is the ultra-high vacuum (UHV) suitability of all used materials and constructions. STM is mostly performed in UHV conditions to prevent contamination and maintain the integrity of the sample surface. Approximately, if all impinging adsorbates stick to the surface, one layer of adsorbates forms within one second at a vacuum of 1×10^{-6} mbar while at UHV conditions, a clean surface can be maintained, at least, for several hours [46]. Experiments requiring a magnetic field will not be prohibited, because cryocoolers can also be used in magnetic fields [47]. The main challenge is to deal with the disadvantage of vibrations caused by the PTC that can be transmitted via the PTC head or the PTC cold stages to the STM [48]. For closed-cycle coolers, a PTC is stated to be the least vibrational one, surpassing the Gifford-McMahon cooler (GMC), because it has no mechanical moving inherent parts, besides a separable turning valve [49]. The PTC also shows inherent mechanical vibrations and acoustic noise due to periodically pulsed flowing ^{4}He. For example, it has been found that the vibrations on the PTC-head are two orders of magnitude smaller than that on top of a Gifford-McMahon cooler [50]. Typical vibration amplitudes are a few micrometers [51], e.g. ∼10 µm at the 60 K stage and ∼15 µm at the second stage [50, 52]. The performance of these coolers is constantly being improved in terms of their vibrational properties. This exploits, e.g. that their vibration amplitude scales linearly with the pressure variation [53]. Mechanical anchoring of the PTC and the rotary valve to a big mass can reduce the noise further [48]. Also, different tube shapes are considered [54], or constructions with multiple tubes [55]. In

addition, intrinsic temperature oscillations can be an issue, leading to vibrations by cyclic contraction and elongation of the materials [56]. Vibration transmission to an experiment is often minimized by using bellows, a ^{4}He exchange gas or soft thermal links [57]. This always deals with the competition between a good thermal connection and a low vibrational transmission.

The cool-down time of the experiment is longer for a cryocooler than for a bath cryostat. However, novel methods can improve this time up to 3.5 times compared to a PTC that is only optimized for its base temperature [58]. This time is typically not a big issue for STM where there is often no high sample throughput.

Another strong argument for the utilization of cryocoolers is their convenience. They come with less safety issues, omitting educated personnel, are easier to use, and one can study the same atomic configuration for weeks without interruption for refilling cryogenic fluids. Such refilling causes thermal drift and includes the chance of destroying the microtip. One should keep in mind that the preparation of the tip is the most time-consuming part in STM experiments.

In recent years, there have been some reports of low-temperature STMs operating with closed-cycle coolers. The first ones were a home-built high vacuum STM system cooled by a commercial PTC combined with an additional dilution refrigerator [59] and a UHV STM system using ^{4}He exchange gas [60]. Some systems are operating without UHV at temperatures of e.g. 1.6 K [61]. Commercially available systems in UHV reach temperatures around 10 K (Scienta Omicron: Fermi DryCool™ SPM), 13 K (RHK Technology) [62] and near 5 K (Unisoku) [63]. Most recently, there have been publications of two other systems, one at 3 K, using a remote liquefaction in combination with a continuous flow cryostat [64] and one operating at 1.4 K in UHV with a PTC as part of the STM chamber [65]. Table 1.1 compares the previously published closed-cycle UHV STM systems, organized by publication date in descending order. The table includes key parameters such as the final temperature achieved at the STM, cooling technology, thermal coupling, mechanical isolation of the cooling units, axial magnetic field, cool-down time, and reported z-noise of the tunnel junction. The system described in this thesis offers several advantages not found in a combined way in any of the previous systems: 1) The PTC must not be removed during the baking of the system. 2) A second PTC is not required for magnet operation. 3) It has the option to use ^{3}He to achieve temperatures down to 500 mK [66]. 4) No needle valve needs to be operated for the 1 K stage. 5)

No requirement of ^{4}He exchange gas, omitting the necessity of large gas storage tanks, complex gas handling systems, and thin-walled tubes or heat exchangers. Overall, the system consistently demonstrates z-noise in the sub-picometer range without feedback regulation at a temperature of 1.5 K. It achieves atomic resolution, demonstrates standing electron waves, as well as superconducting gaps indicating an electronic temperature of 1.7 K. Additionally, Josephson currents reveal residual voltage noise of 140 μV_{pp} while microwave-assisted Cooper-pair tunneling confirms radio frequency capabilities up to 40 GHz. The PTC can be heated up to 150 °C for baking and the rotary valve connection is via a single flexible hose only. Additionally, it allows a tuning of the PTC's operation frequency between 1.1 Hz and 1.6 Hz. Efficient vibration decoupling is achieved through a fully passive design. Each of the two PTC stages is mechanically decoupled using bundles of 50 µm thin copper wires that serve as thermal links towards cooling plates. These cooling plates are directly connected to thermal shields, the JT stage and ultimately the STM, supported using three soft springs. High stiffness and low thermal conductivity are ensured by mounting the cooling plates via honeycomb structures to the UHV chamber surrounding the STM. Further isolation of this chamber from vibrations, generated by the rigidly mounted PTC, is accomplished by incorporating UHV bellows with minimal stiffness, aided by counteracting springs. Consequently, the UHV system, supported by Minus K® vibrational isolators, can move freely in all directions with respect to the floor and the PTC with a resonance frequency below that of the PTC's operational frequency. Finally, the STM body is designed to minimize low-frequency vibration transmission. The measured transmission to the tunnel junction is 10^{-5} at 10 Hz, and extrapolated to 10^{-7} at 1 Hz.

This thesis is structured in the following way: The background is described in Chapter 2. It starts with an introduction of STM and STS (Section 2.1). The cooling by PTC and JT cooler is briefly described in Section 2.2. The necessary vibration isolation of STM systems is summarized in Section 2.3 with the focus on the concept of minimal stiffness. Chapter 3 describes the development of the closed-cycle UHV STM system, starting with the laboratory setup (Section 3.1), the selection of PTC (Section 3.2), the vibration isolation concept (Section 3.3), the cryostat design including its operation (Section 3.4), the STM design itself (Section 3.5.1) and the wiring concept (Section 3.6). Chapter 4 reveals the performance of the system. It starts with the achieved vibration isolation of sub systems (Section 4.1) followed by the cryostat performance (Section 4.2). The STM

performance is afterwards demonstrated by its imaging stability including the z-noise in the tunneling junction, electronic temperature, voltage noise and radio frequency capabilities (Section 4.3).

Table 1.1.: **Table of UHV STM systems precooled with cryocoolers found in the literature and their key parameters. No entry indicates that the value is not given in the publication. Helium exchange gas (^{4}He EXG). Gifford-McMahon cryocooler (GMC). Remote liquefaction (RL). Atomic resolution (AR). Minimal stiffness (MS).**

location	**year**	T (K)	**cryocooler type**	**secondary cooling type**	**thermal coupling-vibration isolation**	**axial magnetic field** (T)	**cooldown time** (h)	**z-noise**
RWTH Aachen University[1]	2024	1.5	PTC	JT	Cu strands bellows and MS	-	40	AR,<1 $\mathrm{pm_{RMS}}$ (feedback off)
Rutgers University[67]	2024	4.6	PTC	-	^{4}He EXG bellows and MS	9	18	AR
Chinese Academy of Sciences[64]	2023	2.84	GMC	JT RL	transfer line springs	-	8.6	AR,<1 pm (feedback on)
Fudan University[65]	2022	1.4	PTC	1K-pot	^{4}He EXG bellows and springs	9	21	AR,0.7 pm(RMS) (feedback on)
UNISOKU Co., Ltd.[63]	2022	5.2	PTC	-	^{4}He EXG bellows and springs	-	12	AR
TIFR[62]	2021	13	GMC	-	^{4}He EXG bellows	5	-	AR
Fudan University[68]	2016	14.3	GMC	-	^{4}He EXG bellows and springs	-	5	AR, 2 pm
University of Oregon[60]	2014	16	GMC	-	^{4}He EXG bellows and springs	-	12	AR, 1.5 pm(feedback off)

2. Background

2.1. Fundamentals of Scanning Tunneling Microscopy

A significant portion of this work concerns the construction and optimization of the scanning tunneling microscope (STM) system. Thus, an extensive treatment of the theory of STM is not required. The scope of its discussion is limited to the understanding of the concepts that are necessary for the following chapters. A more detailed description can be found in the textbooks [69–71].

2.1.1. Scanning tunneling microscopy (STM)

STM started in 1982 with Binnig, Rohrer, Gerber and Weibel presenting their first results [2, 72]. By using a tip as a local probe, the STM is able to facilitate the understanding and manipulation of matter at the molecular and atomic scale. Moreover, access to their electronic and magnetic fundamental properties is provided. The principle is quantum tunneling, which already had been shown in the 1960's in planar junctions [73, 74]. The additional idea is to scan a surface (raster a grid of points on the surface) and thus display physical properties as an image. For example, the tunneling current between the tip and sample is used as a feedback parameter to regulate the tip-sample distance by keeping the current constant. The resulting tip height can be displayed as an image. This mode is called constant current mode. In a classical picture, electrons cannot overcome a potential barrier higher than their energy. In contrast, quantum mechanical particles have a probability to overcome such a barrier. The effect arises from the wave-like probability distribution of particles. Different approximations are used to describe the tunneling. A simple one is a one-dimensional potential barrier model with a barrier of constant potential height. The solution of the time-independent Schrödinger equation is a free electron plane wave outside the barrier. Inside the potential barrier, the solution is

exponentially decaying. At the edges of the barrier, boundary conditions have to be taken into account. The resulting probability to transmit an impinging electron across the potential barrier with width w is given as the transmission coefficient T_R (for $\kappa w \gg 1$):

$$T_\mathrm{R}(\epsilon, \Phi, w) = \frac{16k^2\kappa^2}{(k^2+\kappa^2)^2} e^{-2\kappa w}, \tag{2.1}$$

with the wave number of the electron k and the parameter κ given as:

$$k = \sqrt{\frac{2m_\mathrm{e}}{\hbar^2}\epsilon} \quad \text{and} \quad \kappa = \sqrt{\frac{2m_\mathrm{e}}{\hbar^2}(\Phi - \epsilon)}. \tag{2.2}$$

Here m_e is the electron mass, $\hbar$ is reduced Planck's constant, Φ is the barrier height, and $\epsilon < \Phi$ is the electron energy. In a real experiment, a voltage V of a few mV to Volt is applied between a metallic tip and a sample in a distance of a few Å. This leads to a measurable tunneling current if the sample is conducting current. The tunneling current depends on the density of states of the tip and sample in the energy interval eV around the Fermi level, with e the elementary charge. By convention, the voltage is applied to the sample, such that at positive sample voltage, electrons are tunneling from the tip to the sample. The resulting tunneling current I decreases exponentially with w. For a constant density of states at the tip and sample and $|V| \ll \Phi/e$, it reads:

$$I \propto V e^{-2\bar{\kappa}w}. \tag{2.3}$$

Here $\bar{\kappa} = \sqrt{\frac{2m_\mathrm{e}\overline{\Phi}(\epsilon,V)}{\hbar^2}}$ is the decay constant and $\overline{\Phi}(\epsilon, V) = (\Phi_\mathrm{tip} + \Phi_\mathrm{sample} + eV)/2 - \epsilon$ is the effective barrier height for a trapezoidal tunneling barrier (Figure 2.1). Considering electrons tunneling at $\epsilon = eV$, $\overline{\Phi}(\epsilon = eV, V) = (\Phi_\mathrm{tip} + \Phi_\mathrm{sample} - eV)/2$, with Φ_tip and Φ_sample the work function of the tip and sample, respectively.
The polycrystalline work functions Φ for the used materials in this thesis are [75, 76]:

- W: 4.55 eV, W(100): 4.63 eV
- Mo: 4.6 eV
- Au: 5.1 eV, Au(111): 5.31 eV
- Pb: 4.25 eV

The exponential dependence on w implies that relatively small changes in the tip-sample distance lead to significant variations in the tunneling current. Evaluation of $\bar{\kappa}$ implies a reduction of about 1 order of magnitude per 100 pm, eventually allowing atomic-scale resolution in imaging.

Up to now, the atomic 3D configuration of the tip and sample has been neglected. A three-dimensional model of tunneling was developed by Bardeen in 1961 [77]. In this model the transition between single particle states of the tip and sample, by elastic tunneling, is considered. The model uses the time-dependent perturbation theory, assuming weak coupling between the two sides, specifically Fermi's golden rule is applied at $T = 0\,\mathrm{K}$. This results in:

$$I = \frac{4\pi e}{\hbar} \sum_{i,f} |M_{\mathrm{fi}}|^2 \delta(E_{\mathrm{f}} - E_{\mathrm{i}}). \tag{2.4}$$

Here, E_{f} is the energy of the final state and E_{i} the one of the initial state. The sum runs over all occupied states i of one side and all unoccupied states f of the other side of the tunneling junction. The matrix elements $|M_{\mathrm{fi}}|$ describe the scattering or transfer of initial to final states. Equation 2.4 tells that one must sum over all initial and final states while the Dirac delta function δ shows that only elastic tunneling is possible.

In the *energy dependent approximation of the Bardeen model* the sum of tip and sample states is replaced by the energy-dependent densities of states.

$$I(V) = \frac{4\pi e}{\hbar} \int_0^{eV} \rho_{\mathrm{tip}}(\epsilon + eV) \rho_{\mathrm{sample}}(\epsilon) |M(\epsilon)|^2 \mathrm{d}\epsilon \tag{2.5}$$

Here, ϵ in $\rho_{\mathrm{tip}}(\epsilon + eV)$ is given with respect to the Fermi energy E_{F} of the tip and ϵ in $\rho_{\mathrm{sample}}(\epsilon)$ is given with respect to E_{F} of the sample. The matrix element is derived as:

$$M(\epsilon) = \frac{\hbar^2}{2m_e} \int_{A_{\mathrm{tip/sample}}} \left[\psi_{\mathrm{tip}}(\mathbf{r}, \epsilon) \nabla \psi^*_{\mathrm{sample}}(\mathbf{r}, \epsilon) - \psi^*_{\mathrm{sample}}(\mathbf{r}, \epsilon) \nabla \psi_{\mathrm{tip}}(\mathbf{r}, \epsilon) \right] \mathrm{d}\mathbf{A} \tag{2.6}$$

$A_{\mathrm{tip/sample}}$ is a plane between the tip and the sample. In practice, the atomic configuration of the tip is mostly not known, making it impossible to evaluate the tunneling matrix. Using the one-dimensional model of Equation 2.1, the matrix elements can be roughly approximated as:

$$|M(\epsilon)|^2 \approx T_{\mathrm{R}}(\epsilon, \overline{\Phi}, w) \tag{2.7}$$

At $T = 0\,\mathrm{K}$ the discussed formulas did not take the Fermi-Dirac function $f(\epsilon) = (1+\exp(\epsilon/k_\mathrm{B}T))^{-1}$ into account. Since the occupation of the density of states is broadened for temperatures $T \neq 0\,\mathrm{K}$, the tunneling current must be described by:

$$I(w,V) = \frac{4\pi e}{\hbar}\int_{-\infty}^{\infty}\{f(\epsilon+eV) - f(\epsilon)\}\,\rho_\mathrm{tip}(\epsilon+eV)\rho_\mathrm{sample}(\epsilon)T_\mathrm{R}(\epsilon,\overline{\Phi},w)\mathrm{d}\epsilon. \tag{2.8}$$

Unfortunately, one wants to map the sample surface density of states. However, the formula still contains the properties of the mostly unknown tip.
For $T \to 0\,\mathrm{K}$, a constant ρ_tip and $|V| \ll \overline{\Phi}/e$ the tunneling current favorably gets to:

$$I \propto \rho_\mathrm{sample}(E_\mathrm{F}, \boldsymbol{r}) \tag{2.9}$$

with $\boldsymbol{r}$ the tip position (center of the s-type electrons). The density of states can now be locally determined from the tunneling current as a function of tip position $\boldsymbol{r}$. To explain atomic resolution, a more detailed model must be considered, i.e. the electronic tip states must be taken into account [78]. For atomic resolution, $\mathrm{p_z}$ and $\mathrm{d_{z^2}}$ orbitals at the tip Fermi level are usually required. In STM, typically W, Pt or Ir tips are used, with the d-type states close to the Fermi level. The tip orbital dependence of STM imaging was demonstrated e.g. by Gross [79].

2.1.2. Technical aspects of STM

The most crucial requirements for optimal STM recordings are a clean surface, a precise positioning of the tip in relation to the sample (sub-atomic), a provision of a bias voltage with minimal electrical noise, and a detection/measurement of the tunnel current without noise.
In order to maintain a clean atomic surface of the sample, it is essential to ensure that UHV (ultra-high vacuum: low $10^{-10}\,\mathrm{mbar}$) conditions are consistently met. The absorption of residual particles on the sample surface is affected by pressure, temperature, and the material. As a general guideline, one monolayer of adsorbates is formed in approximately one second at a pressure of $10^{-6}\,\mathrm{mbar}$ if every impinging atom sticks to the surface. However, at UHV conditions, a clean surface can be maintained for at least several hours [46]. Piezo crystals are employed as actuators for precise positioning.

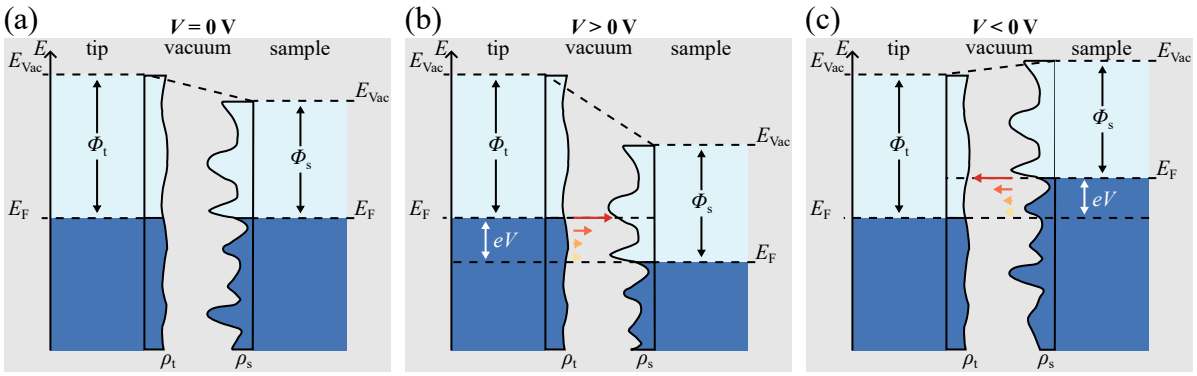


Figure 2.1.: **Principal of STM tunneling.** (a) Density of states of tip ρ_t and sample ρ_s, sketched for zero bias voltage with the Fermi energies E_F aligned. dark blue: occupied states, light blue: empty states, E_{Vac}: vacuum energy, Φ_t, Φ_s: work functions of tip (t) and sample (s). (b)-(c) Applying a bias voltage V, the Fermi levels are shifted by eV for a positive sample voltage in (b) and for a negative bias voltage in (c). Thereby, the direction of tunneling is altered and either occupied or unoccupied states in the sample are contributing to the tunnel current. The tunneling probability is indicated by arrows with the length and color proportional to the tunneling probability.

In our particular system, at the base temperature of ∼1 K, the tube scanners utilized provide approximately 1 nm/V. This indicates that the electrical control must exhibit noise amplitudes of less than 1 mV for pm resolution. For the RHK R9 high voltage output controller, the spectrum shows ∼100 μV_p at 1 Hz and ∼2 μV_p at 1 kHz. Other factors that may exert a detrimental influence on the precise positioning are as follows: 1) Mechanical relative movements between the tip and the sample, for example, caused by mechanical vibrations. 2) Piezo creep. 3) Thermal drift. The origin of mechanical vibrations and their counteraction is discussed in Section 3.3. The performance of thermal drift is described in Section 4.3.4. The piezo creep is caused by the slow deflection of the piezo actuator after applying voltage due to relaxation processes of the piezo material. The deflection depends exponentially on time and is temperature dependent.
The current detection is done using a trans-impedance amplifier (Femto Messtechnik GmbH, DLPCA-200) at low noise setting with a gain of 10^9 V/A and a bandwidth of 1.1 kHz that has a integrated noise of 2.4 pA_p.

2.1.3. Scanning tunneling spectroscopy (STS)

Scanning Tunneling Spectroscopy (STS) is an extension of STM that provides information about the local electronic properties of the sample surface. Other methods, such as photoelectron spectroscopy, only provide an area-averaged electronic density of states without correlation to the topography. In this chapter, the voltage dependence of the tunneling current will be further analyzed. The goal is to extract information on the local density of states (LDOS) of the sample. Using Equation 2.5 and Equation 2.7, a change in voltage will change the total tunneling current (Figure 2.1) according to

$$I(V,T,w) \propto \int_0^{eV} \rho_{\text{sample}}(\epsilon,x,y)\cdot\rho_{\text{tip}}(\epsilon-eV)\cdot T_{\text{R}}(\epsilon,V,w)\,\mathrm{d}\epsilon. \tag{2.10}$$

Recall that ϵ in $\rho_{\text{tip}}(\epsilon-eV)$ is measured with respect to E_{F} of the tip and ϵ in $\rho_{\text{sample}}(\epsilon,x,y)$ with respect to E_{F} of the sample. The x,y dependence indicates the local dependence of ρ_{sample} on the position on the sample. The effective barrier height for each electron is covered by the energy-dependent transmission coefficient:

$$T_{\text{R}}(\epsilon,V,w) \propto exp\left(-\frac{2w}{\hbar}\sqrt{2m_e\overline{\Phi}(\epsilon,V)}\right). \tag{2.11}$$

This does not consider the different decay for different orbital characters of the states, the k-dependence of the effective barrier height, the Fermi distribution for temperatures $T > 0\,\text{K}$ as well as an attractive image charge potential (relevant for larger bias voltages). As a consequence of Equation 2.10 and Equation 2.11, the differential conductance will not only be proportional to the sample LDOS (of interest) $\rho_{\text{sample}}(\epsilon,x,y)$ but also to the probing tip states, except if $\rho_{\text{tip}}(\epsilon-\text{eV})$ =const., and to the barrier height. One can show that the latter influence is small for small voltages. Assuming a constant DOS of the tip and a negligible dependence of T_{R} from V, the differential conductance $\frac{\mathrm{d}I}{\mathrm{d}V}$ is roughly proportional to the local density of states (LDOS) of the sample ρ_{s} at the position of the tip:

$$\frac{\mathrm{d}I}{\mathrm{d}V}(V,x,y) \propto \rho_{\text{s}}(E_{\text{F}}+eV,x,y). \tag{2.12}$$

The obtained $\frac{\mathrm{d}I}{\mathrm{d}V}(V,x,y)$ curves provide local information e.g. on energy band gaps, surface states or localized states. By measuring $\frac{\mathrm{d}I}{\mathrm{d}V}$ as a function of V and position, x,y, STS provides a spatially resolved map of the electronic density of states of the sample.

In order to circumvent feedback loop artifacts in STS, the feedback is typically switched off during the acquisition of a single $\frac{\mathrm{d}I}{\mathrm{d}V}(V,x,y)$ curve. For the acquisition, typically a lock-in technique is used. It enhances the sensitivity and signal-to-noise ratio. The bias voltage is modulated at a fixed frequency with an amplitude smaller than the energy resolution required. The modulation frequency is selected at a frequency that is distinct from the dominating noise frequencies, but within the bandwidth of the current preamplifier and above the feedback loop bandwidth, if this is on. The lock-in amplifier is synchronized with the modulation frequency, so the output is filtered to only the contribution of the applied frequency, filtering out other frequency contributions. The phase between the reference and the signal is adjusted to suppress the capacitive signals.

2.1.4. Limits of the energy resolution of STS

Fluctuations of the bias voltage between tip and sample as well as the broadening by the Fermi function in Equation 2.8 determine the energy resolution of the experiment. Hence, voltage noise reaching the tip or sample, e.g. by inductance in the wiring must be minimized. For room temperature, the thermal broadening is 85 meV and for 1 K 0.3 meV.

Another contribution arises due to the lock-in method adding the modulation voltage amplitude $V_{\mathrm{mod,p}}$ to the bias voltage. The energy resolution is then calculated as [80]:

$$\Delta E \approx \sqrt{(3.3k_{\mathrm{B}}T)^2 + (1.7eV_{\mathrm{mod,p}})^2}. \tag{2.13}$$

The first and second terms will be derived here, as they often show different values in the literature. Recall that the occupation of electronic states is described by the Fermi function:

$$f(\epsilon) = \frac{1}{e^{\frac{\epsilon}{k_{\mathrm{B}}T}} + 1}, \tag{2.14}$$

and the tunneling current from Bardeen (Equation 2.4) by:

$$I(V,T) = \frac{4\pi e}{\hbar}\int_{-\infty}^{\infty}\left[f(\epsilon+eV,T) - f(\epsilon,T)\right]|M(\epsilon)|^2\,\rho_{\mathrm{tip}}(\epsilon+eV)\rho_{\mathrm{sample}}(\epsilon)\mathrm{d}\epsilon, \tag{2.15}$$

with $\epsilon = E - E_{\mathrm{F,tip/sample}}$ the relative energy in tip or sample with respect to its Fermi energy. The matrix elements $M(\epsilon)$ and the tip density of states ρ_{tip} are assumed to be

constant for a small bias. The differential conductance is then:

$$\frac{\mathrm{d}I}{\mathrm{d}V}(V,T) \propto |M|^2 \rho_{\mathrm{tip}} \int_{-\infty}^{\infty} \left[\frac{(1/k_{\mathrm{B}}T)\exp[(\epsilon+eV)/k_{\mathrm{B}}T]}{(\exp[(\epsilon+eV)/k_{\mathrm{B}}T]+1)^2} \right] \rho_{\mathrm{sample}}(\epsilon)\mathrm{d}\epsilon. \tag{2.16}$$

For a delta peak $\rho_{\mathrm{sample}} = \delta(\epsilon - \Delta\epsilon)$ at $\Delta\epsilon \gg k_{\mathrm{B}}T$ the integral can be solved:

$$\frac{\mathrm{d}I}{\mathrm{d}V}(V,T) \propto \frac{1}{k_{\mathrm{B}}T} \cdot \frac{1}{\cosh^2\left(\frac{\Delta\epsilon+eV}{2k_{\mathrm{B}}T}\right)}. \tag{2.17}$$

The following relation is now used: $\cosh^2(x) = \frac{1}{2} + \frac{e^{2x}}{4} + \frac{e^{-2x}}{4}$. This equation can be approximated by a Gaussian distribution with a full width half maximum (FWHM) of $2.36\sigma = 3.3k_{\mathrm{B}}T/e$:

$$\frac{\mathrm{d}I}{\mathrm{d}V}(V,T) \propto e^{-\frac{\Delta\epsilon+eV}{2(1.4k_{\mathrm{B}}T)^2}}. \tag{2.18}$$

Two delta peaks that get broadened into two Gaussian distributions, can be resolved if they exhibit a central minimum. That is the case for a shift of one FWHM. So the shift $\Delta\epsilon$ has to be larger than $3.3k_{\mathrm{B}}T$.

The influence of the lock-in modulation voltage amplitude $V_{\mathrm{mod,p}}$ on the energy resolution can be derived by again calculating the broadening of a delta peak, resulting in a half-sphere of width $2eV_{\mathrm{mod,p}}$ [81]. The FWHM of the half-sphere gives the energy resolution of $1.7eV_{\mathrm{mod,p}}$ in Equation 2.13.

2.2. Closed-cycle cryocooler

The following two sections will describe the cooling, first to 4 K by pulse tube coolers, often also named as pulse tube cryocoolers or pulse tube refrigerators, and second to 1 K by a Joule-Thomson cooler. Other cooling methods at 1 K or below are e.g. described in [82].

2.2.1. Pulse tube cryocooler

Pulse tube cryocoolers (PTCs) offer an alternative to cryogenic liquids, such as LN_2 or L^4He for achieving cryogenic temperatures. This chapter provides a brief overview of the

historical development, theoretical concepts, and operational principles of PTCs.

PTC historical development and introduction

The development of PTCs began in 1963 [83]. The interest was increased in 1980's with their improved performance by adding an orifice and a buffer volume, which led to temperatures as low as 60 K [84, 85]. In 1990, the invention of the orifice, double-inlet PTC further increased the efficiency [86]. It has been demonstrated that single-stage versions are incapable of attaining temperatures below ∼10 K [87]. In 1994, the achievement of temperatures below 4 K was demonstrated by three-stage PTCs as well as by pre-cooled PTCs [88, 89]. The first presented two-stage cooler without pre-cooling was presented in 1997 [90]. The change in temperature is based on adiabatic expansion of the working fluid. Consequently, the limit of a ^{4}He gas operated PTC is determined by the thermal expansion coefficient, which approaches zero before the lambda line [91]. Temperatures as low as 1.3 K could be achieved by using ^{3}He [91].
Applications of cryocoolers span across a broad range of fields, including gas liquefaction [92–95], astronomy [96], magnetic resonance imaging [97], space science [98, 99], medical science [100], security scanners [101] and physics research. In space-based telescopes such as the James Webb Space Telescope, cryocoolers become essential, since it is not possible to refill the cryogens when they are used up [102, 103]. A summary and comparison of cryocoolers is provided at irregular intervals by Radebaugh et al. [104].

A PTC belongs to the group of regenerative cryocoolers, which are characterized by oscillating gas flows and pressures, while the heat is exchanged by a regenerator. The main components of a PTC comprise the compressor, a hot-end heat exchanger (HE), a regenerator, the pulse tube (PT), a cold-end HE (Figure 2.2 (a)) and a phase change ability between the pressure cycle and the mass flow. The phase change components will be explained in the focus section on the two-stage Gifford-McMahon-type, double-inlet, orifice, U-shape PTC and its importance in the cooling power description. The working fluid is typically ^{4}He gas, which remains within that closed-cycle system. Different configurations have been presented. A first categorization distinguishes PTCs using valves (Gifford-McMahon-type (GM) PTC) with a low frequency operation of a few Hz

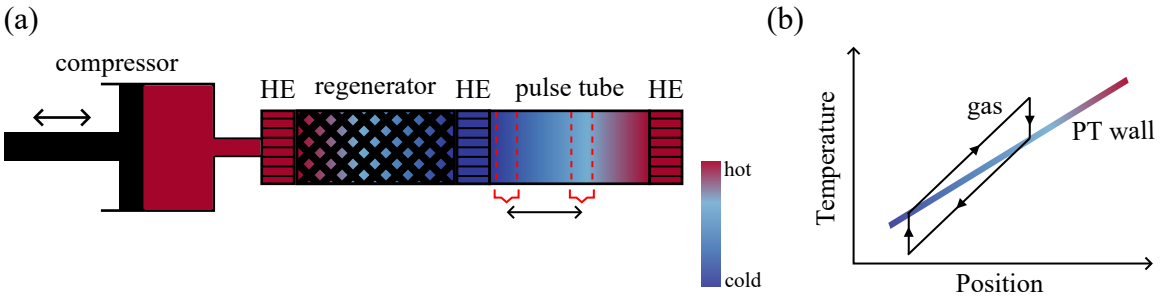


Figure 2.2.: **Schematic of a basic, one-stage, in-line, pulse tube cryocooler.** (a) A compressor delivers oscillating pressure to the gas in the assembly of heat exchangers (HE), regenerator and pulse tube. One gas parcel is marked (red dotted lines) including its movement path caused by the oscillating pressure (double arrow). (b) Temperature-position cycle of the gas parcel marked in (a) (black lines) and the temperature of the PT wall (colored line) acting as heat sink (source) at the hot (cold) end for the gas parcel.

and the Stirling-type PTC that is directly connected to a compressor operating with frequencies above ∼20 Hz. The valve of the GM-type PTC between the compressor and cryocooler allows for a large distance between them such that the compressor can be placed in a separate room. The low-frequency operation allows for better heat transfer in the regenerator at low temperatures and thus achieves lower temperatures, but shows less efficiency [104]. There are other configurations, like U-shaped, in-line, concentric, or multi-stage arrangements. Active buffers, inter-phase, counter-flow, multi-bypass, and cascaded setups can be added [105].
In contrast to other cryocoolers, such as Stirling coolers and GMCs, that both have a moving displacer, a PTC can be made without moving parts close to the cold-end. Hence, they surpass the other coolers in reliability and lifetime. In addition, the maintenance interval is longer as a PTC has no moving piston, which can show wear at the low-temperature seals. Moreover, PTCs exhibit fewer vibrations.

The theoretical description of PTCs uses varying degrees of simplification. The absence of moving parts compared to Stirling and GM coolers makes the description quite complex and often incomplete.
Often, it is stated that the PTC works similarly to a basic Stirling cooler [106]. Both release the heat at a hot-end HE to the environment and draw heat from a cold-end HE. In a PTC, a part of the gas itself takes over the role of the displacement piston; it acts

like a compressible piston. Its movement is controlled by phase change components, an impedance (orifice) and a buffer volume as described later. The cooling is achieved when the gas leaves the regenerator at the cold-end HE and does work on this gas piston. This work is then converted into heat at the hot-end HE of the PT [107].
We will derive an expression for the cooling power (e.g. Equation 2.32) and discuss the optimal phase difference between the mass flow and the pressure.
One theoretical approach describes the cooling by the so-called surface heat pumping effect [108–110]. We will discuss this in the section of the basic PTC.
Another one uses a time-averaged enthalpy flow model. It also shows that the phase shift between pressure and mass flow is critical to obtain the cooling power [85, 106]. A representation of this phase shift is described by the so-called phasor analysis [107, 111–113].
Nowadays, also numerical analysis based on computational fluid dynamics (CFD) has been employed [114–118], including artificial intelligence tools [119]. Nevertheless, the description of the details of the working principles is still not consistent. For example, CFD simulations found that the gas parcels in the PT do not contribute to the cooling, but introduce heat [120], different from the traditional description above. They found that the gas parcels in the regenerator are pumping heat from the cold-end HE to the hot-end HE [121–123], as described in the section of the cooling power by the regenerator side.

Basic PTC, surface heat pumping

In the following, we will describe the working principle via the surface heat pumping effect [108–110].
The basic PT, developed by Gifford and Longsworth in 1966, has no orifice and no double-inlet (Figure 2.2). It employs the transfer of heat between the gas and the adjacent wall of the PT during compression and expansion cycles, while shuttling the gas from the cold-end HE towards the hot-end HE and back to the cold-end HE.
The following provides a detailed, accessible explanation. When the pressure within the PT increases, a gas parcel initially positioned at the cold-end HE is displaced towards the hot-end HE of the PT as depicted in Figure 2.2 (a). During this displacement, the gas is adiabatically compressed, which results in an increase of its temperature (Figure 2.2 (b)).

If the temperature of the gas exceeds that of the adjacent PT wall, heat is transferred from the gas to the wall during the subsequent constant pressure phase. Conversely, when the pressure decreases, the gas parcel is displaced back towards the cold-end HE. Adiabatic expansion takes place, decreasing the gas temperature. If the gas temperature falls below that of the adjacent wall or the cold-end HE, heat flows to the gas and, hence, the cold-end HE provides cooling power. This cyclic process of compression and expansion establishes the gas parcels that pump heat from the cold-end HE to the hot-end HE of the PT.
However, the minimum temperature in a basic PTC is achieved if the temperature gradient of the wall is as large as the temperature change of the gas during compression and expansion. Moreover, it is limited by heat transfer inefficiencies between the gas and the walls [109]. As a result, temperatures of only ∼80 K were achieved by a two-stage basic PTC [110].

Two-stage Gifford-McMahon-type, double-inlet, orifice, U-shape PTC

Next, we focus on the two-stage Gifford-McMahon-type, double-inlet, orifice, U-shape PTC (Figure 2.3). It is widely utilized in laboratory environments and achieves cooling powers of 1 W at 4 K [52, 124]. An overview of other cryocoolers can be found elsewhere [125–127]. We start with a description of its components prior to an explanation of the cooling power that is given in the next chapter.

A schematic of such a PTC is depicted in Figure 2.3 (a). This cryocooler comprises two main components: a ^{4}He compressor and the PTC-head. The PTC-head will be called PTC in the following. The ^{4}He compressors, typically cooled by water or air, supply ∼20 bar of ^{4}He to the PTC. Recent designs also incorporate inverter-driven compressors [53] and oil-free models [128]. The compressor connects to the PTC via two flexible tubes, known as flexlines, one supplying high-pressure (∼23 bar) and the other returning low-pressure gas (∼7 bar). A rotary valve, that connects to the PTC, alternates between the high- and low-pressure at a frequency of approximately 1 Hz. As depicted in Figure 2.3 (b), they are designed such that the pressure will show a

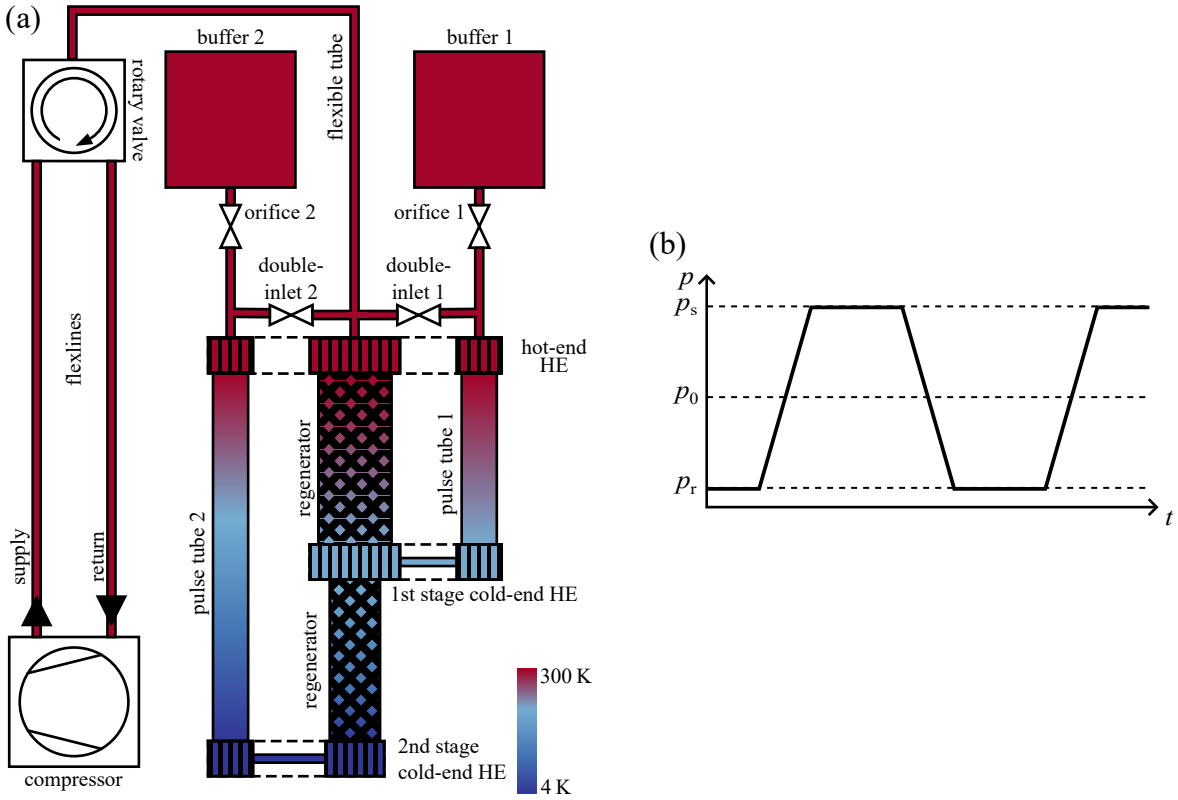


Figure 2.3.: **Schematic of a Gifford-McMahon-type, two-stage, orifice, double-inlet, U-shape pulse tube cryocooler.** (a) A compressor delivers high-pressure gas at the supply flexline and low-pressure at the return flexline. The rotary valve switches between these two flexlines. The phase between pressure and mass flow is adjusted by an orifice valve and a double-inlet valve (sometimes called bypass valve) for each stage 1 or 2 individually. The 1st and 2nd stage cold-end heat exchanger (HE) allows for a thermal connection to an experiment, that will be cooled. (b) Idealized pressure p inside the pulse tube (PT) as a function of time. p_s and p_r mark the supply and return pressure respectively.

rather sharp transition followed by a constant pressure phase [129]. This oscillating pressure is applied to the hot-end HE of the PTC. A so-called remote option is depicted in Figure 2.3 (a). It allows mechanical isolation of the rotary valve from the rest of the PTC by a flexible tube. A regenerator, constructed from a porous material with high heat capacity, is located between the hot- and cold-ends HE of the PTC. This component absorbs heat from the gas as it flows towards the cold-end HE and releases it back to the gas during the flow towards the hot-end HE. It, moreover, sustains a stable temperature gradient across its length. Therefore, materials within the regenerator are tailored to their specific temperature ranges of operation, often utilizing rare earth compounds towards the cold-end HE and a complex, layered structure along the gradient [130]. The PT, a thin-walled tube, thermally isolates the hot- and cold-end HE. Inside the PT, the thermodynamic process of adiabatic expansion and compression of the gas takes place. The cold-end HE, positioned between the regenerator and the PT, features a HE towards the experiment. In the two-stage design, there is a 1st and 2nd stage cold-end HE (Figure 2.3 (a)). The 1st stage provides pre-cooling, enabling the 2nd stage to reach lower temperatures. Typically the 1st stage also anchors components with higher heat loads, such as radiation shields exposed to room temperature radiation. The stages are called 60 K and 3 K stage in the following. Cooling performance is optimized by adjusting flow resistances (orifices) and bypasses (e.g. double-inlet valves). The cooling mechanism relies on the gas expanding near the cold-end HE, absorbing heat from the surroundings, and releasing it near the hot-end HE during compression. The required phase shift between pressure and mass flow is achieved through orifices (labeled orifice 1 and orifice 2 in Figure 2.3 (a)) and buffer volumes connected to the PT's hot-end HE. The orifices regulate the gas flow to the large buffer volumes during the constant pressure phases. This enables the PTC to operate without mechanically moving parts, such as pistons or displacers. In double-inlet PTCs, the double-inlet valve (Figure 2.3 (a)) enhances the efficiency by allowing a portion of the gas to flow directly to the PT's hot-end HE. Thereby, it does not flow through the regenerator, which would lead to pressure drops in the regenerator and thermal losses [86] (explained later).

Cooling power of a Gifford-McMahon-type, double-inlet, orifice PTC

In the following, we partially follow [107, 111–113, 118] to derive the cooling power and the importance of the phase difference θ between mass flow and pressure for a double-inlet, orifice, Gifford-McMahon type PTC. The model is based on an enthalpy flow analysis. This is analogously employed in steady-flow systems, where the enthalpy flow $\dot{H}$ is proportional to the mass flow $\dot{m}$ and the specific enthalpy h ($\dot{H} = \dot{m}h$). Since in a PTC with oscillating flow, the net mass flow is zero, we consider the time-averaged enthalpy flow per cycle at the cold-end HE $\left\langle \dot{H} \right\rangle_{\mathrm{c}} = \frac{1}{\tau} \int_0^\tau \dot{m}_{\mathrm{c}}(t) h_{\mathrm{c}}(t) \mathrm{d}t$, with τ the period of one cycle and h_{c} the specific enthalpy at the cold end. This approach enables the derivation of a relationship between the mass flow rate at the cold-end HE $\dot{m}_{\mathrm{c}}(t)$ and the cooling power $\dot{Q}_{\mathrm{c}}$, defined as the rate of heat transfer from a heat load into the cold-end HE. We assume that the regenerator does not contribute any heat flow. The PT is assumed to be adiabatic, while the hot-end HE and the cold-end HE are considered isothermal, which is realized in practice by the connection of the cold-end HE to the regenerator and the connection of the hot-end HE to the environment, respectively. Using the first law of thermodynamics, the cooling power is the time-averaged net enthalpy flow at the cold-end HE. It reads

$$\dot{Q}_{\mathrm{c}} = \left\langle \dot{H} \right\rangle_{\mathrm{c}} = \frac{C_{\mathrm{p}}}{\tau} \int_0^\tau \dot{m}_{\mathrm{c}}(t) T_{\mathrm{c}}(t) \mathrm{d}t. \tag{2.19}$$

C_{p} is the specific heat at constant pressure for the assumed ideal gas and $T_{\mathrm{c}}(t)$ is the temperature at the cold-end HE.

For the sake of simplicity, the following assumptions are used: 1) Sinusoidal pressure $p(t)$ and temperature $T(t)$ variations are assumed inside the PT, with no phase difference between them (Equations 2.20 and 2.21). 2) The pressure will change almost simultaneously inside the PT, hot-end HE, cold-end HE and regenerator due to its small size relative to the acoustic wavelength (few 100 – 1000 m) [131]. Hence, one gets

$$p(t) = p_0 + p_1 \cos(\omega t), \tag{2.20}$$

$$T(t, x) = T_0(x) + T_1(x) \cos(\omega t). \tag{2.21}$$

p_0 describes the static pressure, p_1 the amplitude of the dynamic pressure, $T_0(x)$ and $T_1(x)$ are temperatures as a function of position x inside the PTC. In the PT, both $T_0(x)$ and $T_1(x)$ are assumed to increase linearly from the cold-end HE to the hot-end HE. In the regenerator $T_0(x)$ is assumed to decrease linearly between the hot-end HE and the cold-end HE with $T_1(x \in \text{regenerator}) = 0\,\text{K}$. The adiabatic equation holds inside the PT:

$$\frac{T(t,x)}{T_0(x)} = \left(\frac{p(t)}{p_0}\right)^{\frac{\gamma-1}{\gamma}}. \tag{2.22}$$

With the adiabatic heat capacity ratio $\gamma = \frac{C_\text{P}}{C_\text{V}} = \frac{5}{3}$ for ^{4}He and C_V the specific heat at constant volume, one gets $\frac{\gamma-1}{\gamma} = \frac{2}{5}$. Taylor expanding Equation 2.22 around $p = p_0$ at the lowest order and inserting Equation 2.20 and Equation 2.21, hence gives:

$$\frac{T_1(x)}{T_0(x)} = \frac{2}{5}\frac{p_1}{p_0}. \tag{2.23}$$

The mass flow at the cold-end $\dot{m}_\text{c}(t)$ is the sum of the rate of density change ($\frac{\text{d}}{\text{d}t}\rho(t)$) in the PT volume V_PT, plus the effective (due to density change) mass flows through the orifice $\dot{m}_\text{o}(t)$ and through the double-inlet valve $\dot{m}_\text{di}(t)$:

$$\dot{m}_\text{c}(t) = \frac{\text{d}}{\text{d}t}\rho(t)V_\text{PT} + \dot{m}_\text{o,eff}(t) - \dot{m}_\text{di,eff}(t). \tag{2.24}$$

The latter two mass flows are caused by mass flows near the hot-end HE, once through the orifice and once through the double-inlet valve (as illustrated in the inset of Figure 2.4). They depend on the local temperature inside the PT and hence the density of the gas. Thus, the effective mass flows $\dot{m}_\text{o,eff}$ and $\dot{m}_\text{di,eff}$ at the cold-end are:

$$\dot{m}_\text{o,eff}(t) = \frac{T_\text{0,h}}{T_\text{0,c}}\zeta_\text{o} p_1 \cos(\omega t), \tag{2.25}$$

$$\dot{m}_\text{di,eff}(t) = \frac{T_\text{0,h}}{T_\text{0,c}}\zeta_\text{di} p_1 \cos(\omega t + \alpha). \tag{2.26}$$

$T_\text{0,h}$ is $T_0(x)$ (in Equation 2.21) for the position at the hot-end HE, while $T_\text{0,c}$ is $T_0(x)$ for the position at the cold-end HE. The equation uses the ideal gas law at constant pressure : $T \sim \frac{V}{N} \sim \frac{1}{\varrho}$ with N the number of particles in volume V. ζ_o and ζ_di are the flow coefficients of the valves relating flow to pressure. The flow through the valves

depends on the pressure difference over the valve. The buffer volume is large, resulting in a roughly constant pressure p_0 inside it. The pressure at the double-inlet valve is assumed to have a phase shift of α, with respect to the pressure at the orifice. Combining Equations 2.24 to 2.26, assuming a mean gas temperature $\overline{T}_{\mathrm{PT}}$ inside the PT and using the ideal gas law $\rho(t) = p(t)/R\overline{T}_{\mathrm{PT}}$ for the first term in Equation 2.24, it follows:

$$\dot{m}_{\mathrm{c}}(t) = \frac{\omega V_{\mathrm{PT}}}{R\overline{T}_{\mathrm{PT}}} p_1 \cos\left(\omega t + \frac{\pi}{2}\right) + \frac{T_{0,\mathrm{h}}}{T_{0,\mathrm{c}}} \zeta_{\mathrm{o}} p_1 \cos(\omega t) - \frac{T_{0,\mathrm{h}}}{T_{0,\mathrm{c}}} \zeta_{\mathrm{di}} p_1 \cos(\omega t + \alpha). \tag{2.27}$$

Inserting Equations 2.21 and 2.27 into Equation 2.19, the first term from $\dot{m}_{\mathrm{c}}(t)$ gives no enthalpy flow after integration since $T_{\mathrm{c}}(t)$ and $\frac{\mathrm{d}\rho(t)}{\mathrm{d}t}$ have a phase shift of $\pi/2$. In other words, there is no contribution by the mass flow due to the pressurization of the gas. So, one gets:

$$\begin{aligned} \dot{Q}_{\mathrm{c}} = \frac{C_{\mathrm{p}}}{\tau} \Bigg[& \int_0^\tau \frac{T_{0,\mathrm{h}}}{T_{0,\mathrm{c}}} \zeta_{\mathrm{o}} p_1 \cos(\omega t) \left(T_{0,\mathrm{c}} + T_{1,\mathrm{c}} \cos(\omega t)\right) \mathrm{d}t \\ & - \int_0^\tau \frac{T_{0,\mathrm{h}}}{T_{0,\mathrm{c}}} \zeta_{\mathrm{di}} p_1 \cos(\omega t + \alpha) \left(T_{0,\mathrm{c}} + T_{1,\mathrm{c}} \cos(\omega t)\right) \mathrm{d}t \Bigg]. \end{aligned} \tag{2.28}$$

After integration, one gets:

$$\dot{Q}_{\mathrm{c}} = \frac{C_{\mathrm{p}}}{2} \left[\frac{T_{0,\mathrm{h}} T_{1,\mathrm{c}}}{T_{0,\mathrm{c}}} \zeta_{\mathrm{o}} p_1 - \frac{T_{0,\mathrm{h}} T_{1,\mathrm{c}}}{T_{0,\mathrm{c}}} \zeta_{\mathrm{di}} p_1 \cos(\alpha) \right]. \tag{2.29}$$

Inserting Equation 2.23 in Equation 2.29, one gets the cooling power of an orifice, double-inlet PTC:

$$\dot{Q}_{\mathrm{c}} = \frac{C_{\mathrm{p}} p_1^2}{5 p_0} T_{0,\mathrm{h}} \zeta_{\mathrm{o}} - \frac{C_{\mathrm{p}} p_1^2}{5 p_0} T_{0,\mathrm{h}} \zeta_{\mathrm{di}} \cos(\alpha). \tag{2.30}$$

The first term is the same as for a pure orifice PTC without double-inlet. It can be tuned by the flow coefficient ζ_{o} at the orifice and the pressure amplitude p_1. In [106], it is shown that opening the orifice valve initially increases the refrigeration power, which then stays the same. The second term describes the contribution of the double-inlet valve which increases $\dot{Q}_{\mathrm{c}}$ for $\alpha \in [90°, 270°]$. In application, α can be adjusted by the opening of the double-inlet valve [113]. Comparing this theory with measurements at a PTC indeed showed that for $\alpha = 180°$, the cooling effect is maximum [113]. In this case,

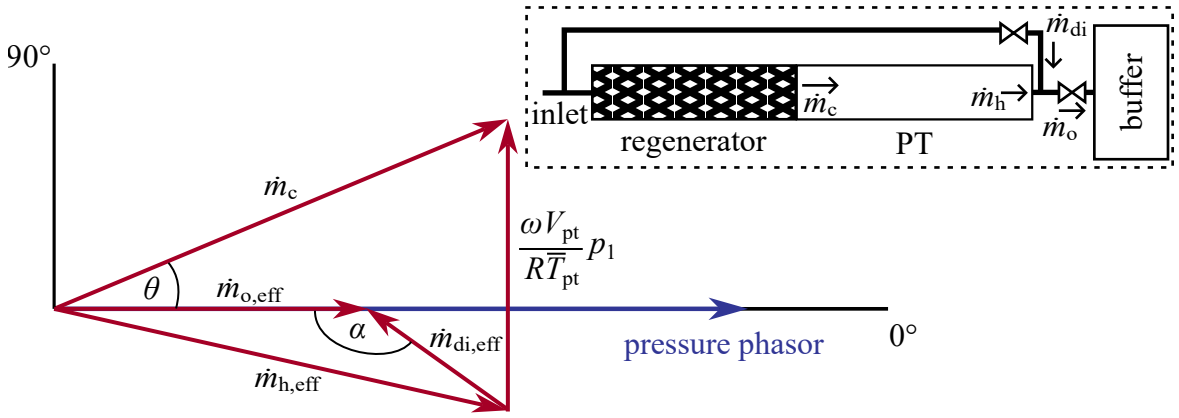


Figure 2.4.: **Phasor diagram of a single-stage, orifice, double-inlet pulse tube cryocooler.** The phasor diagram represents Equation 2.27 for a phase leading angle $\alpha > 90°$, and $t = 0$. Inset: Schematic of a single-stage, orifice, double-inlet PTC as a linear shape, illustrating the contributing mass flows.

the phase difference between pressure $p(t)$ and cold-end mass flow $\dot{m}_c(t)$ is 63°.
A so-called phasor representation (vectorial representation) of these phase angles enables to relate pressure and mass flows (Figure 2.4). The length of the vector corresponds to the amplitude of the oscillating mass flow while the directional angle corresponds to the phase of the sinusoids. Inserting the relation $C_p = 5/2R$ for a monoatomic gas into Equation 2.30 and multiplying it by $\frac{T_{0,c}}{T_{0,c}}$ we get:

$$\dot{Q}_c = \frac{1}{2} R T_{0,c} \frac{p_1}{p_0} \left(\frac{T_{0,h}}{T_{0,c}} \zeta_o p_1 - \frac{T_{0,h}}{T_{0,c}} \zeta_{di} p_1 \cos(\alpha) \right) \tag{2.31}$$

The first term in the brackets of Equation 2.31 is the amplitude of Equation 2.25 and the second term the amplitude of Equation 2.26. From Figure 2.4 the amplitudes $|\dot{m}_c|$, $|\dot{m}_{o,eff}|$ and $|\dot{m}_{di,eff}|$ can be related as: $|\dot{m}_c| \cos(\theta) = |\dot{m}_{o,eff}| - |\dot{m}_{di,eff}| \cos(\alpha)$. Hence, Equation 2.31 can be written in terms of phase angle θ between $p(t)$ and $\dot{m}_c(t)$:

$$\dot{Q}_c = \frac{1}{2} R T_{0,c} \frac{p_1}{p_0} |\dot{m}_c| \cos(\theta) \tag{2.32}$$

For a large cooling power, the term $|\dot{m}_c| \cos(\theta)$ has to be maximized, and a higher pressure ratio would be beneficial. If α increases, θ decreases, and $\dot{Q}_c$ increases. Also, Equation 2.32 shows that the cooling power drops as the temperature at the cold-end HE drops.

In a real PTC, additional losses due to heat loads by conduction and radiation are present, as well as regenerator losses and real gas effects that exist beyond the ideal gas approximation. They lead to a reduction in $\dot{Q}_c$. Regenerator losses are, e.g., a drop in pressure over the length of the regenerator due to a non-zero flow resistance, incomplete heat exchange, and thermal conductance. A full three-dimensional model of an orifice, double-inlet PTC was analyzed by CFD simulations by Banjare et al. [116]. Here, the calculated coldest end temperature is achieved when the phase difference between pressure and cold-end mass flow is 58°.

Cooling power originating from the regenerator side

So far, it has not been clarified how the temperature of the cold-end HE is maintained. The role of the regenerator has to be taken into account, which leads to the earlier mentioned inconsistencies of the corresponding descriptions of the working principle.

Simulations by Qiu et al. [120] challenge the traditional description by showing that the oscillating gas in the PT does not contribute to the cooling power for the case of orifice and double-inlet PTC. Instead, it introduces heat. The model of the simulation consists of the PT and its hot-end HE and cold-end HE only and assumes a phase shift of the cold-end mass flow relative to the pressure. It is speculated that the net cooling power of the whole PTC, including the regenerator, is still positive due to the transport of heat from the cold-end HE via the regenerator to the hot-end HE.

Liang [121] also states that the cooling power originates from the regenerator side and provides a detailed qualitative analysis of the heat pumping by the gas parcels from the cold-end HE to the hot-end HE via the regenerator. This analysis relies on several assumptions: 1) The model consists of a regenerator as a set of capillary tubes with large heat capacities. Thus, the wall's temperature distribution remains steady during each cycle. 2) Gas parcels are small enough that their thermodynamic properties are homogeneous. 3) In the regenerator, the gas has perfect thermal contact with the wall, unlike the adiabatic gas parcels in the PT. Thus, its temperature always matches the local wall temperature. 4) The gas is assumed to be an ideal gas without viscosity.

The pressure, velocity, and displacement of the gas oscillate sinusoidally. The velocity is leading the pressure in phase by θ. As in Equation 2.20, the pressure is expressed as:

$$p(t) = p_0 + p_1 \cos(\omega t). \tag{2.33}$$

The velocity, which is proportional to the mass flow rate, of the gas parcel is given by:

$$v(t) = v_1 \cos(\omega t + \theta), \tag{2.34}$$

with θ the leading phase, $0° < \theta < 90°$. Here, a positive velocity $v(t)$ indicates motion of the gas parcel towards the cold-end HE. The displacement of the gas parcel is calculated as:

$$s(t) = \int_0^t v(\tilde{t})\, \mathrm{d}\tilde{t} = (v_1/\omega) \cos\left[\omega t - ((\pi/2) - \theta)\right] + C. \tag{2.35}$$

The constant C is irrelevant, since only the gas displacement is of interest. $s(t)$ lags $p(t)$ by a phase of $((\pi/2) - \theta)$. The behavior of $p(t)$, $v(t)$, and $s(t)$ are illustrated for $\theta = 60°$ in Figure 2.5.

In Figure 2.5, the pressure-induced expansion ($t_0 < t < t_2$) and the compression ($t_2 < t < t_4$) phases are marked. The phase difference θ, between the displacement and the pressure leads to the predominance of compression at the hot-end and expansion at the cold-end. A positive displacement ($s > 0$) is defined as a movement towards the cold-end. For the case of $t = t_0$, $s(t)$ has not yet reached its maximum while the pressure $p(t)$ is at its maximum. At this time the pressure change is small, leading to almost no heat exchange. Until $t = t_1$ most of the expansion has taken place while the gas parcel is still more towards the cold-end and thus also takes heat from the regenerator material with it. In the time period between $t = t_2$ and $t = t_4$ the compression takes place, while most of the gas is towards the warmer end. This leads to gas parcels absorbing heat at the cold-end and releasing it at the hot-end. For a net cooling effect θ has to be smaller than 90°, i.e. if $\theta = 90°$ there is no phase between the pressure and displacement. The maximum heat transport is achieved for $\theta = 0$, when $p(t)$ and $v(t)$ are in phase. In this case the gas always takes heat for every position $s(t) > 0$ and releases heat for $s(t) < 0$. A comprehensive analysis of this process is available in [121], but it is not included here as it exceeds the scope of this thesis.

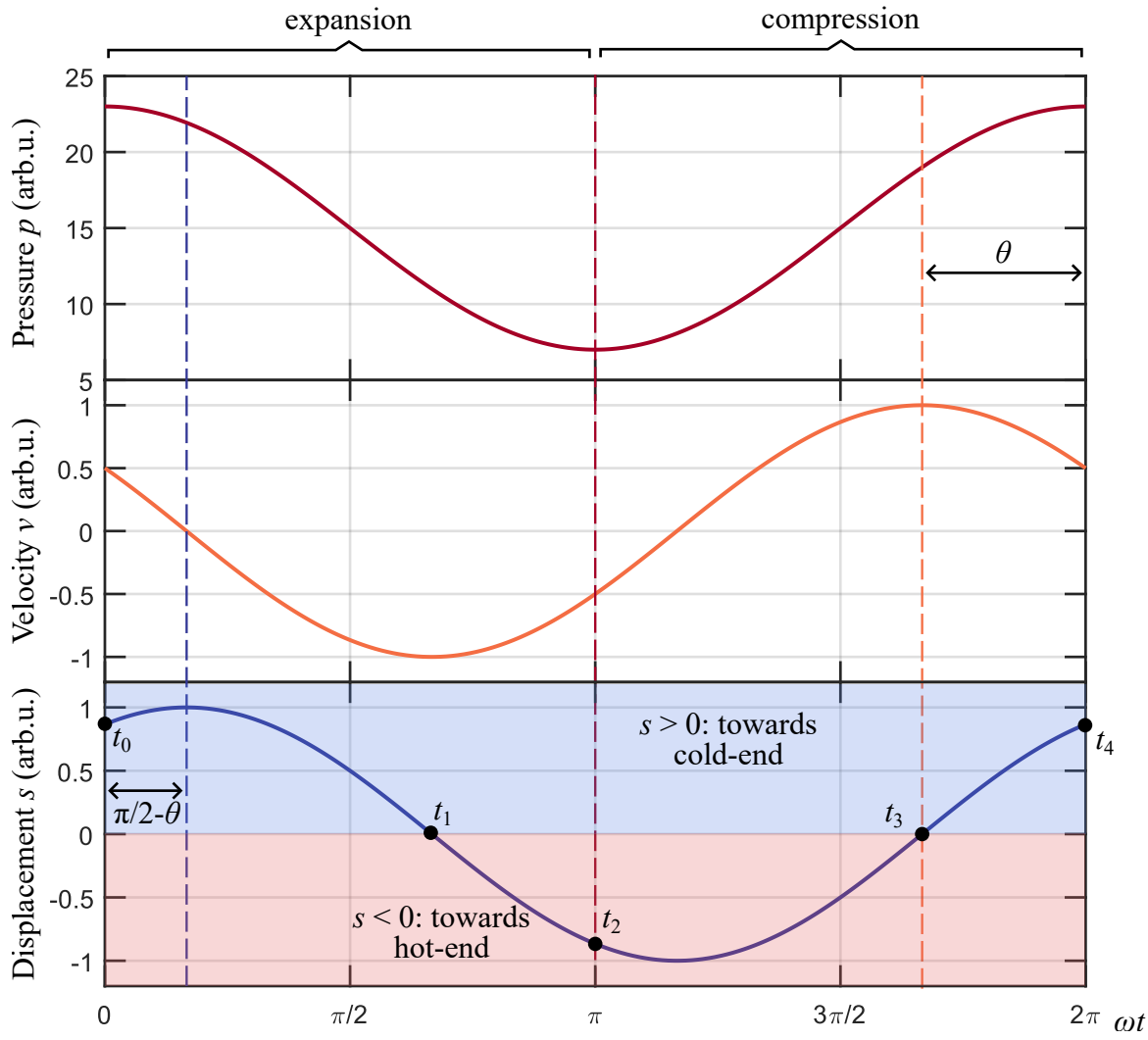


Figure 2.5.: **Time dependency of pressure, velocity and displacement of a gas parcel moving in the regenerator.** The graphs follow from Equation 2.33, Equation 2.34 and Equation 2.35 with the phase leading angle $\theta = 60°$ as indicated. The pressure expansion is predominantly directed towards the cold-end, while the compression is primarily located near the hot-end. This results in the absorption of heat by the gas parcel at the cold-end and its subsequent release at the hot-end.

Chen et al. [122] employed CFD simulations, for a phase changing PTC, to quantitatively study the heat transfer and work process of a gas parcel oscillating in a cycle at either the cold-end of the regenerator, in the regenerator, or at its hot-end. CFD simulations directly compute gas properties like pressure, velocity, and temperature. The results again show that heat is transported from the cold-end to the hot-end of the regenerator.

Zhi et al. [123] finally do not focus on single components like the PT or the regenerator, but they explain the net cooling power by investigating the heat transfer in the PT, the regenerator and the cold-end HE at once. They identified a contradiction in previous analyses due to the oversimplification of the regenerator as a one-dimensional, ideal regenerator with no dead volume and ideal isothermal or adiabatic assumptions. The net cooling power is analyzed for different phases θ between a sinusoidal (40 Hz) pressure and its mass flow at the cold-end. The highest net cooling power is found for $\theta = 0°$ (in consistency with the above description of Liang) while the gas parcel from the PT side introduces heat of 16 %. They compare it to the case of a basic PTC ($\theta = 83°$), where the remaining net cooling power is only 1 % of the highest one. Now the cooling is caused by the gas parcels on the PT side.

Hence, details of the origin of the cooling power in PTC-processes still have to be understood, despite the method being meanwhile widely employed.

2.2.2. Joule-Thomson cryocooler

In comparison to regenerative cryocoolers described in Section 2.2.1, a Joule-Thomson (JT) cooler is a recuperative cooler. A steady flow of refrigerant from a high to a low pressure side, including a counter flow heat exchanger, is used. The Joule-Thomson effect is utilized in gas liquefiers invented by Carl von Linde and William Hampson (Linde-Hampson liquefier). In 1852 Joule and Thomson observed that a gas changes its temperature when it is expanded through a small aperture [132]. The expansion is isenthalpic with enthalpy: $H = U + pV = \text{const.}$ (U: inner energy of gas), such that $\mathrm{d}H = \mathrm{d}U + V\mathrm{d}p + p\mathrm{d}V = 0$. The reason is that the process is adiabatic $\delta Q = 0$ and no external work is produced. A change in temperature T with pressure p does only appear

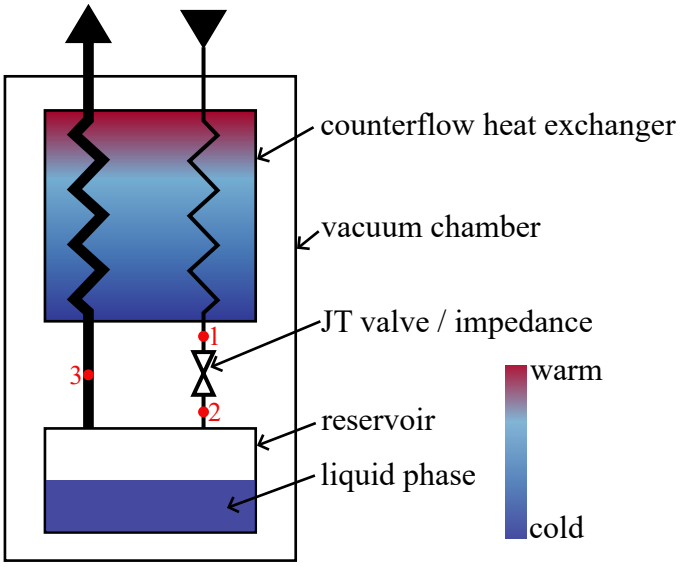


Figure 2.6.: **Schematic of a JT cooler.** Compressed gas enters the vacuum chamber at room temperature. The Gas passes a counterflow heat exchanger towards point 1. The expansion is through the JT valve into a reservoir (point 1 to 2). The thicker line, where the vapor leafs the reservoir in point 3, correspond to a low pressure line, typically connected to a vacuum pump or compressor.

for non-ideal, van der Waals gases based on the work against intermolecular forces. If repulsive (attractive) forces are dominating, the gas heats up (cools down) during expansion.

A schematic of a JT cooler is shown in Figure 2.6. Typically, the main components of a JT cooler are a source of high pressure (e.g. a compressor or a container of high pressurized gas followed by a pressure regulator/reducer), a vacuum chamber for thermal isolation, a counterflow heat exchanger, a JT valve, and a reservoir or stage serving as a heat exchanger for the experiment. The gas entering at room temperature must be precooled below its inversion temperature before it enters the JT valve. Else, the JT coefficient $\mu_{\mathrm{JT}} = (\partial T/\partial p)_{\mathrm{H}}$ will be negative, leading to an increase in temperature after expansion. The index H marks the isenthalpic process.

In the following, the properties of ^{4}He with respect to the JT effect will be described, as this gas is used for the cryostat in this thesis. ^{4}He is special because it does not show a triple point, where a solid, liquid and vapor phase coexist, and it is still fluid for

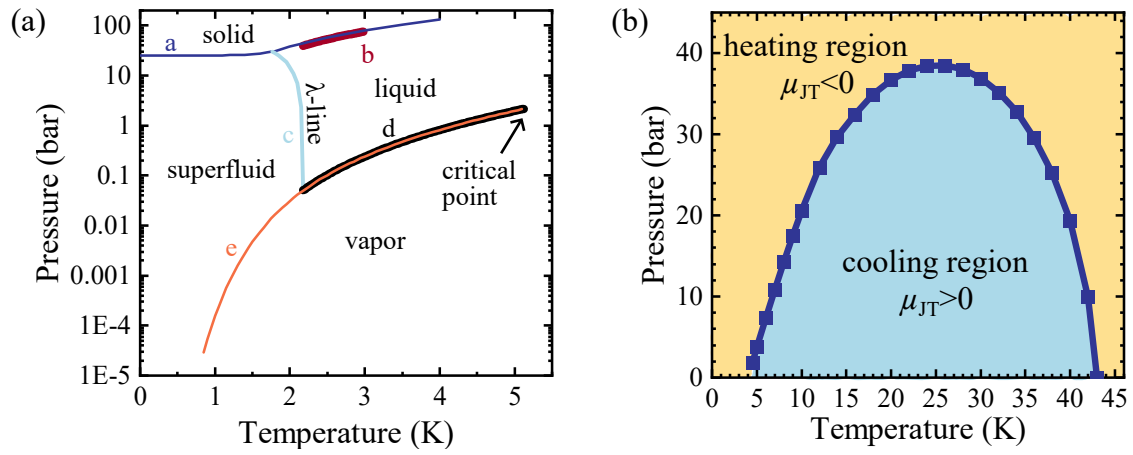


Figure 2.7.: (a) **^{4}He phase diagram.** Depending on the pressure and temperature,^{4}He can exist as a vapor, two liquid forms and as a solid, as marked. The two liquid forms are separated by the λ line, for $T < T_\lambda$ it is superfluid. Data source: a:[133], b and d:[134], c:[135], e:[136]. (b) **^{4}He JT inversion curve.** The blue curve represents the maxima of the isenthalpic $T(p)$ curves ($\mu_{JT} = (\partial T/\partial p)_H = 0\,K/Pa$) where the JT coefficient $\mu_{JT} = (\partial T/\partial p)_H$ is changing sign. Regions of cooling and heating are marked. Data source:[137]

.

$T = 0\,K$ at normal pressure (Figure 2.7 (a)). Solid ^{4}He can be formed for pressures above $\sim$25 bar. For ^{4}He, the critical temperature (above this point, phase boundaries vanish so liquid and vapor cannot be distinguished) is 5.2 K at a pressure of $P_c = 2.3$ bar. Its JT inversion temperature is 43 K (the temperature where the JT coefficient first changes sign) [138]. Taking the maxima of the isenthalpic curves ($\mu_{JT} = (\partial T/\partial p)_H = 0\,K/Pa$) in a temperature T versus pressure p diagram gives the inversion curve (blue line) in Figure 2.7 (b)). The orange area is the region of heating by expansion, and in the blue area, cooling appears. The pre-cooling of the gas starting at room temperature typically is done by heat exchangers thermally connected to other cooling methods (Claude, Kapitza, Heylandt and Collins liquefaction cycle) or by a connection to thermal baths [140, 141]. Before the expansion through the JT valve takes place, a last pre-cooling is done by a counter flow heat exchanger (Figure 2.6). Subsequent to the expansion, the remaining gas flows back through the heat exchanger taking heat from the experiment with it. The absence of moving parts and non-oscillating pressures makes the JT cooler a low vibrational cooling method.

The sign of the JT coefficient μ_{JT} directly shows if the system is cooled or heated by

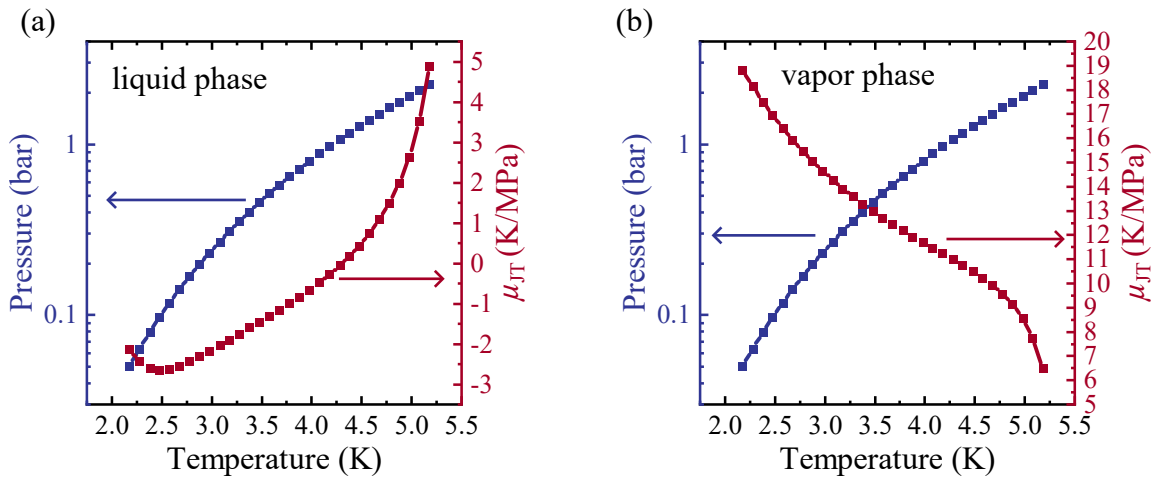


Figure 2.8.: JT coefficient (red) and vapor pressure curve (blue, same as e in Figure 2.7 (a)) for the liquid phase in (a) and the vapor phase in (b) both coexisting at the vapor pressure. Data source: [139]

the pressure reduction. In the case of ^{4}He at pressures of the vapor pressure curve (line between the critical point and the λ-line in Figure 2.7 (a)), the JT coefficient also depends on the ^{4}He phase (Figure 2.8). The vapor has a positive μ_{JT} always, such that a cooling by the JT effect in the vapor phase is always present (Figure 2.8 (b)). In the liquid, however, positive values of the JT coefficient can only be reached for $T > \sim$4.2 K (Figure 2.8 (a)). The saturated superfluid ^{4}He shows a small, but negative JT coefficient [142], hence, it does not enable JT cooling.

For starting temperatures low enough that the helium coexists as a liquid and a vapor, the output temperature of the gas leaving the reservoir no longer depends on the input temperature of the helium prior to the JT valve. It only depends on the boiling temperature of the helium in the reservoir [145]. A short discussion on the efficiency of the JT process can be done by using Figure 2.9 (a), showing the pressure vs. specific enthalpy diagram for ^{4}He , also known as the saturation dome because of its shape. The total cooling power $\dot{Q}_c$ at the reservoir in Figure 2.6 is $\dot{Q}_c = \dot{m}(h_3 - h_1)$. Thereby, $\dot{m}$ is the mass flow into and out of the reservoir, while it is in a steady state. h_3 and h_1 are the specific enthalpies of ^{4}He at the output of the reservoir and input of the JT

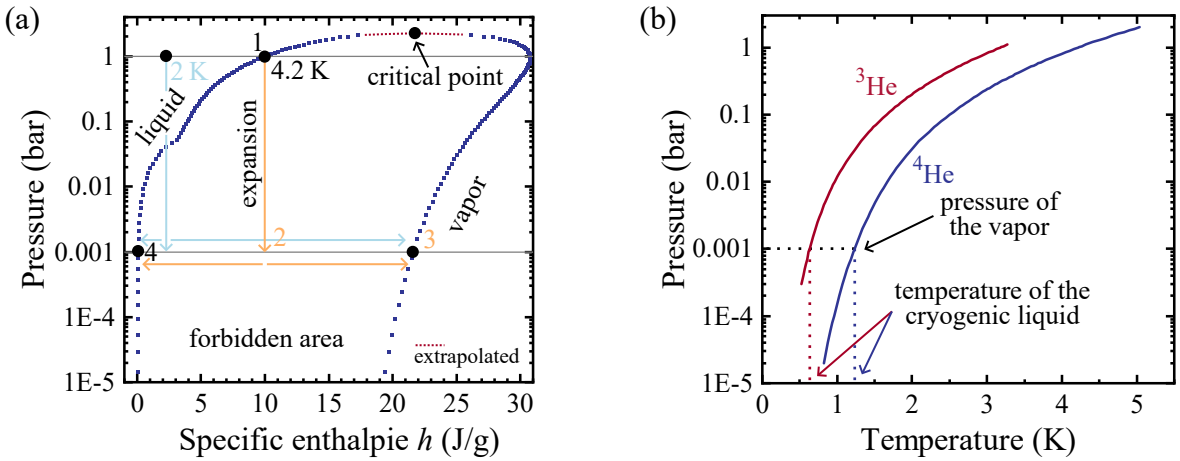


Figure 2.9.: **Properties of ^{4}He** (a) Pressure p vs. specific enthalpy h (saturation dome) for ^{4}He. On the left side below the critical temperature (maximum of the saturation dome) the ^{4}He is liquid. On the right side it is a vapor. The efficiency of the Joule-Thomson expansion from 1 bar to 1 mbar is shown for two examples. First for saturated ^{4}He at 4.2 K (yellow lines) and second for a sub-cooled liquid at 2 K (blue lines). Data source: [136, 143]. (b) Vapor pressure of ^{4}He and ^{3}He with marked examples of reaching 1 mbar. Data source: [144].

valve (Figure 2.6), respectively. The difference $h_3 - h_1$ can be read from the diagram in Figure 2.9 (a). It is the difference between the enthalpy of the vapor at e.g. 1 mbar (point 3 in Figure 2.9 (a)) and the enthalpy of the initial liquid at 1 bar (point 1 in Figure 2.9 (a)). After isenthalpic expansion, one lands in the forbidden region of the $p(h)$ diagram, where ^{4}He separates into a liquid (point 4) and a vapor (point 3) while keeping the total enthalpy. For the saturated ^{4}He of 4.2 K as starting phase, one gets $h_3 - h_1 = 12\,\mathrm{J/g}$, while for a starting phase at 2 K, one gets $h_3 - h_1 = 20\,\mathrm{J/g}$. The yield of liquid in the reservoir from the incoming ^{4}He reads $y = \frac{h_3 - h_1}{h_3 - h_4}$ (numbers are marked in Figure 2.9 (a)). This leads to $y = \sim 55\,\%$ ($\sim 90\,\%$) for a start temperature of 4.2 K (2 K).

A more efficient way than expanding the gas or fluid in a single step is to use the so-called distributed Joule-Thomson effect [146, 147]. Here, multiple expansions and heat exchange processes are utilized, allowing the higher pressure part to be actively cooled by its own JT expansion and passively by exchanging heat with the lower pressure stream.

The combination of a cryocooler, previously described in Section 2.2, with a ^{4}He JT expansion circuit has been developed in the past to achieve temperatures below 2 K

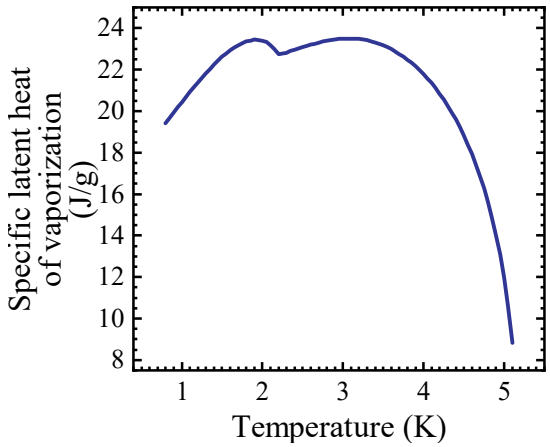


Figure 2.10.: Specific latent heat of vaporization of ^{4}He. The dip at 2.2 K is due to the superfluid transition (Figure 2.7 (a)). Data source: [136].

[148, 149]. Also ^{3}He is used in this combination with achieved temperatures of 0.65 K [150].

Evaporative cooling with ^{4}He

In certain cryogenic systems, cryostats are equipped with a reservoir engineered for alternating filling and pumping operations. Also, the JT stage can be operated in such a so-called single-shot mode. Initially, the JT reservoir is filled with liquid ^{4}He by applying pressure. Subsequently, both the input and output lines are pumped. The liquid in the reservoir is then cooled by evaporative cooling. During this process, atoms possessing the highest kinetic energy escape from the liquid and get pumped, thereby reducing the mean energy of the remaining liquid.
The cooling power $\dot{Q}_c$ is determined by the specific latent heat of vaporization Q_{vap} displayed in Figure 2.10 as follows [151]:

$$\dot{Q}_c = \dot{N}(h_{vap} - h_{liq}) := \dot{N} Q_{vap}. \tag{2.36}$$

Here $\dot{N}$ is the mass flow rate of particles leaving the liquid phase to the pumps, and h_{vap} and h_{liq} are the specific enthalpy of the vapor and the liquid phase, respectively.
Typically, $\dot{N}$ is proportional to the vapor pressure $p_{vap}(T)$. Hence, the cooling power decreases exponentially with decreasing temperature, mirroring the behavior of the vapor

pressure:

$$\dot{Q}_c = Q_{vap}\dot{N} \propto p_{vap}(T) \propto e^{-\Delta E/k_B T}, \tag{2.37}$$

where ΔE is the binding energy of He atoms in the liquid phase. A minimum temperature is reached when the heat flow into the bath is equal to the cooling power of vaporization. The minimum temperature is, therefore, also dependent on the minimum achievable vapor pressure of the gas in the reservoir, respectively the pumping power achieved by the pumping system. ^{3}He has a higher vapor pressure than ^{4}He. So, it requires less pumping to reach the same boiling temperature (Figure 2.9 (b)) and thus provides a higher cooling power at the same temperature than ^{4}He.

2.3. STM vibration isolation in particular the concept of minimal stiffness

The fundamental principles and types of vibration isolation from the surrounding environment are briefly discussed in this section. A more theoretical analysis of vibration-isolating systems for STMs, albeit without minimal stiffness, can be found here: [152].

A persistent challenge in STM is the vibration isolation of the instrument. The primary goal is to obtain a stable tip-sample distance and thus provide a low-vibration environment. Alterations of the tip-sample distance of 0.1 nm already would result in a tenfold variation in the tunneling current. Therefore, it is necessary to isolate the STM from both internal sources of vibration, such as a PTC, and external sources, such as building vibrations or noise from everyday laboratory operations. The origin of mechanical vibrations can be separated into frequencies as follows. Frequencies below 1 Hz are typically not attributable to a local source. They are caused by more distant sources such as meteorological phenomena, the waves of the ocean that interact with the shoreline, or the gravitational forces of the moon. At frequencies of approximately 1 Hz, the sources become more local, such as the action of wind on a building. For frequencies well above 1 Hz, the primary source is human activity, such as the movement of trains and the operation of machinery, including spinning motors. The transmission of mechanical vibrations occurs through various structural elements, such as the floor of the building,

the walls, the frame of the system, the UHV chamber, etc.. In addition, acoustic waves can interact with mechanically isolated STM systems and potentially excite resonance frequencies of the setup (compare Chapter 3). Ground floor vibrations are typically in the order of a few µm. While additional human-caused events, like a smashed door, can lead to higher values. For example, the ground floor noise in our physics department is $1 \times 10^{-7}\,\mathrm{m}/\sqrt{\mathrm{Hz}}$ and $1 \times 10^{-10}\,\mathrm{m}/\sqrt{\mathrm{Hz}}$ at 1 Hz and 100 Hz, respectively. The isolation chain includes internal isolators that are strategically positioned directly before the STM. These isolators may take the form of spring suspensions, rubber isolators, air isolators, or active damping and are intended to dampen the remaining external and internal vibrations. The final isolation is achieved by the STM design itself, as discussed in Section 3.5.

Spring Suspension

STMs suspended by metallic springs are compatible with UHV due to their low outgassing and robustness at elevated temperatures of ∼150 °C used during a UHV chamber bakeout. The resonance frequency in the vertical direction of a system consisting of an STM with mass m, suspended by springs with a combined spring constant k is given as:

$$f_{\mathrm{res}} = \frac{1}{2\pi}\sqrt{\frac{k}{m}} = \frac{1}{2\pi}\sqrt{\frac{g}{\Delta l}}. \tag{2.38}$$

Hook's law is inserted in the right side with $g = 9.8\,\mathrm{m/s^2}$ leading to an elongation of the spring by $\Delta l \approx 6\,\mathrm{cm}$ for 2 Hz resonance frequency. Used metal springs typically show a high quality factor, so an additional damping is added mostly in the form of eddy current damping or UHV compatible elastomers. The resulting transfer function above the resonance frequency is proportional to $1/f^2$ without additional damping and typically $1/f$ for a damped system directly above the resonance frequency [70].

Minimal stiffness for vibration isolation

The predominant configuration of STM systems is supported on air cushions or rubber springs, allowing for isolation from ground vibration. These isolators often have resonance

frequencies of ∼2 Hz with a transfer value of ∼0.1 at 10 Hz [71]. Equation 2.38 shows that lowering the resonance frequency requires larger isolators because softer springs need to be used. An alternative technology exists that enables a reduction in resonance frequency without increasing the size of an isolator. It uses the technique of minimal stiffness, often dubbed negative stiffness or nonlinear vibration isolation [153–157]. This type of isolator compensates the spring constant by a clever mechanism allowing for a reduction in transmitted vibration amplitudes, even at low frequencies <2 Hz. The effect is called negative stiffness, because the force displacement curve of such a system can show areas where the slope or spring constant k_n is negative. In this area, the negative stiffness assists the deformation of a positive stiffness spring with spring rate k_p. For a parallel combination of these two, the combined spring constant calculates to $k_\mathrm{eff} = k_\mathrm{n} + k_\mathrm{p}$ and for a serial combination to $k_\mathrm{eff} = \frac{k_\mathrm{n} k_\mathrm{p}}{k_\mathrm{n}+k_\mathrm{p}}$.

The concept of minimal stiffness is shown in Figure 2.11 (a). It shows the compensation of a load supporting spring with stiffness k_ls. The load can be the STM chamber or any other object to be isolated. The compensation is achieved by a mechanism consisting of pre-loaded springs. The pre-loaded springs exert a force F_ls onto the supported mass. The central position of this mass is unstable if no support is present or if the pre-loading force F_pl is larger, leading to an over-compensation. For small displacements Δz the load supporting spring force F_ls can be compensated by the nonlinear compensating force F_ms. The resulting stiffness $k = k_\mathrm{ls} - k_\mathrm{ms}$ has low values, resulting in low resonance frequencies (Equation 2.38).
Horizontal isolation can be realized by supporting the load on flexible beams or columns (Figure 2.11(b)). In this case, the gravitational force has the role of the pre-loading force F_pl. For both setups, in general, a non-linear force-displacement curve results, with almost zero incline for small displacements (Figure 2.11(c)). Leaf springs are typically used for compensation because they show more stable setups than coil springs [157]. A more stable setup means that the resulting non-linear curve can exceed the values of the linear support force displacement curve, as illustrated in (Figure 2.11(d)). A higher stiffness for larger displacements can protect the system against excessive deformation. The leaf springs and support rods must be properly sized, so that the pre-loading force F_pl is lower than the buckling force of the leaf springs or the support rods. Otherwise, the structure would undergo a sudden deformation instead of a weak restoring force, with

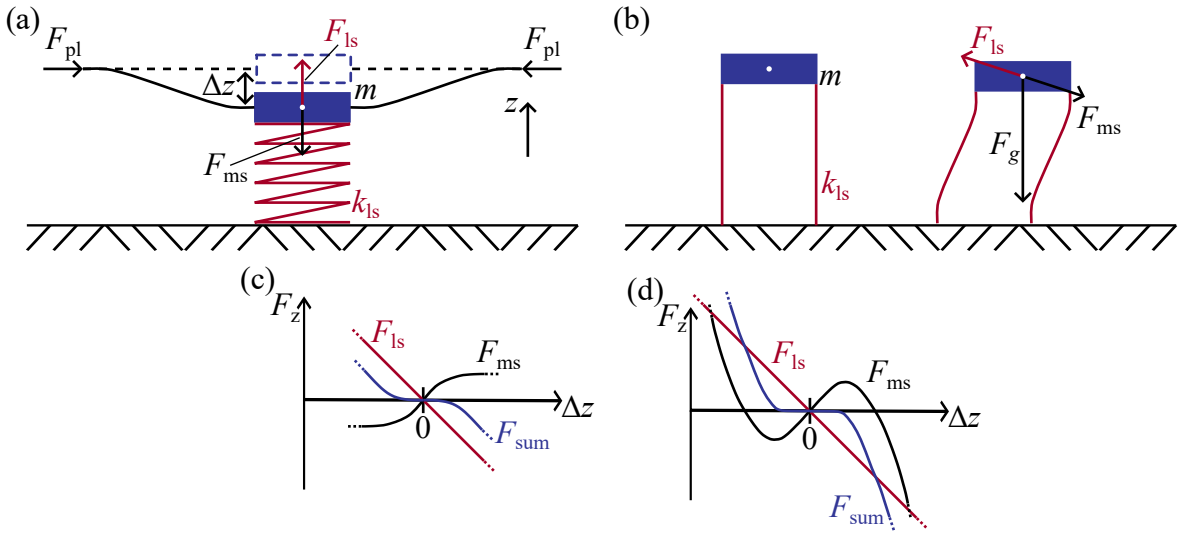


Figure 2.11.: **Minimal stiffness working principal.** (a) Schematic of vertical compensation of a supporting load spring with spring constant k_{ls} that supports an object with mass m. Pre-loaded springs that exert a force F_{pl} lead to a counter acting force F_{ms} if the object is displaced by Δz. (b) Schematic of horizontal compensation of supporting rods with spring constant k_{ls} that supports an object with mass m. The gravitational force F_g leads to a counter acting force F_{ms} to the spring force F_{ls} if the object is displaced. (c) Typical force displacement curve of the supporting springs (red) and the counter acting nonlinear compensating force F_{ms}. The resulting sum shows near zero incline in the center, indicating minimal stiffness. (d) A system combining a spring force F_{ls} with a nonlinear compensating force F_{ms} can lead to a total force F_{sum} that exceeds F_{ls} at large $|\Delta z|$.

a low resonance frequency. According to Euler's formula, the critical buckling force F_{cr} acting in the axial direction onto a column is [158]:

$$F_{cr} = \frac{\pi^2 EI}{l_{eff}^2}. \tag{2.39}$$

Here, E is Young's modulus of the material, I the moment of inertia of the cross section of the column, and l_{eff} is its effective length, that depends on the conditions at the end boundaries (e.g. clamped, hinged,...).

Minimal stiffness isolation concepts were also used for the vibrational pre-isolation in gravitational wave detectors [159, 160] or during the development of the James Webb Space Telescope to create a flight-like environment by suspending the world's largest vacuum chamber [161]. In STM systems, the concept has been used to avoid vibrations

being transferred via pumping lines, e.g. for dilution refrigerators, in the form of a so-called vibration balance [162, 163].

The development of the isolation concept, as outlined in this dissertation, employs the minimal stiffness effect to address the vibration isolation of the PTC from the STM. This concept is elaborated upon in Section 3.3.

3. Design and Development of the STM System

The primary objective is to achieve a stable tip-sample distance and thus provide a low vibration environment for the STM at cryogenic temperature. The following chapters will discuss the laboratory room concept with the UHV STM system, the selection of the cryocooler, the development of the vibration isolation concept, the cryostat design, the STM design, and the wiring concept.

3.1. Room concept and integration into UHV

The room concept, the UHV system, and related details are discussed in this section.

The laboratory room

The UHV STM system is located in a room on the ground floor of the building. A wall with both sound-isolating and sound-absorbing properties divides the room into two sections (Figure 3.1). This ensures that the measurement is protected from both the STM control unit and the operator (human voice spectral range: 80 – 4000 Hz). The external surface of the wall is double-planked with gypsum plasterboard and gypsum fiberboard (in total: 25 mm), which reflects extrinsic sound (Figure 3.1 (a)-(b)). The internal surface of the wall is covered with glass fiber woven fabric (Figure 3.1 (c)). It guides sound into the stone wool filled wall (8 – 18 cm, the constructed wall had to obey space limitations), where it is absorbed. In addition, the room's interior walls are covered with either stone wool–containing panels, secured behind glass fiber woven fabric, or pyramid-shaped polyurethane foam (Figure 3.1 (c)), thereby preventing the formation of acoustic standing waves. For a rectangular room with dimensions l_x, l_y and l_z, the

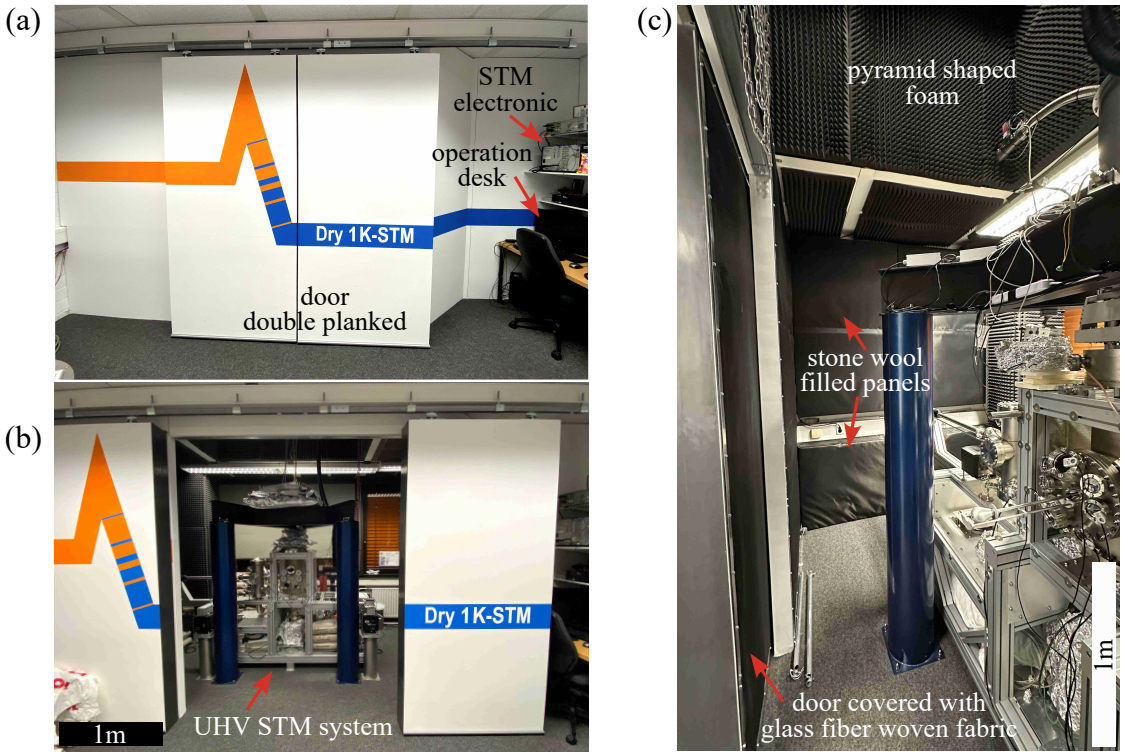


Figure 3.1.: **Room concept** (a) Photograph of the sound-insulating wall from the outside. It separates the UHV STM system from the STM electronics and the operator. (b) Two sliding doors can be opened to access the UHV system. (c) Photograph of the inside of the separated room.

eigenfrequencies are:

$$f \approx \frac{c}{2} \cdot \sqrt{\left(\frac{n_\mathrm{x}}{l_\mathrm{x}}\right)^2 + \left(\frac{n_\mathrm{y}}{l_\mathrm{y}}\right)^2 + \left(\frac{n_\mathrm{z}}{l_\mathrm{z}}\right)^2}. \tag{3.1}$$

Here, $c = 341\,\mathrm{m/s}$ is the speed of sound and $n_\mathrm{x}, n_\mathrm{y}, n_\mathrm{z}$ are mode integer numbers [164]. For our room, the lowest eigenfrequencies are between approximately $30-60\,\mathrm{Hz}$. For the 20 cm mineral wool installed in the side-wall panels, the absorption coefficient is at least 0.1 to 0.3 at these frequencies [165]. The electronics necessary for STM operation and the pump necessary for cooling generate acoustic and mechanical noise. Consequently, they are located outside the room (Figure 3.1 (a)).

The UHV system

Figure 3.2 (a) depicts the operational UHV system. The height of the setup is determined by a number of factors, including the optimal working height of the STM at 1.2 m above the laboratory floor. The UHV system is composed of the STM chamber (center of Figure 3.2 (a)), a preparation chamber with a load lock (Figure 3.2 (c)) and a pre-pumping line (Figure 3.2 (b)). The separation of each chamber is achieved by valves (all metal). A

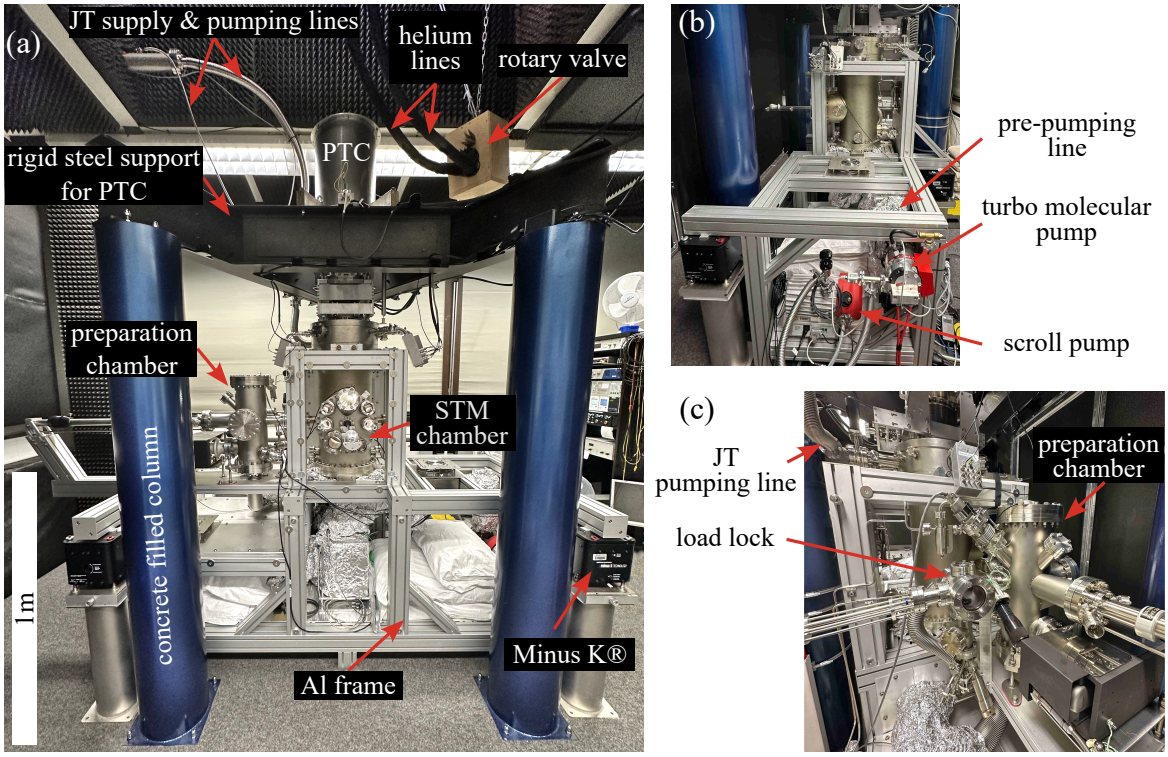


Figure 3.2.: Realized system. (a) Photograph of the system (front view). (b) Right side view. (c) Left side view.

single turbomolecular pump, connected to the pre-pumping line, with a scroll pre-pump (Figure 3.2 (b)), allows for the individual or combined pumping. A mass spectrometer located within this line enables the monitoring of vacuum conditions. Following a baking process, the system is maintained at a base pressure of $\sim 1 \times 10^{-10}$ mbar by the use of vibration-less ion getter and titanium sublimation pumps. The Al frame, which supports the UHV system, is separated from the ground by three isolators (Minus K ® technology) and from the PTC by minimal stiffness isolators. A detailed description of the vibration

isolation is given in Section 3.3.

PTC cooling unit

The STM chamber contains the cooling unit, which is a two-stage pulse tube cryocooler (PTC) (TransMIT PTD 411) with a cooling power of 1 W @ 4 K and 20 W @ 60 K. The selection of the PTC in accordance with vibration considerations is discussed in Section 3.2. Another requirement is the UHV compatibility of the cooler. The materials of the cold-end of the PTC are typically not a concern (Cu and SS). However, the valves (orifice and double-inlet) must be capable of withstanding the baking temperatures (∼150 °C), and the vacuum flange must be a CF type. These requirements are fulfilled by the PTD 411 PTC model.

^{4}He compressor to operate the PTC

The ^{4}He supply and return lines (Figure 3.2 (a)) are fed through the ceiling into a separate room (distance: ∼10 m). They connect to the PTC's rotary valve, which is suspended from the ceiling. Within the separate room, the ^{4}He compressor (Sumitomo F-70H) is housed inside an enclosure for acoustic and vibration insulation (Figure 3.5). It supplies compressed ^{4}He of about 23 bar_{abs} on the high-pressure line and 7 bar_{abs} on the low-pressure return line. The energy consumption is 7 kW and it requires 8 L/min cooling water. The maintenance interval for continuous operation of the compressor is 3.5 years and for the rotary valve 2.3 years. The PTC itself rests on a rigid support structure (steel), directly connected to the ground by three concrete-filled columns (Figure 3.2 (a)). It has been found that the flowing ^{4}He gas, pulsed by the rotary valve of the PTC, can produce acoustic, whistle-like noise within the frequency range of 5 – 10 kHz [166]. In order to mitigate these, the PTC head and rotary valve are enclosed in a stainless steel hat and a wooden box, respectively, both filled with stone wool. The supply, return, and connection line between the PTC and rotary valve are wrapped in butyl rubber and neoprene fabric (black helium lines in Figure 3.2 (a)).

Preparation chamber

The preparation chamber is equipped with the standard sample preparation capabilities, including heating (>2000 °C), Ar^+ sputtering, and O_2 annealing. In the course of two

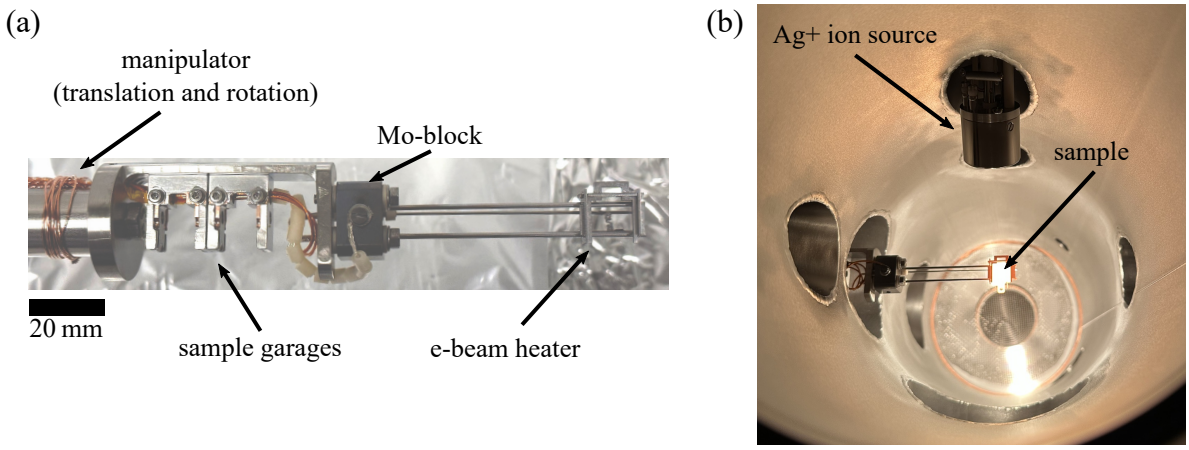


Figure 3.3.: Preparation chamber. (a) Photograph of the e-beam heater on a manipulator. (b) Photograph through the view port into the preparation chamber while a sample is heated to ∼2000 °C.

bachelor's theses of Jonas Beeker and Jean-Marc Grigoleit, an electron beam heater made of tungsten is developed (Figure 3.3 (a)-(b)). It enhances the reliability of the device by constructing the sample stage from 1 mm thick W parts that interfit each other, thereby creating a stable structure. The parts were laser cut from a 1 mm W sheet material, and the assembly was laser spot welded. The heating stage, comprising four sample garages, is mounted to a magnetic-coupled linear and rotational manipulator (travel: 610 mm) (Figure 3.3 (a)). This enables the transfer of samples to the STM cryostat chamber and the heating of samples within the cryostat chamber at a reduced pressure due to the additional pumping of the cold surfaces.

3.2. Selection of pulse tube cryocoolers

Three PTCs are evaluated for their vibration characteristics. Two of these are PTD 411 models from TransMIT, where one is UHV-compatible and equipped with a DN160CF flange. The third PTC is the RP-082E2S model from Sumitomo Heavy Industries, also

featuring a DN160CF flange.

The transducer used for data acquisition is an acceleration sensitive vibration sensor (Wilcoxon Research® 731-207). Its specified frequency response error is ±5 % for 0.6 – 650 Hz. The nominal electrical noise equivalent is $1.7 \times 10^{-8}\,\mathrm{m}/\sqrt{\mathrm{Hz}}$ at 2 Hz, $2.2 \times 10^{-10}\,\mathrm{m}/\sqrt{\mathrm{Hz}}$ at 10 Hz and $7.5 \times 10^{-13}\,\mathrm{m}/\sqrt{\mathrm{Hz}}$ at 100 Hz.
A setup has been developed to mount this sensor on the cold-end of the PTCs. This configuration enables the sensor to maintain its operational ambient temperature. The construction is designed to be mechanically stable, ensuring a rigid coupling between the sensor and the PTC, while also fulfilling the requirement of being thermally insulating. The construction incorporates glass fibre-reinforced plastic and an aluminium mounting plate (Figure 3.4). A lightweight cube made of Mg, Mn, Ce alloy (MnE21, Stolfig GmbH) allows the sensor to be mounted in three orthogonal directions. A temperature sensor and heater are attached to the cube to maintain the stable temperature of 300 K (Figure 3.4). A finite element simulation in SOLIDWORKS® revealed the lowest resonance mode of

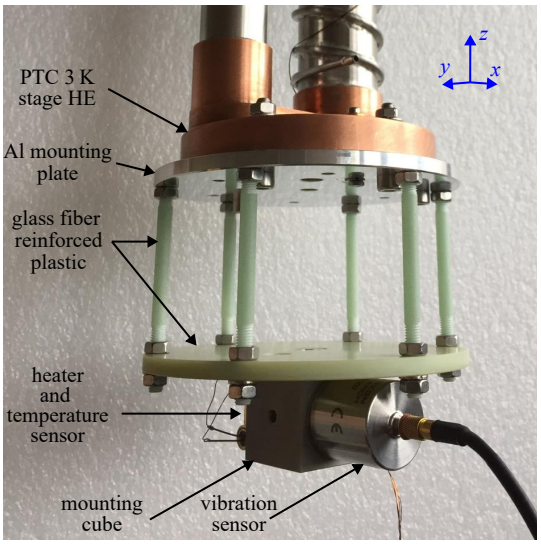


Figure 3.4.: Photograph of the vibration measurement setup at the PTC 3 K stage HE. The evaluated directions of vibrations are marked.

this construction to be a horizontal motion with a resonance frequency at ∼200 Hz. The torsional mode is at ∼400 Hz and the vertical one at ∼1000 Hz.
In order to mitigate the impact of the He compressor on the vibration measurements, a

vibration and sound decoupling is realized by an enclosure (Figure 3.5). Its structure is an aluminum frame, covered with a cladding made of medium-density fiberboard. The inner lining consists of stone wool with a thickness of 7 cm. The compressor is placed inside the enclosure on three layers of "Regupol® vibration 200" tiles, a soft rubber material. The tiles are cut from this material with their size optimized to achieve a resonance frequency below 10 Hz. A labyrinth lined with pyramid-shaped polyurethane foam provides air exchange with cooling fans between the inside and outside of the enclosure.

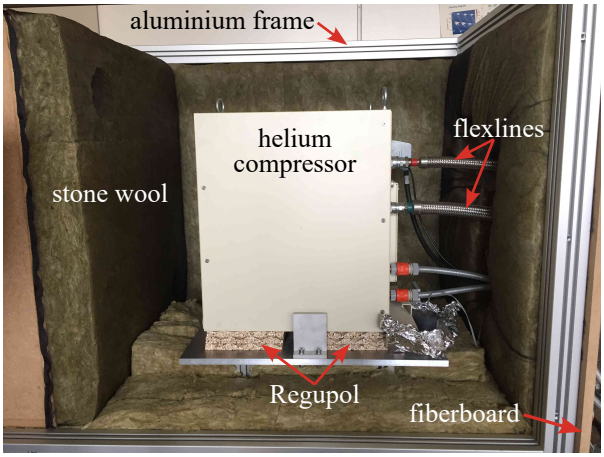


Figure 3.5.: Photograph of the inside of the enclosure for isolation of the helium compressor.

Mechanical vibrations at the cold stages of the PTCs can have several sources and can proceed along different mechanical paths. One source is the pressure change inside the PTC with its operation frequency leading to an elastic deformation of the parts, e.g. the stainless tubes. The flow of ^{4}He gas is producing acoustic noise. Another source is the rotating motor including the inner parts of the PTC rotary valve. The pressurized ^{4}He is supplied by a helium compressor (F-70H Sumitomo Heavy Industries) with rotating inner parts. The background noise is due to the moving of the building lab floor. To separate the impacts of them, vibrations are measured at different locations and, if possible, by an operation of only individual components. The vibrations can be transmitted by the following mechanical path from the compressor to the PTC. By a flexible tube, connecting the PTC to the rotary valve, while itself is connected by flexlines to the compressor. This path is unavoidable. The other path between the compressor and the PTC is via the floor; a decoupling can be applied on either side.
The vibration data of the different PTCs are measured on the third floor of the institute.

The data are recorded with either a sampling rate of 0.5 ms and 20 000 samples or 0.05 ms and 200 000 samples, both resulting in a frequency resolution of 0.1 Hz and a Nyquist frequency of either 1 kHz or 10 kHz, respectively. A low-pass filter of 700 kHz is used to avoid mirroring of higher frequencies. The data displayed are averaged from individual measurements recorded in successive steps.

The first test determines the influence of the setup on the floor noise. This aims to eliminate the background noise for the later measurements of noise at the PTC. The compressor inside the isolation enclosure and the PTC on the vacuum chamber are in the same room but ∼5 m apart. Two setups are tested. First, the vacuum chamber standing on the floor and second isolated from the floor by implementing gimbal air isolators with a 300 kg stone plate on top. The sensor is placed next to the vacuum chamber on the floor. Figure 3.6 shows the vertical vibration amplitude spectra. Placing the chamber

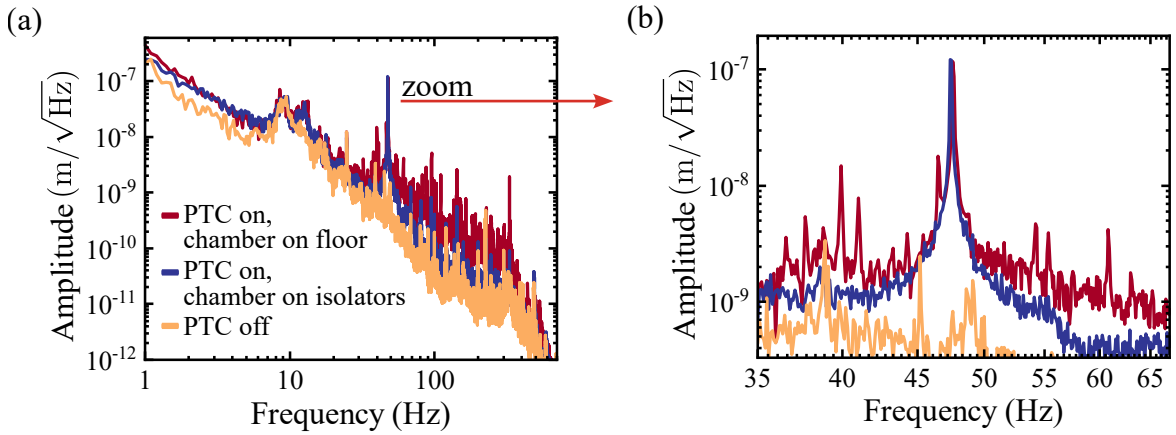


Figure 3.6.: **Floor vibrational noise with compressor on the floor.** (a) Vertical vibration noise amplitude spectrum measured on the floor next to the chamber for the compressor switched off (orange), the compressor running with the chamber standing on the floor (red), and the compressor running with the chamber isolated from the floor (red). TransMIT PTD 411 PTC, sampling rate: 0.5 ms. (b) Zoom into the spectrum of (a) near the operation frequency of the helium compressor.

on the floor lifts the noise between 30 Hz and 300 Hz by up to one order of magnitude. This is likely attributable to vibrations originating from the PTC or the rotary valve. The impact of the compressor shows a peak at 48 Hz, two orders of magnitude larger

than the background. In order to reduce it, the compressor enclosure is placed on gimbal vibration isolators next (Figure 3.7). Figure 3.7 confirms the reduction to a value lower

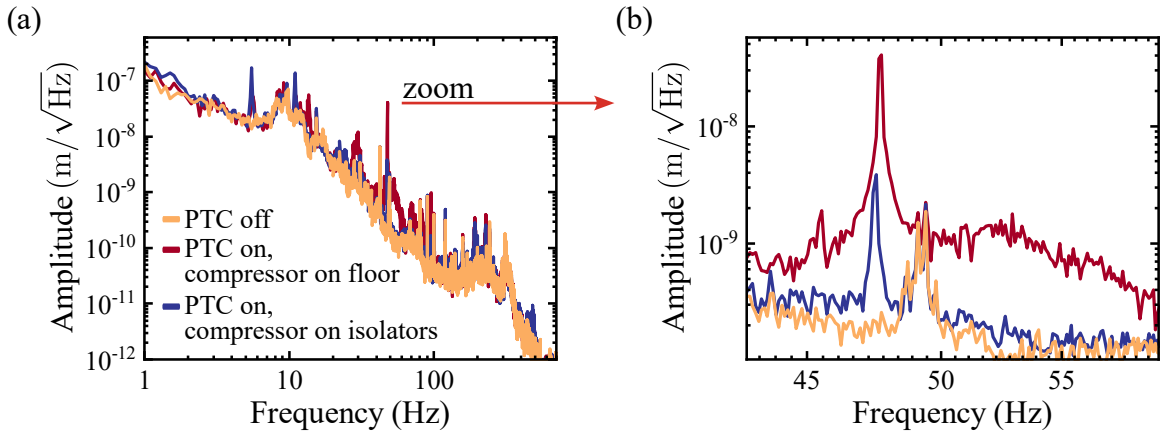


Figure 3.7.: **Floor vibrational noise with compressor on additional isolators.** (a) Vertical vibration noise amplitude spectrum measured on the floor next to the compressor with the compressor switched off (orange), while it is running on additional isolators (blue), and with deactivated isolators (red). Sampling rate: 0.5 ms. Sumitomo PTC, chamber with the PTC is lifted from the floor by a crane suspended on the next floor. (b) Zoom into the spectrum of (a) near the operation frequency of the helium compressor.

than that measured at the PTC stage (Figure 3.8).

Next, the vibration at the PTC 3 K stage is measured, including the effect of coupling the PTC head to a 1 t concrete block with a steel clamp or placing the chamber, with the PTC onto a low resonance air gimbal isolator (Figure 3.8 (c)). The PTC operation frequency was set to the specified one of the manufacturer, i.e. for the PTC 411 to 1.1 Hz, for the CF version of the PTC 411 to 1.2 Hz and for the RP-082E2S to 1.4 Hz. A time domain signal from the sensor is shown in Figure 3.8 (d). The signal is proportional to the acceleration and shows the periodicity of the operation frequency of the PTC. The two minima appear most probably during the two time periods without a pressure change (see Figure 2.3 (b)). The fluctuations in between the minima are most probably due to the flow of the ^{4}He gas. Figure 3.8 shows that clamping the PTC to a mass reduces the peak height at the PTC operation frequency by 25 % as well as the background noise compared to a very soft coupling by suspending the setup on air isolators.

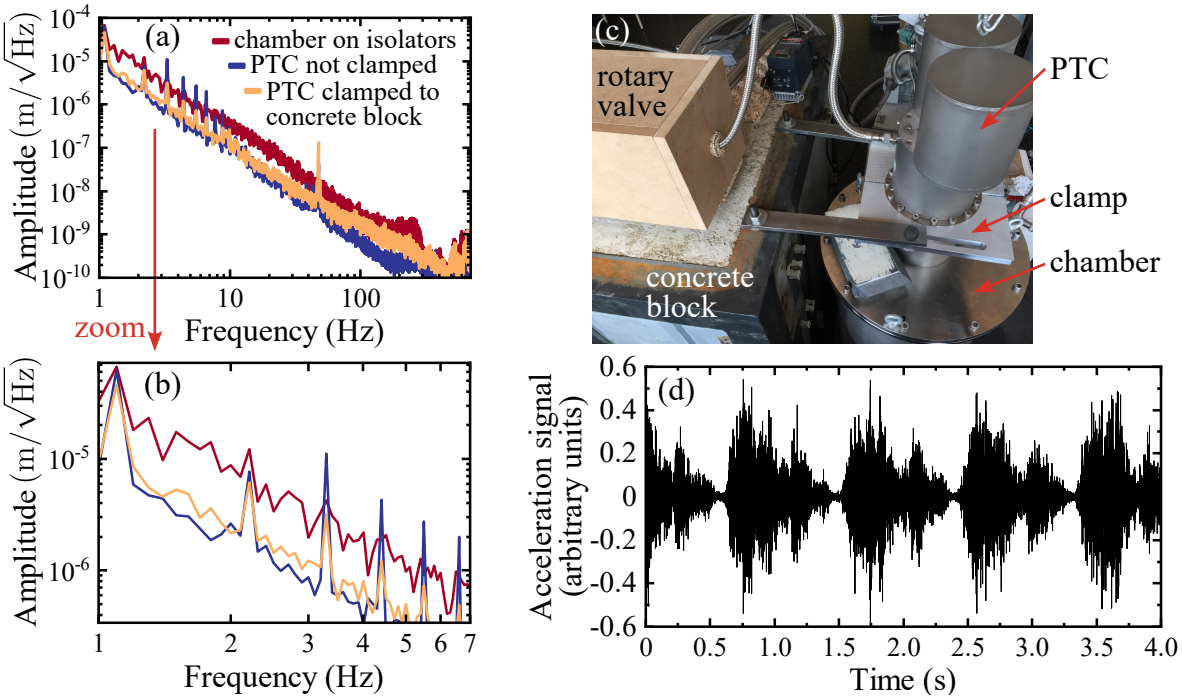


Figure 3.8.: **PTC 3 K stage vibrational noise.** (a) Vibration noise amplitude measured at the PTC (PTD 411) 3 K stage (4 K) in z-direction for three configurations: rigid connection to the concrete block (orange), without the connection (blue), a soft connection to the floor realized by placing the chamber on a plate on air isolators (red). Sampling rate: 0.5 ms. (b) Zoom into the spectrum of (a) showing the first five harmonics of the valve frequency. (c) Photograph of the PTC clamped to the concrete block. (d) Time signal of the acceleration sensor output for the rigid connection to the concrete block.

The comparison of the three different PTCs is carried out at the 3 K stage without the coupling to the concrete block, for the three directions, indicated in Figure 3.4. Figure 3.9 shows the data. The amplitude at the operation frequency of the PTC is lowest for the Sumitomo one in z- and x-direction (Figure 3.9 (a)-(b)). Above 20 Hz, the TransMIT cooler shows often half an order to one order of magnitude less noise in z-direction (Figure 3.9 (a)). Near 60 Hz, the TransMIT is showing peaks for the x-direction (Figure 3.9 (b)). For the x- and y-direction the Sumitomo often exceeds the TransMIT noise in the range between 80 – 200 Hz by one order of magnitude. Note that for the z-direction the sampling rate is increased by a factor of 10.

To find the origin of peaks at the 3 K stage, the noise is measured with just the rotary

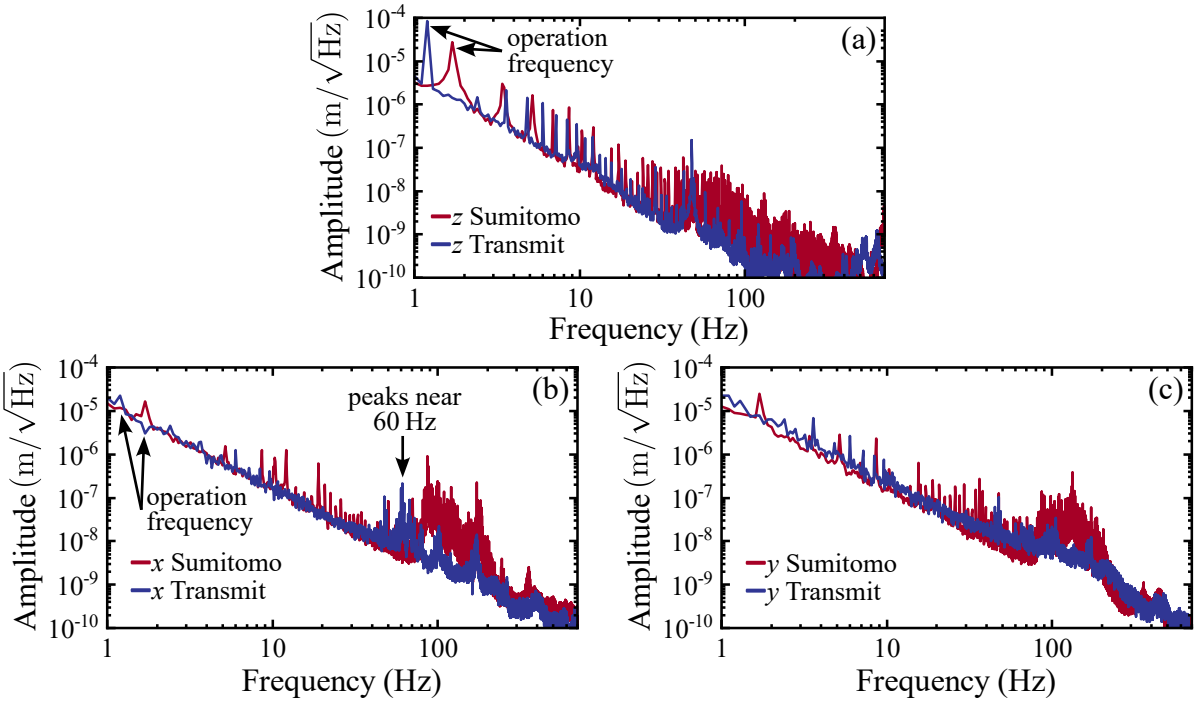


Figure 3.9.: **PTC 3 K stage vibrational noise for different PTC models (Sumitomo RP-082E2S and TransMIT PTD 411 DN160CF).** (a) Vibration noise amplitude measured at the PTC 3 K stage in z-direction with a sampling rate of 0.05 ms. For the shown bandwidth the integrated RMS values are: Sumitomo:$(6.9 \pm 0.2)\,\mu m_{RMS}$, TransMIT: $(19.0 \pm 0.4)\,\mu m_{RMS}$ (b) Vibration noise amplitude measured at the PTC 3 K stage in x-direction with a sampling rate of 0.5 ms. Sumitomo: $(8.6 \pm 1.3)\,\mu m_{RMS}$, TransMIT: $(9.2 \pm 1.6)\,\mu m_{RMS}$ (c) Vibration noise amplitude measured at the PTC 3 K stage in y-direction with a sampling rate of 0.5 ms. Sumitomo: $(9.0 \pm 1.2)\,\mu m_{RMS}$, TransMIT: 0.5ms $(11.0 \pm 2.3)\,\mu m_{RMS}$. (a)-(c) PTC 3 K stage Sumitomo: at 5 K, Transmit: at 4 K.

valve running. The spectra with PTC off are quite similar, independent of whether the rotary valve runs or not, but running the PTC itself increases the vibrations below 8 Hz significantly. So the rotary valve has no significant influence on the PTC vibrations, at least, when it is running without a load (compressor switched off).

The operation frequency can be varied for the PTD 411 model. The effect on the vibration is discussed next. The vibration spectra in z-direction are displayed for five different operation frequencies in Figure 3.11. While increasing the frequency from 1.1 – 1.7 Hz, the measured amplitude at the operation frequency decreases by 40 % at the 3 K stage.

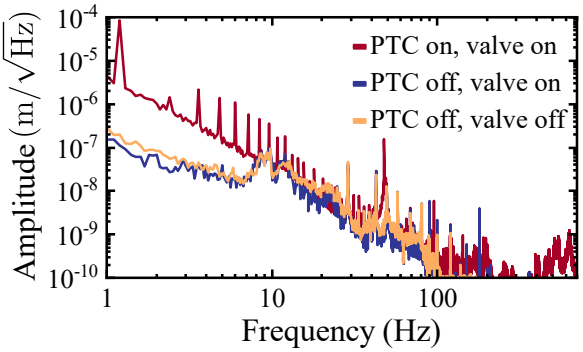


Figure 3.10.: **PTC 3 K stage vibrational noise, rotary valve influence.** Vibration noise amplitude measured at the PTC (PTD 411 DN160CF) 3 K stage in z-direction with the PTC on, with the PTC 3 K stage at 4 K (red), with only the rotary valve running, with the PTC 3 K stage at 300 K (blue) and all switched off state, with the PTC 3 K stage at 300 K (orange). Sampling rate: 0.05 ms.

For the x- and y-direction, the trend is not as clear (Figures 3.12 and 3.13) but with an amplitude that is one order of magnitude lower than in z-direction. Comparing the peak height for the operation frequency of 1.2 Hz (given by the manufacturer) for the three directions, reveals the highest value in z-direction of $(85 \pm 2)\,\mu\text{m}/\sqrt{\text{Hz}}$ while it is lower for the x-direction with $(17 \pm 1)\,\mu\text{m}/\sqrt{\text{Hz}}$ and $(11 \pm 1)\,\mu\text{m}/\sqrt{\text{Hz}}$ for the y-direction (Figures 3.11 to 3.13). The value of $85\,\mu\text{m}/\sqrt{\text{Hz}}$ corresponds to a value of 27 µm amplitude.

We have finally chosen the TransMIT cooler, as it has the advantage of the adjustable operation frequency, which was classified as critical in combination with the other isolation stages enabling to avoid excitation of resonance frequencies. Furthermore, the Sumitomo shows one order of magnitude higher peaks in the frequency range between 80 – 200 Hz.

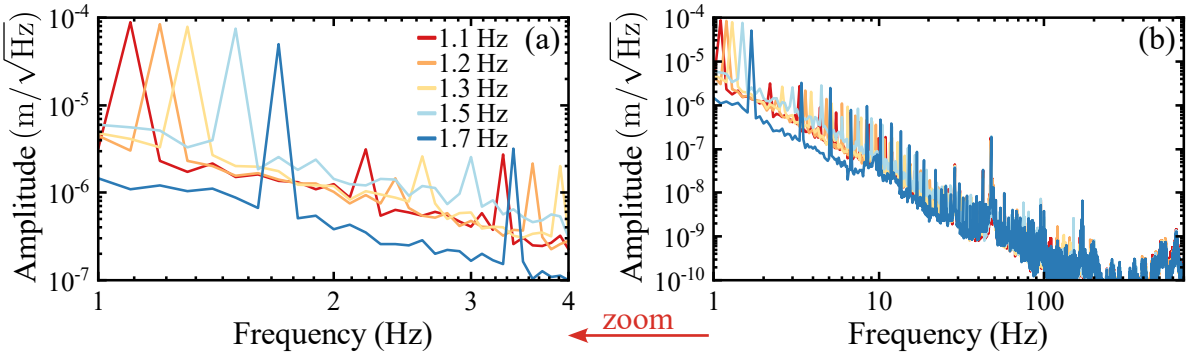


Figure 3.11.: **PTC 3 K stage vibrational noise, operation frequency dependence (*z*-direction).** (a) Vibration noise amplitude measured at the PTC (PTD 411 DN160CF) 3 K stage in z-direction for five different operation frequencies. Sampling rate: 0.05 ms, PTC 3 K stage at 4 K. (b) Complete bandwidth.

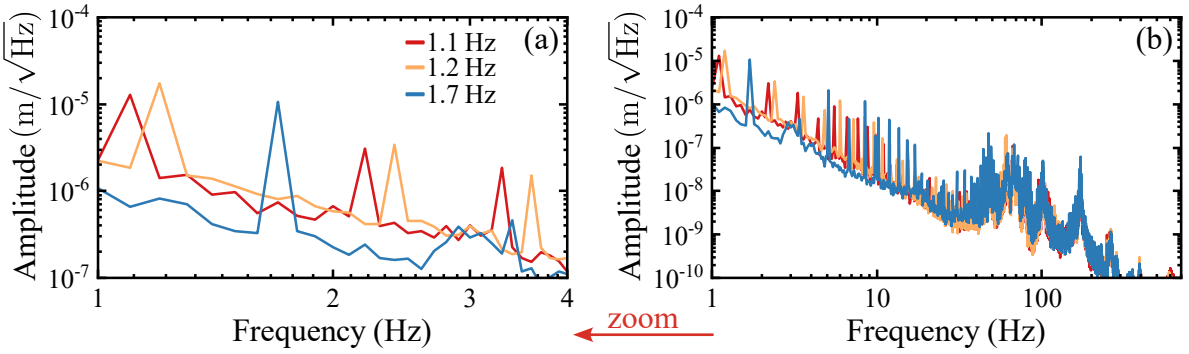


Figure 3.12.: **PTC 3 K stage vibrational noise, operation frequency dependence (*x*-direction).** (a) Vibration noise amplitude measured at the PTC (PTD 411 DN160CF) 3 K stage in x-direction for three different operation frequencies. Sampling rate: 0.05 ms, PTC 3 K stage at 4 K. (b) Complete bandwidth.

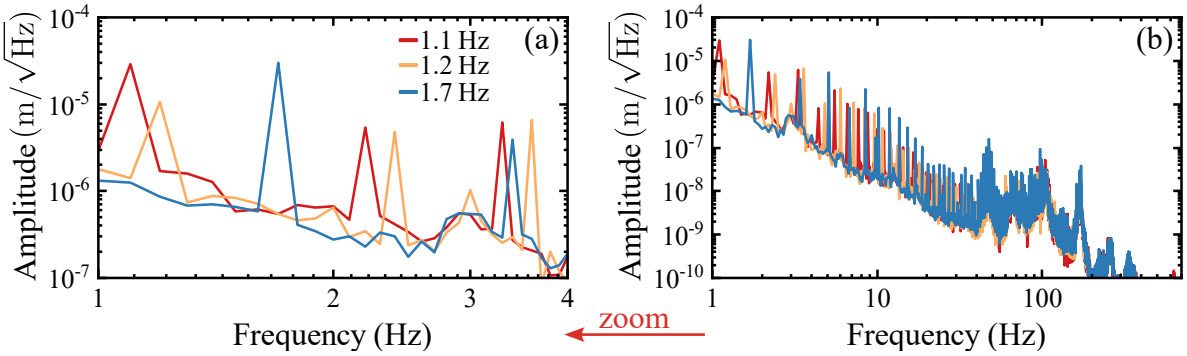


Figure 3.13.: **PTC 3 K stage vibrational noise, operation frequency dependence (*y*-direction).** (a) Vibration noise amplitude measured at the PTC (PTD 411 DN160CF) 3 K stage in y-direction for three different operation frequencies. Sampling rate: 0.05 ms, PTC 3 K stage at 4 K. (b) Complete bandwidth.

3.3. Vibration isolation concept, implementation into the overall concept

In order to develop the concept of vibration isolation, four different sources of vibrational noise must be considered. The PTC itself, the rotary valve, the helium compressor, and the noise from the ground floor.

The helium compressor is isolated in an enclosure for vibration and sound decoupling (Figure 3.5), as described in Section 3.2. It is also located in a separate room with 20 m of flexlines between the compressor and rotary valve, as depicted in Section 3.1. The rotary valve is detached from the PTC and suspended from the ceiling. In order to mitigate the generation of acoustic noise, the PTC head and rotary valve are enclosed in a stainless steel housing and a wooden box, respectively, both filled with stone wool. The supply, return, and connection line between the PTC and rotary valve are wrapped in butyl rubber and neoprene fabric.

The remaining task is to develop a combination of isolation from the ground and the PTC, to form a low vibration coupling to the STM. In the literature, the majority of STM systems are supported by air cushion isolators (e.g. rubber bellows allow to lift the system with pneumatic air pressure) or spring isolators with or without eddy current damping, which isolates the system from ground motion. It is common practice to incorporate multiple insulation stages with different resonance frequencies in a sequence [163, 167–170]. As outlined in Section 2.3, the performance of isolation is represented by a transfer function (Equation 3.3). A compromise between a low transfer function at high frequencies and a small enhancement at resonance frequency must be found. Air cushion isolators often show resonance frequencies of ∼2 Hz with a transfer function value of 0.1 at 10 Hz [71]. A reduction of the resonance frequency would result in the necessity for larger isolators, due to the requirement for softer springs. The technology of active damping is particularly suited to applications at low frequencies. One could detect the vibration at the cold-end of the PTC and counteract it by actuators between the cold-end and the STM. However, such active damping of an STM is challenging [171] due to electrical noise arising from the central unit of counteracting piezos and due to the

additional thermal load from the cabling [172]. Hence, we opted for a passive damping only.
Consequently, the following alternative isolation concept was developed based on the reduction in resonance frequency by minimal or negative stiffness as described in Section 2.3.
The initial concept involved the use of a vibration balance [162, 163] positioned between the PTC and the STM chamber. A vibration balance relies on a 90° configuration to effectively counteract vibrations. However, its implementation resulted in a design that was overly complex and presented numerous practical drawbacks concerning the assembly.

3.3.1. Complemented vibration isolation

The complete vibration isolation system is illustrated in Figure 3.14 (a). A linear minimal stiffness vibration decoupling has been developed as described in Section 3.3.2. The STM chamber is firmly bolted to an aluminium frame (Figure 3.2) below the linear minimal stiffness isolation. As illustrated in Figure 3.14 (b), this STM chamber with frame is floating relative to the floor and the PTC. The frame is made from an aluminium profile (Figure 3.2), allowing adaptation to future structures. It is hollow and filled with sand and concrete. Concrete is used in the lower, the corner, and the supporting profiles to enhance the rigidity and lower the center of mass. The sand filling is adjacent to the STM chamber for the vibrations. In addition to the associated ion getter pump, the frame also carries the preparation chamber and the pump line with a turbomolecular pump and scroll pump. To decouple the frame, including all its components, from the lab floor, three mechanical isolators from Minus K® Technology Inc. are used instead of the commonly employed air spring isolators. These isolators also rely on the principle of minimal stiffness. The manufacturer specifies a vertical resonance frequency of 0.5 Hz across the entire load range and a horizontal resonance frequency of 0.5 Hz near the nominal load [173]. This design achieves transmission coefficients as low as 0.1 at 2 Hz, while air spring isolators typically reach such isolation levels only at ∼10 Hz. Three of such isolators (model: 800CM-1, configured for a total mass of ∼900 kg) are positioned at three corners of the aluminium frame. The isolators are mounted on wedge height adjusters, atop columns fixed to the lab floor. The adjusters allow precise height tuning

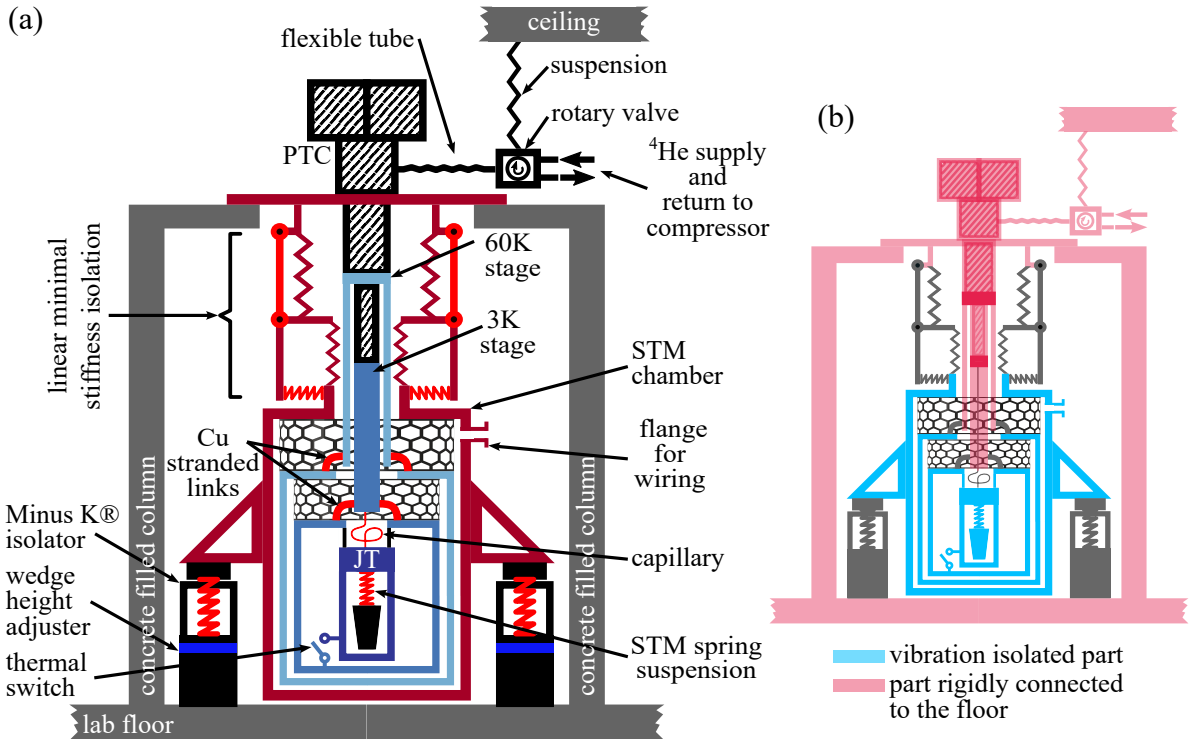


Figure 3.14.: **Complemented vibration isolation.** (a) Schematic cross section of the system showing the vibration isolation concept. (b) Colored version of (a). The STM chamber is supported on isolators and can move relative to the PTC, which is only connected by soft Cu stranded links, the capillary tube and bellows of minimal stiffness.

for the upper linear minimal stiffness setup. The isolators support the frame at a height of 0.8 m, approximately aligning with the system's center of mass to improve isolation performance.

3.3.2. Linear minimal stiffness setup realization

The system is composed of two vibrationally separated sections. The first section includes the two-stage PTC. The second section is vibrationally isolated from the PTC and contains the STM chamber including radiation shields at 80 K, 4 K and 1 K, a JT stage, and the STM.

A linear minimal stiffness vibration isolation mechanism decouples the PTC from the rest of the system, as shown in Figure 3.15. The idea is depicted schematically in Figure 3.15 (a). It uses two soft, stainless steel edge-welded bellows positioned between

the PTC and the STM chamber. One bellow compensates for spring constants in the horizontal direction, while the other compensates in the vertical direction. The upper bellow, with a diameter of 200 mm and a lateral spring constant of 7 N/mm, serves for the compensation in the horizontal direction (x-direction). The lower bellow, with a diameter of 150 mm, and with an axial spring constant of 3 N/mm, handles the compensation in the vertical direction (z-direction). The upper bellow with its upper flange is fixed to the rigid frame. It experiences an upwards compression force due to the air pressure p acting on the flange across the difference in the bellows cross-sectional area. An arrangement of linkages with frictionless pivot bearings (labeled B) are mounted at three evenly spaced positions around the bellow's outer circumference. A photo in Figure 3.15 (b) shows the arrangement of all used components and details are shown in Figure 3.16. These pivot bearings are internally made from leaf springs. Consequently, in contrast to ball bearings, they are frictionless, free of backlash, self-centering, compatible with vacuum environments, and necessitate no maintenance. Commonly, they are used in gimbals, positioners, sensors, optics, and tensiometers.

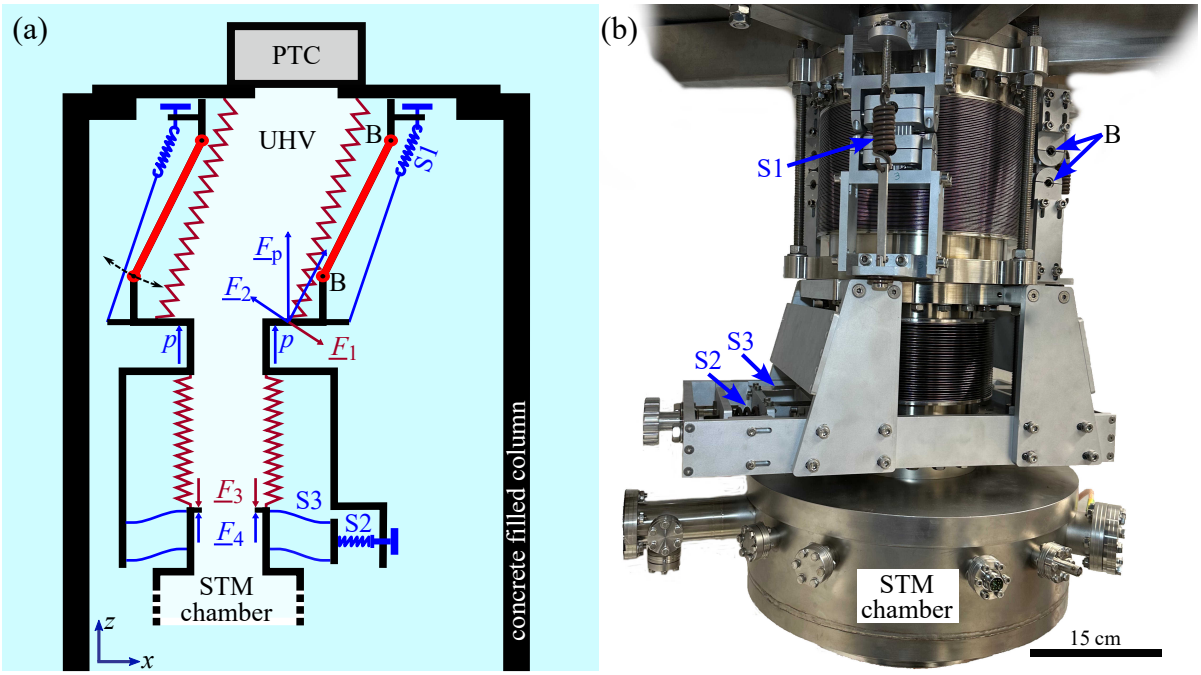


Figure 3.15.: **Vibration isolation linear minimal stiffness setup.** (a) Schematic representation depicts the minimal stiffness configuration. The PTC is resting on two concrete filled columns, while the STM chamber is floating. Two bellows (red zigzag lines) are displaced from their equilibrium position, resulting in the restoring forces $\underline{F}_1$ and $\underline{F}_3$, respectively. In the case of the lower bellow, $\underline{F}_3$ is compensated for by a force $\underline{F}_4$, which originates from preloaded leaf springs S3. The adjustable spring S2 is used to set the preloading, until a low resonance frequency in the vertical direction is achieved (minimal stiffness). At the upper bellow, the horizontal displaced STM chamber is driven backwards by the force $\underline{F}_1$. The counteracting force $\underline{F}_2$ arises due to the configuration of the bearings B, which are connected by the red rods in combination with the upwards, external air pressure that exerts a force onto the flange, resulting in the force $\underline{F}_p$ that effectively acts as F_2 on the pendulum via the red rod at B. The spring S1 can adjust the strength of $\underline{F}_2$. (b) Photograph of the minimal stiffness setup. The springs S1-S3 and bearings B are labeled.

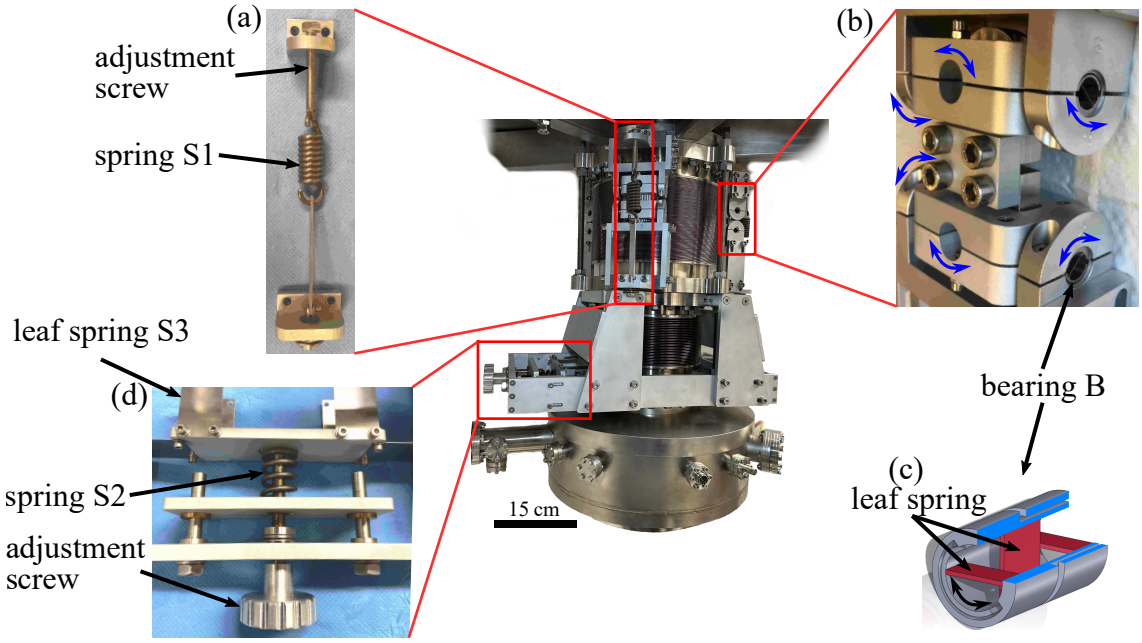


Figure 3.16.: **Vibration isolation linear minimal stiffness setup details.** (a) Photograph of the spring S1 to adjust the minimal stiffness in horizontal direction via a screw. (b) Photograph of the arrangement of linkages with the frictionless pivot bearings (c) allowing the upper bellow to move nearly frictionless in the horizontal plane. Six frictionless pivot bearings are used in each of the tree joints. (c) Cutted viev of CAD drawing of the frictionless pivot bearings. (d) Photograph of the spring arrangement for preloading the leaf spring S3 compensating vertical force.

The minimal stiffness arrangement operates as follows: A bellow naturally tends to keep in its equilibrium position. If the upper bellow is displaced, it exerts a restoring force $\underline{F}_1$ on the flange. The configuration with bearings B, connected by red rods, produces a counteracting force $\underline{F}_2$ that opposes $\underline{F}_1$ via guiding the pressure force on the bottom flange. This force $\underline{F}_2$ is tuned using a spring (S1) mounted parallel to the bellow. The tuning continues until the setup achieves a low horizontal resonance frequency. The spring S1 has a spring constant of 64 N/mm and a pretension of 114 N. The lower, second bellow assembly enables compensation in the vertical direction (z-direction). In total, six leaf springs allow for a movement only in the z-direction (details not shown in the 2D schematic, but can be found in Figure 3.16). Displacing the bellow, either by stretching or compressing, generates a restoring force $\underline{F}_3$. The preloaded leaf springs produce a

force $\underline{F}_4$ that balances $\underline{F}_3$. $\underline{F}_3$ results from the spring constant of the lower bellow. The spring S2 allows for adjustment of the preloading, thus altering the force $\underline{F}_4$.
The leaf springs S3 are designed to resist buckling under the force from S2. They are made of spring steel material, each measuring 3 cm × 6 cm with a thickness of 0.3 mm. The spring S2 has a spring constant of 47 N/mm. The resulting x, y, z decoupling of the vacuum chamber from the PTC is only effective when paired with the three isolators from Minus K® Technology Inc., which support the system's total weight of 800 kg.

In conclusion, the linear minimal stiffness setup allows the tuning of the resonance frequency for the lower part of the assembly (Figure 3.15). The tuning is achieved by adjusting forces using springs to counteract the spring constants of the edge-welded bellows, resulting in minimal stiffness. The configuration is much more compact as a 90° vibration balance setup, improving the thermal contact between the PTC and the vibration isolated section of the cryostat.

3.3.3. Stiff support structure

A stiff support structure has been designed to mechanically couple the STM mounting position (the JT stage, via the 4 K plate) to the 80 K plate and from there to the large mass of the STM chamber and frame without large heat conduction in order to keep low temperatures. The PTC cools the 80 K and 4 K plate using Cu stranded links as illustrated in Figure 3.14 (more details in Section 3.4). Thus, they are a path of vibration transmission. The 4 K plate supports the JT stage and STM, making it critical to connect it rigidly to the chamber. This creates a compact low-frequency system of STM chamber and cooled STM, with a resonance frequency below the PTC excitation. The minimal stiffness of this setup also compensates for the spring constants of the Cu stranded links, which connect the floating and fixed parts of the system (the spring constants of the Cu stranded links are one order of magnitude smaller than the spring constants of the edge-welded bellows). The design has to balance mechanical stability and low thermal conductivity. To reduce heat flow from the room-temperature chamber to the 80 K and 4 K plates, the structure uses materials and shapes that limit heat conduction.
Six designs were tested for their thermal isolation, their first resonance frequency, and their buckling stability (Figure 3.17).

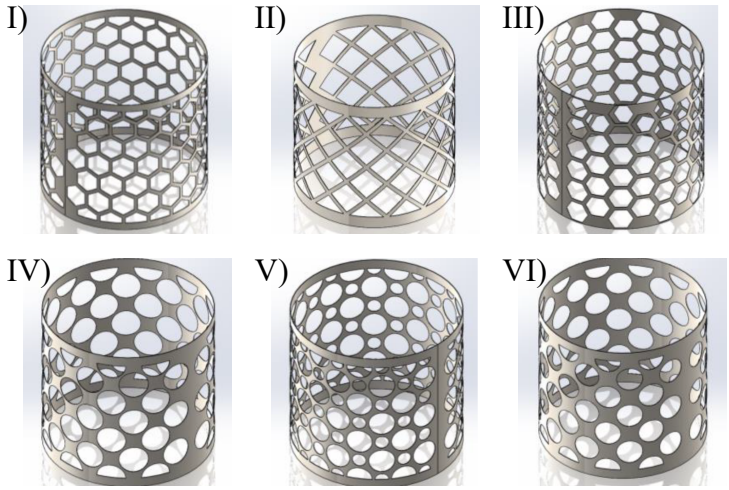


Figure 3.17.: **CAD drawings of cylindrical support structures.** For each design, a stainless steel 0.5 mm thick sheet material is chosen, bend into a cylinder with a diameter of 197 mm with a height of 180 mm. The results of finite element simulations using these designs are listed in Table 3.1.

Table 3.1.: **Table comparing different cylindrical support structures:** Thermal conduction between 50 K plate and 4 K plate, first resonance frequency and buckling in stability force. Using the designs depicted in Figure 3.17. The lower end of the cylinder is fixed for the eigenmode determination. The buckling force is determined in axial direction (vertical force).

design study	**thermal heat load** 50 K to 4 K (mW)	**first eigenmode** (Hz)	**buckling force** (N)	**mass** (g)
I)	44	226	5400	164
II)	46	170	3900	185
III)	52	235	5340	161
IV)	221	212	4200	195
V)	256	252	6900	194
VI)	341	257	10900	237

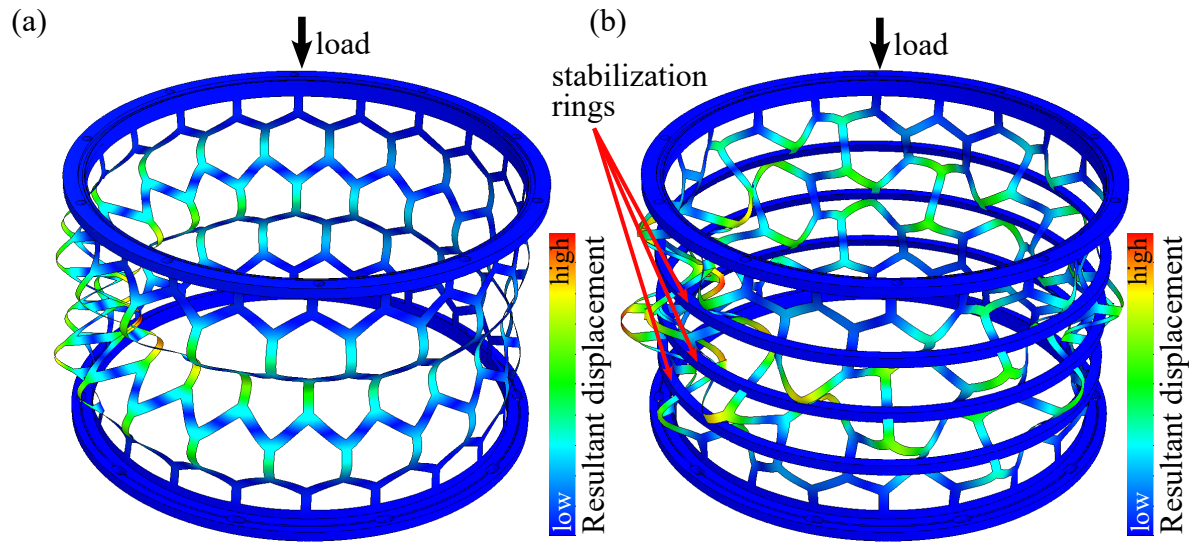


Figure 3.18.: **Buckling mode CAD study of the realized 4 K cylindrical support structure (design I, Figure 3.17).** A critical load of 4800 N is applied without stabilization rings (a) and of 6700 N with stabilization rings (b).

In each case, a stainless steel sheet material with 0.5 mm thickness is selected. It is formed into a cylinder with a diameter of 197 mm and a height of 180 mm. Finite element simulations (using SOLIDWORKS®) with a fixed lower end of the cylinder are used to determine the first eigenmode frequency. The buckling force is determined in the axial direction by applying a vertical force. Results are listed in Table 3.1. The best thermal isolation is achieved by design I, when the hexagons are aligned with two sides parallel to the cylinder's axis. This orientation creates the longest path between the cylinder's ends, reducing heat conduction. Rotating the hexagons by 30° (study III) increases heat transfer. A rectangular grid (study II) has similar heat transfer but lower stability, shown by a reduced first eigenmode frequency and buckling resistance. Circular holes (study VI) double the buckling resistance but increase heat transfer nearly eightfold.
Since the series of finite element simulations revealed the most appropriate solution being a cylindrical, honeycomb-patterned design (design I), it is selected for the final 4 K support structure. Figure 3.18 shows a buckling analysis once as in the design (Figure 3.18 (a)) and once with stabilization rings (Figure 3.18 (b)). Adding a triangular cross-section ring at the center of each honeycomb prevents the first buckling mode, increasing its resistance by 40 %. The rings' small contact area ensures that vertical heat

flow remains unchanged.

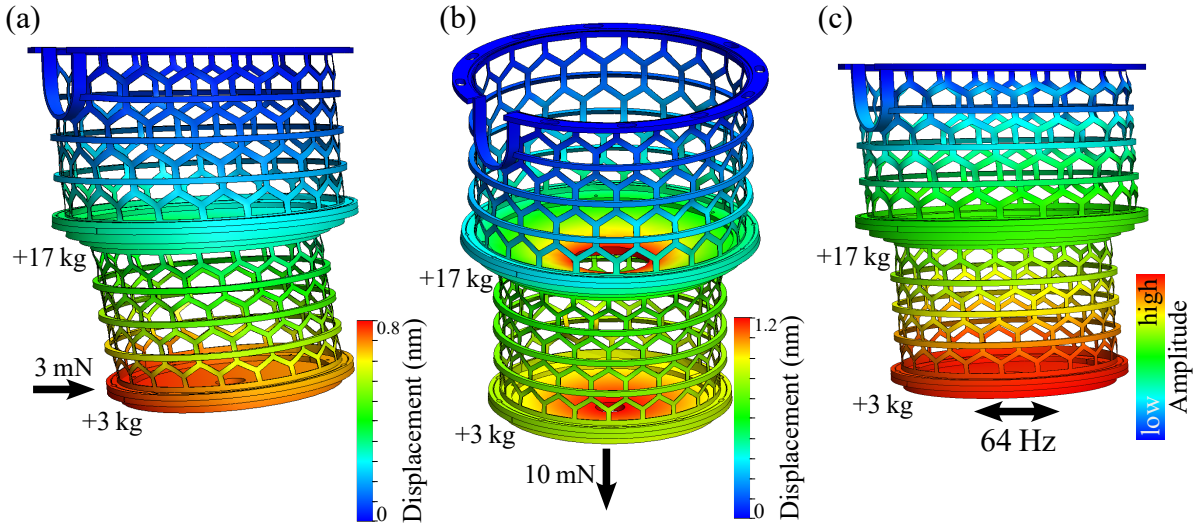


Figure 3.19.: **(a)-(b) Static displacement CAD study of the realized support structure. (c) calculated first eigenmode.** (a) A horizontal static force of 3 mN at the 4 K plate results in a displacement of 0.8 nm at the 4 K plate. (b) A vertical static force of 10 mN results in a displacement of up to 1.2 nm at the 4 K plate. The force are deduced from the measured PTC vibration amplitudes and the measured spring constants of the fine Cu stranded links. (c) Snapshot of the finite element simulation of the first eigenmode of the setup. The masses of the plates as marked include the weight of the radiation shields mounted to them.

A separate study examines the deflection of the combined 80 K and 4 K cylindrical support (Figure 3.19). It aims to estimate the vibrational amplitudes extracted by the PTC forces. Measured PTC vibration amplitudes are approximately 30 µm in the vertical direction and 10 µm in the horizontal direction at its cooling stages (Section 3.2). The PTC operation frequency is well below the first eigenmode of the support structure (Figure 3.19 (c)). Using the stiffness of the Cu stranded links (in total ∼0.3 N/mm), the resulting force acting on the plates is equal to ∼3 mN in the bending direction and ∼10 mN in the vertical direction. The calculations then yield vibration amplitudes of ∼1 nm in both directions (Figure 3.19 (a),(b)).
The realized parts (Figure 3.20) are made from 0.5 mm thin stainless steel sheet material, with a honeycomb-like pattern cut into it, aligning the honeycombs with vertical edges. The sheets are then bent into a cylinder and welded by spot laser welding. Stabilization rings are spot-welded onto the cylinder afterwards. The heat conduction is discussed in

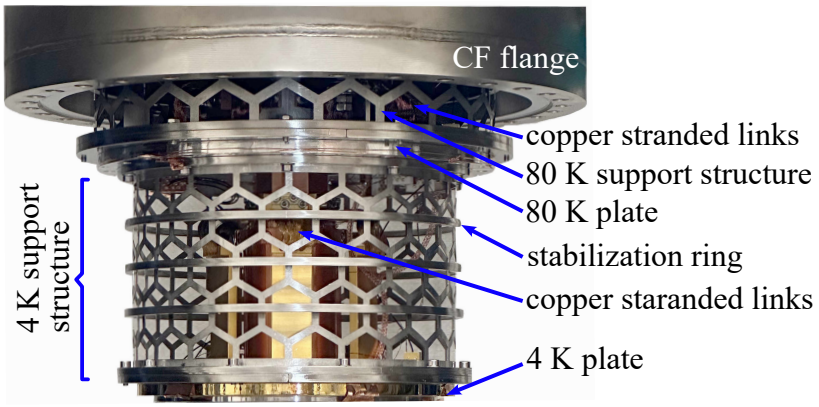


Figure 3.20.: Photograph showing the honeycomb-like cylindrical support structure installed to the DN300CF flange. The cylindrical support structures mechanically couples the DN300CF flange at room temperature to the 80 K plate and 4 K plate.

Section 3.4, with Figure 3.24.

3.3.4. STM spring suspension

A final isolation stage is placed between the STM and the JT stage (Figure 3.21). The STM is suspended by three springs, made from CuBe, which provide a measured vertical resonance frequency of 4 Hz. The setup targets higher frequencies that are not effectively damped by the minimal stiffness setup and therefore are still present at the JT stage. As presented in Section 4.1, in Figures 4.5 to 4.6, vibration measurements at the 4 K plate showed remaining frequencies at approximately 30 Hz, 60 Hz, 200 Hz and above. In detail, the springs are mounted within cylindrical towers that extend upwards through the JT stage (Figure 3.21). This design allows for longer springs, lowering the resonance frequency. Each tower includes an adjustment mechanism enabling horizontal and vertical alignment of the STM within the 1 K radiation shield. The three CuBe springs have a spring constant of 0.025 N/mm and a pre-tension of 0.08 N (Figure 3.22 (a)). At room temperature, the theoretical vertical resonance frequency is 2 Hz and the horizontal one is 1.4 Hz. To dampen the resonance amplitude, a PTFE band is placed inside the springs. The PTFE band (800 GoldEnd®, A.W. Chesterton Co.) is cut into stripes and heated to 150 °C in an oven prior to insertion. The preheating prevents shrinkage during bakeout, ensuring that the STM remains aligned. The resonance frequency and damping are

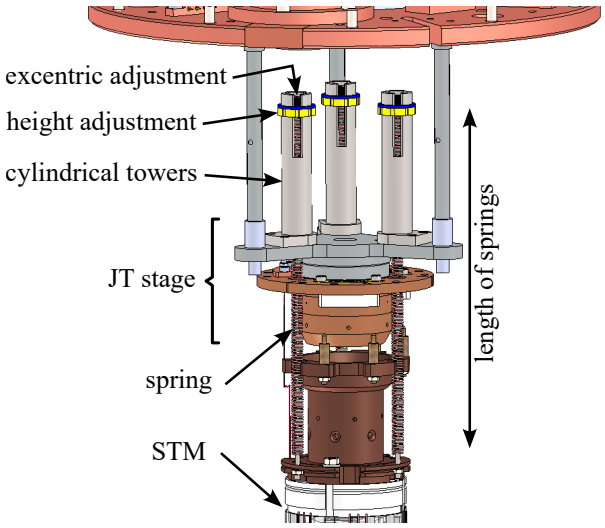


Figure 3.21.: **CAD drawing of the STM spring suspension.** Cylindrical towers allow for longer springs, expanding through the JT stage.

measured by exciting the suspension with a wobblestick and recording the motion with a camera at approximately ∼20 K. A resonance frequency of $f \approx 4$ Hz with a quality factor $Q = 5$ is found (Figure 3.22 (b)). The damping factor γ is calculated from the amplitude decay over time using:

$$\gamma = -\frac{1}{t} \ln\left(\frac{A_1}{A_0}\right), \tag{3.2}$$

where t is the time elapsed between amplitude A_0 and A_1. The quality factor Q is then determined as $Q = \frac{\omega_0}{2\gamma}$, where $\omega_0 = \sqrt{\omega^2 + \gamma^2}$ is the angular frequency of the undamped oscillator, and ω the angular frequency of the damped oscillator. The resulting theoretical transfer function $\kappa(f)$, plotted in Figure 3.22 (b), uses:

$$\kappa(f) = \sqrt{\frac{\omega_0^4 + 4\gamma^2 \cdot (2\pi f)^2}{\left(\omega_0^2 - (2\pi f)^2\right)^2 + 4\gamma^2 \cdot (2\pi f)^2}}, \tag{3.3}$$

with f the excitation frequency.

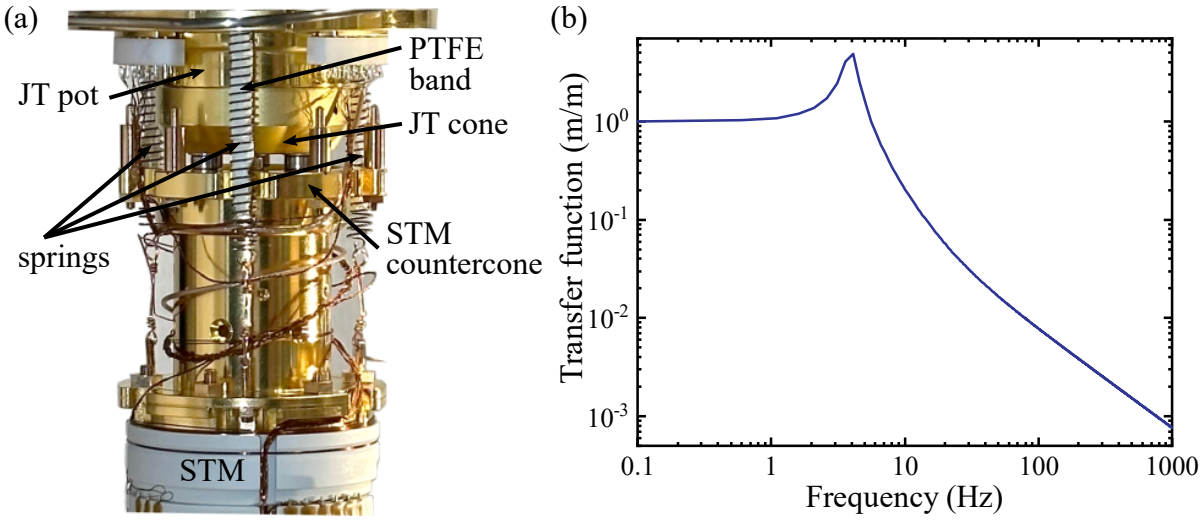


Figure 3.22.: **STM spring suspension.** (a) Photograph showing the STM spring suspension. PTFE band (white) is inserted into the springs. A gap between the JT cone and the STM countercone allows for unimpeded motion. (b) Calculated transfer function of the vertical STM spring suspension for the measured values of $f = 4\,\mathrm{Hz}$ and $Q = 5$.

3.4. Cryostat design

As previously delineated, the cryostat is composed of two distinct sections. The first is an assembly equipped with a two-stage pulse tube cryocooler (TransMIT PTD 411), which exhibits a cooling capacity of 1 W at 4 K and 20 W at 60 K. The second section is vibrationally isolated, comprising radiation shields (at 80 K, 4 K, and 1 K), a Joule-Thomson stage, and the STM.

3.4.1. Supply lines for the JT stage

The cooling, or more precisely, the heat transfer from the STM is achieved by the PTC and a JT stage, both operating with ^{4}He. The PTC operation is detailed in Section 2.2.1 and the JT one in Section 2.2.2. The high-pressure ^{4}He line enters the UHV directly beneath the PTC flange (Figure 3.23 (a)). Initial thermalization of the gas occurs at a copper cylinder mounted to the PTC's 60 K stage. The high-pressure line is soldered to the cylinder. An additional cylinder of aluminum, chosen for its low density, is mounted below the copper cylinder. It extends downwards, carrying the Cu stranded links for thermal connection to the 80 K plate. The two cylinders also serve as radiation shields for

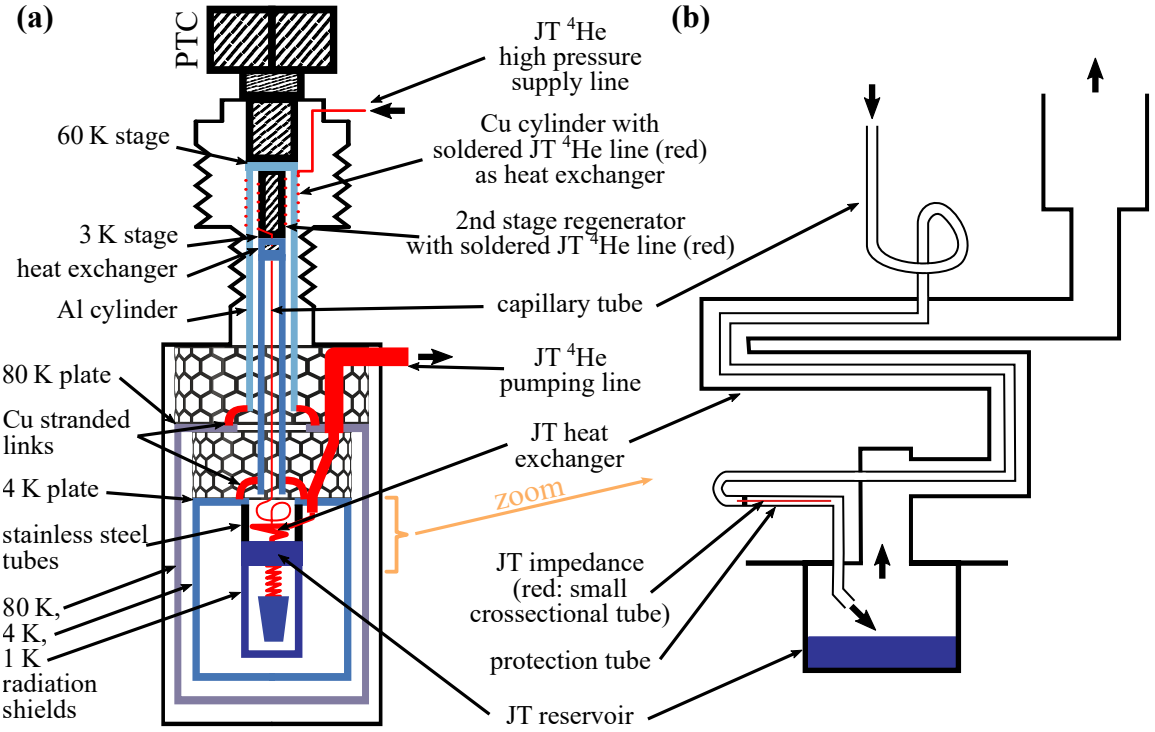


Figure 3.23.: **Cryostat design.** (a) Schematic of the cryostat. (b) Schematic of the JT stage.

the PTC 3 K stage and the ^{4}He high-pressure line. Subsequently, the high-pressure line connects to a tube soldered to the regenerator of the PTC's 3 K stage. It has been shown that the regenerator provides additional cooling power, often called the hidden cooling power, when the thermal connection is carried out along the regenerator [174–177]. The JT stage used in this system is not operated as a JT, but as an evaporation cooler with a continuous supply of liquid ^{4}He. It does not operate with a valve, but with an impedance (Figure 3.23 (b)). At the PTC 3 K stage itself, an additional heat exchanger is installed that liquefies the ^{4}He for optimized operation of the JT stage. From there, a capillary tube delivers the liquid ^{4}He to the JT stage. A copper cylinder, mounted at the PTC 3 K stage, serves as a radiation shield for the capillary tube.

3.4.2. Radiation shields

The vibrationally isolated lower section of the cryostat features three temperature stages: 80 K, 4 K, and 1 K, as shown in Figure 3.23 (a). The 80 K and 4 K plates that are connected

to the 60 K stage and the 3 K stage of the PTC by Cu stranded links, respectively, serve as the top of the radiation shielding. Two cylindrical radiation shields are mounted here. They also serve as thermal anchoring of the JT low-pressure pumping line and as thermal anchoring of the wires for the operation of the STM as described in Section 3.6. The radiation shields include shutters for optical access and in-situ exchange of the tip and sample, detailed in Section 3.5. The outermost 80 K radiation shield, made of aluminum, has an outer and inner shutter, both thermally anchored by soft Cu stranded links to the shield. The 4 K radiation shield is also manufactured from aluminum, but has only one outer shutter. The innermost 1 K radiation shield is mounted to the JT stage. It is constructed from Cu with an Au plating on an Ag diffusion barrier layer. All radiation shields are polished from the outside to minimize radiative heat transfer via reflection. Thermal connections between the vibration-isolated section comprising the plates and the PTC stages are realized by soft copper links mounted at the end of the connecting cylinders (Figure 3.23). The links are bundles of thin, 50 µm diameter, wires. A stiff connection between the UHV chamber and the plates, e.g. to compensate for excitations via the Cu stranded links, is described in Section 3.3.3. It is realized by cylinders made from 0.5 mm thin stainless steel sheet material structured with a honeycomb-like hole pattern (Figure 3.24).

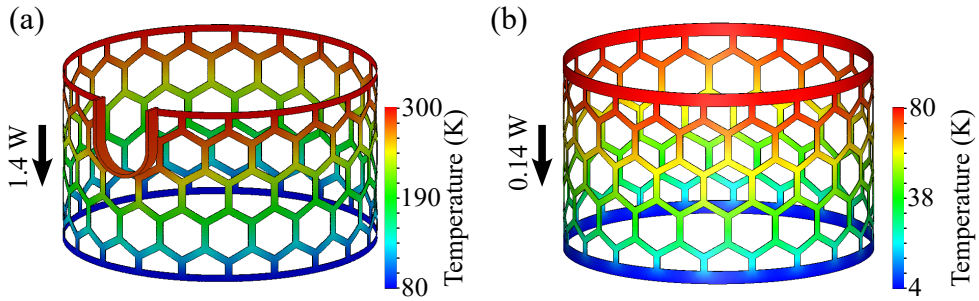


Figure 3.24.: **Thermal heat flow of support structures.** Simulated distribution of temperatures for the 80 K support structure (a) and 4 K support structure (b). The temperatures are fixed on the top and bottom. The resulting heat flow across the structure is marked.

The heat transferred by conduction is evaluated using steady state thermal finite element simulations, presented in Figure 3.24. It reveals heat loads of 1.4 W (<10 % of the cooling power of the PTC stage) and 0.14 W (∼70 % of the cooling power of the PTC stage) for the 80 K plate and the 4 K plate, respectively. The values of cooling power originate from

the PTC manufacturer's manual, showing values of 20 W at 62 K and 195 mW at 2.8 K. For comparison, a solid cylinder of equivalent dimensions, but without the structured design, would increase the heat load of the 4 K plate by a factor of six.

3.4.3. Joule-Thomson stage

The 1 K cooling stage comprises three heat exchangers linked to distinct temperature stages and the Joule-Thomson (JT) stage that achieves 1.2 K. A schematic is provided in

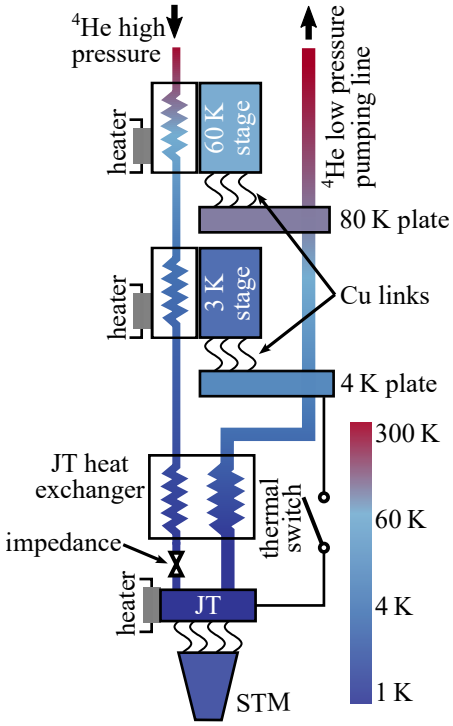


Figure 3.25.: **Schematic of the JT ^{4}He gas cycle inside the cryostat, colored by its local temperature.**

Figure 3.25. The ^{4}He gas from the high pressure inlet tube (up to 6 bar), gets cooled to ∼60 K at the first heat exchanger, directly mounted to the 60 K PTC stage. The second heat exchanger, located at the 3 K PTC stage cools the gas to ∼3 K. The JT stage includes the third counterflow heat exchanger, an impedance acting as a JT valve, and a 1.2 K pot pumped by a low pressure line. It serves as the final cooling step, reducing the temperature to 1.2 K. The JT stage is manufactured by CryoVac. It is supported by 7 cm long stainless steel tubes beneath the 4 K plate. The capillary tube

providing the liquid ^{4}He is wound in a spiral immediately before entering the JT stage heat exchanger for minimizing heat flow via the ^{4}He from the 4 K plate to the JT stage. Subsequently, the ^{4}He flows through the impedance into the JT pot. At the upper end of the JT pot, a low-pressure pumping line is mounted that firstly enters the heat exchanger and is subsequently fixed to the 4 K plate. Between the 4 K plate and room temperature, thin-walled stainless steel bellows are employed to minimize thermal load. Baffles are inserted in the bellows between the 80 K plate and room temperature to reduce radiative heat transfer. From the 300 K outlet of the STM chamber (Figure 3.23), an additional bellow guides the ^{4}He to a turbomolecular pump located in the neighboring room (Figure 3.2).

3.4.4. Precooling of the STM

The steps necessary to operate the cryostat will be discussed in Section 4.2. Here the mechanism to precool the STM to base temperature is described. It employs a wobblestick to move a u-shaped actuator. This elevates the STM (range II) in Figure 3.26) and presses it onto the base of the JT stage (before reaching position III)). This configuration also stabilizes the STM for a tip or sample exchange. A further movement of the actuator (position III) in Figure 3.26), will result in the additional closure of a thermal switch (Figure 3.25). The switch establishes a mechanical, thermal connection between the 4 K and 1 K radiation shields. This connection is essential for the STM cooldown, both for the initial cooldown and in subsequent cooldowns after a tip or sample exchange.

3.4.5. Cryostat: thermal consideration

Radiation heat load

In this section, an estimation is made of the heat load caused by radiation on individual radiation shields.
The heat flow rate $\dot{Q}$ between two plates facing each other is

$$\dot{Q}_{\text{rad plates}} = \sigma \frac{\varepsilon_1 \varepsilon_2}{\varepsilon_2 + \varepsilon_1 - \varepsilon_1 \varepsilon_2} A_1 \left(T_2^4 - T_1^4 \right). \tag{3.4}$$

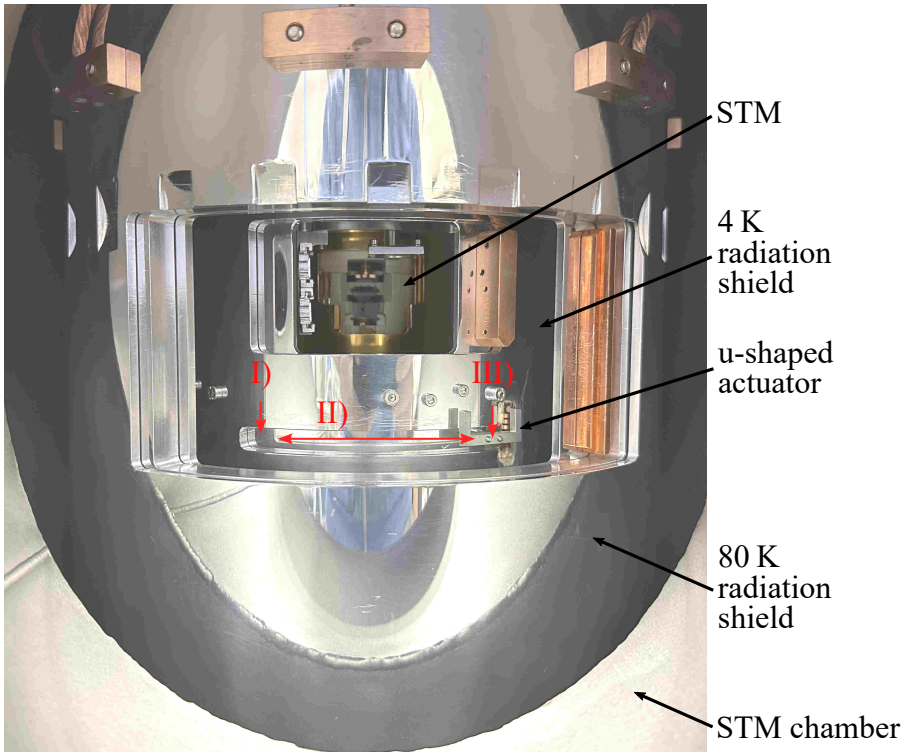


Figure 3.26.: **Photograph of opened shields with STM inside the STM chamber.** Three possible positions of u-shaped actuator are marked: I) STM hanging in springs, thermal switch is open. In the range of II) the STM starts to be moved upwards, thermal switch is open. Before reaching III) the STM is pressed against the JT stage. III) STM is pressed against the JT stage and additionally the thermal switch is closed.

For the case of two concentric cylinders, the relevant expression is

$$\dot{Q}_{\text{rad cylinders}} = \sigma \frac{\varepsilon_1 \varepsilon_2}{\varepsilon_2 + \left(\frac{A_1}{A_2}\right)(\varepsilon_1 - \varepsilon_1 \varepsilon_2)} A_1 \left(T_2^4 - T_1^4\right). \tag{3.5}$$

Here, σ is the Stefan-Boltzmann constant ($5.67 \times 10^{-8}\,\mathrm{W/m^2K^4}$) and ε_n is the emissivity of the surface with temperature T_n and area A_n. Subscript $\mathrm{n} = 1$ denotes the lower temperature surface and subscript $\mathrm{n} = 2$ the higher temperature surface. The following estimates are based on the assumption that all clean, polished aluminium surfaces have an emissivity of 0.03 [178] and all clean, polished Cu surfaces 0.02 [178]. The stainless steel vacuum chamber is assigned an emissivity of 0.15 [151]. These emissivity values apply at ambient temperature. However, it has been observed that low-resistivity metals

typically exhibit reduced emissivity at decreased temperatures [179]. Consequently, the radiation heat load, summarized in Table 3.2, is an estimated upper limit. The total

Table 3.2.: **Table of estimated radiation heat load.** The heat flow rate $\dot{Q}_{\mathrm{rad}}$ is calculated using Equation 3.4 and Equation 3.5. 4 K and 80 K plates include the lower lids of the radiation shields.

position of heatload	T_2 (K)	T_1 (K)	ε_2	ε_1	$\dot{Q}_{\mathbf{rad}}$ (W)
upper Cu cylinder	300	60	0.15	0.02	0.8
upper Al cylinder	300	60	0.15	0.03	1
upper Cu cylinder	60	4	0.03	0.02	10^{-3}
80 K shield cylinder	300	80	0.15	0.03	5.5
80 K plates	300	80	0.15	0.03	1.2
4 K shield cylinder	80	4	0.03	0.03	$8 \cdot 10^{-3}$
4 K plates	80	4	0.03	0.03	$2 \cdot 10^{-3}$

radiation heat load is approximately 9 W (45 % of total heat load) on the PTC 60 K stage and only 10 mW (5 % of total heat load) on the 3 K stage.

Cu stranded links: thermal contact conductance and thermal conductivity

Designing thermal links for STM cryostats poses a challenge, as they must efficiently conduct heat while remaining mechanically soft to reduce vibrational transmission. The trade-off stems from the opposing geometric dependencies of thermal conductance and mechanical stiffness. The thermal conductance is proportional to A/L, with the cross-sectional area A and length L. The spring constant of a rectangular beam, however, is proportional to A^2/L^3, complicating simultaneous optimization. Furthermore, the Cu stranded links must be manufactured in a manner that allows for their subsequent mounting. Our construction of Cu stranded links involves their mounting through the use of screws, leading to thermal contact resistance R_T, i.e. a temperature step of $\Delta T = R_\mathrm{T}\dot{Q}$ at the contact. Contact between pressed surfaces occurs at discrete points rather than across the entire contact area. The number of points rises linearly with applied force until the contact area approaches the apparent area [180, 181]. Another factor is surface conditions such as oxidation, often increasing the thermal resistance.
At the 80 K plate, the links interface Cu and Al, cleaned with an abrasive fleece before mounting. At the 4 K plate the contacts are Au-on-Au and at the Cu cylinder, connected to the 3 K PTC stage, they are Au-on-Cu, also pre-cleaned. The Cu stranded links are fixed using multiple M3 and M4 screws. A torque of 0.9 N m and 1.8 N m, respectively, is applied, providing theoretical clamping forces of >1000 N per screw [182, 183]. The temperature steps deduced from previous measurements are summarized in Table 3.3 and the assumptions are described in the following text.
At a temperature of 4.2 K, an Au-on-Au (490 N) contact can show a thermal contact conductance of $1/R_\mathrm{T} = 0.3\,\mathrm{W/K}$ and an Cu-on-Cu contact exhibits 30 times less [144]. For a Cu-on-Cu contact at 77 K values of 0.09 W/K (490 N) [144] and 0.49 W/K (670 N) [180] were measured.
To provide an initial estimate of the temperature rise at the contacts, the following assumptions are made: 1) A total clamping force of 4 kN is assumed at each contact. 2) The Cu-on-Al contacts at the Cu stranded links, that connect the 80 K plate with the 60 K PTC stage, are estimated by the aforementioned value for a Cu-on-Cu contact due to the lack of data in the literature. 3) For the same reasons the Au-on-Cu contact at the Cu cylinder, connected to the 3 K PTC stage, is conservatively estimated by a Cu-on-Cu contact. 4) Eight Cu stranded links connect the 80 K plate with the 60 K PTC

stage and conduct a heat flow rate of ∼8 W due to radiation (Table 3.2) and conduction (Figure 3.24). 5) Fife Cu stranded links connect the 4 K plate with the 3 K PTC stage and conduct a heat flow rate of ∼150 mW (Table 3.2 and Figure 3.24). The temperature steps are calculated by $\Delta T = \dot{Q} \cdot \frac{N_{\text{contacts}}}{N_{\text{Cu stranded links}}} \cdot \frac{F_{\text{lit}}}{F_{\text{clamping}} G_{\text{lit}}}$, with N_{contacts} the number of contacts with the corresponding force F_{clamping} at each contact, $N_{\text{Cu stranded links}}$ the number of utilized stranded links, and F_{lit} the applied force corresponding to the thermal conductance of the literature G_{lit}.
Additional temperature gradients are introduced by the Cu strands material itself. Assuming a thermal conductivity of 560 W/(m K) (Cu RRR50), for the Cu stranded links mounted between the 80 K plate and the upper Al cylinder, this results in a temperature difference of ∼7 K along the Cu strands. For the Cu stranded links at 4 K, a temperature increase of ∼0.4 K is calculated (using 320 W/(m K)). The findings are summarized in Table 3.3.

Table 3.3.: **Table of expected temperature change according to literature values by contact resistance and thermal conductivity of Cu strands.** Details are given in the text.

position of temperature step	**materials of contact**	**temperature step by thermal contact resistance** (K)	**temperature increase by thermal conductivity of Cu strands** (K)
80 K Cu stranded link	Al-Cu and Cu-Al	0.7-2.7	7
4 K Cu stranded link	Cu-Au and Au-Au	0.4 and 0.01	0.4

Heat load to the JT stage

A minimum temperature is targeted at the final cooling stage, the JT stage, by minimizing the heat flow from the 4 K plate to it. The following values are calculated. The suspension via thin stainless steel tubes (Figure 3.23 (a)) introduces approximately 80 µW to the JT stage through thermal conduction. The wiring contributes additional ∼13 µW. In the absence of holes in the radiation shields, the radiation heat load would be three orders of magnitude lower than the thermal conduction heat load.

3.5. STM

3.5.1. STM design

The development of STMs is influenced by various experimental requirements, such as the aim to scan micron-sized flakes or to apply magnetic fields. The STM presented in this thesis is designed to meet the following criteria:

1. UHV and cryogenic compatibility.
2. High vibration damping.
3. High magnetic field compatibility.
4. $12\times12\,\mathrm{mm}^2$ sample receptacle.
5. Coarse positioning of the sample stage with $4\times4\,\mathrm{mm}^2$ range.
6. In-situ tip exchange mechanism.
7. Optical access.
8. Radio frequency electromagnetic fields in the tunnel junction.

Point two can be met by effective vibration damping and by a resonance frequency of all STM components significantly higher than the feedback cut-off frequency. Additionally, components with similar resonance frequencies should be avoided to eliminate low-frequency beating. The mechanical transfer function of an STM can quantify these properties. It is defined as the ratio of the relative tip-to-sample motion amplitude to the excitation amplitude of the entire STM body. The degree of isolation depends on the resonance frequency of the STM, which is proportional to the square root of the ratio of the material's elastic modulus to its mass density [70]. To ensure a stiff STM, various materials, like metals and ceramics, have been utilized in previous designs, including phosphor bronze [184], titanium [185], MACOR® [186], SiPCu [187], copper beryllium [188], sapphire [189–191] and zirconia [192]. Table 3.4 lists materials historically used or considered for STM construction. The selection of materials features UHV compatibility, non-superconductivity down to 500 mK, no ferromagnetism or strong paramagnetism, and mechanical machinability. Hard and brittle materials can be machined using ultrasonic grinding machines with diamond tools [193]. When operating at cryogenic temperatures, the thermal expansion coefficients must match with other components of the STM, such as piezo actuators or glues, to prevent stress or breakage. Moreover, thermal conductivity is required for conducting heat generated by the STM piezo elements or from residual

Table 3.4.: **Table of properties of possible materials for the construction of an STM body.** The requisite properties of these materials include compatibility with UHV, the absence of superconductivity down to 500 mK, no ferromagnetism or strong paramagnetism, and the ability for machining. Values are for ambient temperature if not specified.

material	E/ρ (10^6 N/m²)/ (kg/m³))	**density** ρ (kg/m³)	**Young's modulus** E (10^9 N/m²)	**thermal expansion** α (10^{-6} 1/K)	**thermal conductivity** λ (W/m · K)	4 K **thermal conductivity** λ (W/m · K)
Be[194–196]	164	1850	287-321	11.3	200	700
Sapphire[194, 197]	101	3970	400	8	40	110
Al2O3[198–201]	98	3800	345-400	9	34	1
Shapal Hi MSoft™[202, 203]	61	2880	177	4.8	92	0.1
Tungsten carbide [198, 204, 205]	39	15600	530-700	5.2	110	
Zirconia [206]	31	6000	186	6.6	2.7	
Macor[207]	27	2520	67	8.5	1.46	
AlMgSi[203, 208]	26	2700	70	23.4	200-220	5
Stainless steel [209, 210]	24	8000	193	17.2	16.2	0.3
W[194, 196]	21	19300	400	4.5	174	6000
CuBe [210, 211]	15	8780	132	36	208	2
Phosphor bronze[212, 213]	13	8800	115	17	59-100	1.5

radiation. It also influences the cool-down time to the base temperature. Insulating materials reduce eddy current heating during magnetic field ramping and lower the risk of electrical shorts. They also prevent mechanical coupling between the magnet and STM via eddy currents, which would otherwise transfer magnet vibrations to the STM. Beryllium may offer the best ratio of elastic modulus to mass density. It is often chosen for components that require stiffness, lightness, and stability. This metal is among the lightest and has an elastic modulus about one third larger than stainless steel. However, beryllium and its salts are toxic, so machining requires strict safety measures. Sapphire (a Al_2O_3 single crystal) can also be used and must be machined with specialized ultrasonic grinding machines equipped with diamond tools. Such an approach has been realized for compact STMs before [189–191].

To fulfill criteria 1., 2., and 3., a compromise was made by using the light and stiff material Shapal Hi MSoft™. Its ratio of elastic modulus to density is about five times larger than that of phosphor bronze. This sintered composite of primarily aluminium nitride and boron nitride is diamagnetic, machinable, nonsuperconducting, has high thermal conductivity at 300 K, shows low outgassing [214], and exhibits a low thermal expansion coefficient [202]. In addition, the used piezo ceramics match the thermal coefficient of Shapal Hi MSoft™. They are PIC181 from PI Ceramic GmbH with a thermal expansion

coefficient of $4-8\times10^{-6}$/K and EBL#4 from EBL Products, Inc.. The glues used are EPO-TEK® H77, a thermally conductive, electrically insulating ceramic particle infused epoxy, and EPO-TEK® E2101, an electrically conductive epoxy, from Epoxy Technology Europe GmbH. Their thermal expansion coefficients are 33×10^{-6}/K and 48×10^{-6}/K respectively [215] i.e. one order of magnitude larger than Shapal.

Considering the transfer function of the STM, it can be optimized not only by the choice of material, but also by the STM design. A series of finite element simulations were conducted in an iterative manner to identify potential weaknesses. A reduction in material at the lower end of the STM (Figure 3.27 (a)) resulted in an increase in the resonance frequency of the pendulum-like motion. The conical shape thus exhibits an advantage compared to a cylindrical shape. Comparing to previous designs, up to 1/5 of the front material of the cylinder was removed to allow mounting of the inner components. This made the first eigenfrequency relatively low at $\sim1-3$ kHz [216]. The design focuses on maintaining the cylindrical or conical design as far as optical access and machinability allows. Previously, due to spatial constraints, the sample stage was constructed in a pendulum-like configuration beneath its piezoelectric elements. The new objective was to ensure that the mechanical path between the tip and sample is as short as possible. Consequently, a new design squeezes the sample stage in between the piezo stacks (Figure 3.33). It consists of a single plate out of Shapal Hi MSoft™, so the mechanical path is minimized by locating the sample directly next to the piezo. In addition, improvements have been made to the tip holder receptacle on the scanner side. Its material is now HeBoSint® CL-S 200, a boron nitride, silicon oxide ceramic that is 0.8 times lighter than Macor® and 0.7 times lighter than Shapal Hi MSoft™[217].

The final design is simulated for its first 10 eigenmodes. The corresponding relative displacement amplitudes are shown in Figure 3.27. SOLIDWORKS® Simulation 2020 x64 SP5.0 is used with a mesh size of $0.5-3$ mm. This results in 93 % of elements having an aspect ratio of less than 3. The results show that the scanner unit is now the weakest element, rather than the sliding table. The movement is a bending of the scanner in the x-direction and a bending in the y-direction at 5.4 kHz (Figure 3.27 (b)-(c)) (6.3 kHz for a tip holder made from Mg). The next two eigenmodes at 7.6 kHz and 7.9 kHz are a combination of bending motions of the STM body and the scanner unit (Figure 3.27 (d)-(e)). At 8.8 kHz, the sample holder lug is at resonance. The tip holder shows a bending at 15.8 kHz and 17.6 kHz (Figure 3.27 (g)-(h)). The second eigenmode of the STM body is

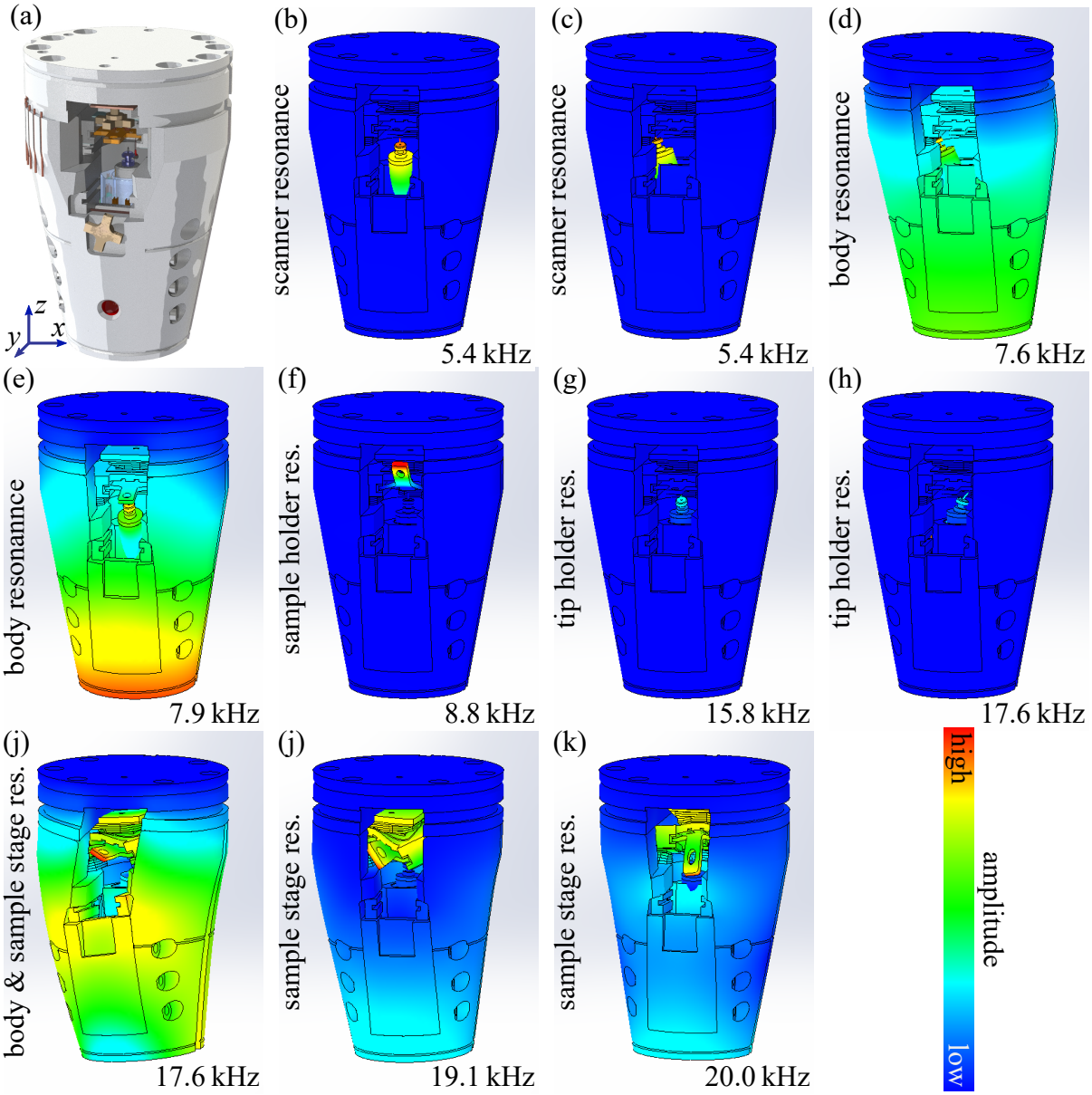


Figure 3.27.: **STM eigenmodes calculated by finite element simulation.** (a) CAD model of the STM. (b)-(k) Snapshots of calculated resonance frequencies. A simplified model of the STM, e.g. excluding screws, is employed to calculate the initial ten eigenmodes and their corresponding eigenfrequencies, as indicated. The STM top plate is fixed. Contacts, such as the walker sliding surfaces, are defined as fixed connections. The tip holder material is Mo. The sample holder material is phosphor bronze.

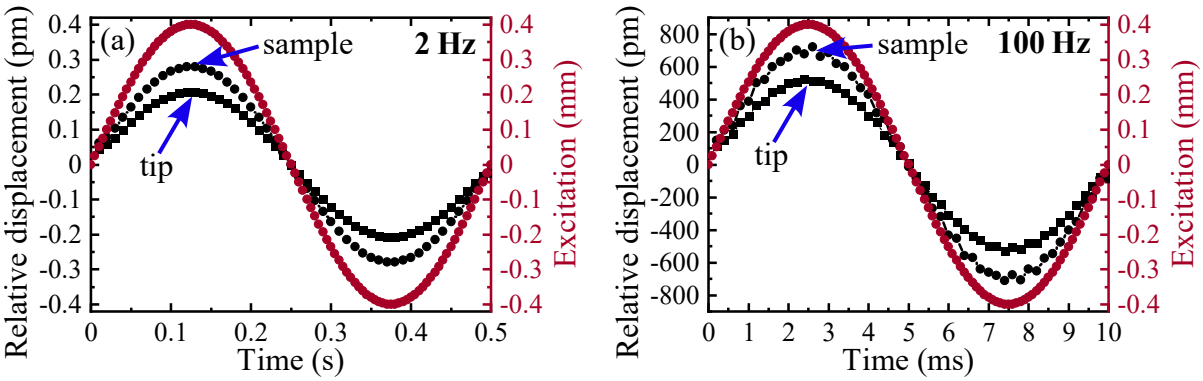


Figure 3.28.: **Calculated dynamic response of the STM during excitation in *z*-direction.** A simplified model of the STM, e.g. excluding screws, is employed to calculate the dynamic response for (a) 2 Hz and (b) 100 Hz. The relative displacement describes the movement relative to the excitation. The STM top plate is excited in z-direction with a sinusoidal frequency as shown. Contacts, such as the walker sliding surfaces, are defined as fixed connections. The tip holder material is Mo. The sample holder material is phosphor bronze.

a complex winding motion, also affecting the sample stage at 17.6 kHz (Figure 3.27 (i)). The sample stage modes are at 19.1 kHz and 20.0 kHz (Figure 3.27 (j)-(k)), hence, rather high with respect to other modes.

It is also possible to execute dynamic time-dependent simulations in SOLIDWORKS®. Using linear dynamic equations, the temporal response is computed for a time-dependent load. In the analysis, the inertia is considered in a mass matrix, while stiffness is included in a stiffness matrix. Damping is not considered, which results in a conservative estimate of the response. The STM support (top of the STM) is excited by defining an external load with an excitation of 0.4 mm amplitude in the z-direction at either a frequency of 2 Hz (Figure 3.28 (a)) or 100 Hz (Figure 3.28 (b)). A mesh with an element size of 0.8 – 4 mm is used, resulting in over 90 % of the elements having an aspect ratio below 3. The first 15 eigenmodes are included to calculate the response. For the 2 Hz case, the time span is set to 0.5 s with a time resolution of 0.01 s. For the 100 Hz case, they are set to 0.01 s and 2×10^{-4} s. The maximum resulting relative displacement is probed at the tip and sample center (Figure 3.28). The relative tip-to-sample motion is 0.07 pm for 2 Hz and 150 pm for 100 Hz, giving transfer function values of 2×10^{-10} and 4×10^{-7}, respectively. The evaluated z-direction amplitudes of up to 30 µm at the PTC operation frequency (Section 3.2) would result in only 6 fm tip-to-sample movement. This is two

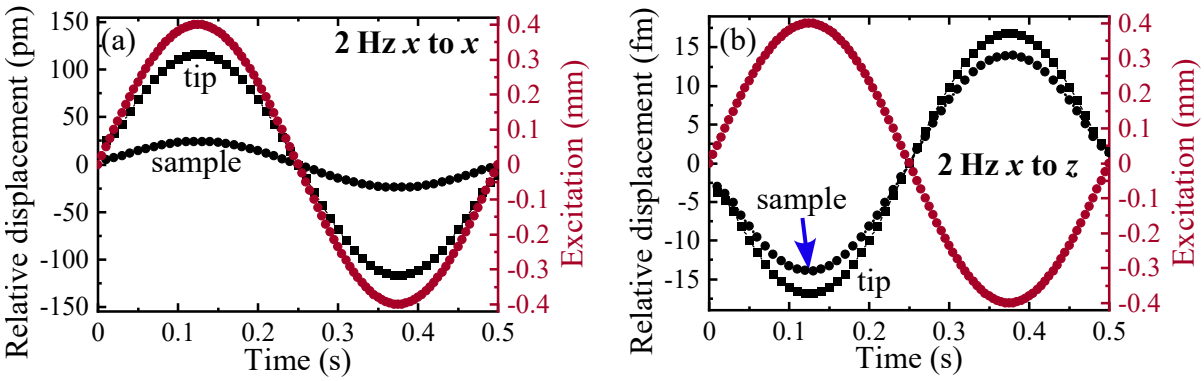


Figure 3.29.: **Calculated dynamic response of the STM during exitation in x-direction.** Relative displacement (black) for a STM top plate excitation in x-direction with a sinusoidal frequency of 2 Hz (red). The resulting relative displacement is once shown for the coupling to the x-direction (a) and once for the coupling to the z-direction (b). A simplified model of the STM, e.g. excluding screws, is employed. The relative displacement describes the movement relative to the excitation. Contacts, such as the walker sliding surfaces, are defined as fixed connections. The tip holder material is Mo. The sample holder material is phosphor bronze.

orders of magnitude less than in typical STM setups without a PTC.

Simulations are also run in the x- and y-direction. The excitation is set to 0.4 mm amplitude in the corresponding direction with a frequency of 2 Hz. The maximum resulting relative displacement is probed at the center of the tip and sample. It is probed once in the parallel direction of the excitation (Figure 3.29 (a) and Figure 3.30 (a)) and once for the coupling to the z-direction (Figure 3.29(b) and Figure 3.30(b)). The parallel direction provides an estimate for the lateral resolution of the STM and the coupling to the z-direction an estimate of the crosstalk to the tunneling current. For the x-direction the resulting calculated transfer function value is 2×10^{-7} at 2 Hz and 8×10^{-12} at 100 Hz. For the y-direction it is 2×10^{-7} at 2 Hz and 6×10^{-9} at 100 Hz. This indicates a stiff STM, albeit material is removed for the optical view. The curves depicted in Figure 3.29 (b) exhibit a phase shift of 180° between excitation and oscillation. An excitation below the resonance frequency will always result in a response in the same direction that is in phase. When the STM is moved to the right (positive x-values) the STM body on the right side is compressed, resulting in an upward movement (positive z-values). When the scanner is bending to the right, the left side of the scanner moves upwards. For a symmetric STM, the resulting movement in z-direction would be zero in the center at the evaluated tip and sample position. The observed phase shift of 180° is most probably due to the

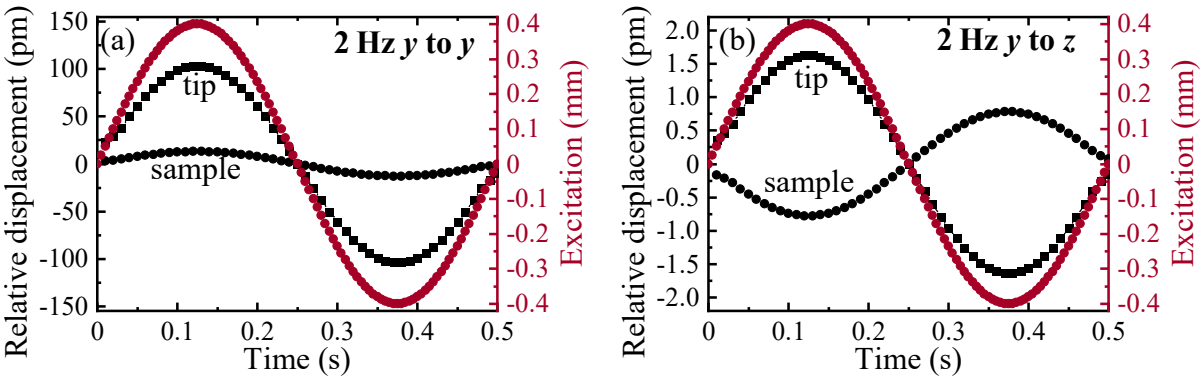


Figure 3.30.: **Calculated dynamic response of the STM during exitation in y-direction.** Relative displacement (black) for a STM top plate excitation in y-direction with a sinusoidal frequency of 2 Hz (red). The resultant relative displacement is once shown for the coupling to the y-direction (a) and once for the coupling to the z-direction (b). A simplified model of the STM, e.g. excluding screws, is employed. The relative displacement describes the movement relative to the excitation. Contacts, such as the walker sliding surfaces, are defined as fixed connections. The tip holder material is Mo. The sample holder material is phosphor bronze.

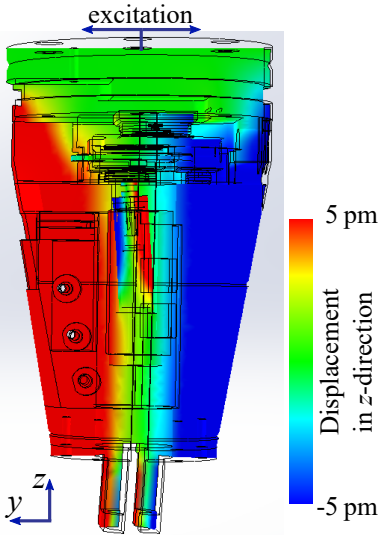


Figure 3.31.: **Sectional view snapshot of calculated dynamic response.** Relative displacement in z-direction for a STM top plate excitation in y-direction with a sinusoidal frequency of 2 Hz. The result corresponds to 0.12 s in Figure 3.30 (b). A simplified model of the STM, e.g. excluding screws, is employed. The relative displacement describes the movement relative to the excitation. Contacts, such as the walker sliding surfaces, are defined as fixed connections. The tip holder material is Mo. The sample holder material is phosphor bronze.

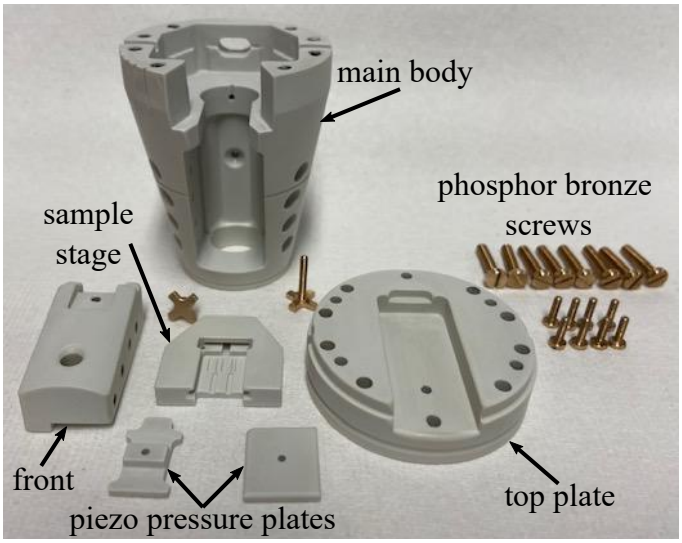


Figure 3.32.: Photograph of some machined STM components.

non-symmetric structure of the STM. For the case of the excitation in y-direction only the sample side is out of phase for z-movement (Figure 3.30 (b)) while the tip remains in phase. In Figure 3.31, the sectional view of the resulting movement of the STM is depicted for the time step of 0.12 s. The evaluated horizontal direction amplitudes of up to 10 µm at the PTC operation frequency (Section 3.2) would result in 2 pm horizontal tip-to-sample movement and sub 0.1 pm movements in z-direction.

For benchmarking the simulations, the measured resonances of the various components, the experimentally determined transfer function, and their comparison with the calculations are presented in Section 4.1.1.

The STM is realized in our mechanical workshop with standard milling cutters (Figure 3.32) under dry machining conditions, where the removed material is continuously vacuumed off. A conical shape is preserved by splitting the STM body into the main body and the top plate (Figure 3.32). This arrangement permits the mounting of the sample stage. Importantly, the mechanical path between the tip and the sample is maintained when the two parts of the STM body are separated. This path is indicated by a red dashed line in Figure 3.33 (a).
The STM features a $12 \times 12\,\mathrm{mm}^2$ sample receptacle with six sample contacts allowing

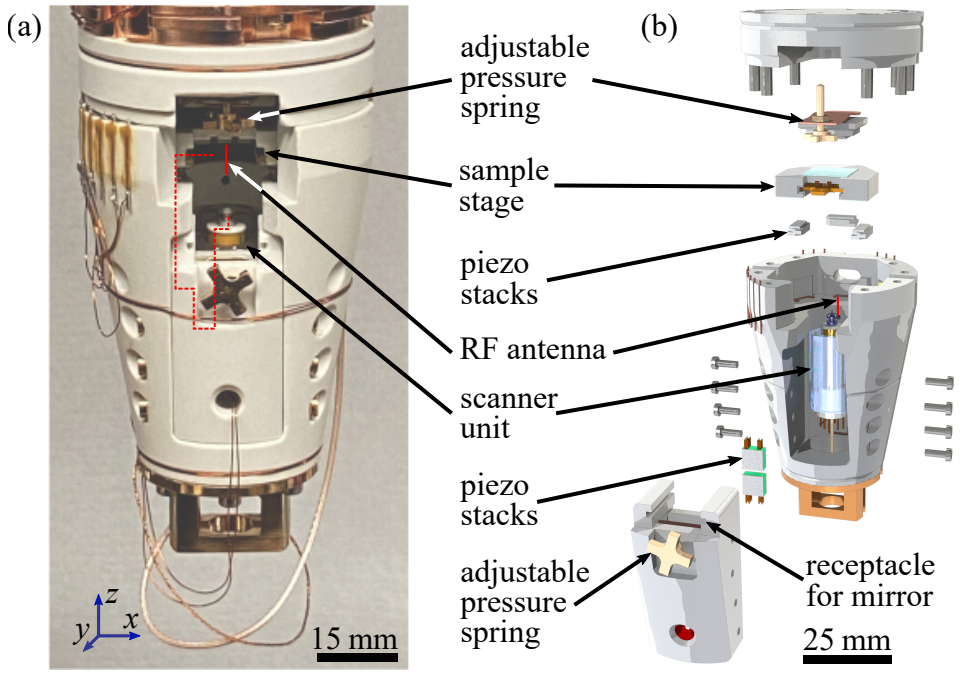


Figure 3.33.: **Realized STM** (a) Photograph of the STM. Dashed red line: mechanical path between tip and sample. Red line: marked radio frequency antenna. (b) Exploded rendering of CAD drawing.

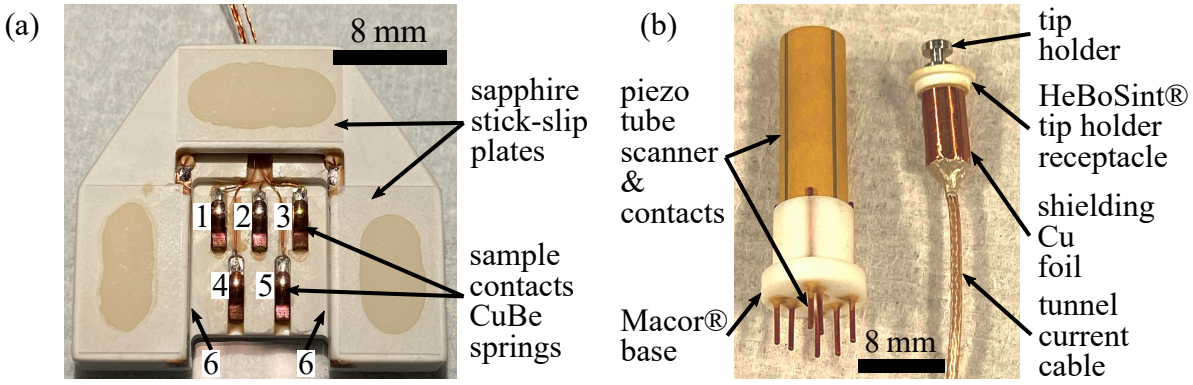


Figure 3.34.: **STM sample stage and scanner.** (a) Sample stage with 12×12 mm² sample receptacle including six sample contacts (Springs: Omega Shielding Products 099-180-NT-20). (b) Scanner prior to final assembly. A Cu foil glued to the tip holder receptacle and to the tunnel current cable allows for a shielding.

transport measurements or application of gate voltages (Figure 3.34 (a)). The coarse positioning piezo stacks allow a 4×4 mm² movement of this stage (Figure 3.33 (b)). The pressure on the piezo stacks is applied through adjustable CuBe springs (Figure 3.33). They are allowed for in-situ adjustment of the tension by a wobblestick. The scan piezo tube is glued within a sapphire prism forming the scanner unit. It enables a coarse approach through a stick-slip motion utilizing three pairs of piezo stacks (Figure 3.33 (b)). Each pair is individually wired for a walker-type stepper motor. At a temperature of 1 K, the scan range is 1 μm^2_{pp} for $\pm 150\,V_p$.

A specialized tip shuttle that fits the 12×12 mm² holders has been designed (Figure 3.35). The design is similar to that previously presented by Florian Muckel [218] for larger 18×15 mm² sample holders. Its purpose is to ensure a safe transfer of tips and to allow an in-situ tip exchange without the risk of applying too large forces onto the piezo scanner. It is equipped with a locking plate that is actuated by a spring mechanism, thereby securing the tip holder in a fixed position during transfer. The tip holder has a notch (similar to the design described in [219]) that interlocks at the position with the small opening on the shuttle (Figure 3.35). The insertion of a new tip, including its tip holder, is carried out as follows: the locking plate nose is pushed to release the tip holder when the shuttle is inserted into the STM using a wobblestick (Figure 3.35 (1.)). The scanner now needs to be optically aligned with the tip holder. Moving the scanner upwards will insert the tip holder into the scanner. Subsequently, the shuttle is moved to the side by

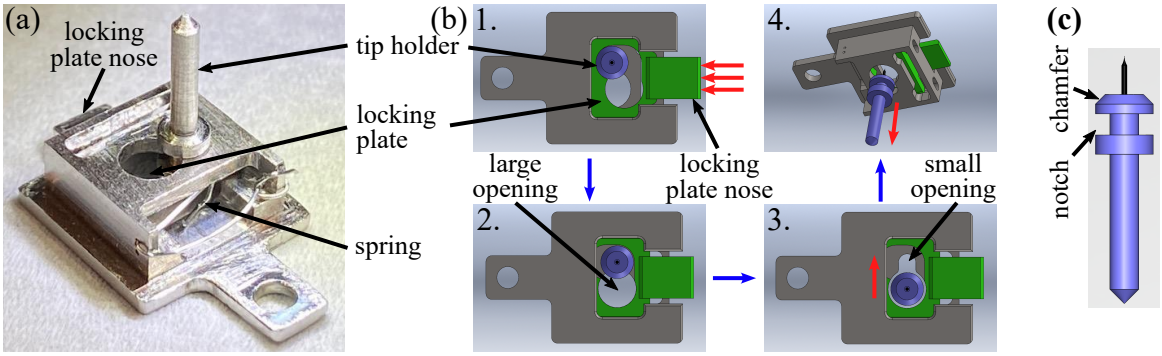


Figure 3.35.: **STM tip shuttle** A tip shuttle with the size of a 12×12 mm² (a) allows to insert a tip holder in-situ into the STM, without the risk of applying too large forces onto the scanner piezo, by four steps (b). The tip holder (c) with a notch is fixed by a locking plate (b), which is shifted by a spring into its locking position, until it is pushed into the STM (1.). The tip holder can only be taken out, if the locking plate is shifted back by pushing the nose of the locking plate (a). Now a sideways movement using the coarse movement is possible, while the tip holder is within the scanner (2. to 3.) and the scanner can subsequently take the tip holder out of the shuttle (4.). One tip shuttle is made of stainless steel and one from Mo.

the purpose of the sample stage (Figure 3.33) until the tip holder is positioned within the larger aperture of the shuttle (Figure 3.35 (2. to 3.)). Now, the scanner with the inserted tip holder can be moved downwards (Figure 3.35 (4.)) and the tip shuttle can be removed. The removal of the tip from the scanner starts with an empty shuttle and proceeds in the reverse order.

3.5.2. Optical access

In order to facilitate the precise positioning of the tip on the sample at the µm level (Figure 3.36 (d)), an optical view to the STM at 45° is integrated.
A chamfer (Figure 3.35 (c)) at the end of the tip holders permits this view, even for tips of relatively short length (∼1.5 mm). An additional receptacle is included in the front of the STM to insert a sample holder with a mirror where the reflecting Ag is deposited on top of a Borosilicate plate (Qioptiq Photonics GmbH & Co. KG) (Figure 3.36 (c)). A second mirror, mounted inside the 4 K radiation shield, enables the observation by the mentioned 45° angle through view port No. 4 (Figure 3.36 (a),(b)). The remaining view ports are arranged in a manner that allows optical access, for the purposes outlined below:

No. 1: transfer of samples e.g. from the transfer rod to the sample garages, opening and closing of shutters.
No. 2,7: opening and closing of shutters, inserting mirror into the STM, inserting tip holders into the scanner, adjustment of screw for the lower piezos moving the scanner.
No. 3, 6: transfer of samples into STM, adjustment of screw for upper piezos moving the sample stage.
No. 5: change of tip via a tip shuttle, tip approach without a mirror, adjustment of screw for upper piezos (sample stage).

3.5.3. Radio frequency antenna

An additional radio frequency antenna has been integrated into the STM. The antenna is positioned parallel to the tip, with a distance of only 7 mm (Figure 3.33). It is constructed from a 50 Ω coaxial cable (Picocoax™, PCX 42 K 10 AK, by Axon Cable) by stripping the outer shield over a length of 4.5 mm (Figure 3.37). The details of the RF wiring are described in Section 3.6.

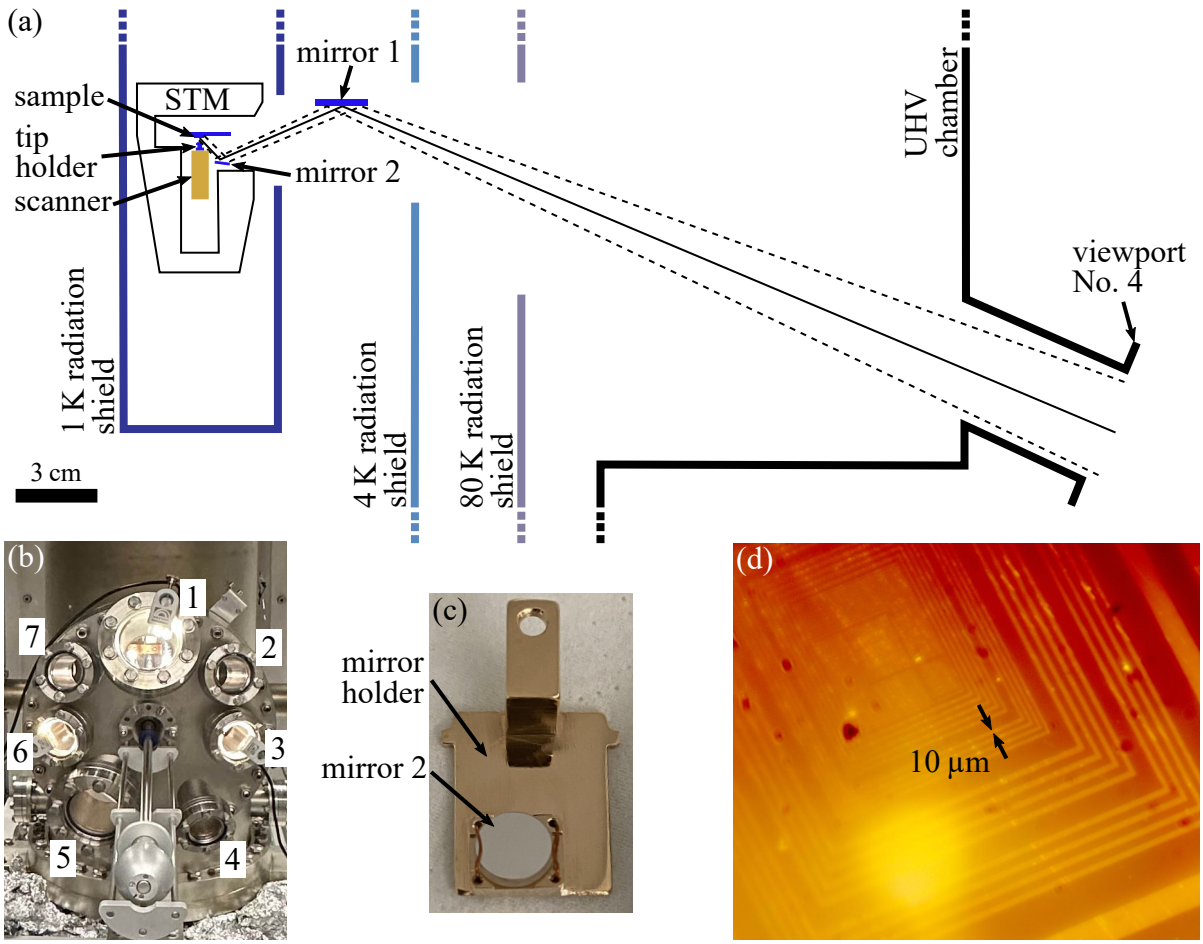


Figure 3.36.: **Optical access to the STM.** (a) Optical path (black line) starting at the UHV viewport 4, reaching the tip and sample via two mirrors. (b) Photograph of the front flange (DN250CF) of the cryostat chamber. The seven view ports are marked. Their purpose is described in the text. (c) Mirror holder with a width of 12 mm that can be inserted into a receptacle in the STM (Figure 3.33 (b)). (d) Optical image of a test grid (Anfatec UMG03/Pt), showing 10 µm resolution for a test setup with the two mirrors at positions as in the cryostat, but outside the cryostat.

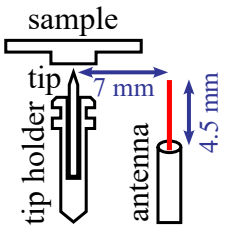


Figure 3.37.: Sketch of the relative positions of the tip, sample and antenna.

3.6. Wiring concept

The wiring concept provides an overview of how components inside the vacuum are connected to the outside via electrical feedthroughs. It focuses on minimizing electrical noise entering the vacuum chamber by using in-house-made filter boxes, thermally anchoring wires to different temperature stages, and employing RF cables. Feedthroughs are placed at two positions: one at the PTC and another at the vibration-isolated, floating STM chamber. An overview is given by the cryostat wiring diagram in Figure 3.38. Generally, MANGANINE® or stainless steel wires connect parts along a temperature gradient, which reduces heat conduction to the cryostat's cold stages. The individual heat loads are calculated at the end of this chapter. Soldering of the wires is done with $Sn_{96.5}Ag_{3.5}$ solder (Fontargen A 611) and with flux (Fontargen F 600). It has been observed that stainless steel wires do not wet with the solder as easily as Cu-containing wires. A reliable connection of e.g. a wire to a pin is realized by pre-tinning both ends, winding the wire around the pin once or twice, and then soldering it.

PTC wiring

The PTC is wired directly underneath its mounting flange (vacuum feedthrough: Allectra 220-CM12-C16). Twisted pair 0.1 mm diameter stainless steel (316L) isolated (ML240 Grad 3) wires with 94 Ω/m from Elektrisola® are used for the temperature sensors. The two heaters on the 60 K and 3 K stage of the PTC use 0.355 mm diameter MANGANINE® wire between 300 – 60 K, followed by 0.1 mm Cu wire down to 3 K.

STM wiring

The vast majority of cabling, which also includes noise-sensitive measuring lines such as the tunnel current, is routed directly into the vibration-isolated part, since mechanical vibrations can influence the electrical signal through triboelectric, piezoelectric or microphonic effects [166, 220, 221]. Also, the inherent temperature oscillations of the PTC can lead to thermoelectric voltage noise. It has been shown that twisted pair wires show a higher noise spectrum than coaxial lines [220]. In general, coaxial lines can be separated into semi-rigid and flexible lines. If the cable is cooled down, a flexible coaxial line with a PTFE outer jacket is showing less noise than semi-rigid versions [166]. The flexible

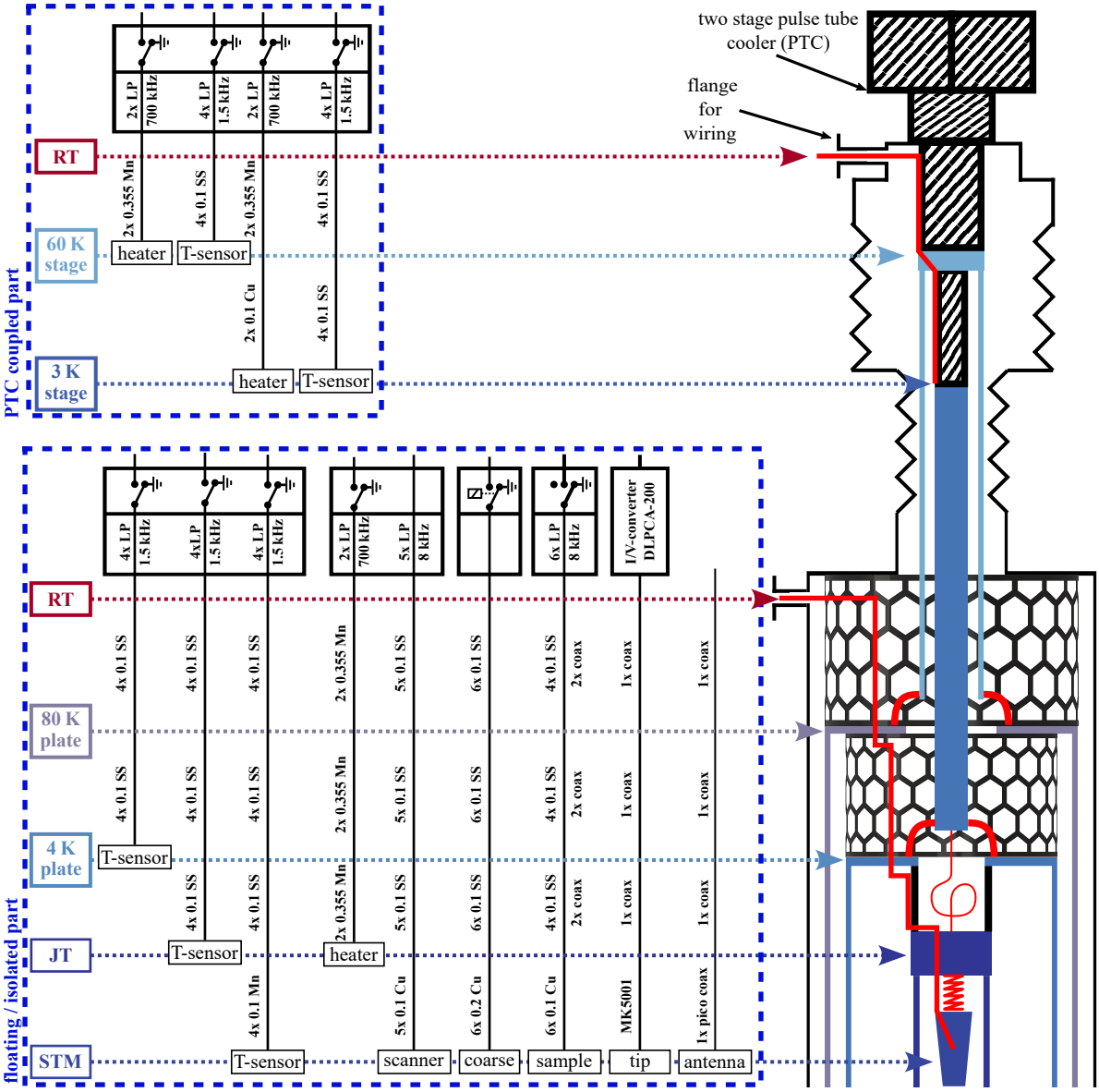


Figure 3.38.: **Cryostat wiring diagram.** Components mounted to the PTC are wired as shown on the PTC coupled upper part. Components of the bottom are wired starting at the floating, vibration isolated part. Coupling boxes at room temperature (RT) houses low-pass filters (LP), if marked, and allow to switch lines to ground or to open by individual switches or by a relay in the case of the coarse piezo wires. The RF frequency line for the antenna has no coupling box, but a shortcut cap allows for grounding. The current to voltage amplifier (Femto DLPCA-200) is also placed close to the vacuum feedthrough at RT. Mn: MANGANINE®, SS: stainless steel, Cu: copper, coax: Elspec SF 034, MK5001: by Elspec, pico coax: Picocoax™ PCX 42 K 10 AK, Axon Cable. Diameters of cables are given in mm. RT: room temperature, T-senor: temperature sensor.

coaxial line outer jacket can hold the shielding, dielectric, and inner conductor tight, while for the semi-rigid lines the layers can separate during cooldown. Consequently, for the sensitive tunneling current line and two sample contacts, we choose the Elspec SF 034, a 0.93 mm diameter coaxial cable made from 304 stainless steel inner conductor (1.2 Ω/m) and braided foil-like clad (0.8 Ω/m) with fluoropolymer (PFA and FEP) as dielectric and outer jacket. Its characteristic impedance is 50 Ω with a capacitance of ∼90 pF/m. A 50 Ω, shielded vacuum feedthrough (Allectra 242-BNC50-C16) is used for the tunneling current signal. Either 10 or 12 pin connectors (Allectra 221-10Al700-10-C16, 220-CM12-C16) are used for the sample contacts, temperature sensors, heaters and piezo wiring. Between the JT stage and the STM, the wire material usually changes from stainless steel to Cu, allowing the STM to be suspended on springs with a low resonance frequency (Section 3.3.4) while improving its thermal connection.
Reducing crosstalk between the wires is tackled by grouping them into three separate bundles. The first bundle contains tip and sample wires, the second includes the scanner and JT heater wires, and the third comprises the coarse piezo and temperature sensor wires. Each bundle is shielded with a CuBe mesh wherever possible. A detailed pin layout can be found in Appendix A.1. The wire harnesses have been specially designed for tabletop assembly, allowing optical microscopic inspection of solder joints. Additionally, they are split into sections with connectors at both ends. This configuration allows only defective sections to be replaced, e.g. in the event of insulation failure. Rather than the conventional method of winding wires around posts, the thermalization of wires to plates and the JT stage is performed by means of copper connectors (Figure 3.39) that can be screwed onto the corresponding thermalization points.

Ambient wiring: RF noise filtering and grounding concept

Sources of noise are not only caused by vibrations acting on the wires in vacuum. External RF noise could also enter the cryostat via the vacuum feedthroughs. Therefore, it is important to minimize the impact of noise (i.e., integrated noise) by reducing the bandwidth to that necessary for STM operation.
Coupling boxes, as close to the feedthroughs as possible, have been developed to filter out frequencies above the bandwidth of the STM's regulation from the measuring lines. They consist of metallic boxes, with either bolt-in capacitors or π-filters mounted on

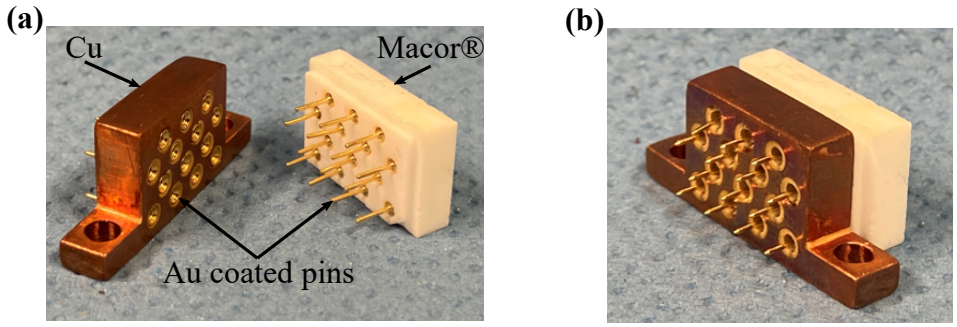


Figure 3.39.: **Connector for thermalization of the wires.** (a) One side of the connector is made from copper. Gold plated pins are electrically isolated glued into the connector. The counterpart is made from MACOR®. (b) Plugged connector.

a plate, separating the noisy part from the filtered section. A low-pass filter without additional resistors would be beneficial for sample contacts, avoiding a voltage drop. A compromise was found by realizing the low-pass filter by 5.5 nF π-filters (1270F-016 Sprectrum Control) with a 3.3 kΩ resistor soldered on the input side. The π-filter was chosen after comparing it with a feedthrough capacitor (2499-003-X5W0-103z Tusonix) that shows even higher capacitance of 10 nF. The π-filter shows higher insertion losses (according to the data sheet) e.g. of −65 dB instead of −35 dB for 100 MHz. The finished coupling boxes of the sample and scanner contacts show a 3 dB point of 7 – 8 kHz (Figure 3.40).

The coupling boxes for temperature sensors have low-pass filters constructed from 10 nF feedthrough capacitors (2499-003-X5W0-103z Tusonix) and 10 kΩ resistors on the input side showing a 3 dB point of 1.5 kHz (Figure 3.40). The insertion loss was measured once up to 510 kHz (Figure 3.40 (a)) and once up to 20 GHz (Figure 3.40 (b)). The values above 20 MHz are in the noise level of the setup.

Further precautions were taken for the sensitive tunneling voltage and current lines. The tunneling current preamplifier links to the feedthrough at the cryostat via only a few centimeters of flexible coaxial cable. The tunneling current is measured relative to ground on its input. The output is measured on a floating input of the STM electronic to avoid a ground loop. A 6 mm^2 cross-section grounding wire connects the STM electronic to the cryostat, thereby minimizing the ground potential difference. Another notable ground loop arises from the shield of the bias line. It can be interrupted by installing a

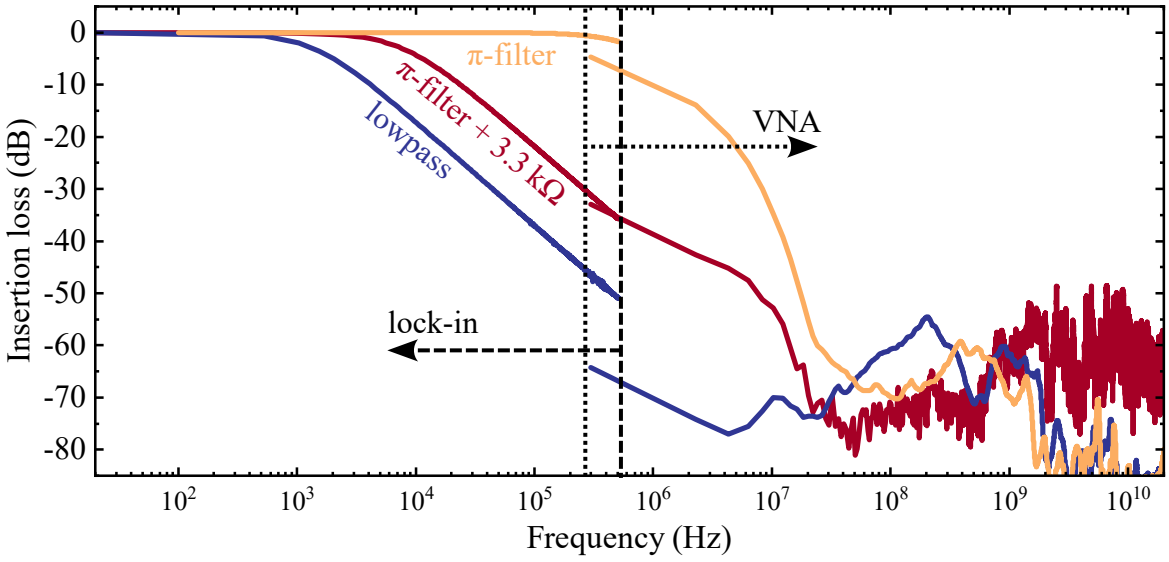


Figure 3.40.: **Low-pass characteristic of the filterboxes.** Measured low-pass characteristic of the different used setups of low-pass filters: A π-filter (1270F-016 Spectrum Control) (orange), a combination of the π-filter with a 3.3 kΩ resistor (red) and a feedthrough capacitors (2499-003-X5W0-103z Tusonix) with 10 kΩ resistor (blue). For the frequency range up to 500 kHz a lock-in amplifier was used and a VNA for up to 20 GHz. Values above 20 MHz are in the noise level of the VNA setup.

home-built instrumentation amplifier with a 1 kHz low-pass filter characteristic and an option to reduce the incoming bias and noise by a factor of ten. It is positioned close to the feedthrough.

RF wiring

The RF antenna, as described in Section 3.5.3, is wired using 50 Ω coaxial cables. The link into the UHV is established through a RF frequency vacuum feedthrough (Vacom CF16-SMA50-40GHz, Typ K, 2.92 mm, 50 Ohm up to 45 GHz). On the vacuum side, a flexible cable (Elspec SF 034, length: ∼70 cm, diameter: 0.93 mm) carries the signal to the JT stage and is thermally anchored at 80 K, 3.6 K and 1.2 K. From there to the antenna, a very thin and flexible cable (Picocoax™ PCX 42 K 10 AK, Axon Cable, length: 22 cm) connected via SMPM connectors (Cinch Connectivity Solutions 125-2592-001, Amphenol 925-124P-51S) is used. A sleeve is made for the connection between the 0.33 mm thin Picocoax™ cable and the SMPM connector, which is first soldered to the outer shielding braid of the cable (Figure 3.41). The Elspec SF 034 cable was selected on the basis of five aspects. The easy installation due to its flexibility, the low thermal conductivity, the compatibility with SMPM connectors, the RF frequency compatibility up to 50 GHz and the UHV suitability. Before forming the antenna and installing it into the cryostat, each wiring setup is tested using a vector network analyzer (VNA) (Figure 3.42). Details of the assembled cables are shown in (Figure 3.42 (b)) and their part numbers are listed in Table 3.5. In general, the transmitted sine wave amplitude at the end of the cable assembly depends on impedance mismatches, frequency-dependent resistivity, and resonances along the cable. A short discussion about the measured transmission is following.

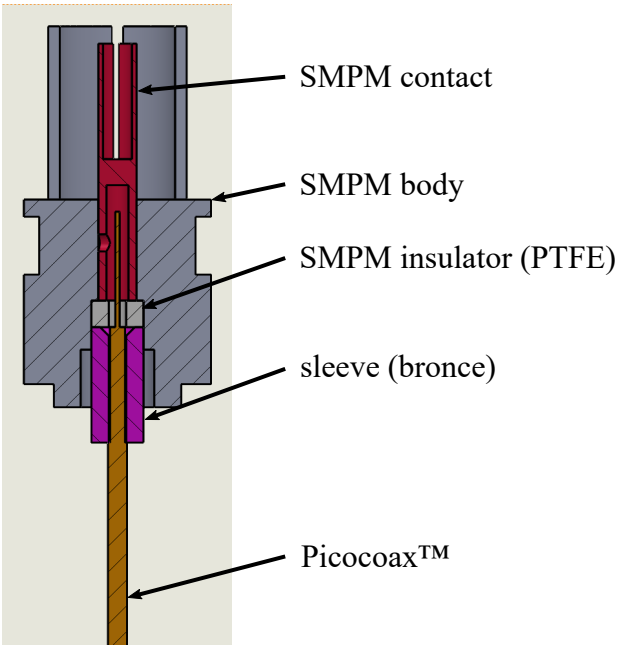


Figure 3.41.: **Assembly SMPM connector to Picocoax™ cable.** CAD model cross section view mounting a 0.33 mm thin Picocoax™ cable via a sleeve into a SMPM connector.

Table 3.5.: **Table of assembled RF cables and adapters.**

part No.	description	part ordering number
01	Elspec SF 034 coaxial cable (71.4 cm) with SMK connector(2.92 mm, male) and SMPM connector (male)	STFlex034-292_11(gerade (m)) Cinch Connectivity Solutions: 125-2592-001
02	Picocoax™ coaxial cable, 26.5 cm with SMPM connectors (female)	Axon Cable: PCX 42 K 10 AK Amphenol: 925-124P-51S
03	vacuum feedthrough SMK (female)	Vacom: 348197 CF16-SMA50-40GHz
04	adapter SMPM (male) to SMA (female)	Amphenol: SF1132-6027
05	adapter SMPM (male) to SMK (female)	Amphenol: SF1115-6084
06	adapter SMPM (female)	Amphenol: 1132-4010
07	adapter SMPM long (female)	Amphenol: 925-166A-51S
08	adapter SMK (female)	-

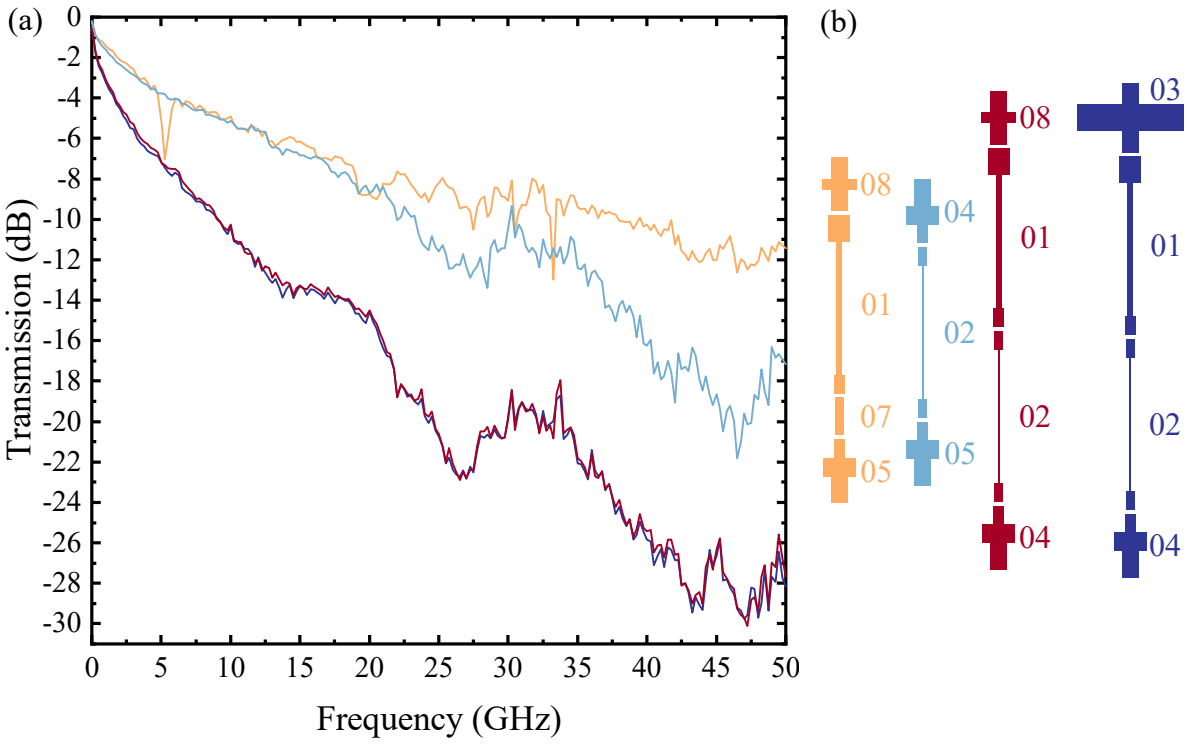


Figure 3.42.: **Transfer function of assembled RF cables and adapters.** (a) VNA transfer function measurements of assembled cables listed in Table 3.5. Transmission of part combination 08-01-07-05 (orange), transmission of part combination 04-02-05 (light blue), transmission of parts combination 08-01-02-04 (red) and transmission of parts combination 03-01-02-04 (blue). The contribution of the connector cables between the VNA and the shown assembled cables, has been subtracted. (b) Sketch of cable combination with used connectors.

At 40 GHz, the setup with the Elspec SF 034 cable shows a transmission of −10 dB (Figure 3.42 (a) orange) while the setup with the Picocoax™ cable shows a value of −16 dB (Figure 3.42 (a) light blue). The expected nominal value evaluated from the data sheet of the Elspec SF 034 cable is −9 dB. The transmission for the setup including both cables and the UHV feedthrough is −25 dB at 40 GHz (Figure 3.42 (a) blue). Replacing the UHV feedthrough by a standard SMK adapter does not show a difference (Figure 3.42 (a) red-blue). All data presented are taken at room temperature. The Picocoax™ will operate at 1 K inside the cryostat. It is mounted at this position by cutting it to its final length of ∼22 cm. The shorter cable should increase the transmission in Figure 3.42 by ∼3 dB at 40 GHz. Typically, a decrease in attenuation is observed when using coaxial cables in a cryogenic environment, since the surface resistance is decreased. T. Balashov recently measured an improvement of 30 dB/m in amplitude transmission at 40 GHz of the Picocoax™ cable at 5 K. The combination of the shorter cable and the reduced temperature will lead to an estimated transmission of only −6.5 dB instead of the shown −16 dB.
The transfer of RF frequencies into the tunneling junction of the final setup, including the RF frequency antenna, will be shown in Section 4.3.8.
Using a time-domain reflectometer (TDR) the impedance mismatch along the RF wire was measured Figure 3.43. For the calculation of length from the measured propagation times, a velocity of $0.705\,c_0$ is used (c_0: speed of light in vacuum, value as given in the data sheet of the Elspec SF 034 cable). The soldered SMPM connectors at a length of 72 cm show a small 12 Ω impedance mismatch. The inclination observed for both cables reflects their resistance. The Picocoax™ cable has a larger inclination, probably due to a higher resistance (datasheet: 8 Ω/m).

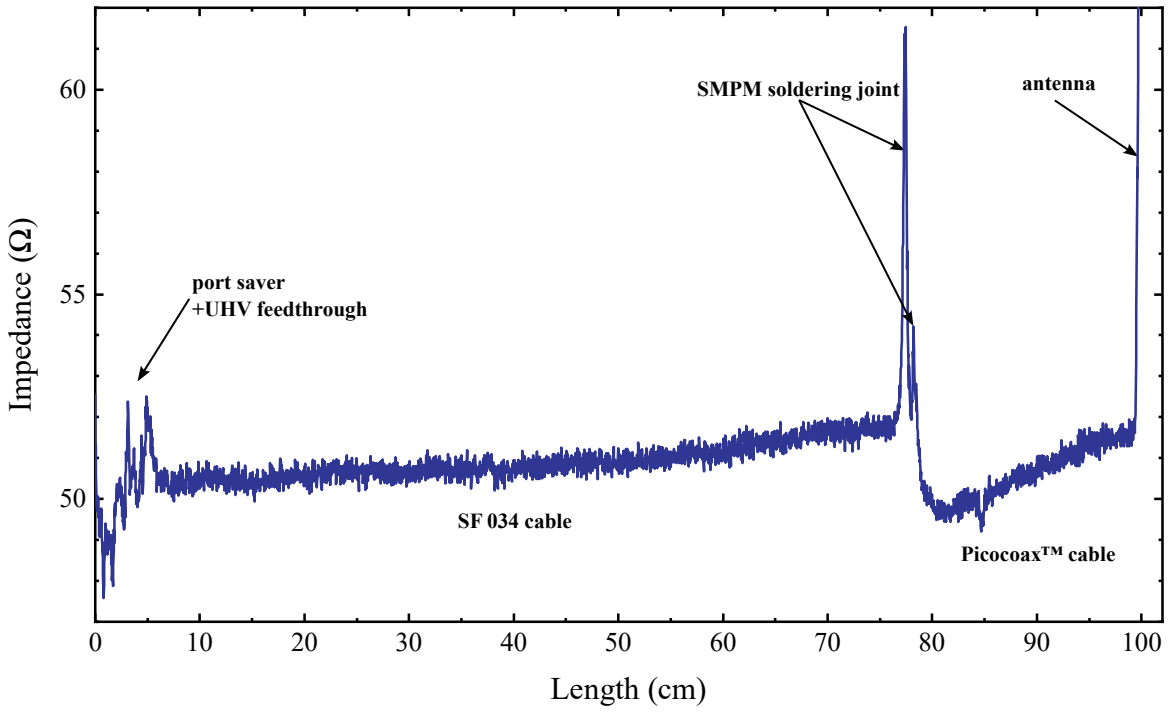


Figure 3.43.: **TDR of cable assembly.** Time domain reflectometer measurement to determine the impedance discontinuity of the cable assembly after forming the antenna and mounting it into the cryostat. The installation into the cryostat includes the vacuum feedthrough and a port saver (Telegärtner 100024795) on the air side of the feedthrough. The antenna near 95 cm is formed by cutting the cable to its desired length (Picocoax™ ∼22 cm) and stripping the outer shield by ∼4.5 mm

.

Heat load by wires

The heat conducted by the wires with cross-sectional area A and length l between temperatures T_1 and T_2 can be calculated by the thermal heat integral of the temperature-dependent thermal conductivity $\lambda(T)$ of the material [178].

$$\dot{Q} = \frac{A}{l} \int_{T_1}^{T_2} \lambda(T)\, dT. \tag{3.6}$$

The calculated total heat load by the wires on the 80 K plate is ∼15 mW. It corresponds to 0.08 % of the PTC 60 K stage cooling power. For the 4 K plate it is ∼2.3 mW (1.2 % of the PTC 3 K stage cooling power). For the JT stage, it is ∼13 µW (1.3 % of its total cooling capacity). The PTC wiring requires only 0.05 % of the total PTC cooling capacity at the 60 K stage, and only 2 % on the 3 K stage.

4. Performance

4.1. Vibration isolation performance

4.1.1. STM

As a first step, the finalized STM is tested under ambient conditions to assess its mechanical stability. The scanner tube, coarse motor, and sample stage resonance frequencies are measured, as well as the vibrational transfer function between vibrations acting on the STM towards the tip-sample distance. The resonance frequencies of the stages are found by exciting one piezo element that contacts the corresponding stage and detecting the piezo response voltage at another element on the same stage. A lock-in amplifier is used for the excitation and the read-out, with 10 $\mathrm{mV_{RMS}}$ excitation amplitudes for the scanner and 100 $\mathrm{mV_{RMS}}$ for the coarse piezos. The excitation frequencies range from 100 Hz up to 20 kHz in steps of 10 Hz.

Theoretical resonances of the STM have been discussed in Section 3.5.1 and are compared to the measurements:

The lowest observed scanner piezo tube resonance frequency in the x-direction is 5 kHz when a Mo tip holder is used (Figure 4.1 (a) red). This likely corresponds to the 5.4 kHz calculated bending mode. Multiple peaks between 4 kHz and 5 kHz appear in the y-direction (Figure 4.1 (b) red). In this direction, the tip carrier is held inside the scanner by a spring, which may cause these peaks by its limited force. By switching to a tip carrier made from Mg, the resonance of the scanner assembly is increased up to 6 kHz (Figure 4.1 (a)-(b) blue).

The z coarse motor is also excited to determine its resonance frequencies. The excitation is performed by the front piezo stacks, while the detection is read out at the ones in the back (Figure 4.2 (b)). It shows strong resonances above 10 kHz and none below 4 kHz (Figure 4.2 (a)). Also, the sample stage (with the configuration shown in Figure 4.2 (d))

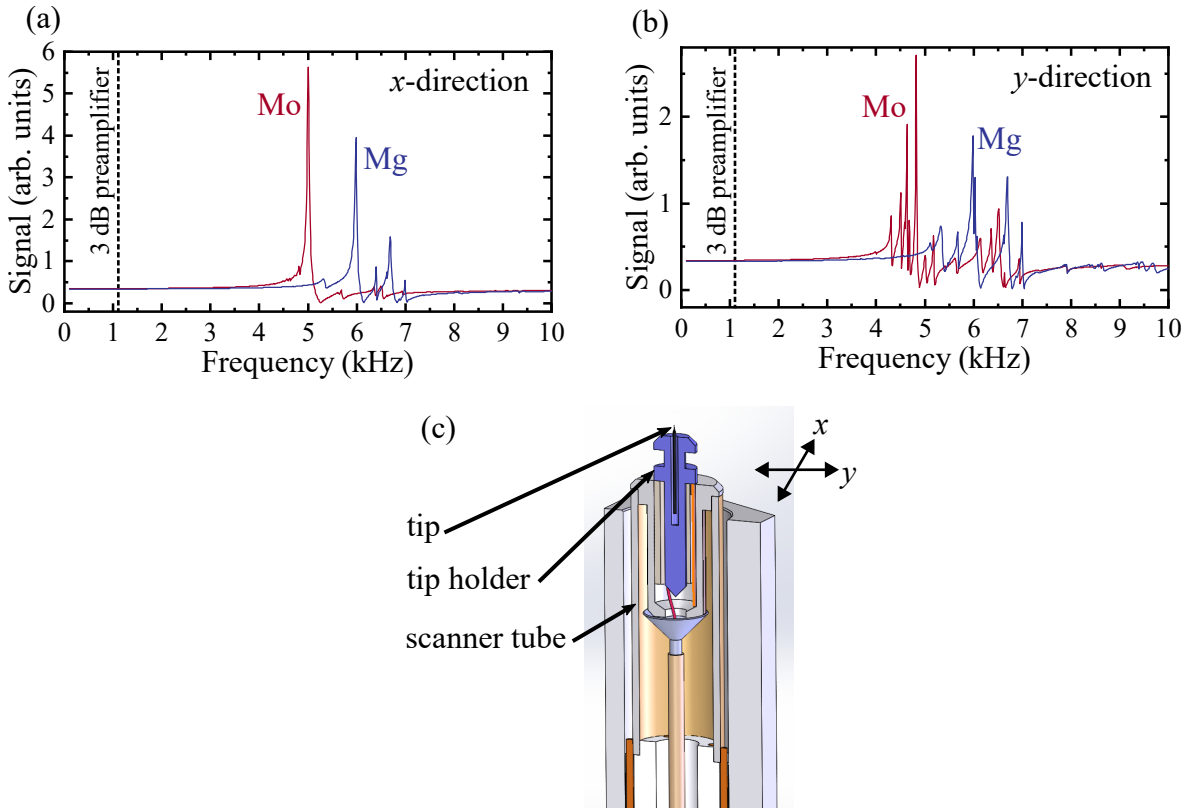


Figure 4.1.: **Measured scanner resonances.** Measured resonance curves of the scanner tube with a Mo tip holder (red) and a Mg tip holder (blue). For the x-direction (a) and for the y-direction (b). The cutted view (c) shows the geometry. The excitation uses one of the piezo elements, while the detection is done on the opposing one.

shows the first strong resonance at ∼16 kHz, near the calculated 17 kHz (Figure 4.2 (c)). Importantly, no observation of resonances in the bandwidth of the preamplifier are present.

The STM's mechanical transfer function is measured at ambient conditions by exciting the top end of the STM and reading out the tip to sample variations through the formerly calibrated tunneling current. A mass actuated by an electric coil provides the excitation. The excitation amplitude detection is realized by a low-frequency acceleration sensor (Wilcoxon Research® 731-207), mounted to the top end of the STM. The resulting vibrational amplitude between tip and sample was deduced from the response of the feedback loop in constant-current mode. It compensates the low-frequency oscillations by more than 98 %, as crosschecked by the current signal. The scanner piezo tube is

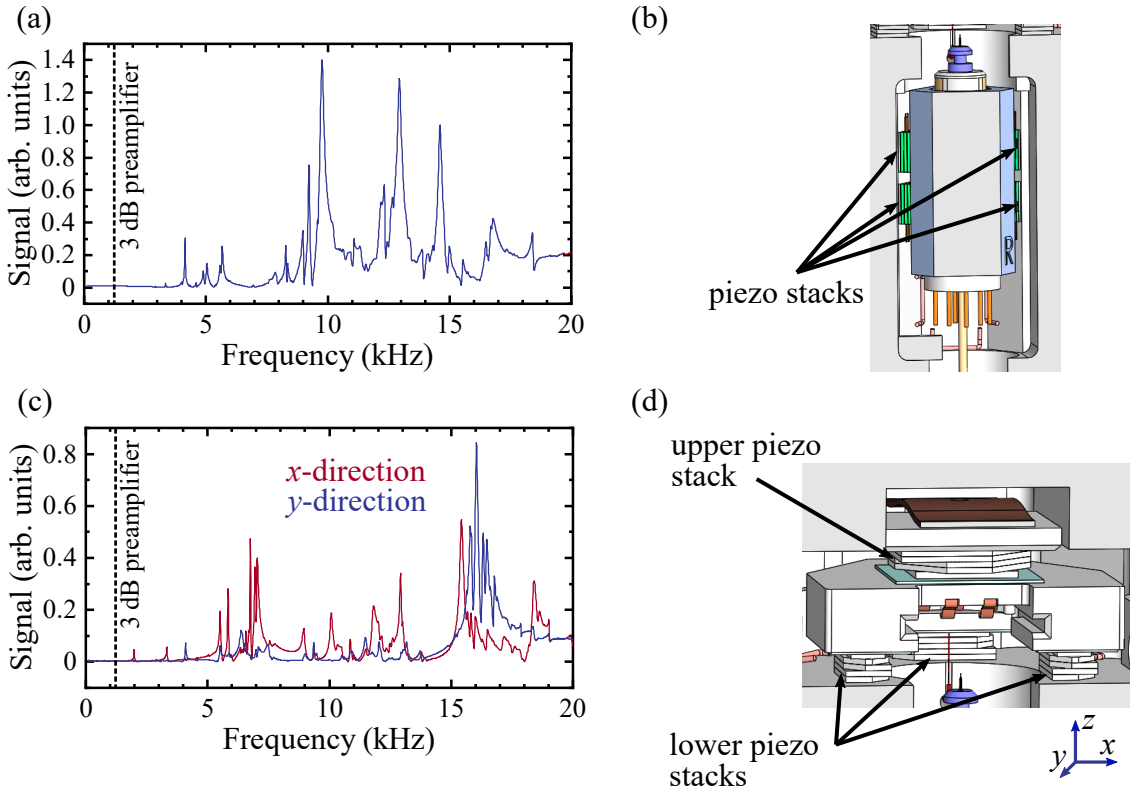


Figure 4.2.: **Measured coarse motor and sample stage resonances.** (a) Resonance curve of the coarse motor. The excitation is done by the front piezo stacks, while the detection is at the ones in the back. The stacks are shown in the drawing in (b). (c) Resonance curves of the sample stage for the x-direction (red) and y-direction (blue). The excitation is done by the lower stacks, while the detection is done on the opposing upper one. The stacks are shown in the drawing in (d).

previously calibrated by scanning step edges on a Au crystal.

The measured amplitude reductions are shown in Figure 4.3 (red squares). Extrapolating them down to the PTC operation frequency (1.1 – 1.6 Hz) reveals a damping of more than six orders of magnitude (blue line in Figure 4.3).

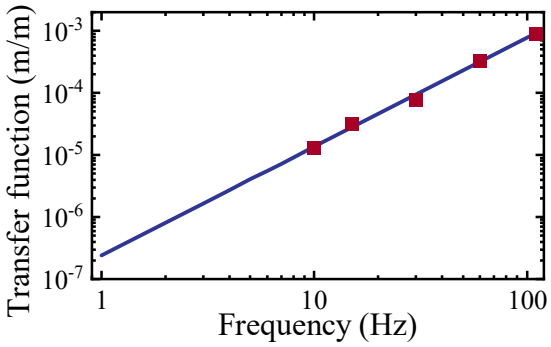


Figure 4.3.: **Measured mechanical transfer function of the STM.** The transfer function (red squares) and fit (blue line) was measured by the tip-sample displacement and an acceleration sensor mounted on top of the STM.

4.1.2. Minimal stiffness

To evaluate the performance of the vibration isolation, the acceleration sensor (Wilcoxon Research® 731-207) is mounted to the 4 K plate (future mounting position of the JT stage) in an intermediate test setup of the cryostat (Figure 4.4).

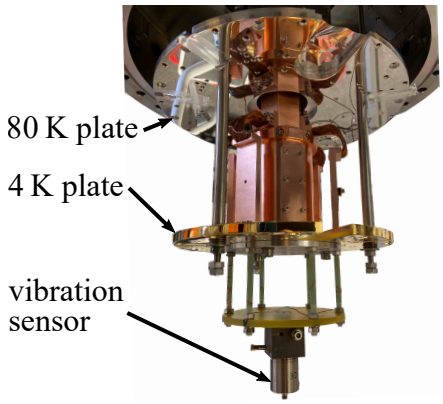


Figure 4.4.: **Photograph of the intermediate vibration test setup.** An acceleration sensor (Wilcoxon Research® 731-207) is mounted to the 4 K plate (later mounting position of the JT stage) with the same thermal isolation setup as described in Figure 3.4. The cylindrical support structures and radiation shields are not yet mounted on the photograph.

The sensor is mounted with the same thermal isolation setup as described in Figure 3.4. The JT stage and the 4 K radiation shield are not installed, and a 80 K radiation shield without the final shutters is used. Figure 4.5 compares the vibrational noise determined on the 4 K plate with the measurements directly on the PTC 3 K stage for all three directions. The PTC data are the same as in Figures 3.11 to 3.13. Its operation frequency is 1.2 Hz. In the z-direction (Figure 4.5 (a)), the 1.2 Hz peaks at the PTC 3 K stage correspond to 26 μm_p and appears as only 5 μm_p on the 4 K plate. This reveals half an order of magnitude in damping at the PTC operation frequency. Around 10 Hz, a damping of two orders of magnitude of vibrational noise amplitude is observed. The decaying background without peaks is close to the sensor noise as marked in Figure 4.6 (according to its datasheet). The peaks up to 20 Hz match the PTC operation frequency and its higher harmonics. Peaks at frequencies above 20 Hz are harder to attribute to a specific origin. Figure 4.6 also compares ground floor noise of the building (PTC off) where the system is situated. Peaks near 25 Hz, 30 Hz, 35 Hz, 37 Hz, 48 Hz, 49 Hz and 54 Hz appear also in the spectrum of the floor. Peaks at 29 Hz and 36 Hz and 72 – 78 Hz align with

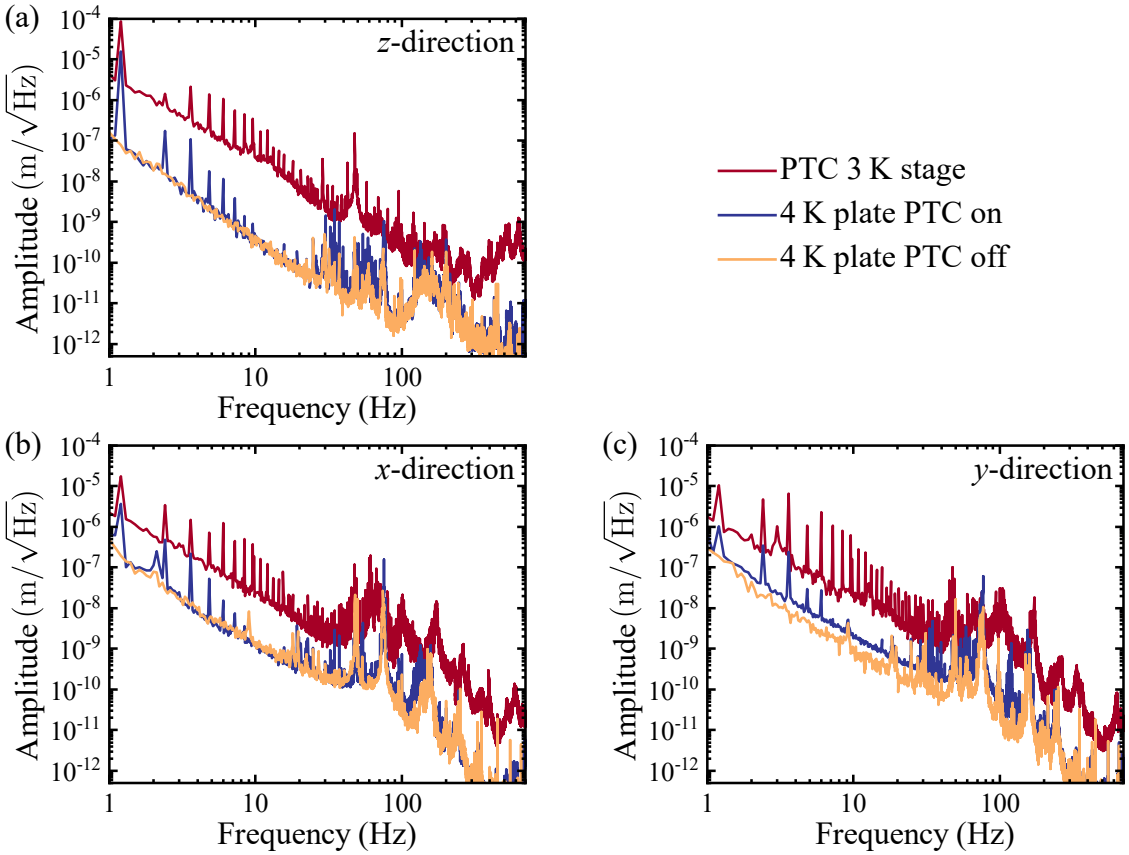


Figure 4.5.: **Vibrational amplitude spectra of the 4 K plate.** (a) Spectrum of the vibrational amplitudes measured at the 4 K plate in vertical direction (blue), (b) in horizontal direction (front/back of the chamber), (c) in horizontal direction (left/right of the chamber). The spectrum without the PTC running is shown in orange. The spectrum measured on the PTC 3 K stage as shown in Figures 3.11 to 3.13 is displayed in red. Sampling rate, each 0.05 ms.

peaks measured at the PTC. In the x-direction (Figure 4.5 (b)), the main PTC peak is also reduced by half an order of magnitude. Peaks at ∼48 Hz and 72 – 78 Hz remain on the 4 K plate. They could be explained by internal resonance frequencies of the setup. No further investigations were done. For the y-direction (Figure 4.5 (c)), the main PTC peak is reduced by one order of magnitude. Comparing the background noise at 10 Hz, it is lowest in z-direction, four times higher in x, and almost six times higher in y-direction.

As demonstrated in the following Section 4.1.3, the combination of the minimal stiffness isolation (Figure 4.5 (a)) with the transfer function of the STM (Figure 4.3) is effective

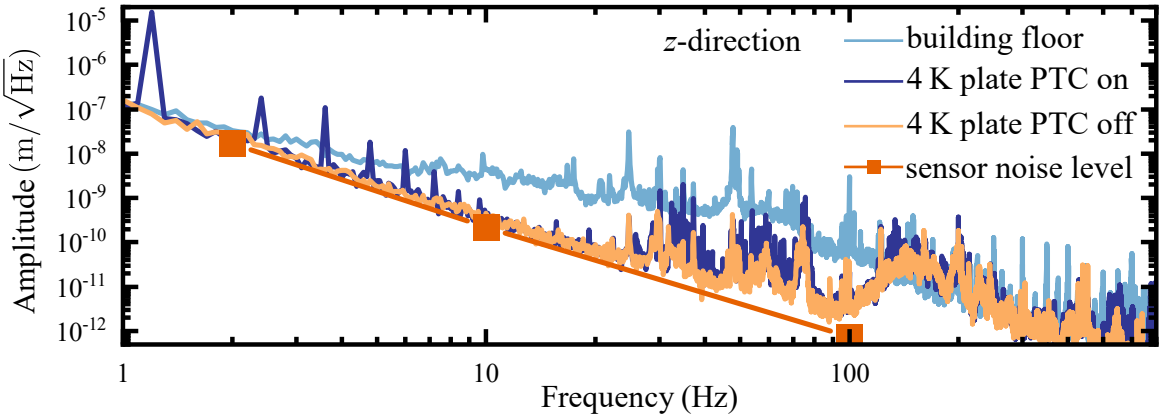


Figure 4.6.: **Vibrational spectra of the** 4 K **plate.** Spectrum measured at the building ground floor (light blue), at the 4 K plate with and without running PTC (blue and orange). The vibration sensor noise level is marked. Sampling rate, each 0.05 ms.

to reach a z-noise in the pm range.

4.1.3. Movement of decoupled STM chamber and *z*-noise in the tunneling junction

The system is complemented by adding the JT stage, the STM, and all radiation shields. The floating chamber's resonance frequency is determined after manual excitation of the STM chamber by a few millimeters. The acceleration sensor was placed on the floating aluminum frame. The measured resonance frequencies for the vertical and the

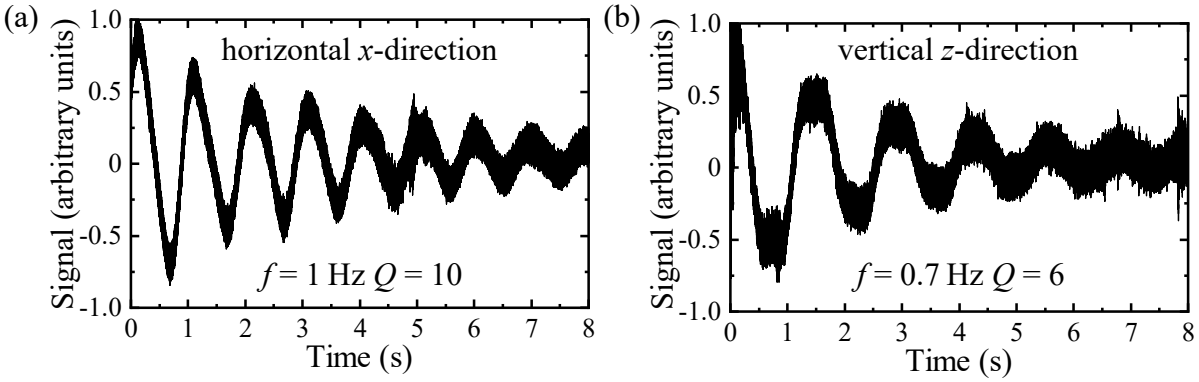


Figure 4.7.: **Low frequency floating system.** Low frequency movements of the UHV system suspended by the Minus K® isolators after optimization of the minimal stiffness forces at the bellows. The acceleration is measured with the same acceleration sensor as in Figure 4.4 after an initial manual displacement in the horizontal x-direction (a) and in the vertical z-direction (b). The displayed resonance frequencies f and quality factors Q are determined by a fit.

horizontal direction are 0.7 Hz (Figure 4.7 (b)) and 1 Hz (Figure 4.7 (a)), respectively. They are both below the operation frequency of the PTC and thus are damping the PTC excitation. The PTC amplitude of 26 µm at its operation frequency is reduced by a factor of 5 to only 5 µm (Section 4.1.2). This value is smaller than expected from the calculated transmission curve, revealing a factor of 0.5, determined from the measurement in Figure 4.7 (b) and using the resonance curve of Equation 3.3. The Q factor might decrease at higher amplitudes, causing this difference.

Finally, the STM tunneling junction is used to determine the relative tip-sample movement. The scanner piezo tube is calibrated in z-direction using single atomic steps of Au(111) and in x-y-direction using the atomic resolution of Au(111). Next, the data collection will be briefly summarized.

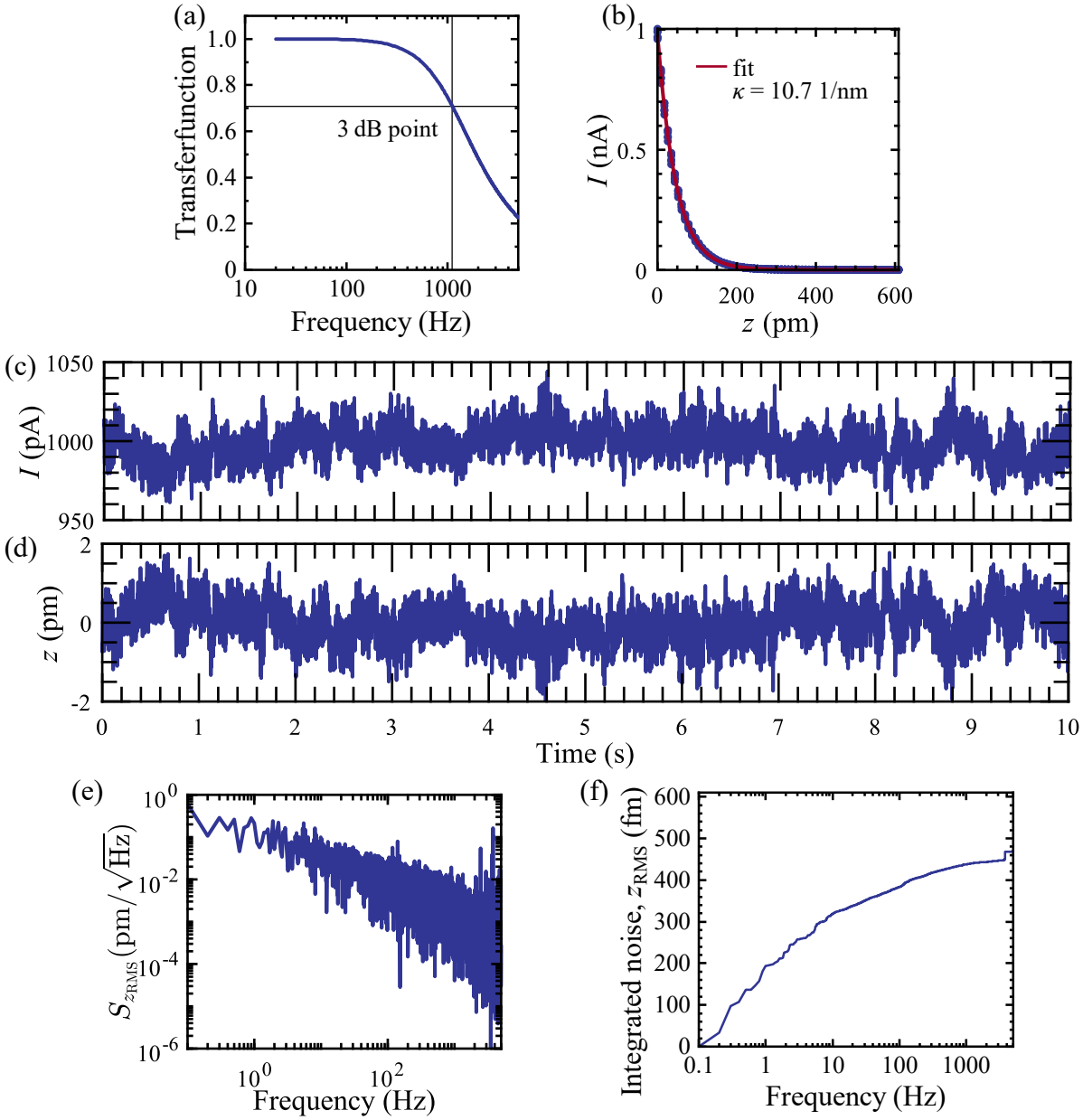


Figure 4.8.: **Determination of vibrations in the tunneling junction.** Steps to determine the z-noise in the tunneling junction while the STM is mounted inside the finalized cryostat at base temperature. (a) Measured low-pass characteristic of the used Femto DLPCA-200 I-V converter. Gain: 1×10^9 V/A, selector switches: full bandwidth, direct current, GND. (b)-(e) Recorded data on Au(111), W-tip, ($V_{\mathrm{stab}} = 300\,\mathrm{mV}$, $I_{\mathrm{stab}} = 1\,\mathrm{nA}$, $T = 1.47\,\mathrm{K}$). (b) Six I(z) curves (blue dots) recorded just before measuring I(t) in (c). A fit (red) according to Equation 4.1 to the mean value of all six curves yields $\kappa = 10.7/\mathrm{nm}$ or an effective barrier hight of $\overline{\Phi} = 4.4\,\mathrm{eV}$. (c) $I(t)$ curve during feedback off (Time interval: 10 s, sampling rate: 0.1 ms). (d) $z(t)$ calculated from the fit results in (b). (e) Spectral density of amplitude deduced from the $z(t)$ data in (d) including the frequency dependent correction of the I-V converter characteristic from (a). (f) Integrated spectral density of (e).

The example shown in Figure 4.8 exemplarily discusses the determination of vibrational z-noise in the tunneling junction.
A Au(111) sample and a W-tip were inserted into the STM. The STM is cooled to base temperature, and the tip is prepared by a controlled indentation into the sample and by applying short voltage pulses until a stable tunneling current is observed. Thermal drift and piezo creep are kept to a minimum by scanning the same area for several hours. Six $I(z)$ curves are recorded, and an exponential fit is applied to their mean value (Figure 4.8 (b)):

$$I(z) = I_0 \exp(-2\kappa z). \tag{4.1}$$

The extracted average barrier height $\overline{\Phi}$ of 4.4 eV (compare Equations 2.1 to 2.3) is typical for these metals. Directly afterwards with the identical tip, $I(t)$ curves are recorded with a duration of 10 s at a sampling rate of 10 ks while the piezo feedback regulation is switched off (Figure 4.8 (c)). The $z(t)$ signal is recovered from $I(t)$ curves by using the inverted results of the previous fit to the $I(z)$ curves (Figure 4.8 (d)). A Fourier transformation of the $z(t)$ signal yields the frequency components. The z-noise spectrum $S_{z_{\mathrm{RMS}}}(f)$ reads:

$$S_{z_{\mathrm{RMS}}}(f) = \sqrt{\frac{1}{2 \cdot df \cdot N^2} |2Y|^2}. \tag{4.2}$$

Here Y is the single sided discrete Fourier transformation of $z(t)$, df the bin width of the frequency axis and N the number of samples. The measurement bandwidth is 5 kHz by taking into account the frequency dependence of the Femto DLPCA-200 I-V converter (Figure 4.8 (a)). In the case of an amplification factor of 1×10^9, the 3 dB point is at $\sim$1.1 kHz. The result is displayed in Figure 4.8 (e). An alternative data representation is chosen, displaying the total z-noise in the junction up to frequency f_{BW} (Figure 4.8 (f)). It is calculated by an integration of the result from Equation 4.2:

$$z_{\mathrm{RMS}}(f_{\mathrm{BW}}) = \sqrt{\int_{f_0}^{f_{\mathrm{BW}}} S_{z_{\mathrm{RMS}}}(f)^2 \, \mathrm{d}f}, \tag{4.3}$$

with $f_0 = 0.1$ Hz. Steps in this representation mark distinct frequency contributions to the z-noise, while a gradual slope indicates broadband noise. The z-noise is measured multiple times, after different cooldowns, with different samples and tips as well as with two STM electronics (Figure 4.9). The example in Figure 4.9 (a) includes ten measurements

acquired within eight minutes. Their mean values and the one sigma range are depicted. The oscillation at the operation frequency of the PTC (1.3 Hz) sometimes appears in the spectrum (Figure 4.9 (b),(c)), but is reduced to a few 100 fm. This indicates the potential for additional improvement by decreasing the minimal stiffness frequencies of the floating UHV system. The total z-noise remains below $1\,\mathrm{pm_{RMS}}$ at the bandwidth of 5 kHz. In all measurements of Figure 4.9 (a)-(c) a step occurs at ∼3770 Hz. Unfortunately, this cannot be related to a specific resonance in the STM (compare Figures 4.1 to 4.2). The other observed steps change for different spectra and, hence, likely do not originate from the construction or the STM electronics, but rather from the mechanical stability of the tip or the sample.

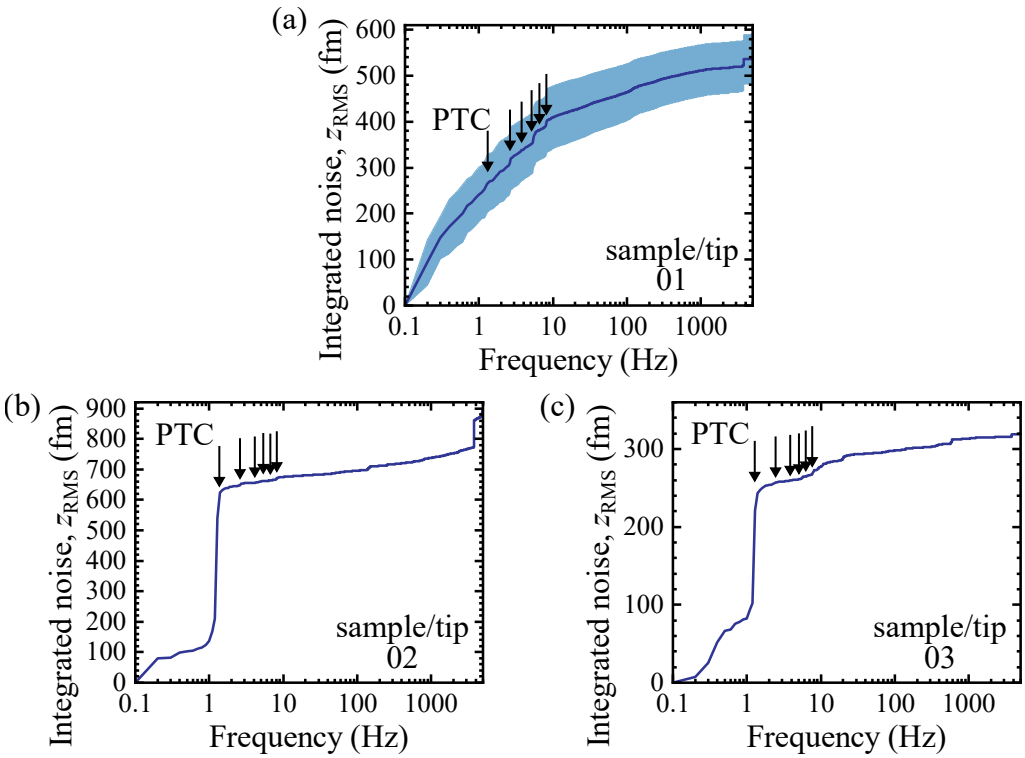


Figure 4.9.: **Integrated z-noise variation in the tunneling junction observed with three different tips or samples.** (a)-(c) Integrated amplitude spectral density data with the PTC operation frequency marked including it's first five harmonics. (a) Mean and standard deviation of ten integrated amplitude spectral density data, that have been recorded subsequently within 8 min (one of them is analyzed in Figure 4.8). Au(111) sample, W-tip, VA-tip-holder, $V_{\mathrm{stab}} = 300\,\mathrm{mV}$, $I_{\mathrm{stab}} = 1\,\mathrm{nA}$, $T = 1.47\,\mathrm{K}$, time interval: 10 s, sampling rate: 0.1 ms, effective barrier hight of $\overline{\Phi} = 4.4\,\mathrm{eV}$. (b) Single curve integrated amplitude spectral density. W(100) sample, W-tip, Mg-tip-holder, $V_{\mathrm{stab}} = -800\,\mathrm{mV}$, $I_{\mathrm{stab}} = -200\,\mathrm{pA}$ $T = 1.46\,\mathrm{K}$, time interval: 10 s, sampling rate: 0.1 ms, effective barrier hight $\overline{\Phi} = 3.0\,\mathrm{eV}$. (c) Single curve integrated amplitude spectral density, Au(111), W-tip, Mg-tip-holder $V_{\mathrm{stab}} = -480\,\mathrm{mV}$, $I_{\mathrm{stab}} = -1.5\,\mathrm{nA}$, $T = 1.48\,\mathrm{K}$, time interval: 10 s, sampling rate: 0.1 ms, effective barrier hight $\overline{\Phi} = 4.4\,\mathrm{eV}$

4.2. Cryostat performance

4.2.1. Temperature drop at the Cu stranded links

In an intermediate test setup of the cryostat, temperature sensors were mounted at multiple positions. The JT stage and the 4 K radiation shield were not installed. A 80 K test radiation shield was used. The 4 K plate has a Cernox® sensor (Lake Shore Cryotronics®, Inc., CX-1050-HT-1.4L) installed, while the others are silicon diode sensors (Lake Shore Cryotronics®, Inc., DT670-A1). The 4 K Cu stranded links had not yet been Au plated. Table 4.1 summarizes the measured temperature drops across the Cu stranded links.

Table 4.1.: **Table of measured and calculated temperature drops.** The calculated values are discussed in Section 3.4.5 (Table 3.3). The Cu stranded links show a temperature drop across their length due to the thermal conductance and due to the interface contact conductance of the screwed connections.

No.	**position of temperature drop**	**measured temperature drop** (K)	**calculated temperature drop** (K)
1	80 K Cu link	14	7
2	80 K Cu link screwed connection	0.7/1.6	0.3-1.4 each
3	4 K Cu link	0.2	0.4
4	4 K Cu link screwed connection	0.1 each	0.4 each

The temperature drop along the 80 K Cu stranded links is twice as high as expected (No.1). These links are mounted between the PTC upper radiation shield and the 80 K plate. One possible cause are different material properties, deviating from Cu RRR50. The manufacturing process of the Cu stranded links may also contribute, since an additional connection between the Cu wires and the Cu blocks has to be made. The discrepancy has not been examined further.
The screwed connection (No.2), located closer towards the PTC, shows a higher temperature difference of 1.6 K compared to the value at the 80 K plate. Here, only two M4 screws are used instead of four M3 screws, which might lower the clamping force and thus cause the higher value. The 4 K Cu stranded links exhibit a total temperature drop

of only ∼0.2 K (No.3), resulting in a temperature of the 4 K plate of ∼3.9 K. This plate is the mounting position of the JT stage. The temperature is favorably lower than the temperature of liquid ^{4}He at 1 bar (4.2 K). It is surprising that the Cu-Cu connection (No.4) shows a comparable temperature increase to the Cu-Au connection (both 0.1 K). Moreover, the value of both connections is 4 times lower than expected.

4.2.2. Cooldown of the finalized system

The cooldown process of a cryostat operated with liquid ^{4}He typically comprises a number of time-consuming steps, including pre-cooling with liquid N_2 partially requiring the operator's presence within the laboratory. In contrast, the PTC-based system requires only the initial setup of the cryostat, followed by a subsequent activation of the PTC without further manual intervention. Specifically, after achieving UHV conditions, the

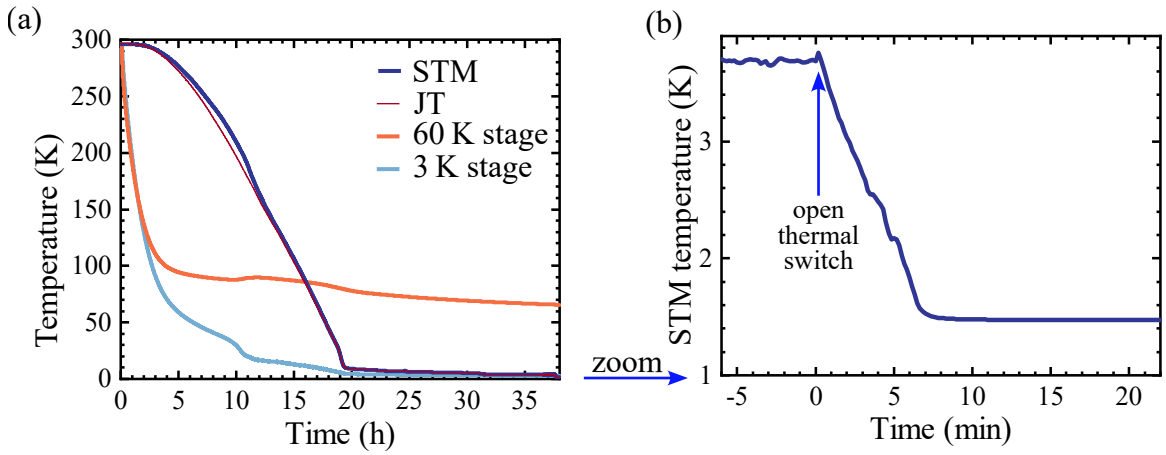


Figure 4.10.: **Cooldown of the cryostat.** (a) Temperature measured at the STM, JT stage, PTC 60 K and 3 K stage after switching on the PTC. The initial cooldown of the system lasts less than two days. (b) Zoom to the time period when the thermal switch is opened and the STM is reaching 1.4 K.

cooldown of the system can begin by setting a pressure of 2 bar at the JT high-pressure supply line. The thermal switch remains in its closed position connecting the JT stage via the 1 K radiation shield to the 4 K plate via the 4 K radiation shield. The radiation shutters stay closed. Once the PTC is switched on, the system progressively cools down, starting at 300 K (Figure 4.10 (a)). After 22 h, the PTC's 3 K stage reaches a

temperature of 4 K. An additional 12 h is required for further thermalization towards stable temperatures. The entire cooldown takes less than two days, mostly without supervision. Only when the JT stage temperature reaches ∼4 K, the thermal switch needs to be operated (Figure 4.10 (b)). A stable temperature of 1.4 K is than reached within 20 min.

4.2.3. Temperature during a sample exchange

A sample or tip exchange, comprising opening the radiation shutters and performing a coarse positioning and coarse approach of the tip, heats the STM to above 30 K (Figure 4.11 (a)). The base temperature is restored within six hours, which includes the

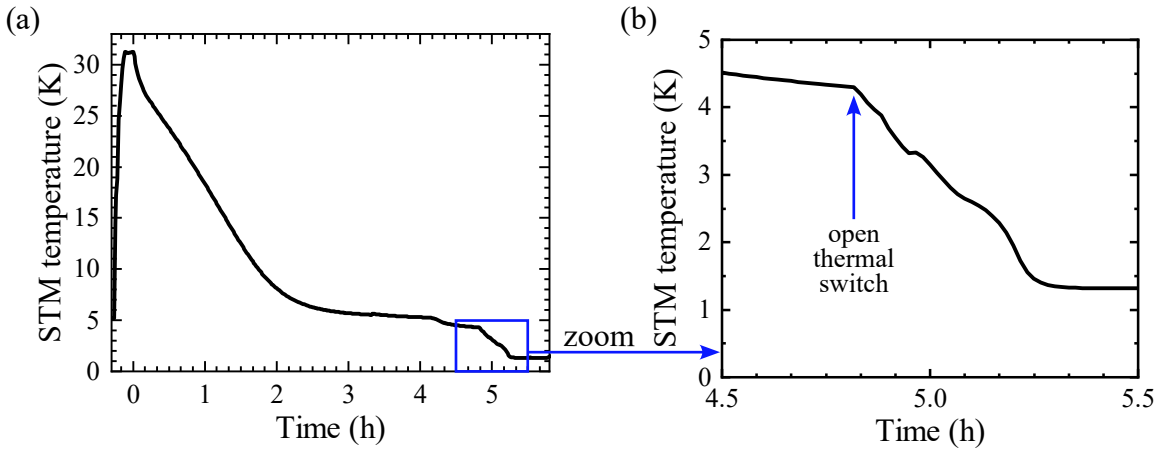


Figure 4.11.: **Cooldown of the STM after a sample exchange.** (a) The STM heats up during a tip and sample exchange. Its base temperature is reached afterwards within less than six hours. (b) Zoom to the time period when the thermal switch is opened and the STM reaching 1.4 K.

opening of the mechanical thermal switch (Figure 4.11 (b)) between the 4 K radiation shield and the JT stage.

4.2.4. Temperature stability

One disadvantage of cryocoolers, that operate with pulsed gas, is the occurrence of temperature oscillations at the operational frequency.

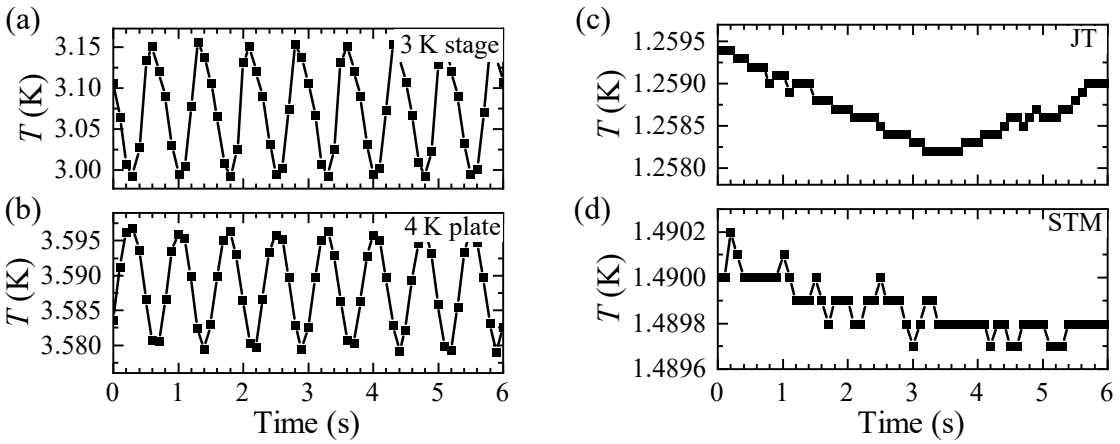


Figure 4.12.: **Temperature oscillations caused by the PTC.** (a) Temperature oscillations of ∼150 mK_{pp} at the PTC 3 K stage. (b) Temperature oscillations of ∼15 mK_{pp} at the 4 K plate. (c) Temperature at the JT stage measured simultaneously to (a). (d) Simultaneously measured temperature at the STM exhibiting oscillations amplitudes less than 1 mK_{pp}. (a)-(d) Sampling period: 100 ms. The data in (b) are not simultaneous recorded with (a), (c), (d); first a connection had to be interchanged.

The amplitudes and damping of these oscillations are measured along our design from the PTC to the STM. The recording is done with a temperature controller (Model 336, Lake Shore Cryotronics®, Inc.) at a sampling period of 100 ms (Figure 4.12 (a)). At the PTC 3 K stage, the oscillations reach a magnitude of ∼150 mK_{pp}. The thermal mass of the 4 K plate, including its mounted components, reduces these oscillations to ∼15 mK_{pp} (Figure 4.12 (b)). The JT stage is suspended from the 4 K plate by three small cross-section stainless steel tubes. This implementation of the JT stage as a final cooling stage serves to reduce temperature oscillations to less than 1 mK_{pp} (Figure 4.12 (c)). The temperature oscillations of 1.3 Hz are also not detectable by the STM temperature sensor (Figure 4.12 (d)). The temperature sensors used on the 3 K stage, 4 K plate, JT stage and STM are from Lake Shore Cryotronics®, Inc. Model DT670 A1, CX-1030, Cx-1030-HT-0.3M, Cx-1030-HT-0.3M, respectively.
The cause of the observed ∼0.2 K temperature difference between the JT stage and STM is still an open question.

4.2.5. Lowest temperatures

Without the STM mounted during an initial cryostat test, we reached a JT stage base temperature of 1.03 K in continuous mode and a single shot temperature of 910 mK lasting 20 h. The JT high pressure supply was set to 0.5 bar, and a gas flow of 7 cm^3/min at 300 K, 1 bar was measured in steady state. Using the latent heat of evaporation 85 J/mol, the molar volume of 27.6 cm^3/mol, and the gas-to-liquid volume ratio of 866 [151], the estimated cooling power is 0.4 mW. The single shot mode, with no ^{4}He applied to the high pressure supply side of the impedance, was initialized by supplying 7 bar of ^{4}He to the high pressure supply line for 2 h to fill the JT reservoir. A gas flow of 4.5 cm^3/min at 300 K, 1 bar was measured in the single shot mode.
After relocating the system into the final laboratory and mounting the STM, a temperature of the JT stage of 1.14 K in continuous mode was achieved with a high pressure supply of 0.5 bar and a steady state gas flow of 31 cm^3/min at 300 K, 1 bar. The estimated cooling power is 1.8 mW. Later the temperature increased to 1.25 K (Figure 4.12 (c)).
We speculate that an unknown heat load became present after moving the cryostat and installing the STM. Possible causes include radiation heat load or a JT stage defect. To decrease the JT stage temperature and lower the temperature difference between the JT stage and STM, the following steps have been carried out. The JT stage temperature is now stable at 1.18 K, but yet no change in temperature difference between the JT stage and STM was achieved:
1) The thermal connection between JT stage and STM was improved by first pressing the STM against the JT stage (using the mechanism described in Section 3.4.4) and second by attaching a Cu stranded link between the STM and the JT stage. 2) The thermal anchoring of the wires reaching the JT stage was improved by clamping them to the 4 K plate using additional screwed connections. 3) Some millimeter-sized gaps in the radiation shields were covered with Cu foil. 4) The wiring of the temperature sensors was checked for the isolation to ground, all exceeding 1 MΩ.

4.3. STM and STS performance

The performance of the STM system is demonstrated through its stability in topographic imaging, its spatial resolution, and its spectroscopic capability, measuring the local

density of states via differential conductivity. The calibration of the x/y-sample stage is provided. The STM's resonances and transfer function are discussed in Section 4.1. The scanner's piezoelectric tube is calibrated in the z-direction using single atomic steps and in the x-y-direction using images with atomic resolution.

4.3.1. Sample and tip preparation

Detailed procedures for preparing each sample are provided in their respective sections. All tips were prepared by electrochemically etching a W wire ex-situ (diameter: 0.2 mm, purity: >99.95 %). In-situ, the tips were further conditioned by applying voltage pulses between the tip and the sample and by controlled indentation into the sample surface.

4.3.2. Sample positioning

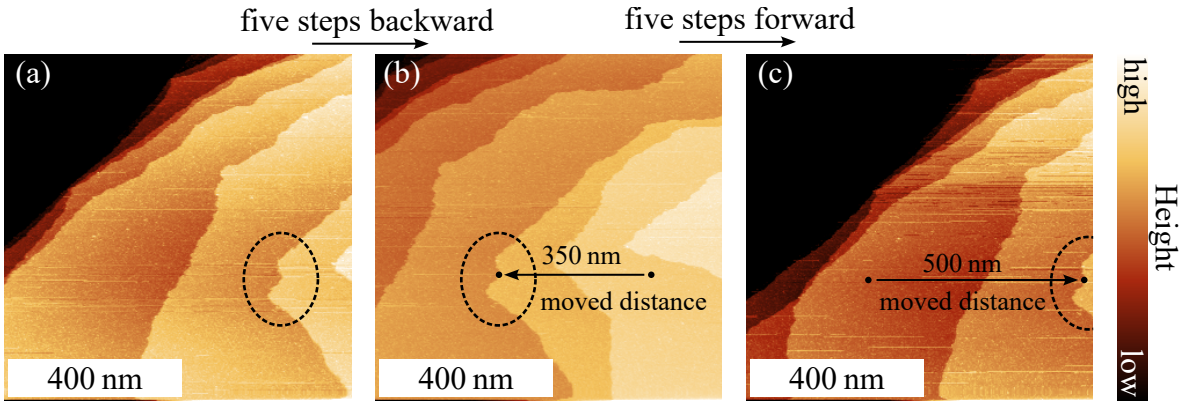


Figure 4.13.: **STM x/y-sample stage movement at** 1.5 K**.** Constant current images of Au(111) with W tip (I = 200 pA, V = 0.9 V, v_{tip} = 75 nm/s). The fast scan direction is horizontal in (a)-(c) and in the y-direction of the x/y-sample stage (as marked in Figure 3.33). The tracked feature is marked. Between (a) and (b) the tip is retracted and the sample stage is moved by five coarse steps to the left (-y-direction of the x/y-sample stage) with a voltage amplitude of 155 V_{p} at the piezoelectric elements. Between (b) and (c) the sample was moved by five steps (155 V_{p}) in the opposite direction. The evaluated distances of the feature are marked.

The x/y-sample stage is designed for moving the sample relative to the tip within a range of 4×4 mm^2 in the horizontal plane. The motors are home-made using shear piezoelectric elements glued to stacks of four (Figure A.4). The piezoelectric constant of the used

piezoelectric material EBL#4 from EBL Products, Inc. is 3.3×10^{-10} m/V at room temperature. This value is typically reduced to one third at liquid helium temperatures [222]. A saw tooth voltage is applied, resulting in a stick-slip motion. For a single saw tooth pulse with a voltage amplitude of 155 V_p, the expected step length is ∼100 nm at ∼1 K. To evaluate the actual step length experimentally, a Au(111) surface is scanned, featuring characteristic step edges, as depicted in Figure 4.13. The Au(111) crystal has an orientation accuracy of <0.1° and a purity larger than 99.999 %. It was not cleaned, but had been stored in UHV at room temperature for one month after the last cleaning prior to the experiment. Before storage, it was exposed to multiple cycles of Ar^+ bombardment (ion energy: 800 eV) with subsequent annealing to 400 °C. During the experiment, the STM was at a temperature of 1.5 K and a voltage of 155 V_p was used at the piezoelectric elements. A scan area of 800× 800 nm^2 was chosen ($I = 200$ pA, $V = 0.9$ V, scan velocity of the tip $v_{tip} = 75$ nm/s). After one image (Figure 4.13 (a)), the tip was retracted (no coarse steps in z-direction) and the sample stage was moved by five steps to the left. The tip was approached at the new location and another image was recorded (Figure 4.13 (b)). Features in the image were moved by ∼350 nm to the left, resulting in a step size of 70 nm. This was confirmed by an additional trial via 10 steps. Using the same procedure, the sample stage is moved back by five steps (Figure 4.13 (c)). Again, an image was taken revealing a movement by ∼500 nm to the right leading to 100 nm per step. This direction-dependent step size must be considered during navigation. Favorably, the movement in the horizontal direction was minimal, if vertical movement was intended. Unfortunately, evaluation in x-direction was not possible due to a loose cable connected to one of the scanner's x-electrodes at that time.

4.3.3. Atomic resolution and standing electron waves

External factors, such as mechanical vibrations, may cause unwanted fluctuations in the tip-sample interface. Such effects compromise the quality of STM imaging.

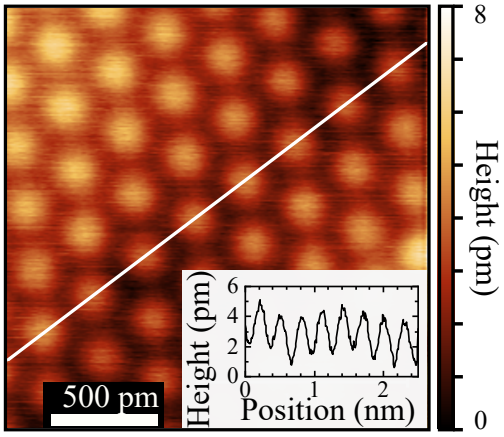


Figure 4.14.: **STM performance on Au(111) at** 1.48 K**.** Constant current image of Au(111) showing atomic resolution, W tip (I =-5 nA, V =-60 mV, v_{tip} = 19.5 nm/s). Inset shows the profile along the white line.

The image stability is initially examined on an Au(111) crystal. The crystal is freshly prepared by multiple cycles of Ar^+ bombardment (ion energy: 800 eV) and annealed to 400 °C (final annealing at $p < 7 \times 10^{-9}$ mbar). At 1.48 K, a constant current image shows an atomic contrast (Figure 4.14). The image represents the raw data, except for a plane slope subtraction and a row-wise height alignment. A profile line is displayed in the inset. The corrugation is 3 $\mathrm{pm_{pp}}$ showing a noise level below 1 pm.
A larger scan area of the same crystal is shown in Figure 4.15 (a). It reveals the $23 \times \sqrt{3}$ herringbone-like surface reconstruction with alternating regions of hexagonal close packed (hcp) and face centered cubic (fcc) stacking [224]. Bright partial dislocation lines [223] are located between these regions. $\mathrm{d}I/\mathrm{d}V(V)$ curves, once recorded at hcp and once recorded at fcc areas, illustrate the difference in the local electronic density of states (Figure 4.15 (b)), with the surface state onset appearing as a step at −480 mV [225]. A $\mathrm{d}I/\mathrm{d}V(x, y)$ map at −480 mV probes the bottom of the Au surface band (Figure 4.15 (c)). It reveals a contrast, caused by localization of surface electrons [225, 226] in the hcp areas. The electrons experience a potential profile with varying heights, lower at the

hcp and higher at the fcc regions, creating the channeling potential. At -50 mV, when $E_{\mathrm{kin}} = E - E_{\Gamma} = 430\,\mathrm{meV}$ with $E_{\Gamma} = -480\,\mathrm{meV}$ (the bottom of the surface band relative to the Fermi level), well above the channeling potential of 38 meV, mostly ring-like standing waves can be observed, possibly caused by point-like scatterers (Figure 4.15 (d)). Additionally, standing plane waves are observed indicating wave guiding along the potential troughs (arrow in Figure 4.15 (d)) [223].

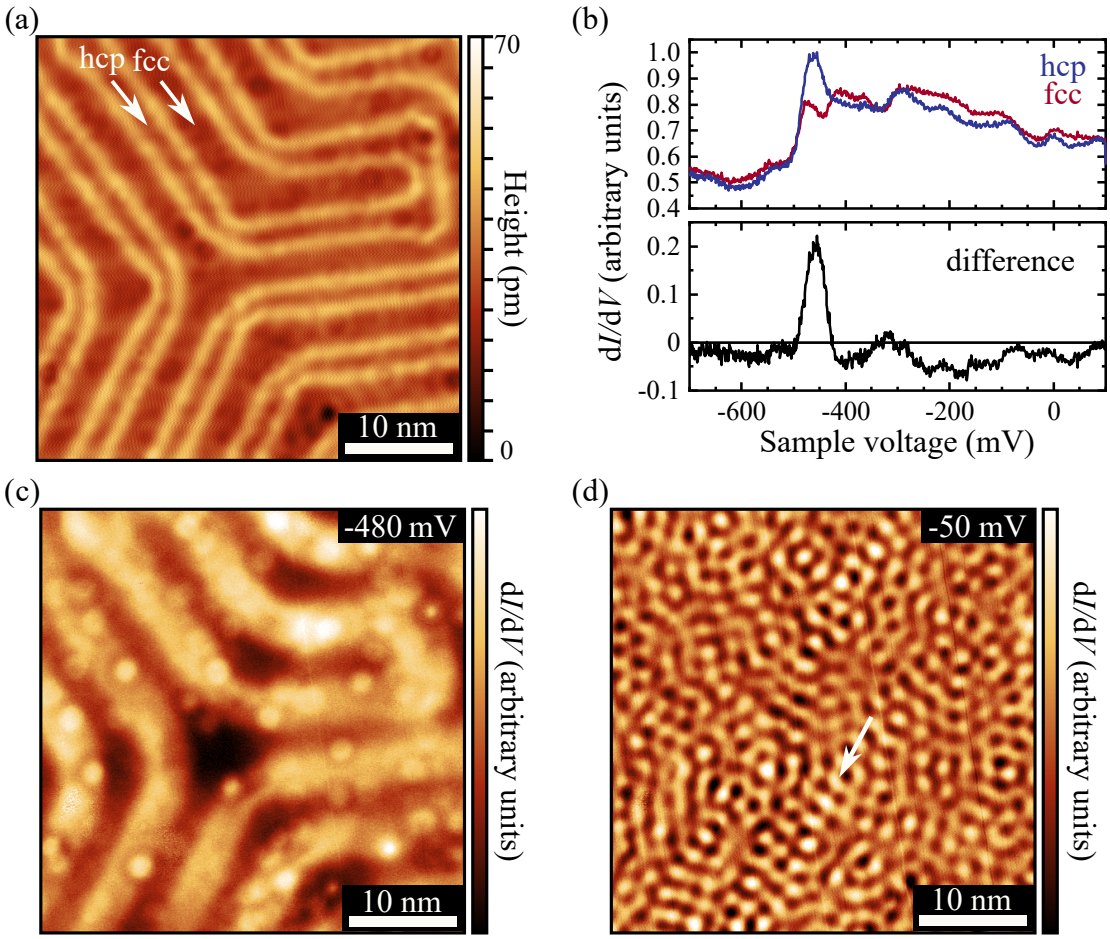


Figure 4.15.: **STM and STS performance on Au(111) at** 1.48 K**.** (a) Constant current image of Au(111) showing the herringbone reconstruction, W tip, hcp and fcc areas are marked ($I = -1\,\mathrm{nA}$, $V = -50\,\mathrm{mV}$, $v_{\mathrm{tip}} = 2.5\,\mathrm{nm/s}$). (b) Differential conductance curves $\mathrm{d}I/\mathrm{d}V(V)$ recorded at a hcp and fcc position and their difference ($V_{\mathrm{stab}} = 100\,\mathrm{mV}$, $I_{\mathrm{stab}} = 400\,\mathrm{pA}$, $V_{\mathrm{mod}} = 10\,\mathrm{mV_p}$). (c) Differential conductance map $\mathrm{d}I/\mathrm{d}V(x, y)$, showing confined states in the hcp areas ($V_{\mathrm{mod}} = 10\,\mathrm{mV_p}$, $V = -480\,\mathrm{mV}$). (d) Differential conductance map $\mathrm{d}I/\mathrm{d}V(x, y)$ recorded simultaneously with (b), ($V_{\mathrm{mod}} = 10\,\mathrm{mV_p}$). Arrow marks diffractive wave guiding along the herringbone structure [223].

4.3.4. Lateral drift

The tip-sample lateral drift is evaluated by taking 40×40 nm² images of the Au surface in a continuous sequence of up and down scans over a period of 57.4 h (Figure 4.16). Prior to the experiment, the tip remained at the same position of the sample for 7 h.

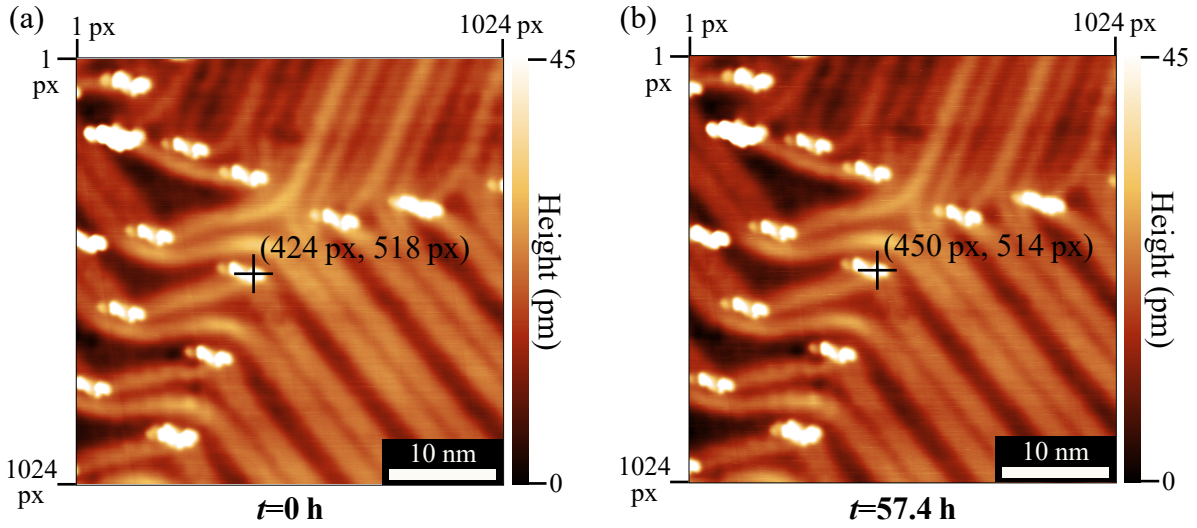


Figure 4.16.: **STM drift on Au(111).** Consecutively recorded constant current image (40×40 nm²) of Au(111) at 1.48 K with W tip (I =400 pA, V =220 mV, v_{tip} = 20 nm/s). (a) Image with marked position of one feature. (b) Image after 57.4 h with the new position of the same feature marked.

Moreover, the cryostat was maintained at base temperature for seven days. To determine the drift, several adsorbates on the surface are used as references. Although tip artifacts are visible leading to the regular patterned appearance of the adsorbates, they do not affect the drift measurement because the tip remains stable. Comparing the position of the marked feature in Figure 4.16 (a) and (b), the determined lateral drift of the tip with respect to the sample is only 18 pm/h. Images recorded in between show that the tip drifts continuously in the same direction such that one can divide the movement length by time to obtain the drift velocity.

4.3.5. Electronic temperature

Lowering the STM temperature can enhance its energy resolution [169, 170]. The important temperature is the electronic temperature, limiting resolution by Fermi level broadening (Section 2.1.4). The electrons with temperature T_{el} can decouple from the phononic temperature T below $\sim$1 K [80]. Thus, the temperature measured by the resistive thermometers can differ from that determined by dI/dV spectroscopy.

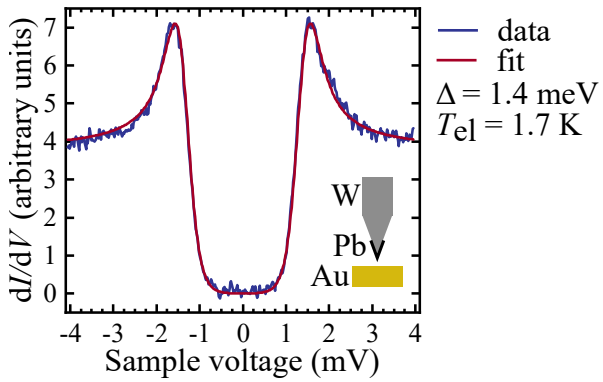


Figure 4.17.: **STM electronic temperature.** $dI/dV(V)$ curve (blue) measured with a superconducting Pb covered tip on a Au(111) crystal (inset). $T = 1.48$ K, $V_{stab} = 6$ mV, $I_{stab} = 100$ pA, $V_{mod} = 20\,\mu V_{RMS}$. A fit constructed from the convolution of BCS density of states with the derivative of the Fermi Dirac distribution is revealing $T_{el} = 1.7$ K and a superconducting gap size $\Delta = 1.4$ meV (red line).

To measure T_{el} of the sample, a superconducting tip with sharp coherence peaks is chosen. It is produced as follows. Using a custom-made electron beam W-crucible evaporator, Pb with a bulk energy gap of $\Delta = 1.35$ meV [227] and a superconducting transition temperature of $T_c = 7.19$ K [228, 229] was deposited at 300 K onto a W(100) sample (accuracy of crystal orientation <0.1°). The W(100) crystal has previously been prepared by several cycles of annealing at 950°C in an O_2 pressure of $p_{O_2} = 1 \cdot 10^{-7}$ mbar and subsequent flashing to 2100 °C. The W tip was indented into the Pb film to create a superconducting tip.

Figure 4.17 shows STS data recorded at T =1.48 K with the superconducting tip on a Au(111) sample. It reveals the superconducting gap in between the two coherence peaks. A fit with the BCS theory is shown in red. It is a convolution of the analytic solution of the Maki equation with the Fermi-Dirac distribution function (Equation 2.14) derivative at a pair breaking parameter of $\xi = 0$ [35, 169]. Hence, the density of states of the tip is

given by the Bardeen Cooper Schrieffer formula:

$$\rho_{\mathrm{sc}}(E) = \begin{cases} \rho_0 \cdot \frac{|E|}{\sqrt{E^2-\Delta^2}} & |E| \geq \Delta, \\ 0 & |E| < \Delta. \end{cases} \tag{4.4}$$

Here Δ is half of the superconducting gap and ρ_0 is the density of states of the non-superconducting state assumed to be constant in energy.
A temperature of $T_{\mathrm{el}} = 1.7\,\mathrm{K}$ and a gap of $\Delta = 1.4\,\mathrm{meV}$, close to the bulk value, is revealed from the fit. The electronic temperature is slightly elevated compared to the lattice temperature of 1.48 K measured by the Cernox sensor at the STM body. The energy resolution can now be calculated as $3.3 k_{\mathrm{B}} T_{\mathrm{el}} = 0.48\,\mathrm{meV}$ (Equation 2.13). An elevated electronic temperature at the sample or tip side can result from electronic noise, for example, RF voltage entering at the cryostat via the electrical feedthroughs. This partly happens via electromagnetic fields, although RF filter boxes are installed at the feedthroughs and the cables inside the cryostat show low-pass characteristics. For the wiring, the following low pass values are determined. In the cold state, the twisted pair cables towards the sample have a measured capacitance of 60 pF, and the coaxial ones measure 120 pF. Their resistances are 78 Ω and 0.5 Ω, respectively, resulting in an estimated equivalent bandwidth of ∼40 MHz and ∼3 GHz, respectively. The tip side tunneling current cable is 0.16 nF to ground, and its measured resistance is 1.4 Ω at room temperature for the inner conductor and 1 Ω for the shield leading to a bandwidth of ∼0.5 GHz. All these values are too small to explain a temperature increase of the electrons at the sample.

4.3.6. Voltage noise

Further benchmarking of the STM uses phenomena from superconductivity, in particular multiple Andreev reflections [230, 231] and the Josephson supercurrent [232].
For exactly zero bias, a current can flow between two superconducting electrodes via Cooper-pair tunneling, as B. D. Josephson published in 1962. In honor of him, the phenomenon is called the Josephson effect [232, 233]. Using this effect, the energy resolution can be further improved, since it is not affected by the Fermi Dirac distribution function [234]. Mostly, residual voltage noise in the tunneling lines broadens the zero

voltage peak of Cooper-pair tunneling.

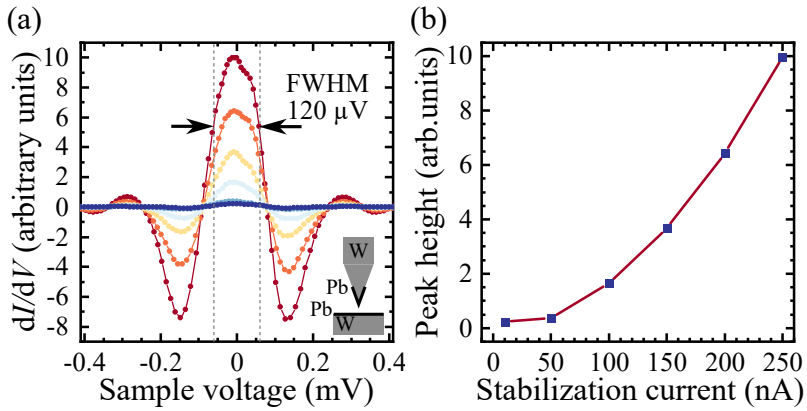


Figure 4.18.: **Superconductor-superconductor tunneling and voltage noise.** (a) $\mathrm{d}I/\mathrm{d}V(V)$ curve of Josephson peak with decreasing peak height for $I_{\mathrm{stab}} = 250\,\mathrm{nA}$, 200 nA, 150 nA, 100 nA, 50 nA, 10 nA measured with a superconducting Pb covered W tip on a W(100) crystal covered with Pb (inset), $T = 1.48\,\mathrm{K}$, $V_{\mathrm{stab}} = 5\,\mathrm{mV}$, $V_{\mathrm{mod}} = 15\,\mu\mathrm{V_{RMS}}$. The FWHM with respect to the value ($\mathrm{d}I/\mathrm{d}V(V) = 0$) is marked. (b) The height of the Josephson peaks from (a) rising superlinear with I_{stab}.

To achieve an energy resolution lower than 1 meV, sources of electrical and thermal noise have to be minimized as done by using the Josephson peak for monitoring. Thus, measurements are conducted at the cryostat base temperature of 1.48 K. The bias modulation is kept at $15\,\mu\mathrm{V_{RMS}}$. The modulation frequency of 962 Hz is chosen to lie in a low noise region of the tunneling current spectrum, but still within the bandwidth of the tunneling current amplifier. The electrical connections on the cryostat are optimized (detailed description in Section 3.6). Low-pass filters are installed on the electrical feedthroughs, the amplifier input is shielded, a coupling box with a 1/10 division factor is placed in the bias line near the electrical feedthrough at the cryostat (the coupling box with the differential amplifier breaks the ground loop). In addition, the following electrical connections are disconnected and grounded: coarse piezoelectric elements, temperature sensors, turbomelecular pump, scroll pump, getter pumps, pressure sensors, RF antenna. A clean W(100) crystal is covered by several layers of Pb. The W-tip is immersed into the Pb layer to form a Pb micro tip. This method provides tips that are stable up to a current of 250 nA at a tunnel gap resistance of 20 kΩ at the stabilization voltage V_{stab} outside the gap. Figure 4.18 (a) shows the Josephson peak inside the gap getting larger with increasing stabilization current. The peak shape shows dips with negative

$\mathrm{d}I/\mathrm{d}V$ values, caused by a decreasing tunneling current for voltages where the probability of Cooper-pair tunneling gets suppressed. The peaks next to the Josephson peak are described in the second half of Section 4.3.7. The marked FWHM in Figure 4.18 (a) is given with respect to the zero line. Its value of 120 µV is below the energy resolution of $3.3k_BT_{\mathrm{el}} = 480\,\mu\mathrm{eV}$ for $T_{\mathrm{el}} = 1.7\,\mathrm{K}$. This appears because Cooper pairs do not follow the Fermi-Dirac distribution, but instead form a BCS state. The remaining width can be attributed to residual voltage noise. The input noise from the preamplifier is likely not the cause, since the same model showed a FWHM of only 40 µV in another STM setup at 410 mK [35]. Also, Johnson-Nyquist noise can be excluded, since it is only ∼5 µV for the tunneling current and tunnel voltage lines used (∼20 cm Elspec Storm Flex 034 cable at 300 K with a bandwidth of 5 GHz). During noise optimization, I measured the voltage noise with an RF oscilloscope before installing the low-pass filter boxes. It was determined to $30\,\mu\mathrm{V_{RMS}}$ integrated noise for a bandwidth of 150 MHz, though not excluding higher frequency noise that could enter the cryostat. Hence, the origin of the voltage noise in the tunneling junction remains unknown.
To confirm that the zero bias peak is caused by Cooper-pair tunneling, the peak height was measured as a function of stabilization current (Figure 4.18 (b)). Since the tunnel current depends on $I \sim e^{\frac{\sqrt{m\Phi}}{\hbar}z}$, the exponential decay for Cooper pairs is larger by a factor of $\sqrt{2}$ than the decay of single electrons, leading to a superlinear behavior of $I_{0\mathrm{V}}(I_{\mathrm{stab}})$. The peak height rises indeed superlinearly with I_{stab}. For example, increasing the stabilization current from 100 nA by a factor of 2.5 to 250 nA the Josephson peak height rises by a factor of five.
Note: The voltage of the $\mathrm{d}I/\mathrm{d}V$ curve in Figure 4.18 (a) are corrected for an instrumental voltage offset (∼0.06 mV), i.e. the Josephson peak is shifted to $V = 0\,\mathrm{mV}$. In addition, the data are corrected for a voltage drop at the resistors of the RF filter boxes (3370 Ω), which is, e.g. ∼15 % for the current at 4 mV.

A major achievement in the noise optimization using the Josephson peak was the proper shielding of the input of the transimpedance tunneling current amplifier. It has an input that allows the outer contact to be biased via a selector switch. Hence, by design, there is insulating material in the connector (white ring in Figure 4.19 (a)). This location was found to be a gap in shielding and introduced noise. By applying self-adhesive aluminum tape to this area, the noise was reduced significantly (Figure 4.19 (b)). The

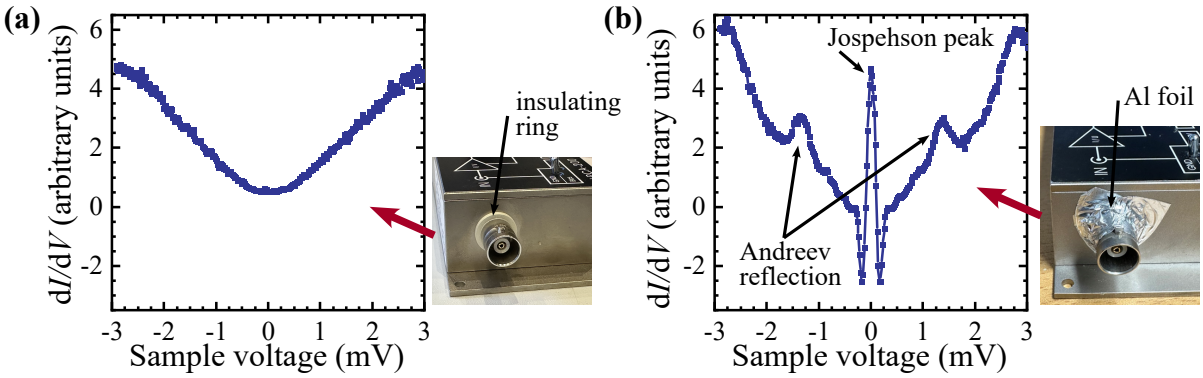


Figure 4.19.: **Noise introduced by insufficient shielding.** (a) $\mathrm{d}I/\mathrm{d}V(V)$ curve for a insufficient shielding of the input of the transimpedance tunneling current amplifier a superconducting Pb covered W tip on a W(100) crystal covered with Pb. $I_{\mathrm{stab}} = 150\,\mathrm{nA}$, $T = 1.48\,\mathrm{K}$, $V_{\mathrm{stab}} = 3.5\,\mathrm{mV}$, $V_{\mathrm{mod}} = 20\,\mu\mathrm{V_{RMS}}$. No superconducting features are visible in the gap region ($\pm 4\,\mathrm{mV}$). (b) $\mathrm{d}I/\mathrm{d}V(V)$ curve with the same conditions as in (a), except of an additional shielding at the input of the transimpedance tunneling current amplifier with self-adhesive aluminum tape, as shown in the photograph. The Josephson peak and Andreev reflections are clearly visible.

additional aluminum tape does not affect the measurements elsewhere, because the input line is grounded at the cryostat flange electrical feedthrough. Moreover, the selector switch of the Femto preamplifier is set to ground. Figure 4.18 was recorded with the amplifier wrapped in aluminum foil.

Future additional noise reduction is possible. The concept for grounding (Section 3.6) of the whole system is not yet fully optimized. Although the grounding loops of the tunneling lines are broken at the current input terminal and bias box, there are still ground loops between the cryostat and attached peripherals via the fuse box ground line, the helium compressor flexlines, the JT pumping tube, pumps, and the conducting carpet. All of these may cause voltage fluctuations of the cryostat ground. Technical measures could isolate these connections. For example, galvanic isolation is available for the PTC and can be installed between the PTC head and the rotary valve. Plastic gaskets and clamps or isolating transformers can be used to separate the pumps.

4.3.7. Subgap features in tip-sample Josephson junction

The theory of superconductivity is described by the BCS model after J. Bardeen, L. N. Cooper, and J. R. Schrieffer [235]. A central characteristic of superconductivity is zero electrical resistance below a critical temperature T_c [236]. Another characteristic is the energy gap of width 2Δ in the density of states for single electrons as observed in tunneling experiments. Exciting an electron from an occupied state in the superconductor to an empty state requires, also, at least, the energy 2Δ. For a coupled superconductor-superconductor tunneling junction, new features appear inside the gap measured by tunneling. One origin are Andreev reflections [230, 237]. For two equal superconductors, forming a symmetric tunneling junction, at a bias voltage of $|eV| < 2\Delta$, an incoming electron, e.g. from a superconducting tip, cannot propagate into electron-like empty states of the superconducting sample. But, it can create a Cooper pair, while it is reflecting as a hole (2nd order Andreev reflection) (Figure 4.20 (c)). The Cooper pair is then created from two electrons tunneling simultaneously from the tip into a Cooper pair of the sample. Another possibility is the annihilation of a Cooper pair by tunneling of a hole, followed by a reflection as an electron, respectively the tunneling of a Cooper pair from the tip into two empty electron states of the sample. Higher order MARs involve more reflections; for example, three particles are effectively tunneling, while on one side a Cooper pair is created and on the other it is annihilated (3rd order Andreev reflection) (Figure 4.20 (d)). The two electrons of the sample originate from one single electron of the tip and one electron from a Cooper pair of the tip that match in energy with the Cooper pair of the sample. The other electron from the Cooper pair of the tip gains energy, such that it can propagate to empty electron states in the sample. In an n-th order Andreev reflection process, n charges are transported effectively and $n-1$ Andreev reflections occur (Figure 4.20 (c-f)). In a symmetric superconductor tunneling junction, i.e. the same superconducting gap on both sides, these Andreev reflections are at bias voltages of $eV = \pm\frac{2\Delta}{n}$, $n = 2, 3, \ldots$ For $\Delta = 0.67\,\mathrm{eV}$ as in our case, peaks should occur at $V = \pm 1.35\,\mathrm{mV}$, $\pm 0.9\,\mathrm{mV}$, $\pm 0.7\,\mathrm{mV}$ and $\pm 0.5\,\mathrm{mV}$. Figure 4.20 (a) shows the measured gap structure. The outer peaks correspond to coherence peaks from the process illustrated in Figure 4.20 (b). The two more inner peaks at $eV = \Delta$ match the second-order Andreev reflections. The third peak at $V = 0.9\,\mathrm{mV}$ matches a third-order Andreev reflection.

The remaining peaks next to the Josephson peak might arise from the interaction of tunneling Cooper pairs with the junction's surroundings or, more precisely, the impedance of the electrodynamic environment [238, 239]. The tip (length: ∼0.8 mm) inside its tip holder (diameter: 3 mm) is the closest surrounding. This geometry acts like a $\lambda/4$-monopole antenna. The tunneling process is inelastic, where a tunneling Cooper pair is emitting excess kinetic energy as a resonantly amplified photon with energy $\hbar\omega = 2eV \approx 0.7\,\mathrm{meV}$. Due to the resonant amplification, the photon can facilitate Cooper-pair tunneling, leading to discrete current peaks in the spectrum. A schematic representation is given in Figure 4.20 (g). These peaks correspond to standing wave eigenmodes at the tip of $f_n = (2n+1)c/(4(l+l_0))$, with $n = 0, 1, 2, ...$ Here, l is the length of the tip and l_0 is an electrical lengthening [240]. In our case, the first pronounced peaks in the current (not shown) are at $V \approx 330\,\mu\mathrm{V}$, corresponding to the third zero crossing in the $\mathrm{d}I/\mathrm{d}V(V)$ curve in Figure 4.20 (a). This corresponds to a frequency $f = 2eV/h = 155\,\mathrm{GHz}$ or a wavelength of 1.9 mm. Assuming a similar $l_0 = 0.46\,\mathrm{mm}$, as found in [240], it most probably corresponds to the eigenmode f_1. For f_0, the resulting l of the tip would be more than one order of magnitude smaller than in reality ($l = 0.8\,\mathrm{mm}$).

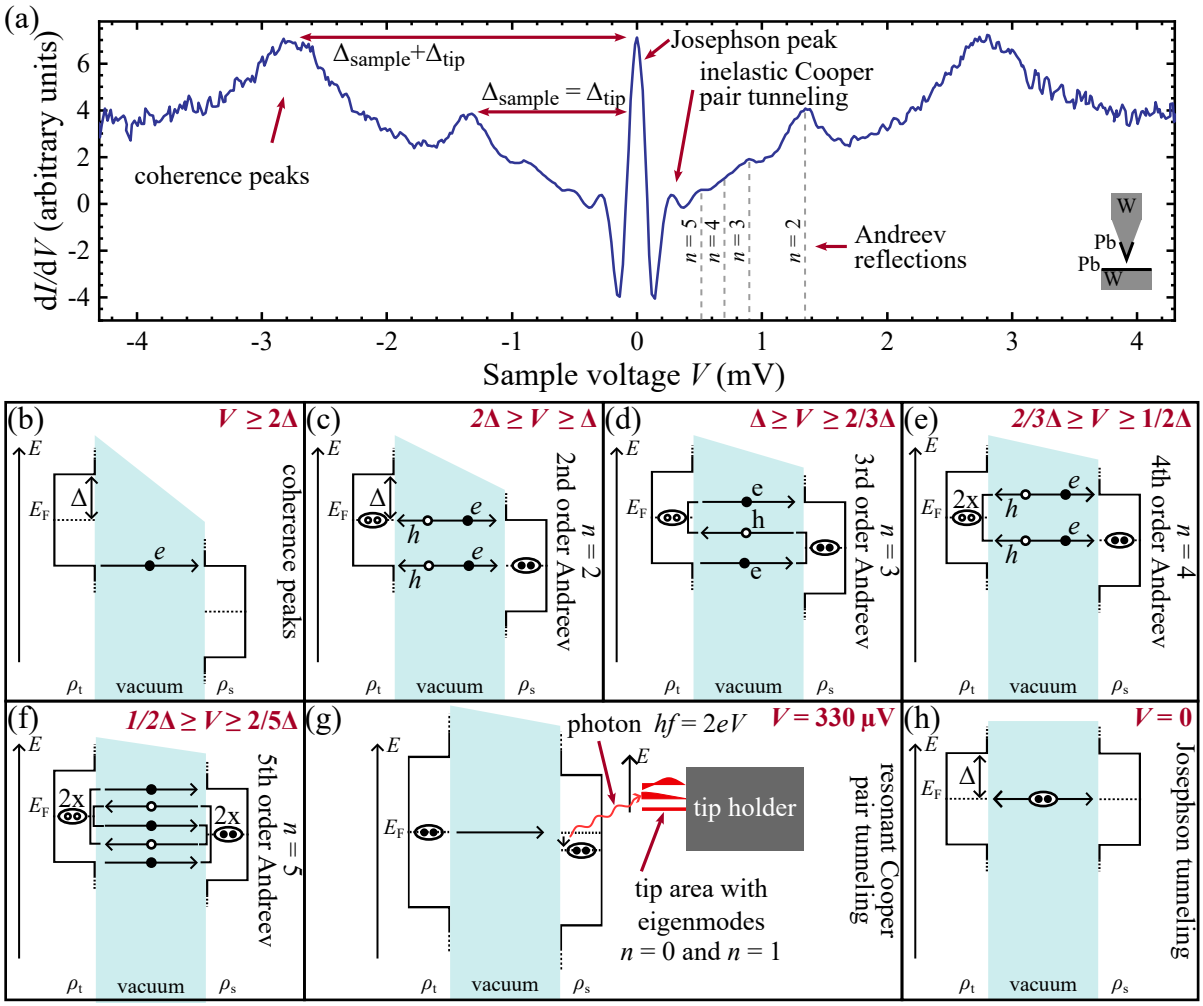


Figure 4.20.: **STM subgap features for superconductor-superconductor tunneling.** (a) $\mathrm{d}I/\mathrm{d}V(V)$ curve measured with a superconducting Pb covered W tip on a W(100) crystal covered with Pb (inset). $T = 1.48\,\mathrm{K}$, $V_{\mathrm{stab}} = 5\,\mathrm{mV}$, $I_{\mathrm{stab}} = 200\,\mathrm{nA}$, $V_{\mathrm{mod}} = 15\,\mu\mathrm{V_{RMS}}$. Outermost peaks correspond to the coherence peaks as marked, appearing at the voltage the sum of the gaps of tip and sample. A schematic of this process is given in (b). The peaks marked $n = 2$ and $\Delta_{\mathrm{sample}} = \Delta_{\mathrm{tip}}$ are due to second order Andreev reflections with the corresponding schematic in (c) involving two quasiparticles (electrons, holes) to create a Cooper pair (two dots in the oval). Higher order Andreev reflections are also marked upto $n = 5$ and drawn in (d-f). The peak at zero bias is due to direct Cooper-pair tunneling, the so called Josephson tunneling effect (h) (Section 4.3.6). Peaks close to the Josephson peak might be attributed to inelastic Cooper-pair tunneling with the corresponding schematic in (g) where the excess energy of the Cooper pair is coupled at specific energy's to the eigenmodes of the tip-sample area via a photon (tip length: $\sim$0.8 mm).

4.3.8. Radio frequency in the tunneling junction

Studying fast and local dynamics in STM often uses radio frequency (RF) voltages in the tunneling junction. Sometimes the radiation is continuous [241, 242], and sometimes pulse-like waves are employed [243–245]. The RF signal can be delivered via two methods: through a direct wiring to the tip or sample [241–249], or via an antenna or a coil placed near the tunneling junction [187, 250–256]. A direct wired RF transmission up to the tip or sample is elaborate, and consequently, these setups mostly exhibit reduced RF transmission.

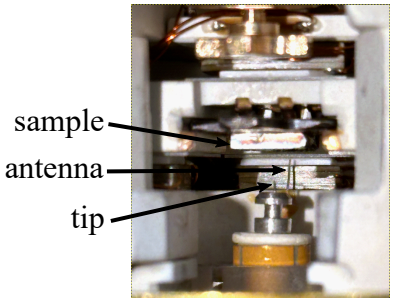


Figure 4.21.: **STM radio frequency setup.** Photograph of the geometry between RF antenna, retracted tip, and sample.

In our STM setup, we installed an RF antenna near the tip (Figure 4.21), which allows to supply radio frequencies to the tunneling junction from 0.3 – 40 GHz. These correspond to wavelengths of 1 m to 1 mm. The following section demonstrates the performance of the installed RF antenna. Specifically, the effect of a 40 GHz RF signal on the tunneling process of a superconductor-vacuum-superconductor junction is shown. Microwave-assisted Cooper-pair tunneling is observed in a Josephson junction between a superconducting Pb tip and a superconducting Pb sample. In this process, RF radiation impinges on the junction. Such that photons assist the Cooper-pair tunneling resulting in additional subgap peaks [251–253]. The voltage positions and heights of these peaks depend on the frequency and amplitude of the RF voltage. The spacing between the peaks confirms that the charge carriers of the tunneling process are Cooper pairs rather than quasiparticles. Additionally, the variation of the Josephson peak's amplitude with the RF

amplitude demonstrates that the tunneling current originates from microwave-assisted, phase-incoherent tunneling of the Cooper pairs, rather than from the phase-coherent tunneling, which is known as Shapiro steps.
For the sake of completeness, and because macroscopic Josephson junctions exhibit features similar to those observed here, a brief distinction is made to the phenomenon of Shapiro steps [257]: 1) Shapiro steps typically occur in macroscopic Josephson junctions with large capacitance (pF) and large critical currents (µA), where tunneling is phase-coherent. 2) Shapiro steps appear as discrete current steps at quantized voltages under combined DC and AC voltages. In contrast, in an STM junction, the junction has a small capacitance (fF) and small critical currents (nA), leading to a phase-incoherent pair tunneling of individual pairs only.
Cooper pairs tunnel in the direction of an applied voltage across the tunneling junction while carrying an energy of $\pm 2eV$ with respect to the Cooper-pair energy of the other superconductor. This energy needs to be provided or dissipated to or from the environment [258]. The observed patterns are interpreted either as microwave-assisted tunneling or as microwave emission, respectively [252, 259]. For the mentioned Josephson junction exposed to radiation with frequency f, the Josephson peak develops into multiple peaks in tunneling voltage with distances:

$$\Delta V = hf/2e. \tag{4.5}$$

Here h is the Planck's constant and e is the elementary charge. Under these conditions, the time-averaged dc tunneling current I_f behavior is quantitatively described by the Tien-Gordon equation.

$$I_\mathrm{f}(V, V_\mathrm{ac,J}) = \sum_{n=-\infty}^{\infty} J_\mathrm{n}^2 \left(\frac{2eV_\mathrm{ac,J}}{hf} \right) I_0 \left(V - \frac{nhf}{2e} \right), \tag{4.6}$$

where J_n is the n^th Bessel function, $I_0(V) = I_\mathrm{f}(V, V_\mathrm{ac,J})|_{V_\mathrm{ac,J}=0}$ is the DC tunneling current without RF excitation, and $V_\mathrm{ac,J}$ is the RF amplitude in the junction [253, 260, 261]. The model is also capable of describing other subgap features. The corresponding

time-averaged conductance is:

$$\frac{\mathrm{d}I_\mathrm{f}}{dV}(V,\, V_\mathrm{ac,J}) = \sum_{n=-\infty}^{\infty} J_\mathrm{n}^2\left(\frac{2eV_\mathrm{ac,J}}{hf}\right)\frac{\mathrm{d}I_0}{\mathrm{d}V}\left(V - \frac{nhf}{2e}\right), \tag{4.7}$$

where $\mathrm{d}I_0/\mathrm{d}V(V)$ is the conductance without RF.
The experimental setup includes an RF generator (Agilent E8254A 1E1 1EA UNJ) connected to a vacuum feedthrough (Vacom CF16-SMA50-40GHz, Typ K, 2.92 mm, 50 Ohm up to 45 GHz) using a flexible cable (Mini-Circuits CBL-SMSM+). Inside the vacuum, the RF signal is guided to the JT stage through another flexible cable (Elspec Storm Flex 034, length: ∼70 cm). A highly flexible cable (Picocoax™ PCX 42 K 10 AK, Axon Cable, length: 22 cm), linked by an SMPM connector (Cinch Connectivity Solutions 125-2592-001, Amphenol 925-124P-51S), is then employed to the antenna. For the final 4.5 mm, the cable's shielding is stripped to create the antenna. Wiring details are available in Section 3.6. The tip and sample preparation follows the descriptions in Section 4.3.6.

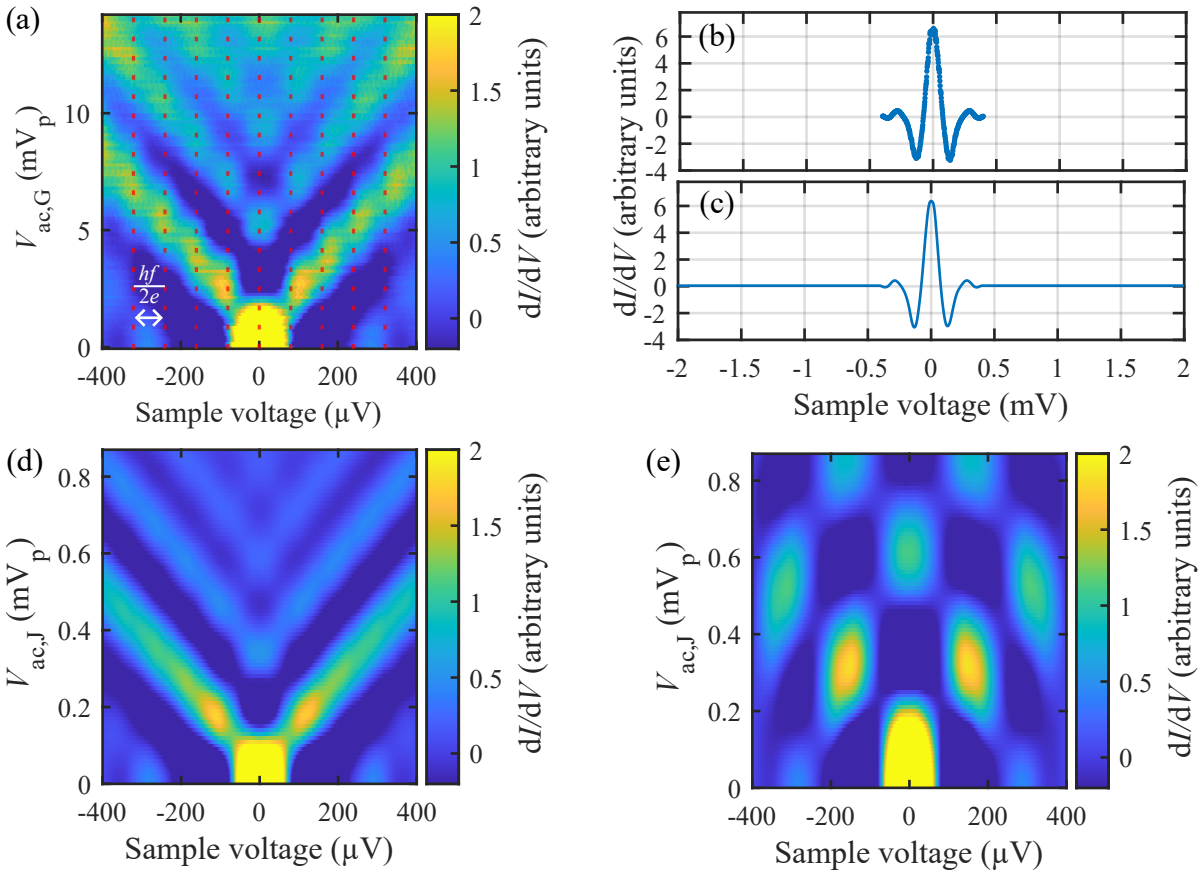


Figure 4.22.: **STM radio frequency performance.** (a) Differential conductance map of a superconductor-vacuum-superconductor Josephson junction, recorded with an increasing RF voltage $V_{\mathrm{ac,G}}$ of the generator and a Pb covered W tip on a W(100) crystal covered with Pb. $f = 38.73\,\mathrm{GHz}$, $V_{\mathrm{stab}} = 5\,\mathrm{mV}$, $I_{\mathrm{stab}} = 150\,\mathrm{nA}$, $T = 1.48\,\mathrm{K}$, $V_{\mathrm{mod}} = 10\,\mu\mathrm{V_{RMS}}$, CBL-2M-SMSM+ cable. Red dotted lines mark positions of expected peaks with distance ΔV according to Equation 4.5. (b) $\mathrm{d}I/\mathrm{d}V(V, V_{\mathrm{ac,G}})$ for $V_{\mathrm{ac,G}} = 0\,\mathrm{V}$ from (a). (c) Smoothed and extended curve towards higher voltages from (b), which is used as input for (d). (d) Calculated differential conductance map using Equation 4.7. The y-axis is adapted until the V-shape fits the one in (a) revealing the ration between $V_{\mathrm{ac,G}}$ at the generator and $V_{\mathrm{ac,J}}$ at the tunneling junction. (e) Calculated differential conductance map using Equation 4.7 without the factors of 2, assuming quasiparticles of charge e are the charge carriers, and the measured conductance curve of (c) as input. The data do not fit the measured one in (a), excluding quasiparticle tunneling with charge e.

Plotting the experimentally determined peak sequence in a (V, $V_{\mathrm{ac,G}}$) plane, where $V_{\mathrm{ac,G}}$ is the generator's voltage amplitude, allows identification of the tunneling type by comparison with theoretical models. The recorded $\mathrm{d}I_{\mathrm{f}}/\mathrm{d}V(V, V_{\mathrm{ac,G}})$ signal, obtained with an RF excitation at $f \approx 40\,\mathrm{GHz}$, is shown in Figure 4.22 (a). As $V_{\mathrm{ac,G}}$ is increasing, the Josephson peak develops into multiple peaks along the V-direction. According to Equation 4.5, their theoretical distance is $\Delta V = \frac{hf}{2e} = 80\,\mu\mathrm{V}$, indicated by a double white arrow and roughly fitting the experimentally observed peak distances. The peak sequence forms a V-shape in the $(V, V_{\mathrm{ac,G}})$-plane.
By using the measured $\mathrm{d}I_{\mathrm{f}}/\mathrm{d}V(V, V_{\mathrm{ac,G}})|_{V_{\mathrm{ac,J}}=0}$ as an input in Equation 4.7, the y-axis of Figure 4.22 (a) can be calibrated for the RF amplitude in the tunneling junction $V_{\mathrm{ac,J}}$. Figure 4.22 (b) shows the $\mathrm{d}I_{\mathrm{f}}/\mathrm{d}V(V, V_{\mathrm{ac,G}})|_{V_{\mathrm{ac,J}}=0}$ and Figure 4.22 (c) the smoothed one extended to higher voltages by $\mathrm{d}I_{\mathrm{f}}/\mathrm{d}V(V, V_{\mathrm{ac,G}}) = 0$. This is then used as the input for Equation 4.7 to obtain Figure 4.22 (d). The simulated results in Figure 4.22 (d)

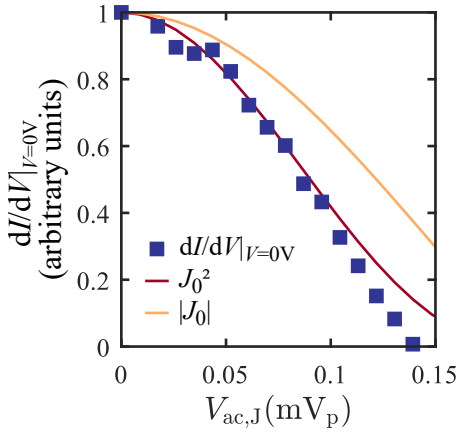


Figure 4.23.: **Josephson peak development under radiation at $V = 0\,\mathrm{V}$.** Data points are extracted from Figure 4.22 (a) along the profile line at $V = 0\,\mathrm{V}$ for an increasing RF voltage and normalized to the value at $V_{\mathrm{ac,J}} = 0\,\mathrm{V}$. The red line is the Bessel function of zeroth order squared (microwave-assisted model) and the orange one the absolute value of the Bessel function of zeroth order (Shapiro model), both for $2eV_{\mathrm{ac,J}}/hf$. The Shapiro model does not fit the measured data points.

reproduce the experimental data in Figure 4.22 (a) after adopting $V_{\mathrm{ac,J}}$ to $V_{\mathrm{ac,G}}$, and revealing an attenuation of roughly a factor of 20. This confirms that phase-incoherent, microwave-assisted tunneling of Cooper pairs is present. Evidence that phase-coherent tunneling showing Shapiro steps can be excluded is shown in Figure 4.23. Shapiro steps

would feature a supercurrent proportional to J_n rather than J_n^2, and I_C (critical current) instead of $I_0\left(V - \frac{nhf}{2e}\right)$ in Equation 4.6 [253]. Data points extracted from Figure 4.22 (a) along the profile line at $V = 0\,\mathrm{V}$ with rising RF voltage deviate from the Shapiro model but largely fit the incoherent model. For $V_{ac,J} > 0.1\,\mathrm{mV_p}$, the deviation from the Bessel function of zeroth-order squared can be explained by the first satellite peaks at $V = \pm 80\,\mu\mathrm{V}$ in Figure 4.22 (a) overlapping with the Josephson peak.
Comparing the y-axes of Figure 4.22 (a) and Figure 4.22 (d), using Equation 4.8 below yields an attenuation $T = -24\,\mathrm{dB}$ from the generator to the junction at this frequency. This value is rather similar to the combination of damping by the cable connecting the RF generator to the cryostat ($-7.4\,\mathrm{dB}$ @ $40\,\mathrm{GHz}$) and the cables inside the cryostat. The cable inside the cryostat showed $-16.5\,\mathrm{dB}$ @ $40\,\mathrm{GHz}$ in the VNA measurements (Figure 3.42) if corrected for low temperatures and the final cable length.
For tunneling of quasi particles of charge e, Equation 4.7 must be used without the factor of 2 in the first and second terms. The resulting simulated data are shown in Figure 4.22 (e). They do not fit the data at all, excluding tunneling of charge e quasi particles as the origin for the data in Figure 4.22 (a).

Another method for determining the RF amplitude $V_{ac,J}$ in the tunneling junction employs a non-linear $I(V)$ dependency. For example, one can use the onset of the Au(111) surface state at $-480\,\mathrm{mV}$ [225]. Figure 4.24 (a)-(b) shows the $\mathrm{d}I_0/\mathrm{d}V$ signal without RF radiation, along with its broadened form under RF radiation for two different RF excitation frequencies. A fit of these $\mathrm{d}I_f/\mathrm{d}V(V, V_{ac,G})$ curves, which includes a convolution of the $\mathrm{d}I_0/\mathrm{d}V(V)$ curve recorded without RF with a normalized arcsine distribution, yields $V_{ac,J}$ [246, 254]. Applying this method at multiple frequencies can determine the transfer function $T(f)$ for any frequency according to:

$$T[\mathrm{dB}] = 20\log_{10}\left(\frac{V_{ac,J}}{V_{ac,G}}\right). \tag{4.8}$$

Different RF amplitudes resulting in $V_{ac,J} = 10-40\,\mathrm{mV_p}$ are tested, showing that the transfer function is amplitude independent (Figure 4.24 (c)). For the highest generator frequency ($40\,\mathrm{GHz}$), $-28\,\mathrm{dB}$ is determined, in good agreement with the value determined by the microwave-assisted tunneling ($-24\,\mathrm{dB}$) concerning the shorter cable between the

RF generator and the cryostat. Figure 4.24 (d) shows the power to set at the generator in dBm (the most typical unit for RF signal generators) for achiving $V_{\mathrm{ac,J}}$, given by

$$P_{\mathrm{GEN}}[\mathrm{dBm}] = 10\ \log_{10}\left(\frac{V_{\mathrm{ac,G}}^2[\mathrm{V_p}]\cdot 1000}{2\cdot 50\,\Omega}\right). \tag{4.9}$$

The signal generator used (Agilent E8254A 1E1 1EA UNJ) provides a maximum power of 25 dBm (5.6 $\mathrm{V_p}$) at 10 GHz and drops to 17.5 dBm (2.4 $\mathrm{V_p}$) at 40 GHz enabling still higher $V_{\mathrm{ac,J}}$, albeit this starts causing a temperature increase in the STM.

This method for determining the transfer function is time-consuming, particularly

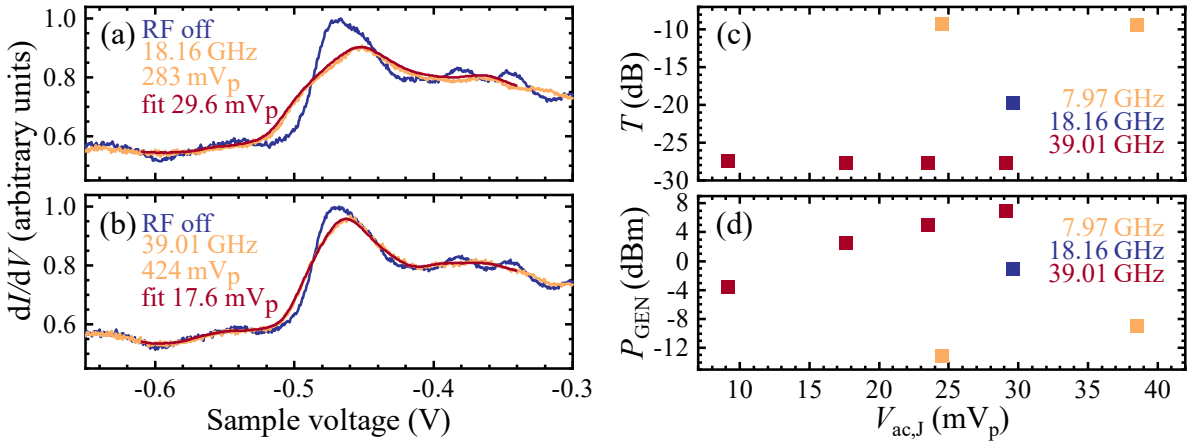


Figure 4.24.: **STM radio frequency performance, antenna transfer function.** (a),(b) Differential conductance curves featuring the Au(111) surface state without RF (blue) and with RF (yellow). The red line is a fit to the yellow line (see text). The frequencies and amplitudes at the RF generator are marked in yellow. The amplitude in the tunneling junction resulting from the fit is marked in red. $V_{\mathrm{stab}} = -650\,\mathrm{mV}$, $I_{\mathrm{stab}} = -1\,\mathrm{nA}$, $T = 1.48-1.76\,\mathrm{K}$, $V_{\mathrm{mod}} = 10\,\mathrm{mV_p}$, CBL-12FT-SMSM+ cable. (c) Transfer function T(dB) from the RF generator towards the tunneling junction for different amplitudes $V_{\mathrm{ac,J}}$ and frequencies as marked, determined by the method shown in (a) and (b). (d) Same data as in (c) but displayed in decibel milliwatts, providing the necessary settings for the RF signal generator.

when applied at each frequency of interest. An additional experiment is conducted to perform relative measurements for a wide bandwidth. Afterwards, the relative measurement is calibrated to its absolute value at one frequency using the method of Figure 4.24. The relative measurement setup, as depicted in Figure 4.25, includes a trigger signal line between the RF signal generator ($\mathrm{Ref_{out}}$) and the lock-in amplifier ($\mathrm{Ref_{in}}$) that allows

the RF signal to be switched on and off at the lock-in frequency. A chopping frequency is chosen such that it is still amplified by the transimpedance amplifier. In this way, a so-called rectified tunneling current [242] can be measured at a voltage where $I(V)$ is non-linear, while the feedback loop of the STM is active being more slow than the chopping frequency. Here, we choose the $I(V)$ nonlinearity of the Au surface state to determine the RF transfer function for 0.3 – 40 GHz.

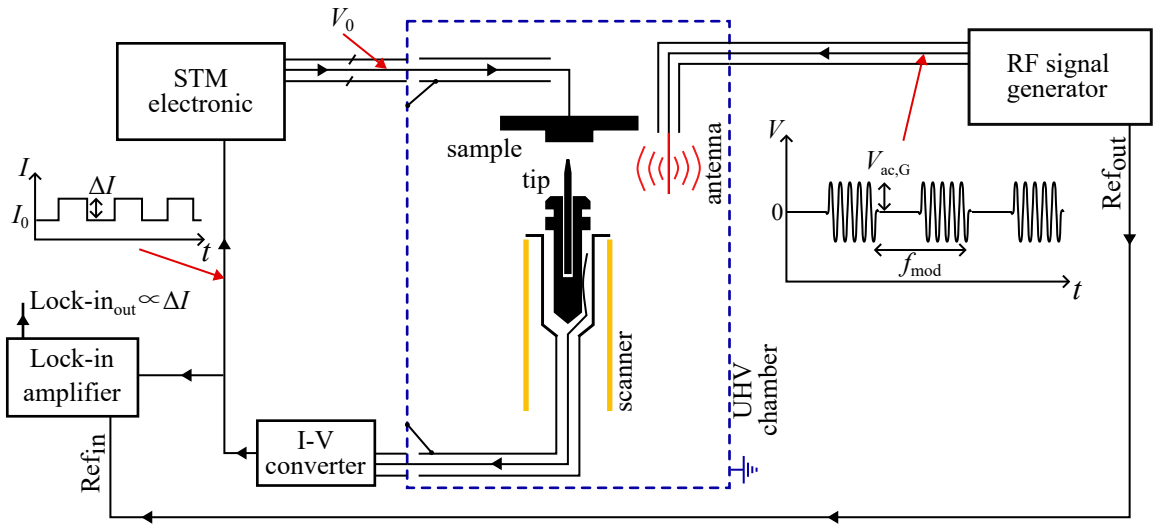


Figure 4.25.: **Simplified schematic of the determination of the transfer function.** A chopping module inside the RF signal generator is switching the radio frequency signal, with amplitude $V_{ac,G}$, on and off. This modulation frequency f_{mod} is inside the bandwidth of the preamplifier (I-V converter). This signal is transferred to the tunneling junction via a shielded radio frequency cabling. During active, but slow STM feedback, with the tunneling voltage V_0, the chopped response ΔI is read out via the lock-in technique.

The rectification of an AC RF voltage in the tunneling junction leads to a DC current depending on the AC voltage in the tunneling junction. Losses or resonances in the wiring or the tunneling junction would change this voltage and, hence, the rectified current. This is used to determine the transfer function by adjusting the signal generator output power to get the same DC current at various frequencies.
In more detail, the rectification functions as follows (adapted from [246]): We assume a $I(V)$ curve that has two different slopes m_1 for $V < V_0$ and m_2 for $V > V_0$ (V_0: set bias

voltage):

$$I(V) = \begin{cases} m_1 V, & \text{if } V \leq V_0, \\ m_1 V_0 + m_2 (V - V_0), & \text{if } V \geq V_0. \end{cases} \tag{4.10}$$

Without an AC voltage, at $V = V_0$, the current I_0 flows. For an RF electric field applied to the tunneling junction by the antenna, the bias voltage can be described by a normalized arcsine distribution ($f \gg$ BW of preamplifier):

$$w(V) = \begin{cases} \frac{1}{\pi V_{\mathrm{ac,J}} \sqrt{1 - \left(\frac{V - V_0}{V_{\mathrm{ac,J}}}\right)^2}}, & \text{if } V \in (V_0 - V_{\mathrm{ac,J}}, V_0 + V_{\mathrm{ac,J}}), \\ 0, & \text{if } V \notin (V_0 - V_{\mathrm{ac,J}}, V_0 + V_{\mathrm{ac,J}}) \end{cases} . \tag{4.11}$$

The tunneling current can be calculated by the convolution with the arcsine distribution:

$$\begin{aligned} I_{\mathrm{f}}(V_0, V_{\mathrm{ac,J}}) &= \int_{V_0 - V_{\mathrm{ac,J}}}^{V_0 + V_{\mathrm{ac,J}}} I(V)\, w(V)\, \mathrm{d}V = m_1 V_0 + \frac{m_2 - m_1}{\pi} V_{\mathrm{ac,J}} \\ &= I_0 + \frac{m_2 - m_1}{\pi} V_{\mathrm{ac,J}}. \end{aligned} \tag{4.12}$$

According to Equation 4.12, the tunneling current $I_{\mathrm{f}}(V_0, V_{\mathrm{ac,J}})$, with activated RF, is the current I_0, with deactivated RF, plus an offset, which depends on the RF amplitude $V_{\mathrm{ac,J}}$. The offset is linear in $V_{\mathrm{ac,J}}$ for the piecewise linear case. In the experiment, the RF signal is modulated at the lock-in modulation frequency, such that the lock-in output is proportional to the current change. For a constant RF frequency, the RF amplitude is varied until a desired set point is reached.

The procedure starts by selecting a reference frequency where the complete $I(V)$ curve is measured with and without RF. An automated Matlab script to adapt the power output from the RF signal generator is employed. It adjusts the output to match the reference lock-in signal for every frequency. As a result, a signal attenuation curve is recorded (Figure 4.26). The relative measurement is calibrated to its absolute value at 39.01 GHz, showing -27.7 dB (Figure 4.24 (b)). For the used signal generator, this attenuation e.g. allows a maximum amplitude in the tunneling junction of $V_{\mathrm{ac,J}}$=390 $\mathrm{mV_p}$ at 10 GHz, and 63 $\mathrm{mV_p}$ at 40 GHz. In comparison to an RF wiring that is directly addressing the tip or sample, an antenna transfers no radiation for small frequencies to the tunneling junction.

Therefore, the assumption of no attenuation (0 dB) at low frequencies used in that case does not hold.

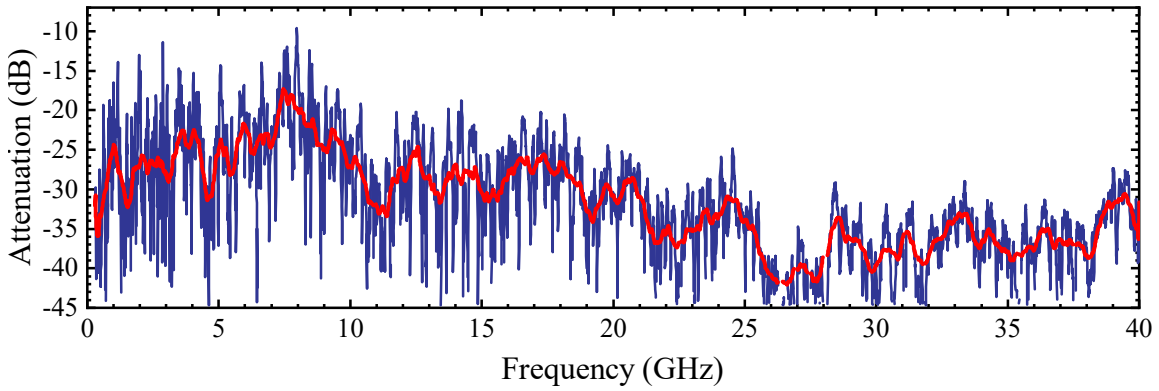


Figure 4.26.: **Transfer function of the STM radio frequency antenna for** $0.3-40\,\mathrm{GHz}$**.** Transfer function (blue) from RF generator to the tunneling junction determined by the RF chopping scheme Figure 4.25. The relative measurement was adapted by the calibration at 39.01 GHz showing $-27.7\,\mathrm{dB}$ (Figure 4.24 (b)). The red curve is the moving average of 50 points. Au(111), $\Delta f = 10\,\mathrm{MHz}$, $V_{\mathrm{stab}} = -483\,\mathrm{mV}$, $I_{\mathrm{stab}} = -1\,\mathrm{nA}$, $T = 1.49\,\mathrm{K}$, $f_{\mathrm{ref}} = 6.2\,\mathrm{GHz}$, $f_{\mathrm{mod}} = 2423\,\mathrm{Hz}$, $V_{\mathrm{ac,G}} = 150\,\mathrm{mV_{rms}}$, CBL-12FT-SMSM+ cable. The lower limit of the displayed attenuation is caused by the limited power ($1\,\mathrm{V_p}$) of the frequency generator, i.e. points at $-45\,\mathrm{dB}$ might be even lower.

Prior to the calibration, typically a frequency sweep is conducted and the lock-in signal is recorded (Figure 4.27 (b)). This helps to select the frequency of the reference signal. Additionally, the data in Figure 4.26 can be used to compensate for the transfer function of the setup delivering constant $V_{\mathrm{ac,J}}(f)$ to the tunneling junction. This is used, e.g. in electron spin resonance STM experiments [262]. Finally, we show the reproducibility of the transfer curves on two different samples (Figure 4.27). The transfer curve of Pb has not been calibrated. Hence, we use the lock-in signal at 6.2 GHz for $V_{\mathrm{ac,G}} = 30\,\mathrm{mV_{rms}}$ and adapt $V_{\mathrm{ac,G}}(f)$ such that the lock-in output remains the same. The resulting two curves are similar, but also show discrepancies, e.g. at the dips around $-15\,\mathrm{dB}$. Such changes have been observed previously also at subsequent measurements on Co atoms on MgO/Ag(001) (6 dB variations) [246]. This has been attributed to the $\mathrm{L^4He}$ level, RF line disturbances, or external magnetic field ramping [187, 246, 251]. Figure 4.27 (b) shows the lock-in signal of the measurement on the Au(111) surface state with constant $V_{\mathrm{ac,G}}(f)$. Applying the previous calibration from the red transfer curve in Figure 4.27 (a)

to automatically adjust $V_{\mathrm{ac,G}}(f)$, the lock-in output gets significantly smoothed with variations of $\pm 30\,\%$ only, except of a peak at 2.9 GHz (Figure 4.27 (c)). The calibration curve in Figure 4.27 (a) has been measured six days prior to the measurement of Figure 4.27 (c).

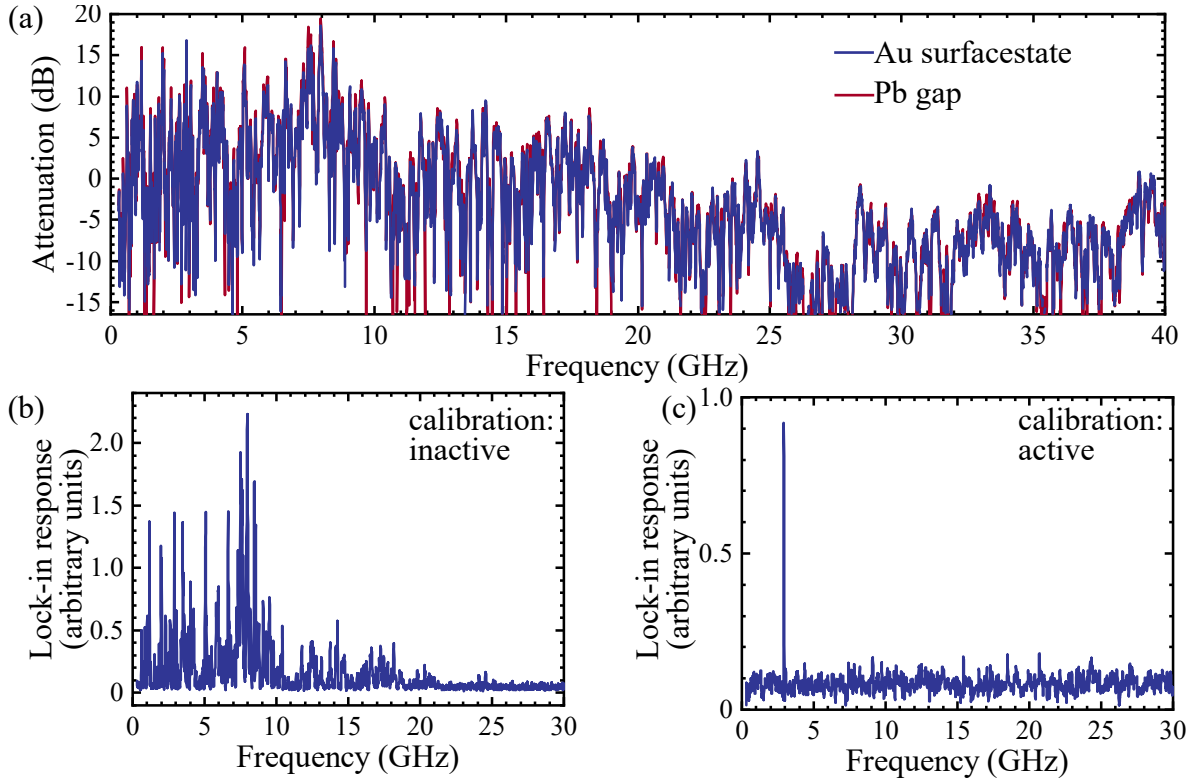


Figure 4.27.: **Transfer function of the STM radio frequency antenna and lock-in signal.** (a) Relative transfer function from the RF generator to the tunneling junction determined by the RF chopping scheme using the lock-in signal obtained at $V_{\mathrm{ac,G}} = 30\,\mathrm{mV_{rms}}$ and $f_{\mathrm{ref}} = 6.2\,\mathrm{GHz}$ for adaption of $V_{\mathrm{ac,G}}(f)$. Blue curve is determined at the Au(111) surface state ($V_{\mathrm{stab}} = -483\,\mathrm{mV}$), other parameters as in Figure 4.26. The red curve is determined six days earlier at the superconducting gap of Pb, $V_{\mathrm{stab}} = -1.3\,\mathrm{mV}$, $I_{\mathrm{stab}} = 400\,\mathrm{pA}$, $T = 1.49\,\mathrm{K}$, $f_{\mathrm{ref}} = 6.2\,\mathrm{GHz}$, $\Delta f = 10\,\mathrm{MHz}$, $f_{\mathrm{mod}} = 2423\,\mathrm{Hz}$, $V_{\mathrm{ac,G}} = 30\,\mathrm{mV_{rms}}$, CBL-12FT-SMSM+ cable. The average difference between the two curves is 0.9 dB only. (b) Typical lock-in response using the method of Figure 4.25 with constant $V_{\mathrm{ac,G}}(f)$. The average of five curves is shown. (c) Lock-in response using the adoption of $V_{\mathrm{ac,G}}(f)$ via the previously determined transfer curve (red curve in (a)). The average of two curves is shown. Now the response is nearly constant.

5. Summary and outlook

This study presents a compact UHV STM system primarily cooled by a two-stage pulse tube cryocooler, with an additional JT stage. The JT stage reaches a temperature below 1.3 K for cooling the STM below 1.5 K. The origin of the different temperatures measured by Cernox® sensors at the STM and the JT stage is not known.

The system achieves reliable atomic-scale stability with a z-noise Δz ($<1\,\mathrm{pm_{RMS}}$) in a bandwidth of 5 kHz through a combination of soft mechanical coupling and optimized thermal connections. Vibrations from the PTC are mitigated using flexible stainless steel membrane bellows combined with a minimal stiffness spring mechanism, and a suspended STM made from ceramic and optimized in shape for high resonance frequencies (>4 kHz). Performance tests demonstrate atomic resolution and standing electron waves on Au(111) surfaces. An electronic temperature of 1.7 K, low voltage noise as indicated by 120 µV FWHM of the Josephson peak, and minimal lateral drift (18 pm/h) is achieved. An integrated antenna enables RF coupling up to 40 GHz, as demonstrated by microwave-assisted Cooper-pair tunneling. The voltage noise could be further optimized. The grounding concept and shielding of e.g. the tunneling current preamplifier could be reconsidered. At present, we can rule out Johnson-Nyquist noise as a source, since it is calculated to be only ∼5 µV. Moreover, the preamplifier model can be ruled out, as another system showed 40 µV [35].

The design of the UHV PTC operated STM system includes the space and mounting holes for an installation of a superconducting split coil magnet up to 3 T, and its current leads. In addition, the concept of the closed-cycle UHV STM system described in this thesis has the potential for lower temperatures through the utilization of ^{3}He. In principle, other downstream cooling units can be mounted instead of the JT stage, such as dilution cryostats. The only significant difference is the larger diameter of the pumping bellow for ^{3}He, which may require an additional decoupling mechanism via the concept of minimal stiffness. This would ensure uninterrupted operation of STM systems across the

entire temperature range used so far for STM measurements, employing helium-loss-free cryostats.

Bibliography

(1) Eßer, M.; Pratzer, M.; Frömming, M.; Duffhauß, J.; Bhaskar, P.; Krzyzowski, M. A.; Morgenstern, M. "An ultra-high vacuum scanning tunneling microscope with pulse tube and Joule–Thomson cooling operating at sub-pm z-noise". *Rev. Sci. Instrum.* **2024**, *95*, 123703 (cit. on pp. 4, 6, 16).

(2) Binnig, G.; Rohrer, H.; Gerber, C.; Weibel, E. "Surface Studies by Scanning Tunneling Microscopy". *Phys. Rev. Lett.* **1982**, *49*, 57–61 (cit. on pp. 11, 17).

(3) Hla, S.-W.; Bartels, L.; Meyer, G.; Rieder, K.-H. "Inducing All Steps of a Chemical Reaction with the Scanning Tunneling Microscope Tip: Towards Single Molecule Engineering". *Phys. Rev. Lett.* **2000**, *85*, 2777 (cit. on p. 11).

(4) Repp, J.; Meyer, G.; Paavilainen, S.; Olsson, F. E.; Persson, M. "Imaging Bond Formation Between a Gold Atom and Pentacene on an Insulating Surface". *Science* **2006**, *312*, 1196–1199 (cit. on p. 11).

(5) Stipe, B. C.; Rezaei, M. A.; Ho, W. "Single-Molecule Vibrational Spectroscopy and Microscopy". *Science* **1998**, *280*, 1732–1735 (cit. on p. 11).

(6) Guckenberger, R.; Hartmann, T.; Wiegräbe, W.; Baumeister, W. In "Scanning Tunneling Microscopy II: Further Applications and Related Scanning Techniques", Wiesendanger, R., Güntherodt, H.-J., Eds.; Springer Berlin Heidelberg: Berlin, Heidelberg, 1992, pp 51–98 (cit. on p. 11).

(7) Eigler, D. M.; Schweizer, E. K. "Positioning single atoms with a scanning tunnelling microscope". *Nature* **1990**, *344*, 524–526 (cit. on p. 11).

(8) Roushan, P.; Seo, J.; Parker, C. V.; Hor, Y. S.; Hsieh, D.; Qian, D.; Richardella, A.; Hasan, M. Z.; Cava, R. J.; Yazdani, A. "Topological surface states protected from backscattering by chiral spin texture". *Nature* **2009**, *460*, 1106–1109 (cit. on p. 11).

(9) Crommie, M. F.; Lutz, C. P.; Eigler, D. M. "Confinement of electrons to quantum corrals on a metal surface". *Science* **1993**, *262*, 218–220 (cit. on p. 11).

(10) Yazdani, A.; Jones, B. A.; Lutz, C. P.; Crommie, M. F.; Eigler, D. M. "Probing the local effects of magnetic impurities on superconductivity". *Science* **1997**, *275*, 1767–1770 (cit. on p. 11).

(11) Fischer, O.; Kugler, M.; Maggio-Aprile, I.; Berthod, C.; Renner, C. "Scanning tunneling spectroscopy of high-temperature superconductors". *Rev. Mod. Phys.* **2007**, *79*, 353 (cit. on p. 11).

(12) Hanaguri, T.; Niitaka, S.; Kuroki, K.; Takagi, H. "Unconventional s-wave superconductivity in Fe(Se, Te)". *Science* **2010**, *328*, 474–476 (cit. on p. 11).

(13) Manassen, Y.; Hamers, R. J.; Demuth, J. E.; Castellano Jr., A. J. "Direct observation of the precession of individual paramagnetic spins on oxidized silicon surfaces". *Phys. Rev. Lett.* **1989**, *62*, 2531–2534 (cit. on p. 11).

(14) Liu, X.; Farahi, G.; Chiu, C.-L.; Papic, Z.; Watanabe, K.; Taniguchi, T.; Zaletel, M. P.; Yazdani, A. "Visualizing broken symmetry and topological defects in a quantum Hall ferromagnet". *Science* **2022**, *375*, 321–326 (cit. on p. 11).

(15) Hashimoto, K.; Sohrmann, C.; Wiebe, J.; Inaoka, T.; Meier, F.; Hirayama, Y.; Römer, R. A.; Wiesendanger, R.; Morgenstern, M. "Quantum Hall transition in real space: from localized to extended states". *Phys. Rev. Lett.* **2008**, *101*, 256802 (cit. on p. 11).

(16) Coissard, A.; Wander, D.; Vignaud, H.; Grushin, A. G.; Repellin, C.; Watanabe, K.; Taniguchi, T.; Gay, F.; Winkelmann, C. B.; Courtois, H.; Sellier, H.; Sacépé, B. "Imaging tunable quantum Hall broken-symmetry orders in graphene". *Nature* **2022**, *605*, 51–56 (cit. on p. 11).

(17) Meier, F.; Zhou, L.; Wiebe, J.; Wiesendanger, R. "Revealing Magnetic Interactions from Single-Atom Magnetization Curves". *Science* **2008**, *320*, DOI: 10.1126/science.1154415 (cit. on p. 11).

(18) Heinrich, A. J.; Gupta, J. A.; Lutz, C. P.; Eigler, D. M. "Single-Atom Spin-Flip Spectroscopy". *Science* **2004**, *306*, 466–469 (cit. on p. 11).

(19) Madhavan, V.; Chen, W.; Jamneala, T.; Crommie, M. F.; Wingreen, N. S. "Tunneling into a single magnetic atom: spectroscopic evidence of the Kondo resonance". *Science* **1998**, *280*, 567–569 (cit. on p. 11).

(20) Li, J.; Schneider, W.-D.; Berndt, R.; Delley, B. "Kondo scattering observed at a single magnetic impurity". *Phys. Rev. Lett.* **1998**, *80*, 2893 (cit. on p. 11).

(21) Wahl, P.; Simon, P.; Diekhöner, L.; Stepanyuk, V. S.; Bruno, P.; Schneider, M. A.; Kern, K. "Exchange interaction between single magnetic adatoms". *Phys. Rev. Lett.* **2007**, *98*, 056601 (cit. on p. 11).

(22) Smith, D. P. E.; Binnig, G.; Quate, C. F. "Detection of phonons with a scanning tunneling microscope". *Appl. Phys. Lett.* **1986**, *49*, 1641–1643 (cit. on p. 11).

(23) Gawronski, H.; Mehlhorn, M.; Morgenstern, K. "Imaging Phonon Excitation with Atomic Resolution". *Science* **2008**, *319*, 930–933 (cit. on p. 11).

(24) Vitali, L.; Schneider, M. A.; Kern, K.; Wirtz, L.; Rubio, A. "Phonon and plasmon excitation in inelastic electron tunneling spectroscopy of graphite". *Phys. Rev. B* **2004**, *69*, 121414 (cit. on p. 11).

(25) Reihl, B.; Coombs, J.; Gimzewski, J. "Local inverse photoemission with the scanning tunneling microscope". *Surf. Sci.* **1989**, *211–212*, 156–164 (cit. on p. 11).

(26) Nadj-Perge, S.; Drozdov, I. K.; Li, J.; Chen, H.; Jeon, S.; Seo, J.; MacDonald, A. H.; Bernevig, B. A.; Yazdani, A. "Observation of Majorana fermions in ferromagnetic atomic chains on a superconductor". *Science* **2014**, *346*, 602–607 (cit. on p. 11).

(27) Blumenstein, C.; Schäfer, J.; Mietke, S.; Meyer, S.; Dollinger, A.; Lochner, M.; Cui, X. Y.; Patthey, L.; Matzdorf, R.; Claessen, R. "Atomically controlled quantum chains hosting a Tomonaga–Luttinger liquid". *Nat. Phys.* **2011**, *7*, 776–780 (cit. on p. 11).

(28) Jolie, W.; Murray, C.; Weiß, P. S.; Hall, J.; Portner, F.; Atodiresei, N.; Krasheninnikov, A. V.; Busse, C.; Komsa, H.-P.; Rosch, A.; Michely, T. "Tomonaga-Luttinger liquid in a box: electrons confined within MoS_2 mirror-twin boundaries". *Phys. Rev. X* **2019**, *9*, 011055 (cit. on p. 11).

(29) Jia, J.; Marcellina, E.; Das, A.; Lodge, M. S.; Wang, B.; Ho, D.-Q.; Biswas, R.; Pham, T. A.; Tao, W.; Huang, C.-Y.; Lin, H.; Bansil, A.; Mukherjee, S.; Weber, B. "Tuning the many-body interactions in a helical Luttinger liquid". *Nat. Commun.* **2022**, *13*, 6046 (cit. on p. 11).

(30) Veldman, L. M.; Stolte, E. W.; Canavan, M. P.; Broekhoven, R.; Willke, P.; Farinacci, L.; Otte, S. "Coherent spin dynamics between electron and nucleus within a single atom". *Nat. Commun.* **2024**, *15*, 7951 (cit. on p. 11).

(31) Elrod, S. A.; de Lozanne, A. L.; Quate, C. F. "Low-temperature vacuum tunneling microscopy". *Appl. Phys. Lett.* **1984**, *45*, 1240–1242 (cit. on p. 11).

(32) Morgenstern, M.; Schwarz, A.; Schwarz, U. D. In "Springer Handbook of Nanotechnology", Bhushan, B., Ed.; Springer Berlin Heidelberg: Berlin, Heidelberg, 2004, pp 413–447 (cit. on p. 11).

(33) Ast, C. R.; Jäck, B.; Senkpiel, J.; Eltschka, M.; Etzkorn, M.; Ankerhold, J.; Kern, K. "Sensing the quantum limit in scanning tunnelling spectroscopy". *Nat. Commun.* **2016**, *7*, 13009 (cit. on p. 11).

(34) Tersoff, J.; Hamann, D. R. "Theory of the scanning tunneling microscope". *Phys. Rev. B* **1985**, *31*, 805–813 (cit. on p. 11).

(35) Liebmann, M.; Bindel, J. R.; Pezzotta, M.; Becker, S.; Muckel, F.; Johnsen, T.; Saunus, C.; Ast, C. R.; Morgenstern, M. "An ultrahigh-vacuum cryostat for simultaneous scanning tunneling microscopy and magneto-transport measurements down to 400 mK". *Rev. Sci. Instrum.* **2017**, *88*, 123707 (cit. on pp. 11, 132, 135, 153).

(36) Halperin, W. P. "The impact of helium shortages on basic research". *Nat. Phys.* **2014**, *10*, 467–470 (cit. on p. 12).

(37) Seidler, C. *Forscher warnen vor weltweiter Heliumkrise*, Accessed: 2023-10-09, 2019 (cit. on p. 12).

(38) Appel, D. "Weltweite Heliumknappheit". *Spectrum* **2022**, *166*, 1–2 (cit. on p. 12).

(39) Böck, A. *Geht der Welt das Helium aus?*, Accessed: 2023-10-09, 2022 (cit. on p. 12).

(40) Rosen, J. "Impending U.S. helium sale worries researchers". *Science* **2023**, *382*, 624–625 (cit. on p. 12).

(41) US Geological Survey, "Mineral Commodity Summaries 2001"; U.S. Geological Survey, Reston, VA: 2001 (cit. on p. 12).

(42) US Geological Survey, "Mineral Commodity Summaries 2023"; U.S. Geological Survey, Reston, VA: 2023 (cit. on p. 12).

(43) Garvey, M. D., "The 2023 worldwide helium market"; gasworld: 2023 (cit. on p. 12).

(44) Provornaya, I.; Filimonova, I.; Eder, L.; Nemov, V.; Zemnukhova, E. "Prospects for the global helium industry development". *Energy Reports* **2022**, *8*, The 8th International Conference on Energy and Environment Research –"Developing the World in 2021 with Clean and Safe Energy", 110–115 (cit. on p. 12).

(45) Committee on the Impact of Selling the Federal Helium Reserve, "The Impact of Selling the Federal Helium Reserve"; The National Academies Press: Washington, DC, 2000 (cit. on p. 12).

(46) Hoffman, D.; Singh, B.; Thomas III, J. H., "Handbook of vacuum science and technology"; Elsevier: 1997 (cit. on pp. 12, 20).

(47) Hirayama, T.; Morie, T.; Xu, M. "Experimental investigation of cooling capacity of 4K pulse tube cryocooler in magnetic fields". *IOP Conf. Ser-Mar. Sci.* **2019**, *502*, 012035 (cit. on p. 12).

(48) Olivieri, E.; Billard, J.; De Jesus, M.; Juillard, A.; Leder, A. "Vibrations on pulse tube based Dry Dilution Refrigerators for low noise measurements". *Nuclear Instruments and Methods in Physics Research Section A: Accelerators, Spectrometers, Detectors and Associated Equipment* **2017**, *858*, 73–79 (cit. on p. 12).

(49) Wang, C.; Gifford, P. In "Cryocoolers 12", Ross, R. G., Ed.; Springer US: Boston, MA, 2003, pp 293–300 (cit. on p. 12).

(50) Tomaru, T.; Suzuki, T.; Haruyama, T.; Shintomi, T.; Yamamoto, A.; Koyama, T.; Li, R. "Vibration analysis of cryocoolers". *Cryogenics* **2004**, *44*, 309–317 (cit. on p. 12).

(51) Chijioke, A.; Lawall, J. "Vibration spectrum of a pulse-tube cryostat from 1Hz to 20kHz". *Cryogenics* **2010**, *50*, 266–270 (cit. on p. 12).

(52) Nakano, K.; Xu, M.; Takayama, H.; Tsuchiya, A.; Saito, M. "Development of high efficiency 4 K two-stage pulse tube cryocoolers with split valve unit". *AIP Conf. Proc.* **2012**, *1434*, 532–539 (cit. on pp. 12, 28).

(53) Schmidt, J.-A.; Schmidt, B.; Spagna, S.; Dietzel, D.; Falter, J.; Thummes, G.; Schirmeisen, A. "Low input power 4 K pulse tube cryocooler driven by an inverter helium compressor: Intrinsic temperature oscillations and mechanical vibrations". *Cryogenics* **2020**, *108*, 103085 (cit. on pp. 12, 28).

(54) Xu, M.; Nakano, K.; Saito, M.; Takayama, H.; Tsuchiya, A.; Maruyama, H. "Study of low vibration 4 K pulse tube cryocoolers". *AIP Conf. Proc.* **2012**, *1434*, 190–197 (cit. on p. 12).

(55) Suzuki, T.; Tomaru, T.; Haruyama, T.; Shintomi, T.; Sato, N.; Yamamoto, A.; Ikushima, Y.; Li, R. "Ultra-low Vibration Pulse Tube Cryocooler with a New Vibration Cancellation Method". *AIP Conf. Proc.* **2006**, *823*, 1325–1331 (cit. on p. 12).

(56) Allweins, K.; Qiu, L. M.; Thummes, G. "DAMPING OF INTRINSIC TEMPERATURE OSCILLATIONS IN A 4 K PULSE TUBE COOLER BY MEANS OF RARE EARTH PLATES". *AIP Conf. Proc.* **2008**, *985*, 109–116 (cit. on p. 13).

(57) Ikushima, Y.; Li, R.; Tomaru, T.; Sato, N.; Suzuki, T.; Haruyama, T.; Shintomi, T.; Yamamoto, A. "Ultra-low-vibration pulse-tube cryocooler system – cooling capacity and vibration". *Cryogenics* **2008**, *48*, 406–412 (cit. on p. 13).

(58) Snodgrass, R.; Kotsubo, V.; Backhaus, S.; Ullom, J. "Dynamic acoustic optimization of pulse tube refrigerators for rapid cooldown". *Nat. Commun.* **2024**, *15*, 3386 (cit. on p. 13).

(59) Den Haan, A. M. J.; Wijts, G. H. C. J.; Galli, F.; Usenko, O.; van Baarle, G. J. C.; van der Zalm, D. J.; Oosterkamp, T. H. "Atomic resolution scanning tunneling microscopy in a cryogen free dilution refrigerator at 15 mK". *Rev. Sci. Instrum.* **2014**, *85*, 035112 (cit. on p. 13).

(60) Hackley, J. D.; Kislitsyn, D. A.; Beaman, D. K.; Ulrich, S.; Nazin, G. V. "High-stability cryogenic scanning tunneling microscope based on a closed-cycle cryostat". *Rev. Sci. Instrum.* **2014**, *85*, 103704 (cit. on pp. 13, 16).

(61) Geng, T.; Wang, J.; Meng, W.; Zhang, J.; Feng, Q.; Hou, Y.; Lu, Q. "A novel atomically resolved scanning tunneling microscope capable of working in cryogen-free superconducting magnet". *Micromachines* **2023**, *14*, 637 (cit. on p. 13).

(62) Chaudhary, S.; Panda, J. J.; Mundlia, S.; Mathimalar, S.; Ahmedof, A.; Raman, K. V. "A low noise cryogen-free scanning tunneling microscope–superconducting magnet system with vacuum sample transfer". *Rev. Sci. Instrum.* **2021**, *92*, 023906 (cit. on pp. 13, 16).

(63) Kasai, J.; Koyama, T.; Yokota, M.; Iwaya, K. "Development of a near-5-Kelvin, cryogen-free, pulse-tube refrigerator-based scanning probe microscope". *Rev. Sci. Instrum.* **2022**, *93*, 043711 (cit. on pp. 13, 16).

(64) Ma, R.; Li, H.; Shi, C.; Wang, F.; Lei, L.; Huang, Y.; Liu, Y.; Shan, H.; Liu, L.; Huang, S.; Niu, Z.-C.; Huan, Q.; Gao, H.-J. "Development of a cryogen-free sub-3 K low-temperature scanning probe microscope by remote liquefaction scheme". *Rev. Sci. Instrum.* **2023**, *94*, 093701 (cit. on pp. 13, 16).

(65) Huang, H.; Shuai, M.; Yang, Y.; Song, R.; Liao, Y.; Yin, L.; Shen, J. "Cryogen free spin polarized scanning tunneling microscopy and magnetic exchange force microscopy with extremely low noise". *Rev. Sci. Instrum.* **2022**, *93*, 073703 (cit. on pp. 13, 16).

(66) Zhang, L.; Miyamachi, T.; Tomanić, T.; Dehm, R.; Wulfhekel, W. "A compact sub-Kelvin ultrahigh vacuum scanning tunneling microscope with high energy resolution and high stability". *Rev. Sci. Instrum.* **2011**, *82*, 103702 (cit. on p. 13).

(67) Coe, A. M.; Li, G.; Andrei, E. Y. "Cryogen-free modular scanning tunneling microscope operating at 4-K in high magnetic field on a compact ultra-high vacuum platform". *Rev. Sci. Instrum.* **2024**, *95*, 083702 (cit. on p. 16).

(68) Zhang, S.; Huang, D.; Wu, S. "A cryogen-free low temperature scanning tunneling microscope capable of inelastic electron tunneling spectroscopy". *Rev. Sci. Instrum.* **2016**, *87*, 063701 (cit. on p. 16).

(69) Wiesendanger, R., "Scanning Probe Microscopy and Spectroscopy: Methods and Applications"; Cambridge University Press: Cambridge, 1994 (cit. on p. 17).

(70) Voigtländer, B., "Scanning Probe Microscopy: Atomic Force Microscopy and Scanning Tunneling Microscopy"; Springer Berlin Heidelberg: 2015 (cit. on pp. 17, 45, 84).

(71) Chen, C. J., "Introduction to scanning tunneling microscopy third edition", 3rd ed.; Monographs on the Physics and Chemistry of Materials; Oxford University Press: London, England, 2021 (cit. on pp. 17, 46, 63).

(72) Binnig, G.; Rohrer, H.; Gerber, C.; Weibel, E. "Tunneling through a controllable vacuum gap". *Appl. Phys. Lett.* **1982**, *40*, 178–180 (cit. on p. 17).

(73) Giaever, I. "Energy Gap in Superconductors Measured by Electron Tunneling". *Phys. Rev. Lett.* **1960**, *5*, 147–148 (cit. on p. 17).

(74) Fisher, J. C.; Giaever, I. "Tunneling Through Thin Insulating Layers". *J. Appl. Phys.* **1961**, *32*, 172–177 (cit. on p. 17).

(75) Michaelson, H. B. "The work function of the elements and its periodicity". *J. Appl. Phys.* **1977**, *48*, 4729–4733 (cit. on p. 18).

(76) Bergmann, L.; Schaefer, C., "Lehrbuch der Experimentalphysik Band 6 Festkörper"; De Gruyter: Berlin, 2005 (cit. on p. 18).

(77) Bardeen, J. "Tunnelling from a Many-Particle Point of View". *Phys. Rev. Lett.* **1961**, *6*, 57–59 (cit. on p. 19).

(78) Chen, C. J. "Origin of atomic resolution on metal surfaces in scanning tunneling microscopy". *Phys. Rev. Lett.* **1990**, *65*, 448–451 (cit. on p. 20).

(79) Gross, L.; Moll, N.; Mohn, F.; Curioni, A.; Meyer, G.; Hanke, F.; Persson, M. "High-Resolution Molecular Orbital Imaging Using a *p*-Wave STM Tip". *Phys. Rev. Lett.* **2011**, *107*, 086101 (cit. on p. 20).

(80) Morgenstern, M. "Probing the local density of states of dilute electron systems in different dimensions". *Surf. Rev. Lett.* **2003**, *10*, 933–962 (cit. on pp. 23, 132).

(81) Ternes, M. *Scanning tunneling spectroscopy at the single atom scale*, Ph.D. Thesis, ÉCOLE POLYTECHNIQUE FÉDÉRALE DE LAUSANNE, 2006 (cit. on p. 24).

(82) Cao, H. "Refrigeration Below 1 Kelvin". *J. Low. Temp. Phys.* **2021**, *204*, 175–205 (cit. on p. 24).

(83) Gifford, W. E.; Longsworth, R. C. "Pulse-Tube Refrigeration". *J. Eng. Ind.* **1964**, *86*, 264–268 (cit. on p. 25).

(84) Mikulin, E. I.; Tarasov, A. A.; Shkrebyonock, M. P. In "Advances in Cryogenic Engineering: Volume 29", Fast, R. W., Ed.; Springer US: Boston, MA, 1984, pp 629–637 (cit. on p. 25).

(85) Radebaugh, R.; Zimmerman, J.; Smith, D. R.; Louie, B. In "Advances in Cryogenic Engineering: Volume 31", Fast, R. W., Ed.; Springer US: Boston, MA, 1986, pp 779–789 (cit. on pp. 25, 27).

(86) Shaowei, Z.; Peiyi, W.; Zhongqi, C. "Double inlet pulse tube refrigerators: an important improvement". *Cryogenics* **1990**, *30*, 514–520 (cit. on pp. 25, 30).

(87) Gan, Z.; Dong, W.; Qiu, L.; Zhang, X.; Sun, H.; He, Y.; Radebaugh, R. "A single-stage GM-type pulse tube cryocooler operating at 10.6K". *Cryogenics* **2009**, *49*, 198–201 (cit. on p. 25).

(88) Matsubara, Y.; Gao, J. "Novel configuration of three-stage pulse tube refrigerator for temperatures below 4 K". *Cryogenics* **1994**, *34*, 259–262 (cit. on p. 25).

(89) Gao, J.; Matsubara, Y. "Experimental investigation of 4 K pulse tube refrigerator". *Cryogenics* **1994**, *34*, 25–30 (cit. on p. 25).

(90) Chen, G.; Qiu, L.; Zheng, J.; Yan, P.; Gan, Z.; Bai, X.; Huang, Z. "Experimental study on a double-orifice two-stage pulse tube refrigerator". *Cryogenics* **1997**, *37*, 271–273 (cit. on p. 25).

(91) Jiang, N.; Lindemann, U.; Giebeler, F.; Thummes, G. "A 3He pulse tube cooler operating down to 1.3 K". *Cryogenics* **2004**, *44*, 809–816 (cit. on p. 25).

(92) Thummes, G.; Wang, C.; Heiden, C. "Small scale 4He liquefaction using a two-stage 4K pulse tube cooler1Dedicated to J.E. Zimmerman on the occasion of his 75th birthday1". *Cryogenics* **1998**, *38*, 337–342 (cit. on p. 25).

(93) Wang, C. "Helium liquefaction with a 4 K pulse tube cryocooler". *Cryogenics* **2001**, *41*, 491–496 (cit. on p. 25).

(94) Wang, C. "Efficient helium recondensing using a 4K pulse tube cryocooler". *Cryogenics* **2005**, *45*, 719–724 (cit. on p. 25).

(95) Wang, C.; Scurlock, R. "Improvement in performance of cryocoolers as condensers". *Cryogenics* **2008**, *48*, 169–171 (cit. on p. 25).

(96) Risacher, C. et al. In "2014 39th International Conference on Infrared, Millimeter, and Terahertz waves (IRMMW-THz)", 2014, pp 1–2 (cit. on p. 25).

(97) Thompson, P. S.; Ackermann, R. A.; Hedeen, R. A. "A two-stage pulse tube cryo-cooled MRI magnet". *AIP Conf. Proc.* **2002**, *613*, 649–653 (cit. on p. 25).

(98) Duband, L. "Space Cryocooler Developments". *Physics Procedia* **2015**, *67*, Proceedings of the 25th International Cryogenic Engineering Conference and International Cryogenic Materials Conference 2014, 1–10 (cit. on p. 25).

(99) Richards, L. W.; Meyer, M. L.; Feller, J. R.; Rhodes, A. C.; Rosner, S.; Stevanovic, D.; Kashani, A. *Cryogenic Technologies for the Stratospheric Observatory for Infrared Astronomy (SOFIA) Science Instruments*, 2020 (cit. on p. 25).

(100) Stautner, W. In "Cryocoolers: Theory and Applications", Atrey, M. D., Ed.; Springer International Publishing: Cham, 2020, pp 191–204 (cit. on p. 25).

(101) Knipper, R.; Brahm, A.; Heinz, E.; May, T.; Notni, G.; Meyer, H.-G.; Tünnermann, A.; Popp, J. "THz Absorption in Fabric and Its Impact on Body Scanning for Security Application". *IEEE T. THz. Sci. Techn.* **2015**, *5*, 999–1004 (cit. on p. 25).

(102) Durand, D.; Raab, J.; Colbert, R.; Michaelian, M.; Nguyen, T.; Petach, M.; Tward, E. "NGST Advanced Cryocooler Technology Development Program (ACTDP) Cooler System". *AIP Conf. Proc.* **2006**, *823*, 615–622 (cit. on p. 25).

(103) Banks, K.; Larson, M.; Aymergen, C.; Zhang, B. In "Modeling, Systems Engineering, and Project Management for Astronomy III", ed. by Angeli, G. Z.; Cullum, M. J., SPIE: 2008; Vol. 7017, 70170A (cit. on p. 25).

(104) Radebaugh, R. "Cryocoolers: the state of the art and recent developments". *J. Phys. Condens. Matter* **2009**, *21*, 164219 (cit. on pp. 25, 26).

(105) Steijaert, P. *Thermodynamical aspects of pulse-tube refrigerators*, English, Phd Thesis 1 (Research TU/e / Graduation TU/e), Applied Physics and Science Education, 1999 (cit. on p. 26).

(106) Radebaugh, R. "Pulse Tube Refrigeration–A New Type of Cryocooler". *Jpn. J. Appl. Phys.* **1987**, *26*, 2076 (cit. on pp. 26, 27, 33).

(107) Kittel, P.; Kashani, A.; Lee, J.; Roach, P. "General pulse tube theory". *Cryogenics* **1996**, *36*, 1995 Space Cryogenics Workshop, 849–857 (cit. on pp. 27, 31).

(108) Gifford, W. E.; Longsworth, R. C. In "Advances in Cryogenic Engineering", ed. by Timmerhaus, K. D., Springer US: 1966, pp 171–179 (cit. on p. 27).

(109) Yang, L. W. In "Cryocoolers 11", Ross, R. G., Ed.; Springer US: Boston, MA, 2002, pp 353–362 (cit. on pp. 27, 28).

(110) Parikh, K.; Sapariya, D.; Mehta, K. "A Review of Pulse Tube Refrigerator". *International Journal of Engeneering Research & Technology (IJERT) NCIMACEMT* **2016**, *4* (cit. on pp. 27, 28).

(111) Storch, P. J.; Radebaugh, R.; Zimmerman, J. E. "Analytical model for the refrigeration power of the orifice pulse tube refrigerator". *NIST, Tech Note 1343* **1990** (cit. on pp. 27, 31).

(112) Hofmann, A.; Pan, H. "Phase shifting in pulse tube refrigerators". *Cryogenics* **1999**, *39*, 529–537 (cit. on pp. 27, 31).

(113) Mohanta, L.; Atrey, M. In "Cryocoolers 16", 2011, pp 299–308 (cit. on pp. 27, 31, 33).

(114) Wang, C.; Wu, P.; Chen, Z. "Numerical modelling of an orifice pulse tube refrigerator". *Cryogenics* **1992**, *32*, 785–790 (cit. on p. 27).

(115) Wang, C.; Wu, P.; Chen, Z. "Numerical analysis of double-inlet pulse tube refrigerator". *Cryogenics* **1993**, *33*, 526–530 (cit. on p. 27).

(116) Banjare, Y.; Sahoo, R.; Sarangi, S. "CFD simulation and experimental validation of a GM type double inlet pulse tube refrigerator". *Cryogenics* **2010**, *50*, 271–280 (cit. on pp. 27, 35).

(117) Gujarati, P. B.; Desai, K. P.; Naik, H. B.; Atrey, M. D. "Transient analysis of single stage GM type double inlet pulse tube cryocooler". *IOP Conf. Ser-Mar. Sci.* **2015**, *101*, 012033 (cit. on p. 27).

(118) Almtireen, N.; Brandner, J. J.; Korvink, J. G. "Pulse Tube Cryocooler: Phasor Analysis and One-Dimensional Numerical Simulation". *J. Low. Temp. Phys.* **2020**, *199*, 1179–1197 (cit. on pp. 27, 31).

(119) Panda, D.; Kumar, M.; Satapathy, A. K.; Sarangi, S. K.; Sahoo, R. K. "Performance Evaluation of a GM-Type Double Inlet Pulse Tube Refrigerator Using Artificial Intelligence Approach with Experimental Validation". *Arab. J. Sci. Eng.* **2020**, *45*, 9579–9597 (cit. on p. 27).

(120) Qiu, L.; Zhi, X.; Gan, Z.; Zhang, X.; Zhang, X. "Function of gas parcels in the pulse tube". *International Journal of Refrigeration* **2014**, *38*, 358–366 (cit. on pp. 27, 35).

(121) Liang, J. "Thermodynamic cycles in oscillating flow regenerators". *Journal of Applied Physics* **1997**, *82*, 4159–4165 (cit. on pp. 27, 35, 36).

(122) Chen, L.; Zhang, Y.; Luo, E.; Li, T.; Wei, X. "CFD analysis of thermodynamic cycles in a pulse tube refrigerator". *Cryogenics* **2010**, *50*, 743–749 (cit. on pp. 27, 38).

(123) Zhi, X.; Qiu, L.; Pfotenhauer, J. M.; Gan, Z.; Yan, Y. "Refrigeration mechanism of the gas parcels in pulse tube cryocoolers under different phase angles". *International Journal of Heat and Mass Transfer* **2016**, *103*, 382–389 (cit. on pp. 27, 38).

(124) Tsuchiya, A.; Lin, X. G.; Takayama, H.; Saito, M.; Xu, M. Y. "Development of 1.5 W 4 K Two-Stage Pulse Tube Cryocoolers with a Remote Valve Unit". **2014** (cit. on p. 28).

(125) Atrey, M. D., "Cryocoolers: Theory and Applications"; Springer International Publishing: 2020 (cit. on p. 28).

(126) De Waele, A. T. A. M. "Basic Operation of Cryocoolers and Related Thermal Machines". *J. Low. Temp. Phys.* **2011**, *164*, 179–236 (cit. on p. 28).

(127) Cardwell, D. A.; Larbalestier, D. C.; Braginski, A. I., "Handbook of Superconductivity: Processing and Cryogenics, Volume Two"; CRC Press: 2022 (cit. on p. 28).

(128) Hoehne, J. "Development of a dry linear compressor for GM and pulse tube cryocoolers". *IOP Conf. Ser-Mar. Sci.* **2015**, *101*, 012008 (cit. on p. 28).

(129) Will, M.; Tanaeva, I.; Li, R.; de Waele, A. "New rotary valves for pulse-tube refrigerators". *Cryogenics* **2004**, *44*, 793–800 (cit. on p. 30).

(130) Kashani, A.; Helvensteijn, B. P. M.; Kittel, P.; Gschneidner, K. A.; Pecharsky, V. K.; Pecharsky, A. O. In "Cryocoolers 11", Ross, R. G., Ed.; Springer US: Boston, MA, 2002, pp 475–480 (cit. on p. 30).

(131) Mc Carty, R. D. "Thermodynamic Properties of Helium 4 from 2 to 1500 K at Pressures to 108 Pa". *J. Phys. Chem. Ref. Data* **1973**, *2*, 923–1042 (cit. on p. 31).

(132) Joule, J.; Thomson, W. "LXXVI. On the thermal effects experienced by air in rushing through small apertures". *The London, Edinburgh, and Dublin Philosophical Magazine and Journal of Science* **1852**, *4*, 481–492 (cit. on p. 38).

(133) Swenson, C. A. "The Liquid-Solid Transformation in Helium near Absolute Zero". *Phys. Rev.* **1950**, *79*, 626–631 (cit. on p. 40).

(134) NIST *Standard Reference Database 23*, miniREFPROP Software,Version 9.5 (cit. on p. 40).

(135) Mc Carty, R. D. "Thermodynamic Properties of Helium 4 from 2 to 1500 K at Pressures to 108 Pa". *J. Phys. Chem. Ref. Data* **1973**, *2*, 923–1042 (cit. on p. 40).

(136) Arp, V.; Mccarty, R. "Thermophysical properties of Helium-4 from 0.8 to 1500 K with pressures to 2000 MPa". **1989** (cit. on pp. 40, 42, 43).

(137) McCarty, R., "Thermophysical Properties of Helium-4 from 4 to 3000 R with Pressures to 15000 Psia"; NBS technical note Bd. 13; U.S. Government Printing Office: 1972 (cit. on p. 40).

(138) Lebrun, P.; Tavian, L.; Vandoni, G.; Wagner, U. *Cryogenics for Particle Accelerators and Detectors*; tech. rep., revised version number 1 submitted on 2002-12-20 15:27:54; Geneva: CERN, 2002 (cit. on p. 40).

(139) NIST *Saturation Properties for Helium*, Data from NIST Standard Reference Database 69: NIST Chemistry WebBook (cit. on p. 41).

(140) Collins, S. C. "A Helium Cryostat". *Rev. Sci. Instrum.* **1947**, *18*, 157–167 (cit. on p. 40).

(141) De Waele, A. T. A. M. "Basics of Joule–Thomson Liquefaction and JT Cooling". *J. Low. Temp. Phys.* **2017**, *186*, 385–403 (cit. on p. 40).

(142) Huang, B. "Joule—Thomson effect in liquid He II". *Cryogenics* **1986**, *26*, 475–477 (cit. on p. 41).

(143) Lebrun, P. "Superfluid helium as a technical coolant". **1997** (cit. on p. 42).

(144) Ekin, J., "Experimental Techniques for Low-Temperature Measurements: Cryostat Design, Material Properties and Superconductor Critical-Current Testing"; Oxford Univ. Press: 2006 (cit. on pp. 42, 82).

(145) Maytal, B.-Z.; Pfotenhauer, J. M., "Miniature Joule-Thomson Cryocooling"; Springer New York: 2013 (cit. on p. 41).

(146) Jeong, S.; Park, C.; Kim, K. "Design of distributed JT (Joule-Thomson) effect heat exchanger for superfluid 2 K cooling device". *J. Phys. Conf. Ser.* **2018**, *969*, 012084 (cit. on p. 42).

(147) Ni, F.; Huang, Y.; Cao, H. "Thermodynamic limits of 4He and 3He Joule–Thomson cryocoolers". *Energy* **2024**, *313*, 133780 (cit. on p. 42).

(148) Sato, A.; Nimori, S.; Maeda, M.; Nagai, H.; Matsumoto, F.; Takahashi, M.; Kuriyama, T.; Fujioka, T.; Ito, T.; Okamura, T. "Development of a High Field Superconducting Magnet Cooled by a 2 K Cryocooler (2) — Characteristics of 2 K Cryocooler". *AIP Conf. Proc.* **2004**, *710*, 742–749 (cit. on p. 43).

(149) Shimazaki, T.; Toyoda, K.; Tamura, O. "Gifford-McMahon/Joule-Thomson cryocooler with high-flow-conductance counterflow heat exchanger for use in resistance thermometer calibration". *Rev. Sci. Instrum.* **2006**, *77*, 034902 (cit. on p. 43).

(150) Shimazaki, T.; Toyoda, K.; Oota, A.; Nozato, H.; Usuda, T.; Tamura, O. "Closed-Cycle Joule–Thomson Cryocooler for Resistance Thermometer Calibration down to 0.65K". *Int. J. Thermophys.* **2008**, *29*, 42–50 (cit. on p. 43).

(151) Pobell, F., "Matter and Methods at Low Temperatures"; Springer Berlin Heidelberg New York: 2007; Vol. 3 (cit. on pp. 43, 80, 125).

(152) Schmid, M.; Varga, P. "Analysis of vibration-isolating systems for scanning tunneling microscopes". *Ultramicroscopy* **1992**, *42-44*, 1610–1615 (cit. on p. 44).

(153) Molyneux, W. "Supports for Vibration Isolation". *ARC-CP-0322* **1957** (cit. on p. 46).

(154) van Eijk, J.; Dijksman, J. "Plate spring mechanism with constant negative stiffness". *Mech. Mach. Theory* **1979**, *14*, 1–9 (cit. on p. 46).

(155) Platus, D. L. In "Vibration Control in Microelectronics, Optics, and Metrology", ed. by Gordon, C. G., SPIE: 1992; Vol. 1619, pp 44–54 (cit. on p. 46).

(156) Ibrahim, R. "Recent advances in nonlinear passive vibration isolators". *J. Sound Vib.* **2008**, *314*, 371–452 (cit. on p. 46).

(157) Li, H.; Li, Y.; Li, J. "Negative stiffness devices for vibration isolation applications: a review". *Adv. Struct. Eng.* **2020**, *23*, 1739–1755 (cit. on p. 46).

(158) Heyman, J., "Structural Analysis: A Historical Approach"; Cambridge University Press: 1998 (cit. on p. 47).

(159) Blair, D. G.; Ju, L.; Peng, H. "Vibration isolation for gravitational wave detection". *Class. Quant. Gravity* **1993**, *10*, 2407–2418 (cit. on p. 47).

(160) DeSalvo, R. "Passive, nonlinear, mechanical structures for seismic attenuation". *J. Comput. Nonlinear Dynam.* **2007**, *2*, 290–298 (cit. on p. 47).

(161) Feinberg, L. D.; Keski-Kuha, R.; Atkinson, C.; Booth, A.; Whitman, T. In "Space Telescopes and Instrumentation 2014: Optical, Infrared, and Millimeter Wave", ed. by Oschmann, J. M.; Clampin, M.; Fazio, G. G.; MacEwen, H. A., SPIE: 2014 (cit. on p. 47).

(162) Kirk, W. P.; Twerdochlib, M. "Improved method for minimizing vibrational motion transmitted by pumping lines". *Rev. Sci. Instrum.* **1978**, *49*, 765–769 (cit. on pp. 48, 64).

(163) Misra, S.; Zhou, B. B.; Drozdov, I. K.; Seo, J.; Urban, L.; Gyenis, A.; Kingsley, S. C. J.; Jones, H.; Yazdani, A. "Design and performance of an ultra-high vacuum scanning tunneling microscope operating at dilution refrigerator temperatures and high magnetic fields". *Rev. Sci. Instrum.* **2013**, *84*, 103903 (cit. on pp. 48, 63, 64).

(164) Möser, M., "Technische Akustik"; Springer Vieweg Berlin, Heidelberg: 2015; Vol. 10 (cit. on p. 50).

(165) acousticmodelling.com 2011 *Porous Absorber Calculator*, Accessed: 2024-10-24 (cit. on p. 50).

(166) Kalra, R.; Laucht, A.; Dehollain, J. P.; Bar, D.; Freer, S.; Simmons, S.; Muhonen, J. T.; Morello, A. "Vibration-induced electrical noise in a cryogen-free dilution refrigerator: characterization, mitigation, and impact on qubit coherence". *Rev. Sci. Instrum.* **2016**, *87*, 073905 (cit. on pp. 52, 97).

(167) Jung, J.-O.; Choi, S.; Lee, Y.; Kim, J.; Son, D.; Lee, J. "Versatile variable temperature and magnetic field scanning probe microscope for advanced material research". *Rev. Sci. Instrum.* **2017**, *88*, 103702 (cit. on p. 63).

(168) Wong, D.; Jeon, S.; Nuckolls, K. P.; Oh, M.; Kingsley, S. C. J.; Yazdani, A. "A modular ultra-high vacuum millikelvin scanning tunneling microscope". *Rev. Sci. Instrum.* **2020**, *91*, 023703 (cit. on p. 63).

(169) Assig, M.; Etzkorn, M.; Enders, A.; Stiepany, W.; Ast, C. R.; Kern, K. "A 10 mK scanning tunneling microscope operating in ultra high vacuum and high magnetic fields". *Rev. Sci. Instrum.* **2013**, *84*, 033903 (cit. on pp. 63, 132).

(170) Song, Y. J.; Otte, A. F.; Shvarts, V.; Zhao, Z.; Kuk, Y.; Blankenship, S. R.; Band, A.; Hess, F. M.; Stroscio, J. A. "Invited review article: a 10 mK scanning probe microscopy facility". *Rev. Sci. Instrum.* **2010**, *81*, 121101 (cit. on pp. 63, 132).

(171) Assig, M.; Koch, A.; Stiepany, W.; Straßer, C.; Ast, A.; Kern, K.; Ast, C. R. "Miniature active damping stage for scanning probe applications in ultra high vacuum". *Rev. Sci. Instrum.* **2012**, *83*, 033701 (cit. on p. 63).

(172) C. Ast, private communication (cit. on p. 64).

(173) Minus K Technology Inc. *CM-1 Low Frequency Vibration Isolator*, Accessed: 2024-09-25 (cit. on p. 64).

(174) Falter, J.; Schmidt, J.; Herrmann, X.; Schmidt, B.; Dietzel, D.; Schirmeisen, A. *Intermediate Heat Exchanger for accessing Regenerator Cooling Capacity*, Prepint at http://dx.doi.org/10.2139/ssrn.4814535, 2024 (cit. on p. 76).

(175) Snodgrass, R.; Swift, G.; Ullom, J.; Backhaus, S. "Intermediate cooling from pulse tube refrigerator regenerators operating in the real-fluid regime". *Cryogenics* **2023**, *132*, 103685 (cit. on p. 76).

(176) Radebaugh, R.; Marquardt, E. D.; Gary, J.; O'Gallagher, A. In "Cryocoolers 11", Ross, R. G., Ed.; Springer US: Boston, MA, 2002, pp 409–418 (cit. on p. 76).

(177) Zhu, S.; Ichikawa, M.; Nogawa, M.; Inoue, T. "4 K pulse tube refrigerator and excess cooling power". *AIP Conf. Proc.* **2002**, *613*, 633–640 (cit. on p. 76).

(178) White, G. K.; Meeson, P. J., "Experimental Techniques in Low-temperature Physics"; Monographs on the physics and chemistry of materials; Clarendon Press: 2002 (cit. on pp. 80, 107).

(179) Dickson, P., "Infrared Reflectances of Metals at Cryogenic Temperatures: A Compilation from the Literature"; U.S. Government Printing Office: 1966 (cit. on p. 81).

(180) Berman, R. "Some Experiments on Thermal Contact at Low Temperatures". *J. Appl. Phys.* **1956**, *27*, 318–323 (cit. on p. 82).

(181) Salerno, L.; Kittel, P., "Thermal contact conductance"; NASA technical memorandum; National Aeronautics and Space Administration, Ames Research Center: 1997 (cit. on p. 82).

(182) Spura, C.; Wittel, H.; Jannasch, D., "Roloff/Matek Maschinenelemente Formelsammlung"; PUBDB-2024-05842; Springer: 2023 (cit. on p. 82).

(183) Wegertseder GmbH *Technische Daten (TD), Werkstoffe - Edelstähle*, Accessed: 2025-05-21 (cit. on p. 82).

(184) Wachowiak, A. *Aufbau einer 300mK-Ultrahochvakuum-Rastertunnelmikroskopie-Anlage mit 14 Tesla Magnet und spinpolarisierte Rastertunnelspektroskopie an ferromagnetischen Fe-Inseln*, Ph.D. Thesis, Universität Hamburg, 2003 (cit. on p. 84).

(185) Dubois, J. G. A.; Gerritsen, J. W.; Hermsen, J. G. H.; van Kempen, H. "A low temperature scanning tunneling microscope for use in high magnetic fields". *Rev. Sci. Instrum.* **1995**, *66*, 4146–4149 (cit. on p. 84).

(186) Mashoff, T. *Aufbau eines UHV-Rastertunnelmikroskops mit X-Y-Verschiebetisch fÄur den Einsatz bei tiefen Temperaturen und im Magnetfeld*, Diplomathesis, Universität Hamburg, 2004 (cit. on p. 84).

(187) Hwang, J.; Krylov, D.; Elbertse, R.; Yoon, S.; Ahn, T.; Oh, J.; Fang, L.; Jang, W.-j.; Cho, F. H.; Heinrich, A. J.; Bae, Y. "Development of a scanning tunneling microscope for variable temperature electron spin resonance". *Rev. Sci. Instrum.* **2022**, *93*, 093703 (cit. on pp. 84, 140, 149).

(188) Foley, E. T.; Yoder, N. L.; Guisinger, N. P.; Hersam, M. C. "Cryogenic variable temperature ultrahigh vacuum scanning tunneling microscope for single molecule studies on silicon surfaces". *Rev. Sci. Instrum.* **2004**, *75*, 5280–5287 (cit. on p. 84).

(189) White, S. C.; Singh, U. R.; Wahl, P. "A stiff scanning tunneling microscopy head for measurement at low temperatures and in high magnetic fields". *Rev. Sci. Instrum.* **2011**, *82*, 113708 (cit. on pp. 84, 85).

(190) Battisti, I.; Verdoes, G.; van Oosten, K.; Bastiaans, K. M.; Allan, M. P. "Definition of design guidelines, construction, and performance of an ultra-stable scanning tunneling microscope for spectroscopic imaging". *Rev. Sci. Instrum.* **2018**, *89*, 123705 (cit. on pp. 84, 85).

(191) "Cryogenic spectroscopic imaging scanning tunnelling microscope in a water-cooled magnet down to 1.7 K". *Ultramicroscopy* **2023**, *253*, 113773 (cit. on pp. 84, 85).

(192) Wang, J.; Li, Z.; Zhao, K.; Dong, S.; Wu, D.; Meng, W.; Zhang, J.; Hou, Y.; Lu, Y.; Lu, Q. "Isolated scan unit and scanning tunneling microscope for stable imaging in ultra-high magnetic fields". *Ultramicroscopy* **2024**, *261*, 113960 (cit. on p. 84).

(193) Singh, J.; Singh, C.; Singh, K. "Rotary ultrasonic machining of advance materials: A review". *Materials Today: Proceedings* **2023**, DOI: https://doi.org/10.1016/j.matpr.2023.01.159 (cit. on p. 84).

(194) Lide, D., "CRC Handbook of Chemistry and Physics, 79th edn." CRC Press LLC: 1998 (cit. on p. 85).

(195) Walsh, K.; Vidal, E., "Beryllium Chemistry and Processing"; ASM International: 2009 (cit. on p. 85).

(196) Ho, C. Y.; Powell, R. W.; Liley, P. E. "Thermal Conductivity of the Elements". *J. Phys. Chem. Ref. Data* **1972**, *1*, 279–421 (cit. on p. 85).

(197) Rayotek Scientific Inc. *SAPPHIRE PROPERTIES DATA SHEET*, Accessed: 2024-09-18 (cit. on p. 85).

(198) Groover, M., "Fundamentals of Modern Manufacturing: Materials, Processes, and Systems"; John Wiley & Sons: 2010 (cit. on p. 85).

(199) Ghavami, A.; Ghiaasiaan, S. M. "Thermal Conductivity of Some Ceramic Materials at Cryogenic Temperatures". *ASME Journal of Heat and Mass Transfer* **2022**, *145*, 043501 (cit. on p. 85).

(200) NEMOTO, T.; SASAKI, S.; HAKURAKU, Y. "Thermal conductivity of alumina and silicon carbide ceramics at low temperatures". *TEION KOGAKU (Journal of Cryogenics and Superconductivity Society of Japan)* **1985**, *20*, 166–167 (cit. on p. 85).

(201) De Faoite, D.; Browne, D.; Chang-Díaz, F.; Stanton, K. "A review of the processing, composition, and temperature-dependent mechanical and thermal properties of dielectric technical ceramics". *J. Mater. Science* **2012**, *47*, 4211–4235 (cit. on p. 85).

(202) Precision Ceramics USA, inC. *Shapal Hi M Soft™*, Accessed: 2024-05-14 (cit. on p. 85).

(203) Tuttle, J.; Canavan, E.; Jahromi, A. "Cryogenic thermal conductivity measurements on candidate materials for space missions". *Cryogenics* **2017**, *88*, 36–43 (cit. on p. 85).

(204) MatWeb, LLC *Tungsten Carbide, WC*, Accessed: 2024-09-18 (cit. on p. 85).

(205) Blau, P.; Bayer, R., "Wear of Materials"; Wear of Materials: Proceedings of the Fourteenth International Conference on Wear of Materials, Washington, DC, USA, 30 March-3 April 2003; Elsevier Science: 2003 (cit. on p. 85).

(206) MatWeb, LLC *CeramTec 848 Zirconia (ZrO2)*, Accessed: 2024-09-18 (cit. on p. 85).

(207) Corning SAS *MACOR® Maschinell bearbeitbare Glaskeramik für Industrieanwendungen*, Accessed: 2024-09-18 (cit. on p. 85).

(208) Thyssenkrupp Materials Services GmbH *Material Data Sheet Aluminium alloy*, Accessed: 2024-09-18 (cit. on p. 85).

(209) Thyssenkrupp Materials (UK) Ltd *Stainless Steel 304 1.4301*, Accessed: 2024-09-18 (cit. on p. 85).

(210) National Institute of Standards and Technology *Index of Material Properties Properties of solid materials from cryogenic- to room-temperatures*, Accessed: 2024-09-18 (cit. on p. 85).

(211) Copper Development Association Inc. *C17510 Copper Beryllium*, Accessed: 2024-09-18 (cit. on p. 85).

(212) Walter Looser AG *Caro Bronze – CuSn8P DIN EN 12163/12167/12449*, Accessed: 2024-09-18 (cit. on p. 85).

(213) Tuttle, J.; Canavan, E.; DiPirro, M. "THERMAL AND ELECTRICAL CONDUCTIVITY MEASUREMENTS OF CDA 510 PHOSPHOR BRONZE". *AIP Conf. Proc.* **2010**, *1219*, 55–62 (cit. on p. 85).

(214) Precision Ceramics USA, inC. *OUTGASSING DATA of Shapal M -ceramic As received , Cleaned With Alcohol*, Accessed: 2024-09-16 (cit. on p. 85).

(215) EPOXY TECHNOLOGY, INC. *Technical Data Sheet*, Accessed: 2024-09-18 (cit. on p. 86).

(216) Montag, D. *Aufbau eines Multikontakt-Rastertunnelmikroskops für Einzelelektron Messungen bei tiefen Temperaturen und im Magnetfeld*, Diplomathesis, RWTH Aachen University, 2014 (cit. on p. 86).

(217) Henze Boron Nitride Products AG *HeBoSint® CLASSIC LINE*, Datasheet Accessed: 2020-08-10 (cit. on p. 86).

(218) Muckel, F. *Sub 1K uhv scanning tunneling microscope made of shapal and mapping of magnetic skyrmion collapse rates*, Ph.D. Thesis, RWTH Aachen University, 2020 (cit. on p. 93).

(219) Wiebe, J.; Wachowiak, A.; Meier, F.; Haude, D.; Foster, T.; Morgenstern, M.; Wiesendanger, R. "A 300 mK ultra-high vacuum scanning tunneling microscope for spin-resolved spectroscopy at high energy resolution". *Rev. Sci. Instrum.* **2004**, *75*, 4871–4879 (cit. on p. 93).

(220) Mykkänen, E.; Lehtinen, J. S.; Kemppinen, A.; Krause, C.; Drung, D.; Nissilä, J.; Manninen, A. J. "Reducing current noise in cryogenic experiments by vacuum-insulated cables". *Rev. Sci. Instrum.* **2016**, *87*, 105111 (cit. on p. 97).

(221) Ong, P. P. "Supersensitive electrical measurements and their associated techniques". *Eur. J. Phys.* **1987**, *8*, 280 (cit. on p. 97).

(222) Geringer, V. *Aufbau und Charakterisierung eines Rastertunnelmikroskops mit Verschiebetisch für den Einsatz im Ultrahochvakuum, bei tiefen Temperaturen und im Magnetfeld*, Diplomathesis, RWTH Aachen University, 2006 (cit. on p. 127).

(223) Libisch, F.; Geringer, V.; Subramaniam, D.; Burgdörfer, J.; Morgenstern, M. "Diffractive-wave guiding of surface electrons on Au(111) by the herringbone reconstruction potential". *Phys. Rev. B* **2014**, *90*, 035442 (cit. on pp. 128–130).

(224) Barth, J. V.; Brune, H.; Ertl, G.; Behm, R. J. "Scanning tunneling microscopy observations on the reconstructed Au(111) surface: atomic structure, long-range superstructure, rotational domains, and surface defects". *Phys. Rev. B* **1990**, *42*, 9307–9318 (cit. on p. 128).

(225) Chen, W.; Madhavan, V.; Jamneala, T.; Crommie, M. F. "Scanning tunneling microscopy observation of an electronic superlattice at the surface of clean gold". *Phys. Rev. Lett.* **1998**, *80*, 1469–1472 (cit. on pp. 128, 145).

(226) Fujita, D.; Amemiya, K.; Yakabe, T.; Nejoh, H.; Sato, T.; Iwatsuki, M. "Anisotropic Standing-Wave Formation on an Au(111)- $(23 \times \sqrt{3})$ Reconstructed Surface". *Phys. Rev. Lett.* **1997**, *78*, 3904–3907 (cit. on p. 128).

(227) McMillan, W. L.; Rowell, J. M. "Lead Phonon Spectrum Calculated from Superconducting Density of States". *Phys. Rev. Lett.* **1965**, *14*, 108–112 (cit. on p. 132).

(228) Franck, J. P.; Martin, D. L. "THE SUPERCONDUCTING TRANSITION TEMPERATURE OF LEAD". *Can. J. Phys.* **1961**, *39*, 1320–1329 (cit. on p. 132).

(229) Townsend, P.; Sutton, J. "Investigation by Electron Tunneling of the Superconducting Energy Gaps in Nb, Ta, Sn, and Pb". *Phys. Rev.* **1962**, *128*, 591–595 (cit. on p. 132).

(230) Klapwijk, T.; Blonder, G.; Tinkham, M. "Explanation of subharmonic energy gap structure in superconducting contacts". *Physica B+C* **1982**, *109-110*, 16th International Conference on Low Temperature Physics, Part 3, 1657–1664 (cit. on pp. 133, 137).

(231) Ternes, M.; Schneider, W.-D.; Cuevas, J.-C.; Lutz, C. P.; Hirjibehedin, C. F.; Heinrich, A. J. "Subgap structure in asymmetric superconducting tunnel junctions". *Phys. Rev. B* **2006**, *74*, 132501 (cit. on p. 133).

(232) Josephson, B. "Possible new effects in superconductive tunnelling". *Physics Letters* **1962**, *1*, 251–253 (cit. on p. 133).

(233) Josephson, B. D. "Coupled Superconductors". *Rev. Mod. Phys.* **1964**, *36*, 216–220 (cit. on p. 133).

(234) Rodrigo, J. G.; Suderow, H.; Vieira, S. "On the use of STM superconducting tips at very low temperatures". *Eur. Phys. J. B* **2004**, *40*, 483–488 (cit. on p. 133).

(235) Bardeen, J.; Cooper, L. N.; Schrieffer, J. R. "Theory of Superconductivity". *Phys. Rev.* **1957**, *108*, 1175–1204 (cit. on p. 137).

(236) Onnes, H. K. "The disappearance of the resistivity of mercury". *Comm. Leiden* **1911**, *122* (cit. on p. 137).

(237) Andreev, A. "The Thermal Conductivity of the Intermediate State in Superconductors". *JETP* **1964**, *19*, 1228 (cit. on p. 137).

(238) Averin, D.; Nazarov, Y.; Odintsov, A. "Incoherent tunneling of the cooper pairs and magnetic flux quanta in ultrasmall Josephson junctions". *Physica B: Condensed Matter* **1990**, *165-166*, LT-19, 945–946 (cit. on p. 138).

(239) Ingold, G.-L.; Grabert, H.; Eberhardt, U. "Cooper-pair current through ultrasmall Josephson junctions". *Phys. Rev. B* **1994**, *50*, 395–402 (cit. on p. 138).

(240) Jäck, B.; Eltschka, M.; Assig, M.; Hardock, A.; Etzkorn, M.; Ast, C. R.; Kern, K. "A nanoscale gigahertz source realized with Josephson scanning tunneling microscopy". *Appl. Phys. Lett.* **2015**, *106*, 013109 (cit. on p. 138).

(241) Müllegger, S.; Das, A. K.; Mayr, K.; Koch, R. "Radio-frequency excitation of single molecules by scanning tunnelling microscopy". *Nanotechnology* **2014**, *25*, 135705 (cit. on p. 140).

(242) Hervé, M.; Peter, M.; Wulfhekel, W. "High frequency transmission to a junction of a scanning tunneling microscope". *Appl. Phys. Lett.* **2015**, *107*, 093101 (cit. on pp. 140, 147).

(243) Moult, I.; Herve, M.; Pennec, Y. "Ultrafast spectroscopy with a scanning tunneling microscope". *Appl. Phys. Lett.* **2011**, *98*, 233103 (cit. on p. 140).

(244) Saunus, C.; Raphael Bindel, J.; Pratzer, M.; Morgenstern, M. "Versatile scanning tunneling microscopy with 120 ps time resolution". *Appl. Phys. Lett.* **2013**, *102*, 051601 (cit. on p. 140).

(245) Grosse, C.; Etzkorn, M.; Kuhnke, K.; Loth, S.; Kern, K. "Quantitative mapping of fast voltage pulses in tunnel junctions by plasmonic luminescence". *Appl. Phys. Lett.* **2013**, *103*, 183108 (cit. on p. 140).

(246) Paul, W.; Baumann, S.; Lutz, C. P.; Heinrich, A. J. "Generation of constant-amplitude radio-frequency sweeps at a tunnel junction for spin resonance STM". *Rev. Sci. Instrum.* **2016**, *87*, 074703 (cit. on pp. 140, 145, 147, 149).

(247) Baumann, S.; McMurtrie, G.; Hänze, M.; Betz, N.; Arnhold, L.; Malavolti, L.; Loth, S. "An Atomic-Scale Vector Network Analyzer". *Small Methods* **2024**, *8*, 2301526 (cit. on p. 140).

(248) Feigl, S.; Vranik, R.; Wit, B.; Müllegger, S. "Frequency-independent voltage amplitude across a tunnel junction". *Rev. Sci. Instrum.* **2021**, *92*, 043710 (cit. on p. 140).

(249) Schwenk, J.; Soulard, C. M.; Shan, S.; Patthey, F.; Brune, H. "A high bandwidth and high transmission STM bias line for ESR and quantum stochastic resonance measurements at 0.4 K". *Rev. Sci. Instrum.* **2025**, *96*, 023706 (cit. on p. 140).

(250) Tu, X. W.; Lee, J. H.; Ho, W. "Atomic-scale rectification at microwave frequency". *J. Chem. Phys.* **2006**, *124*, 021105 (cit. on p. 140).

(251) Peters, O.; Bogdanoff, N.; Acero González, S.; Melischek, L.; Simon, J. R.; Reecht, G.; Winkelmann, C. B.; von Oppen, F.; Franke, K. J. "Resonant Andreev reflections probed by photon-assisted tunnelling at the atomic scale". *Nat. Phys.* **2020**, *16*, 1222–1226 (cit. on pp. 140, 149).

(252) Kot, P.; Drost, R.; Uhl, M.; Ankerhold, J.; Cuevas, J. C.; Ast, C. R. "Microwave-assisted tunneling and interference effects in superconducting junctions under fast driving signals". *Phys. Rev. B* **2020**, *101*, 134507 (cit. on pp. 140, 141).

(253) Roychowdhury, A.; Dreyer, M.; Anderson, J. R.; Lobb, C. J.; Wellstood, F. C. "Microwave photon-assisted incoherent Cooper-pair tunneling in a Josephson STM". *Phys. Rev. Appl.* **2015**, *4*, 034011 (cit. on pp. 140, 141, 145).

(254) Seifert, T. S.; Kovarik, S.; Nistor, C.; Persichetti, L.; Stepanow, S.; Gambardella, P. "Single-atom electron paramagnetic resonance in a scanning tunneling microscope driven by a radio-frequency antenna at 4 K". *Phys. Rev. Res.* **2020**, *2*, 013032 (cit. on pp. 140, 145).

(255) Doležal, J.; Merino, P.; Švec, M. "Constant amplitude driving of a radio frequency excited plasmonic tunnel junction". *Appl. Phys. Lett.* **2021**, *118*, 193301 (cit. on p. 140).

(256) Drost, R.; Uhl, M.; Kot, P.; Siebrecht, J.; Schmid, A.; Merkt, J.; Wünsch, S.; Siegel, M.; Kieler, O.; Kleiner, R.; Ast, C. R. "Combining electron spin resonance spectroscopy with scanning tunneling microscopy at high magnetic fields". *Rev. Sci. Instrum.* **2022**, *93*, 043705 (cit. on p. 140).

(257) Shapiro, S. "Josephson Currents in Superconducting Tunneling: The Effect of Microwaves and Other Observations". *Phys. Rev. Lett.* **1963**, *11*, 80–82 (cit. on p. 141).

(258) Ingold, G.-L.; Nazarov, Y. V. In "Single Charge Tunneling: Coulomb Blockade Phenomena In Nanostructures", Grabert, H., Devoret, M. H., Eds.; Springer US: Boston, MA, 1992, pp 21–107 (cit. on p. 141).

(259) Peters, O. J. *Transport Processes through Superconducting Junctions at the Atomic Scale*, Ph.D. Thesis, Freien Universität Berlin, 2020 (cit. on p. 141).

(260) Tien, P. K.; Gordon, J. P. "Multiphoton process observed in the interaction of microwave fields with the tunneling between superconductor films". *Phys. Rev.* **1963**, *129*, 647–651 (cit. on p. 141).

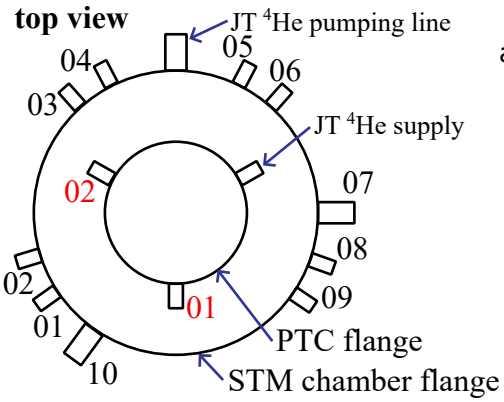
(261) Falci, G.; Bubanja, V.; Schön, G. "Quasiparticle and Cooper pair tenneling in small capacitance Josephson junctions: effects of the electromagnetic environment". *Z. Phys. B: Cond. Mat.* **1991**, *85*, 451–458 (cit. on p. 141).

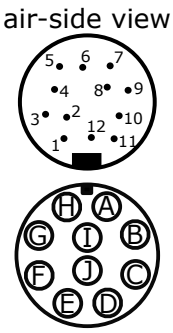
(262) Baumann, S.; Paul, W.; Choi, T.; Lutz, C. P.; Ardavan, A.; Heinrich, A. J. "Electron paramagnetic resonance of individual atoms on a surface". *Science* **2015**, *350*, 417–420 (cit. on p. 149).

A. Appendix

A.1. Wiring pin layout

The wiring pin layout is given in the following pages. The pin layout of the UHV feedthroughs is given in Figure A.1 and Figure A.2, including the type and resistance of the complete wires in UHV at room temperature up to the JT stage connector or up to the temperature sensor or heater attached. The pin layout of the thermalization connectors inside UHV, mounted at the 4 K and 80 K plate, is given in Figure A.3. The connectors are physically marked by engraving numbers I to VIII on top of them. The STM wire pin layout at the JT stage connectors and at the STM is given in Figure A.4. The capacitances measured at the UHV feedthroughs of the piezos are given in Figure A.5.





abbreviations	
TS	temperature sensor
HE	heat exchanger
TP	twisted pair
Mn	manganine
Cu	copper
SS	stainless steel
CSF	coaxial steel flex

connector 01 Allectra 220-CM12-C16			
function	**pin**	**wire**	**R (Ω)(300K)**
TS HE 4K DT-670-A1-CO D6097499 V+	1	TP 0,1 SS	151
V-	2		151
I+	3	TP 0,1 SS	151
I-	4		151
TS PTC 50K DT-670-A1-CO D6065751 V+	5	TP 0,1 SS	75
V-	6		75
I+	7	TP 0,1 SS	75
I-	8		75
heater PTC 50K 50Ω	9	TP 0,355 Mn	2
	10		2
heater HE 4K 50Ω	11	TP 0,355 Mn; 0,1 Cu (4K-50K)	5,4
	12		5,4

connector 02 Allectra 220-CM12-C16			
function	**pin**	**wire**	**R (Ω)(300K)**
TS JT CX-1030-CO-HT-0,3M X163902 V+	1	TP 0,1SS	112,9
V-	2		124,3
I+	3	TP 0,1SS	114,5
I-	4		113,5
TS STM CX-1030-SD-HT-0,3M V+	5	TP 0,1SS	99,5
V-	6		99,5
I+	7	TP 0,1SS	99,4
I-	8		99,8
TS 4KPlate NTCRTD X78611 V+	9	TP 0,1SS	
V-	10		
I+	11	TP 0,1SS	
I-	12		

Figure A.1.: **Wiring UHV feedthroughs.**

connector 04 Allectra 220-CM12-C16			
function	**pin**	**wire**	**R (Ω)(300K)**
sample contact 1	1	TP 0,1SS	98
sample contact 2	2		98
sample contact 3	3	CSF	1,3
sample contact 3 GND	4		x
sample contact 4	5	CSF	1,3
sample contact 4 GND	6		x
sample contact 5	7	TP 0,1SS	98
sample contact 6	8		98

connector 09 Allectra 221-10AL700-10-C16			
function	**pin**	**wire**	**R (Ω)(300K)**
scanner z	A		88
scanner x+	B	TP 0,1 SS	89
scanner x-	C		89
scanner y+	D	TP 0,1 SS	89
scanner y-	E		89
heater JT 200 Ω	F	TP 0,355 Mn	215,8
heater JT	G		connected

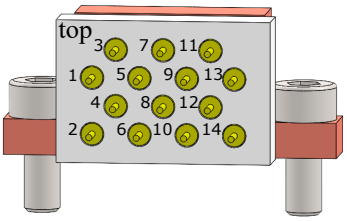
connector 08 Allectra 221-10AL700-10-C16			
function	**pin**	**wire**	**R (Ω)(300K)**
coarse z left	A	0,1 SS	87,5
coarse z right	B	0,1 SS	87,3
coarse z front	C	0,1 SS	87,5
GND piezo	D	0,1 SS	87,4
sample stage x	E	0,1 SS	87,4
sample stage y	F	0,1 SS	87,3

Figure A.2.: **Wiring UHV feedthroughs.**

I 50K	
function	**pin**
sample contact 1	1
sample contact 2	2
sample contact 3	3
sample contact 3 GND	4
sample contact 4	5
sample contact 4 GND	6
sample contact 5	7
sample contact 6	8
Tip	13
Tip GND	14

V 4K	
function	**pin**
sample contact 1	1
sample contact 2	2
sample contact 3	3
sample contact 3 GND	4
sample contact 4	5
sample contact 4 GND	6
sample contact 5	7
sample contact 6	8
Tip	13
Tip GND	14

ceramic side view



II 50K	
function	**pin**
scanner z	1
scanner x+	2
scanner x-	3
scanner y+	4
scanner y-	5
heater JT	11
heater JT	12

VI 02 4K	
function	**pin**
scanner z	1
scanner x+	2
scanner x-	3
scanner y+	4
scanner y-	5
heater JT	11
heater JT	12

IV 50K	
function	**pin**
TS JT V+	1
V-	2
I+	3
I-	4
TS STM V+	5
V-	6
I+	7
I-	8
TS 4KPlate V+	11
I+	12
V-	13
I-	14

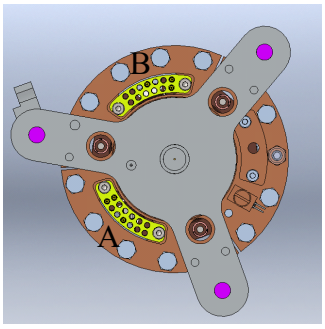
VIII 4K	
function	**pin**
TS JT V+	1
V-	2
I+	3
I-	4
TS STM V+	5
V-	6
I+	7
I-	8

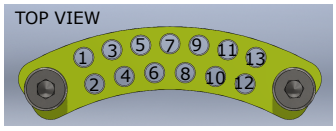
III 50K	
function	**pin**
coarse z left	1
coarse z right	2
defect(Isolation)	3
GND Piezo	4
sample stage x	5
sample stage y	6
coarse z front	7

VII 4K	
function	**pin**
coarse z links	1
coarse z rechts	2
coarse z vorne	3
GND Piezo	4
sample stage x	5
sample stage y	6

Figure A.3.: **Pin layout of thermalization connectors in UHV.**

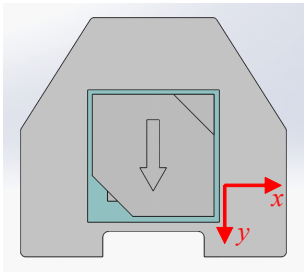
STM pin layout at JT stage

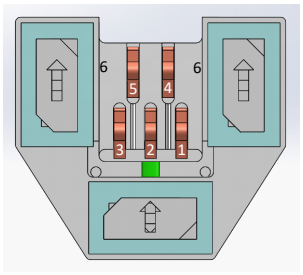


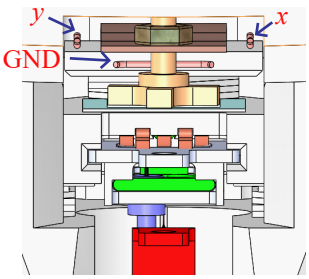


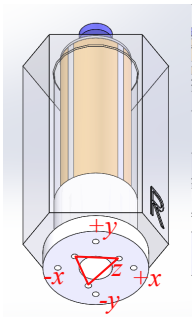
A	B
1: tip	1: TS STM V+
2: tip GND	2: TS STM V-
3: sample contact 1	3: TS STM I+
4: sample contact 2	4: TS STM I-
5: sample contact 3	5: coarse z left
6: sample contact 4	6: coarse z right
7: sample contact 5	7: coarse z front
8: sample contact 6	11: piezo GND
9: scanner z	12: sample stage x
10: scanner x+	13: sample stage y
11: scanner x-	
12: scanner y+	
13: scanner y-	

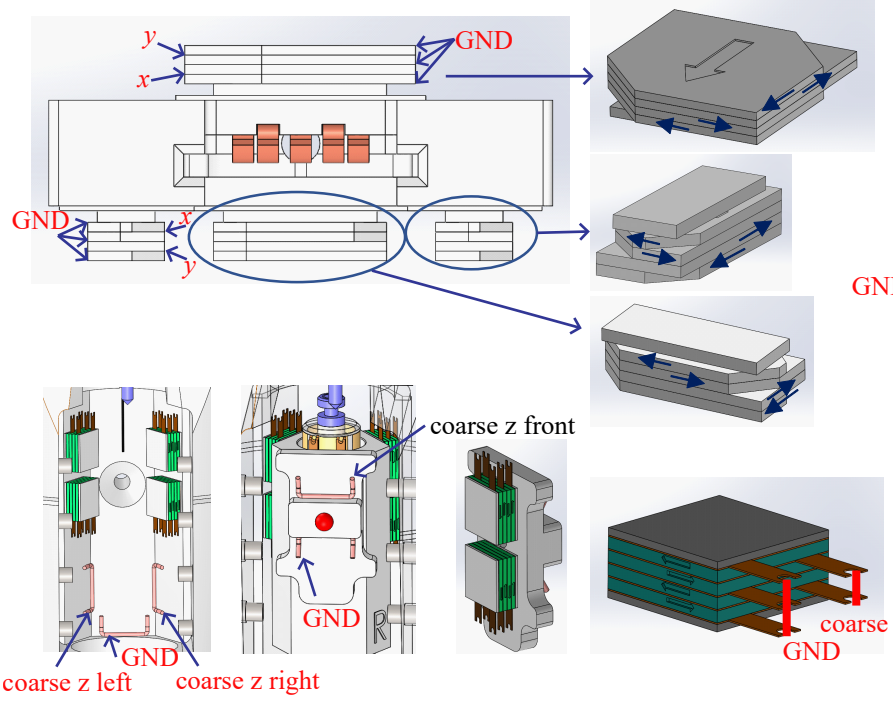
STM pin layout











sample stage contacts:
TP Cu 0.1 mm
1&2
3&4
5&6

piezo wires:
Cu 0.2 mm

Figure A.4.: **STM pin layout at the JT stage connectors and at the STM.**

	test configuration	C (nF) STM in cryo 300K	C (nF) STM in cryo 12K
scanner	z, +x	1.84	0.82
	z, -x	1.86	0.83
	z, +y	1.86	0.83
	z, -y	1.84	0.83
	+x, -x	0.99	0.52
	+x, -y	0.94	0.49
	-x, +y	0.95	0.49
	-x, -y	0.95	0.49
	+y, -y	0.99	0.52
	coarse z left, GND	5.41	2.16
	coarse z right, GND	5.42	2.17
	coarse z front, GND	5.45	2.18
	sample stage x, GND	10.22	3.85
	sample stage y, GND	10.47	4.19
	sample stage x, y	5.19	2.09

Figure A.5.: **Piezo capacitances.**

B. Acknowledgments

First and foremost, I would like to express my gratitude to my supervisor, *Prof. Dr. Markus Morgenstern* for his invaluable guidance, continuous support, and insightful discussions throughout the course of this research. He made the project of developing the PTC operated STM possible by providing the resources of his institute.
Special thanks go to my office colleague *Dr. Marco Pratzer*. Daily discussions about novel ideas could always be addressed and helped my work progress. I could benefit from his huge gathered knowledge of technical aspects. His sporting events organized alongside work provided the necessary balance. Thanks for the continuous support and the nice working environment. Both their expertise and encouragement have been essential in shaping this work.
I like to thank *Prof. Dr. Markus Ternes* for being my second examiner.
Furthermore, I acknowledge the invaluable contribution of CryoVac with all their employees, and particularly *Dr. Michael Krzyzowski*, with whom we had many meetings resulting in a fruitful cooperation. Their knowledge in cryogenics, optimization of key cryogenic components, and support in the assembly played a crucial role in the success of this project.
I want to thank the German Ministry for Economic Affairs and Climate Action (BMWK) via the ZIM project ZF 4367101SY6 for financial support.
A significant part of this thesis involved the fabrication and assembly of experimental setups, and I am grateful to *Frank Neubauer*, *Raoul Sous* and the whole team of the mechanical workshop for their dedication in manufacturing many of the essential components. Their craftsmanship and problem-solving skills were instrumental in realizing the setup.
Similarly, my thanks go to the electrical workshop, *Uwe Wichmann*, *Guido Geulen*, *Lars van Hove* and *Paul Dinslage* for their expertise in integrating various components, ensuring the smooth operation of the system.

I want to thank *Jörg Schirra* and *Sascha Mohr* for the supply of cryoliquids as well as for the plumbing work done at the PTC helium compressor.
I would also like to thank *Dr. Jens Falter* very much for the good advice regarding the PTC integrated into the system and the brief introduction to its working principle.
I am grateful for the discussions with *Prof. Dr. Christian Ast* and *Prof. Dr. Stefan Hild*.
I thank *Margaret Betger*, *Beate Nagel*, *Beatrix Dangela*, *Alice Neycken* and *Nermina Ferhatbegovic* for the helpful navigation through bureaucracy.
I would also like to extend my sincere appreciation to all the other members of the 2nd Institute of Physics B of the RWTH Aachen for their collaboration, stimulating discussions, and the supportive environment that made this journey both productive and enjoyable. Thanks to my students *Marc Frömming* and *Jean-Marc Grigoleit* for their excellent work on the project. Thanks to *Jonas Duffhauß* introducing me to the radio frequency measurement setup and multiple discussions in the office. Thanks to my colleagues *Dr. Timofey Balashov*, *Jonas Beeker*, *Dr. Priyamvada Bhaskar*, *Dr. Biplab Bhattacharyya*, *Dr. Kilian Flöhr*, *Kanji Furuta*, *Dishi Gangwar*, *Reza Habibipour*, *Dr. Christian Holl*, *Tim Jacobs*, *Dr. Felix Jekat*, *Dr. Tjorven Johnsen*, *Dr. Philipp Küppers*, *Niklas Leuth*, *Dr. Marcus Liebmann*, *Dr. Florian Muckel*, *Benjamin Pestka*, *Michiel Reul*, *Dr. Sayanti Samaddar* and *Jeff Strasdas* for the help during my years at the institute, it was always a pleasant working environment.
I would like to thank the group of *Prof. Dr. Bluhm*, *Prof. Dr. Klemradt* and *Prof. Dr. Stampfer* for sharing institute resources, for having a good community and good discussions e.g. in Söllerhaus.
Finally, I am indebted to my family and friends for their unwavering encouragement, patience, and support throughout this journey. Their belief in me has been a constant source of motivation.
This work would not have been possible without the collective efforts of all those mentioned above, and for that, I am truly grateful.

Publications

Publications described within this thesis

M. Eßer, M. Pratzer, M. Frömming, J. Duffhauß, P. Bhaskar, M. Krzyzowski, M. Morgenstern. "An ultra-high vacuum scanning tunneling microscope with pulse tube and Joule–Thomson cooling operating at sub-pm z-noise". *Rev. Sci. Instrum.*, 95, 1237032024, **2024**. https://doi.org/10.1063/5.0230892.

Eidesstattliche Erklärung

Marcus Pascal Eßer

erklärt hiermit, dass diese Dissertation und die darin dargelegten Inhalte die eigenen sind und selbstständig, als Ergebnis der eigenen originären Forschung, generiert wurden. Hiermit erkläre ich an Eides statt

1. Diese Arbeit wurde vollständig oder größtenteils in der Phase als Doktorand dieser Fakultät und Universität angefertigt;

2. Sofern irgendein Bestandteil dieser Dissertation zuvor für einen akademischen Abschluss oder eine andere Qualifikation an dieser oder einer anderen Institution verwendet wurde, wurde dies klar angezeigt;

3. Wenn immer andere eigene- oder Veröffentlichungen Dritter herangezogen wurden, wurden diese klar benannt;

4. Wenn aus anderen eigenen- oder Veröffentlichungen Dritter zitiert wurde, wurde stets die Quelle hierfür angegeben. Diese Dissertation ist vollständig meine eigene Arbeit, mit der Ausnahme solcher Zitate;

5. Alle wesentlichen Quellen von Unterstützung wurden benannt;

6. Wenn immer ein Teil dieser Dissertation auf der Zusammenarbeit mit anderen basiert, wurde von mir klar gekennzeichnet, was von anderen und was von mir selbst erarbeitet wurde;

7. Ein Teil oder Teile dieser Arbeit wurden zuvor veröffentlicht und zwar in:
   Rev. Sci. Instrum. **95**, 123703 (2024).